

# Sheffield Hallam University

*Synthesis and characterisation of sol- gel based ionogels as electrolyte for supercapacitors*

JANANI, Ronak

Available from the Sheffield Hallam University Research Archive (SHURA) at:

<http://shura.shu.ac.uk/24807/>

## A Sheffield Hallam University thesis

This thesis is protected by copyright which belongs to the author.

The content must not be changed in any way or sold commercially in any format or medium without the formal permission of the author.

When referring to this work, full bibliographic details including the author, title, awarding institution and date of the thesis must be given.

Please visit <http://shura.shu.ac.uk/24807/> and <http://shura.shu.ac.uk/information.html> for further details about copyright and re-use permissions.

# Synthesis and Characterisation of Sol-Gel Based Ionogels as Electrolyte for Supercapacitors

Ronak Janani

A thesis submitted in partial fulfilment of the requirements of  
Sheffield Hallam University  
for the degree of Doctor of Philosophy

January 2019

## **Declaration**

I hereby declare that this thesis submitted for the degree of PhD is the result of my own research and that this thesis has not been submitted for higher degree to any other university or institution.

Ronak Janani

## **Dedication**

To my loving and supportive parents, brother, grandmother and partner.

## Acknowledgements

First and foremost, I'd like to thank my PhD director of studies, Dr. Nick Farmilo, for his endless support and guidance throughout my PhD. Dr. Farmilo's patience, enthusiasm and knowledge of academic research, gave my PhD project its direction and gave me the confidence to overcome difficulties along the way.

I owe my deepest gratitude to my PhD supervisor, Professor Chris Sammon, who adopted me as his PhD student towards the end of my PhD and guided me to reach a new scientific level in my research work. The publication stemming from this work would have not been possible without his supervision. Working with Professor Sammon has truly expanded my intellectual horizons.

I'd like to extend my gratitude to my external advisor, Dr. Alexander Roberts whose vast knowledge in the field of energy storage and his humble and continuous support have been a tremendous help to my PhD project. Because of Dr. Roberts' support, I was given the opportunity to execute part of my PhD characterisations in WMG innovative centre, Warwick University.

I would also like to express my appreciation to Dr. Kerstin Mader, Dr. Francis Clegg, Dr. Lyuba Alboul, and Professor Paul Bingham for their help and support during my work.

Words cannot express my sincere gratitude to everyone in MERI, from the admin team who helped me pick up some of the stones in the way of my PhD to the technical support team who enabled me to independently execute the characterisations needed for my PhD project.

I am thankful for the friendships made in the past four years at Sheffield Hallam University. From emotional support to scientific input they have been there for me, Mirjam, Daniel, Barnali, Matt, Ekaterina, Hadi, Hassan, Shrutti, Becky, Suchi and everyone who helped me along this journey, I thank you all from the bottom of my heart.

I'd like to thank my beloved Alex, who stood by me in the hardest of days and kept me sane by bringing motivation and direction into my life. I am always and forever grateful for you.

I am forever thankful for my family whose love and support got me to where I am today. My parents sacrificed their best years of life for the bettering of their children's lives. They are my heroes, saviours and the most valuable gifts in life.

## Abstract

With growing public demand for consumer safety regarding electronic devices, ionogels have recently been suggested as a safe and solid replacement for the conventional flammable and toxic organic electrolytes used for various energy storage devices including batteries and supercapacitors. Ionogels are porous solid scaffolds that encapsulate ionic liquids and prevent electrolyte leakage which can otherwise be a potential hazard to the consumer or the surrounding circuitry. In this work, sol-gel was utilised as a manufacturing technique for 1-ethyl-3-methylimidazolium trifluoromethanesulfonate based-ionogels. Sol-gel chemistry is a facile and industrially relevant technology that allows the formation of solid scaffolds from homogenous precursors including a variety of silicon alkoxides. Previous studies have used a single or a mixture of silicon alkoxides to fabricate ionogels. In this work, four different precursors (two tetraalkoxysilanes and two alkyltrialkoxysilanes) were utilised to explore the influence of the type of silicon alkoxide on the reaction kinetics, thermal stability, microstructure and the electrochemical performance of the ionogels as electrolyte for electric double-layer capacitors (EDLCs).

Furthermore, thermally-cured 1-ethyl-3-methylimidazolium trifluoromethanesulfonate-based ionogels have been realised for the first time in this work. The influence of curing temperature on the structure of the ionogels and their electrochemical performance as the electrolyte for EDLCs have been investigated. Ionogels were synthesised via a non-hydrolytic sol-gel route and were fully gelled post heat-treating at 125, 150, 175 and 200°C for 60 minutes with minimal shrinkage. Charge transfer resistance (a rate-limiting parameter in cell kinetics during charge/discharge cycles) was reduced by ~80% via increasing the heat-treatment temperature; this was partially attributed to the interlocking effect at the electrode-electrolyte interface facilitated by high curing temperature. The fast-cure fabrication process for ionogels removes one of the major hurdles in their industrial application, their long curing and aging time, while the improved room temperature ion transport kinetics expands the potential application of ionic liquid-based electrochemical systems. Finally, an exploratory investigation on the long-term stability of the fabricated EDLCs indicated that cells with 150°C-

cured ionogels show an improved electrochemical performance compared to the EDLCs with ionic liquid electrolyte without the gel network.

The results gathered in this work provide an insight into sol-gel processed ionogels as a replacement for the conventional electrolyte formulations and further proves that, this class of materials has the potential to be a safe, solid and durable electrolyte for EDLCs.

## List of publication, conferences and competitions

- R. Janani, K. Mader, A.J. Roberts, N. Farmilo, C. Sammon, Fast-cure ionogel electrolytes with improved ion transport kinetics at room temperature, J. Power Sources. 406 (2018) 141–150.  
doi:10.1016/J.JPOWSOUR.2018.10.049.
- Skeptics in the pub 2018, Barnsley, Oral presentation: Safe and solid electrolytes
- Sol-gel 2017 Conference, Liege, Oral presentation: Influence of fast-curing on the performance of silica-based ionogels as electrolyte for energy storage applications
- ANNIC 2016 Conference, Barcelona, Oral Presentation: Comparative study of inorganic and hybrid ionogels as electrolyte for supercapacitors
- Three minutes thesis competition 2016, Sheffield, Topic: Safe and solid electrolytes  
~Awarded as the 2016 winner in Sheffield Hallam University~
- MERI Symposium 2016, Sheffield, Oral Presentation: A New Class of Ionogels as electrolyte for supercapacitors  
~Awarded as the 1st prize winner for the best PhD student talk~
- ECRC 2016 Conference, Oxford, Oral Presentation: A new class of ionogels
- UKES 2015 Conference, Coventry, Oral Presentation: Investigation of novel sol-gel derived quasi-solid electrolytes for supercapacitors

## List of Abbreviations

AC	Activated Carbon
ac	Alternating Current
ALS	Alternating Least Squares
AN	Acetonitrile
BET	Brunauer-Emmett-Teller
BSE	Back-Scattered Electron
BSH	Battery-Supercapacitor Hybrid
CA	Citric Acid
CCD	Charged-Couple Device
CE	Counter Electrode
CV	Cyclic Voltammetry
DEMS	Differential Electrochemical Mass Spectroscopy
D.I. Water	Deionised Water
DOE	United States Department of Energy
EC	Electric Capacitor
EDLC	Electric Double-Layer Capacitors
EDX	Energy Dispersive X-Ray
EIS	Electrochemical Impedance Spectroscopy
Eq.	Equation
ESR	Equivalent Series Resistance
ETD	Everhart-Thornley Detector
FA	Formic Acid
FTIR	Fourier-Transform Infrared Spectroscopy
FWHM	Full Width at Half Maximum
GCD	Galvanostatic Charge-Discharge
IHP	Outer Helmholtz Plane
IL	Ionic Liquid
LMWG	Low Molecular Weight Gelator
MTES	Methyltriethoxysilane
MCR	Multivariate Curve Resolution
MTMS	Methyltrimethoxysilane

NEC	Nippon Electric Company
NIPALS	Non-Linear Iterative Partial Least Squares
NMP	N-Methyl Pyrrolidinone
NMR	Nuclear Magnetic Resonance
OHP	Outer Helmholtz Plane
PC	Propylene Carbonate
PVDF	Polyvinylidene Fluoride
RE	Reference Electrode
rms	Root Mean Square
rpm	Revolutions Per Minutes
RTIL	Room Temperature Ionic Liquid
SE	Secondary Electron
SEM	Scanning Electron Microscopy
SOHIO	Standard Oil Company of Ohio
TEM	Transmission Electron Microscopy
TEOS	Tetraethoxysilane
TGA	Thermogravimetric Analyses
TMOS	Tetramethoxysilane
VTES	Vinyltriethoxysilane
WE	Working Electrode

## Table of Contents

1. Introduction and thesis outline	1
1.1 Research motivation	1
1.2 Thesis outline	3
1.3 References	5
<hr/>	
2. Literature Review	8
2.1 From capacitors to supercapacitors	8
2.2 Electric double-layer capacitors (EDLCs)	10
2.2.1 Electric double-layer models	10
2.2.2 Operating principle	12
2.3 Pseudocapacitors	13
2.3.1 Operating principle	13
2.3.2 Difference between rechargeable batteries and pseudo-capacitors	13
2.4 Hybrid supercapacitors	14
2.5 Fundamental characteristics of supercapacitors	15
2.5.1 Capacitance	15
2.5.2 Equivalent series resistance	17
2.5.3 Energy density and Power density	17
2.5.4 Long-term stability	18
2.6 Activated carbon as electrode material for EDLCs	19
2.7 Ionic liquids	22
2.8 Immobilisation of ionic liquids for electrochemical applications	28
2.8.1 Different methods of ionic liquid confinement	29
2.8.2 Ionogels through sol-gel processing	30
2.8.3 Influence of formulation on ionogels	33
2.8.4 Influence of ionic liquid on the structure of the solid network	35
2.9 References	39
<hr/>	

3. Methodology and characterisation techniques	52
3.1 Electrode fabrication	52
3.2 Coin cell assembly tools	52
3.3 Physical and chemical characterisation techniques	54
3.3.1 Raman spectroscopy and multivariate curve resolution	54
3.3.2 Scanning electron microscopy and Energy dispersive X-ray analysis	59
3.3.3 Thermogravimetric analysis	61
3.3.4 Contact angle measurements	62
3.3.5 Surface tension measurement	63
3.3.6 Viscosity measurements	64
3.3.7 Brunauer–Emmett–Teller	65
3.3.8 Karl Fischer titration	66
3.4 Electrochemical characterisation techniques	67
3.4.1 Cyclic voltammetry	68
3.4.2 Galvanostatic charge-discharge	70
3.4.3 Electrochemical impedance spectroscopy	72
3.5 References	75
<hr/>	
4. Comparative studies of the gelation kinetics and structure of TEOS, TMOS, MTMS and MTES based silica gels synthesised through a non-hydrolytic sol-gel route	81
4.1 Introduction	81
4.2 Materials	83
4.3 In situ reaction monitoring	83
4.3.1 Experimental procedure	83
4.3.2 Results and discussion	84
4.4 Morphology of silica network	111
4.4.1 Experimental procedure	111
4.4.2 Results and discussion	111
4.5 Conclusions	120
4.6 References	122
<hr/>	

5. Comparative studies of the gelation kinetics and the physical and electrochemical properties of TEOS, TMOS, MTMS and MTES based ionogels synthesised through a non-hydrolytic sol-gel route	127
5.1 Introduction	127
5.2 Materials	127
5.3 In situ reaction monitoring	130
5.3.1 Experimental procedure	130
5.3.2 Results and discussion	130
5.3.3 Ionic liquid-pore wall interactions	145
5.4 thermal stability and microstructure of the ionogels	151
5.4.1 Experimental procedure	151
5.4.2 Results and discussion	152
5.5 Application of the ionogels as EDLC electrolytes	162
5.5.1 EDLC fabrication	162
5.5.2 Electrochemical experiment design	162
5.5.3 Characterisation of the activated carbon	163
5.5.4 Results and discussion	164
5.6 Conclusions	179
5.7 References	181
<hr/>	
6. Influence of curing temperature on the performance of silica-based ionogels as electrolyte for supercapacitors	188
6.1 Introduction	188
6.2 Experimental procedure	190
6.2.1 Electrolyte preparation and EDLC fabrication	190
6.2.2 Electrochemical characterisation	191
6.2.3 Viscosity measurements	191
6.2.4 Surface tension measurements	191
6.2.5 Scanning electron microscopy (SEM) characterisation	191
6.2.6 Raman spectroscopy measurements	191

6.3 Results and discussion	192
6.3.1 Formulation optimisation	192
6.3.2 Changes in penetration coefficient of [Emim][TfO] ionic liq- uid with temperature	197
6.3.3 Effect of temperature on the physical structure of electrode-electrolyte interface	199
6.3.4 Evolution of impedance with respect to temperature and time	200
6.3.5 Visualisation of wettability using Raman line-mapping	212
6.4 Conclusions	215
6.5 References	217
<hr/>	
7. Exploratory investigation of the influence of ionic liquid water con- tent, curing process and cell potential on the long-term stability of EDLCs containing 150°C-cured ionogels	222
7.1 Introduction	222
7.2 Experimental	223
7.2.1 Electrolyte preparation and EDLC fabrication	223
7.2.2 Measurement of ionic liquid water content	224
7.2.3 Thermal stability of TMOS-MTMS ionogel	224
7.2.4 Long-term stability characterisation	224
7.3 Results and discussion	225
7.3.1 Ionic liquid water content	225
7.3.2 Influence of ionic liquid water content on aging rate of EDLCs	228
7.3.3 Influence of curing process on aging rate of EDLCs	234
7.3.3 Influence of cell potential on aging rate of EDLCs	237
7.4 Conclusions	240
7.5 References	241

8. Conclusions and future work	246
8.1 Summary of the research questions	246
8.2 Summary of the findings	246
8.3 Key conclusions	249
8.4 Placement of this work against published works	250
8.5 Future work	251
8.6 References	253

# 1. Introduction and thesis outline

## 1.1 Research motivation

Since the advent of consumer energy storage devices with mobile phones, laptops and in more recent history, wearable electronics and hybrid cars, the demand for performance has increased rapidly. The rate of these technological advancements has made the smart phone an affordable staple for most people, whereas their initial cost meant they were only for the wealthy, only 30 years ago. Similar technological growth has been observed as a direct result of energy storage improvements in defence, medicine, and every other field that incorporated any form of electronics. As the demands from consumers for electronics with longer life-time (such as longer lasting batteries) and lighter and thinner electronic devices grew, manufacturers were forced to introduce products meeting consumer demands rapidly, in order to remain competitive. This has resulted in some tragic events in recent years. In September 2016, Samsung issued a formal recall of their *Galaxy Note 7*, following multiple reports of the explosion of these devices. The company promised consumers a quick replacement for the recalled smartphones which ended in a second round of product recall only a month later. Samsung later announced that the cause of device failure was poor battery manufacturing that resulted in short circuits in batteries of both the original series of *Galaxy Note 7* and the replaced smartphones [1,2]. This incident is a reminder of the explosive nature of commonly used lithium ion batteries; one key component of the device that contributes to this issue is the flammable [3], organic electrolyte – other factors include poor configuration of internal components and incomplete testing of the new batteries. In an electrochemical cell, electrolyte is responsible for providing ionic conduction between the positive and negative electrodes. The safety issue associated with flammable electrolytes is not unique to batteries since similar formulations are commonly utilised for supercapacitors [4,5]. Supercapacitors are energy storage devices that possess higher power density and lower energy density compared to batteries [6,7].

One potential way to overcome the safety hazard associated with organic electrolytes is to replace them with a relatively new class of non-flammable electrolytes called ionic liquids, which are simply salts with low melting points (typically below room temperature), and free of any solvents [8]. Since the discovery of air and water stable ionic liquids in 1992 [9], there has been an increasing focus into these new materials in the field of electrochemistry, as they are able to operate within a larger potential window than organic electrolytes while reducing the risk of flammability [8,10–12].

A second major concern for electrolytes which is not limited to the conventional type is the possibility of leakage, which can cause damage to the surrounding circuitry as well as being a potential health hazard to the consumer. This issue was briefly addressed by Chiu and Moore in a 2003 publication [13].

To effectively resolve the latter issue, the electrolyte may be encapsulated within a solid membrane to prevent electrolyte leakage. Gel networks derived by sol-gel chemistry confining ionic liquids have been suggested as a potential candidate to address issues associated with flammability and leakage of electrolytes [14–18]. These gel networks are referred to as ‘ionogels’. Studies dedicated to ionogels (and ionic liquids) in the past decade have been mainly focused on suitable formulations for a desired mechanical structure [17,19,20], high ionic conductivity [21,22], and enhanced performance at high temperatures [15,23–25]. There are a number of areas regarding sol-gel derived ionogels that require further investigation in order to improve these materials to an industrially scalable level with a desirable electrochemical performance. Some examples of the remaining questions are:

- 1) What influence does the silica precursor have on the resultant ionogel?
- 2) Does the presence of ionic liquid influence the kinetics of the sol-gel process?
- 3) Can a one-step heat-treatment be used as an effective method to reduce gelation time for ionogels?
- 4) How does the long-term stability of the ionogel-based supercapacitors compare to that of cells without the encapsulating gel network?

The present work was designed to address the above questions or at the very least provide the baseline for the next generation of studies on ionogel electrolytes in energy storage devices.

## 1.2 Thesis outline

The outline of this thesis is provided below:

Chapter 2 – This chapter provides a review of the most relevant literature in relation to supercapacitors and their main components, sol-gel chemistry and finally an overview of relevant studies in relation to ionogels.

Chapter 3 – This chapter describes the key supercapacitor fabrication tools and characterisation techniques utilised in this work. For all the instrumentation used in this project a brief overview of the method and a description of the collection parameters are discussed at the level and detail commensurate with their use in the thesis.

Chapter 4 – This chapter showcases a comparative investigation on the sol-gel process kinetics of four different silicon alkoxide precursors namely, tetramethoxysilane (TMOS), tetraethoxysilane (TEOS), methyltrimethoxysilane (MTMS) and methyltriethoxysilane (MTES). The purpose of this chapter is to provide an understanding of the sol-gel process kinetics and the topography of the resultant gels as a function of the precursor (under ambient conditions) and in the absence of ionic liquid for benchmarking in the future chapters. This was executed using a combination of Raman spectroscopy (*in situ*) and scanning electron microscopy (SEM).

Chapter 5 – This chapter is a combination of a number of studies. Firstly, the influence of the ionic liquid (1-ethyl-3-methylimidazolium trifluoromethanesulfonate) on sol-gel process kinetics is understood using *in situ* and *ex situ* Raman analyses together with the complementary information gathered from Chapter 4. Secondly, the thermal stability of the ionogels and the topography of the solid scaffolds are characterised. Finally, the influence of the ionogel pre-

cursor on the electrochemical performance of the ionogel electrolytes were elucidated using a series of electrochemical characterisations.

Chapter 6 – Based on the conclusions of the previous chapters, two of the most suitable precursors were chosen in this chapter to create a hybrid solid scaffold for the ionogel electrolytes and to examine the applicability of a thermal curing process as a measure to reduce the gelation time of the ionogels. This chapter further characterises the influence of four different curing temperatures (125, 150, 175, and 200°C) on the electrochemical properties of the ionogels as electrolyte for EDLCs.

Chapter 7 – A key aspect of supercapacitors is their long-term stability which was characterised in this chapter in an exploratory investigation. This part of the thesis explores the long-term stability of cells containing 'dried' and 'as-received' [Emim][TfO] ionic liquids to understand the extent to which ionic liquid water content can degrade the capacitance of the supercapacitors over time and to further examine the influence of the curing process discussed in Chapter 6 on the degradation rate of the cells. Lastly, this chapter seeks to determine the operational limit of the supercapacitors with thermally-cured ionogels by exposing the cells to potential windows above 2.5 V. The long-term stability tests listed in this chapter have been conducted at Warwick University.

Chapter 8 – Provides a summary of the key findings of the thesis together with suggested future work to complement the current findings.

### 1.3 References

- [1] K. Samuelson, A brief history of Samsung's troubled Galaxy Note 7 smartphone, *Time*. (2016). <http://time.com/4526350/samsung-galaxy-note-7-recall-problems-overheating-fire/> (accessed January 1, 2019).
- [2] A. Heathman, We finally know why Samsung's Galaxy Note 7s "exploded," *WIRED*. (2017). <https://www.wired.co.uk/article/galaxy-note-7-issues-what-happened> (accessed January 1, 2019).
- [3] M.H. Braga, C. M Subramaniam, A.J. Murchison, J.B. Goodenough, Nontraditional, safe, high voltage rechargeable cells of long cycle life, *J. Am. Chem. Soc.* 140 (2018) 6343–6352. doi:10.1021/jacs.8b02322.
- [4] C. Zhong, Y. Deng, W. Hu, J. Qiao, L. Zhang, J. Zhang, A review of electrolyte materials and compositions for electrochemical supercapacitors, *Chem. Soc. Rev.* 44 (2015) 7484–7539. doi:10.1039/C5CS00303B.
- [5] C. Zhong, Y. Deng, W. Hu, D. Sun, X. Han, J. Qiao, J. Zhang, *Electrolytes for electrochemical supercapacitors*, CRC Press, 2016. <https://books.google.co.uk/books?id=Wu0bDAAAQBAJ>.
- [6] P. Simon, Y. Gogotsi, B. Dunn, Where do batteries end and supercapacitors begin?, *Science* (6176). 343 (2014) 1210–1211. doi:10.1126/science.1249625.
- [7] M.R. Lukatskaya, B. Dunn, Y. Gogotsi, Multidimensional materials and device architectures for future hybrid energy storage, *Nat. Commun.* 7 (2016) 12647. doi:10.1038/ncomms12647.
- [8] M. Galiński, A. Lewandowski, I. Stępnia, Ionic liquids as electrolytes, *Electrochim. Acta.* 51 (2006) 5567–5580. doi:10.1016/J.ELECTACTA.2006.03.016.
- [9] J.S. Wilkes, M.J. Zaworotko, Air and water stable 1-ethyl-3-methylimidazolium based ionic liquids, *J. Chem. Soc. Chem. Commun.* (1992) 965–967. doi:10.1039/C39920000965.

- [10] Q. Zhu, Y. Song, X. Zhu, X. Wang, Ionic liquid-based electrolytes for capacitor applications, *J. Electroanal. Chem.* 601 (2007) 229–236. doi:10.1016/j.jelechem.2006.11.016.
- [11] A. Eftekhari, Supercapacitors utilising ionic liquids, *Energy Storage Mater.* 9 (2017) 47–69. doi:10.1016/j.ensm.2017.06.009.
- [12] M.C. Buzzeo, R.G. Evans, R.G. Compton, Non-haloaluminate room-temperature ionic liquids in electrochemistry - A review, *ChemPhysChem.* (2004). doi:10.1002/cphc.200301017.
- [13] Y.-T. Chiu, S.K. Moore, Leaking capacitors muck up motherboards, *IEEE Spectr.* 40 (2003) 16–17. doi:10.1109/MSPEC.2003.1176509.
- [14] M. Brachet, T. Brousse, J. Le Bideau, All solid-state symmetrical activated carbon electrochemical double layer capacitors designed with ionogel electrolyte, *ECS Electrochem. Lett.* 3 (2014) A112–A115. doi:10.1149/2.0051411eel.
- [15] L. Negre, B. Daffos, V. Turq, P.L. Taberna, P. Simon, Ionogel-based solid-state supercapacitor operating over a wide range of temperature, *Electrochim. Acta.* 206 (2016) 490–495. doi:https://doi.org/10.1016/j.electacta.2016.02.013.
- [16] S. Wang, B. Hsia, J.P. Alper, C. Carraro, Z. Wang, R. Maboudian, Comparative studies on electrochemical cycling behavior of two different silica-based ionogels, *J. Power Sources.* 301 (2016) 299–305. doi:10.1016/J.JPOWSOUR.2015.09.121.
- [17] A. Taubert, R. Löbbecke, B. Kirchner, F. Leroux, First examples of organosilica-based ionogels: synthesis and electrochemical behavior, *Beilstein J. Nanotechnol.* 8 (2017) 736–751. doi:10.3762/bjnano.8.77.
- [18] Y.J. Li, C. Guo, L.S. Yue, W.J. Qu, N. Chen, Y.J. Dai, R.J. Chen, F. Wu, Organosilicon-group-derived silica-ionogel electrolyte for lithium ion batteries, *Rare Met.* 37 (2018) 504–509. doi:10.1007/s12598-018-1056-4.

- [19] A.I. Horowitz, M.J. Panzer, High-performance, mechanically compliant silica-based ionogels for electrical energy storage applications, *J. Mater. Chem.* 22 (2012) 16534–16539. doi:10.1039/C2JM33496H.
- [20] A.I. Horowitz, K. Westerman, M.J. Panzer, Formulation influence on the sol-gel formation of silica-supported ionogels, *J. Sol-Gel Sci. Technol.* 78 (2016) 34–39. doi:10.1007/s10971-015-3918-7.
- [21] J. Vila, P. Ginés, J.M. Pico, C. Franjo, E. Jiménez, L.M. Varela, O. Cabeza, Temperature dependence of the electrical conductivity in EMIM-based ionic liquids: Evidence of Vogel-Tamman-Fulcher behavior, *Fluid Phase Equilib.* 242 (2006) 141–146. doi:10.1016/j.fluid.2006.01.022.
- [22] R. Gobel, P. Hesemann, J. Weber, E. Moller, A. Friedrich, S. Beuermann, A. Taubert, Surprisingly high, bulk liquid-like mobility of silica-confined ionic liquids, *Phys. Chem. Chem. Phys.* 11 (2009) 3653–3662. doi:10.1039/B821833A.
- [23] V. Ruiz, T. Huynh, S.R. Sivakkumar, A.G. Pandolfo, Ionic liquid-solvent mixtures as supercapacitor electrolytes for extreme temperature operation, *RSC Adv.* 2 (2012) 5591–5598. doi:10.1039/C2RA20177A.
- [24] L. Dagousset, G. Pognon, G.T.M. Nguyen, F. Vidal, S. Jus, P.H. Aubert, Electrochemical characterisations and ageing of ionic liquid/ $\gamma$ -butyrolactone mixtures as electrolytes for supercapacitor applications over a wide temperature range, *J. Power Sources.* 359 (2017) 242–249. doi:10.1016/j.jpowsour.2017.05.068.
- [25] R. Newell, J. Faure-Vincent, B. Iliev, T. Schubert, D. Aradilla, A new high performance ionic liquid mixture electrolyte for large temperature range supercapacitor applications ( $-70^{\circ}\text{C}$  to  $80^{\circ}\text{C}$ ) operating at 3.5 V cell voltage, *Electrochim. Acta.* 267 (2018) 15–19. doi:10.1016/j.electacta.2018.02.067.

## 2. Literature Review

### 2.1 From capacitors to supercapacitors

Supercapacitors are the third generation of electric capacitors (ECs). The history of ECs goes back to 1745 and to the invention of Leyden (or Leiden) jar by Ewald Georg von Kleist [1]. During an experiment with electricity, he connected an electric generator to a nail stuck into the cork of a glass medicine jar. He later received an electric shock by holding the jar in one hand and touching the nail with the other hand. Although he didn't fully understand the phenomenon, he realised that electric charges can be stored temporarily in such a setting. In fact, the earliest version of Leyden jar was capable of storing 1 nF of capacitance [2]. Pieter van Musschenbroek discovered and explained the same phenomenon a year later and claimed credit for the Leyden jar invention. As shown in Figure 2.1a, a Leyden jar consists of a glass vessel (a dielectric material) with its interior and exterior covered with metal foil (electrodes). They were first put to use in the beginning of the 20<sup>th</sup> century in radio telegraphy transmitters as a high-voltage capacitor [3]. At this time, the German government capitalised the Leyden jar industry, but this only lasted till the end of World War I. In addition, these devices suffered from being bulky, fragile, and having limited life time and, as capacitors became more prevalent, their structural designs became more practical and economical. These first-generation capacitors are grouped as electrostatic capacitors which consist of two metallic plates separated by a dielectric material and their yield capacitance ranges between 0.1 to 1  $\mu\text{F}$  [4]. Through polarisation of dipoles in the dielectric medium, electric charge can be accumulated at the electrode-dielectric material interface [5].

Second-generation ECs are electrolytic capacitors, in which positive and negative ions can freely move inside a solid or liquid ion conducting medium i.e. the electrolyte. A typical electrolytic capacitor consists of two metallic plates (most commonly aluminium), one of which is coated with an insulating layer (e.g. a metal oxide layer), which acts as a thin layer of electrically insulating material (separator) to remove the possibility of short circuit [6], and finally the electrolyte which fills up the space between the two metallic plates. The electrolyte and the

non-oxidised metal plate act as the cathode and the current collector (ensures uniform distribution of electric current), respectively [7]. Figure 2.1b illustrates the internal structure of a typical electrolytic capacitor. In these devices, electrical charge can be stored by accumulation of ions at the electrode-electrolyte interface. When charge density on the electrode is increased, more oppositely charged ions are attracted (from the electrolyte) and packed onto the electrode surface, and for this reason higher capacitance (in mF range) is achievable in electrolytic capacitors compared to dielectric capacitors [5]. The principle of electrolytic capacitors was discovered by Charles Pollak in 1886 during his research on anodising metals, but it wasn't until World War II that more research and resources were dedicated on the ECs industry and as a result of which electrolytic capacitors became more efficient and reliable [7].

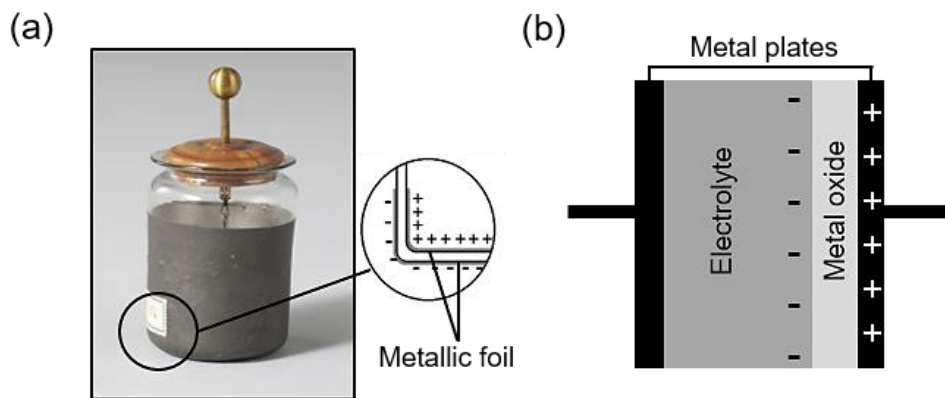


Figure 2.1 (a) An early version of Leyden jar dated back to 1755-1799 (available at Teylers museum, Haarlem, Netherlands) [8] and an illustration of electrostatic charges accumulated on the glass jar. (b) Internal structure of an electrolytic capacitor.

The first and second generations of ECs are conventionally utilised as primary circuit elements to store small amount of electric charges and/or for frequency filtration in alternating current circuits [7]. Fast development of materials and electronic devices led into the invention of supercapacitors or electrochemical capacitors (in late 1950s) that are energy storage devices with high power density (from  $<10 \text{ kW kg}^{-1}$  to  $10\text{-}50 \text{ kW kg}^{-1}$  depending on the type of supercapacitor [6]) and long cycling life. Double-layer theory proposed by Hermann von Helmholtz in 1879 was the underlying concept behind the invention of supercapacitors and it predicts the presence of a double-layer at the interface between a conductive material and an electrolyte [9]. The first supercapacitor was invented by H. I. Becker from General Electric in 1957 [10]. In 1966 a more ad-

vanced patent was awarded to R. A. Rightmire who was a chemist at Standard Oil Company of Ohio (SOHIO) [11]. In 1971, SOHIO licenced the double-layer capacitor technology to Nippon Electric Company (NEC) and by 1978, NEC's supercapacitor was commercialised. Rapid development of electric vehicles and mobile electronics called for more advancements in the battery and supercapacitor industry, and in 1990s more research funding was advocated by United States Department of Energy (DOE) due to an increasing awareness of the extensive applications of battery and supercapacitors [7]. Today, the application of supercapacitors in the fields of electronics and electrochemistry are diverse. They can be used to generate power and be a peak assist in industry or for automotive applications [4]. They can also replace or supplement batteries in consumer electronics. In addition, micro-sized supercapacitors are widely utilized in biosensors and microelectromechanical systems as an on-chip element [6]. Depending on the type of application, the requirements and thus, supercapacitor cell design may vary. Based on the mechanism of charge storage, supercapacitors are divided into three major types, namely electric double-layer capacitors, pseudocapacitors and hybrid cells. The following sections (2.2-2.4) provide an overview of their working principles.

## **2.2 Electric double-layer capacitors (EDLCs)**

### **2.2.1 Electric double-layer models**

An EDLC consists of two electrodes separated by an ion permeable separator. The space between the electrodes is filled with a liquid or quasi-solid electrolyte and it usually consists of solvated positive and negative ions suspended in solvent(s), or moving inside the quasi-solid backbone. When an EDLC is charged, two layers with opposite charges form at each electrode-electrolyte interface; these layers are commonly described as electric double-layers and they resemble two capacitors in series (Figure 2.2).

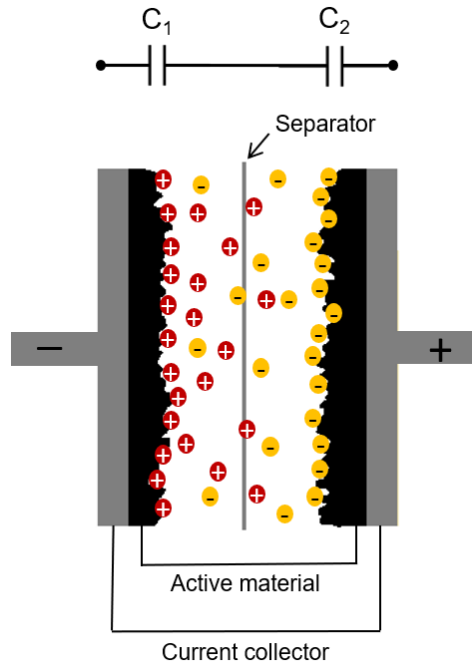


Figure 2.2 Schematic representation of an EDLC supercapacitor. Each electrode-electrolyte interface in EDLC can be represented by a capacitor ( $C_1$  and  $C_2$ ).

Hermann von Helmholtz proposed the electric double-layer capacitor model in 1879 [9] and since then it has been further developed and improved by many including Gouy (1910) [12], Chapman (1913) [13], Stern (1924) [14] and Grahame (1943) [15]. Figure 2.3 compares the most significant molecular models proposed for EDLCs. H. Helmholtz stated that in an EDLC, the charged electrode and the oppositely charged ions adsorbed on the electrode surface can be assumed as parallel plates separated by a small distance (Helmholtz layer) at the electrode-electrolyte interface (displayed in Figure 2.3a). This model is analogous to that of dielectric capacitors and ignores the mobile nature of ions inside the electrolyte. This model was later modified by Gouy and Chapman with the consideration that ions are free to move and thus, their concentration must be continuous in the electrolyte solution [12,13]. This meant that ions are distributed in a region (diffuse layer) with a thickness larger than that of Helmholtz layer. Stern combined these two models to account for the adsorbed ions (Stern layer) as well as the continuous concentration of ions (shown in Figure 2.3b). Grahame further improved this model by dividing the Stern layer into inner and outer Helmholtz planes (IHP and OHP respectively) to distinguish between layers of ions adsorbed by covalent forces and the ones attracted by electrostatic forces (Figure 2.3c) [16,17].

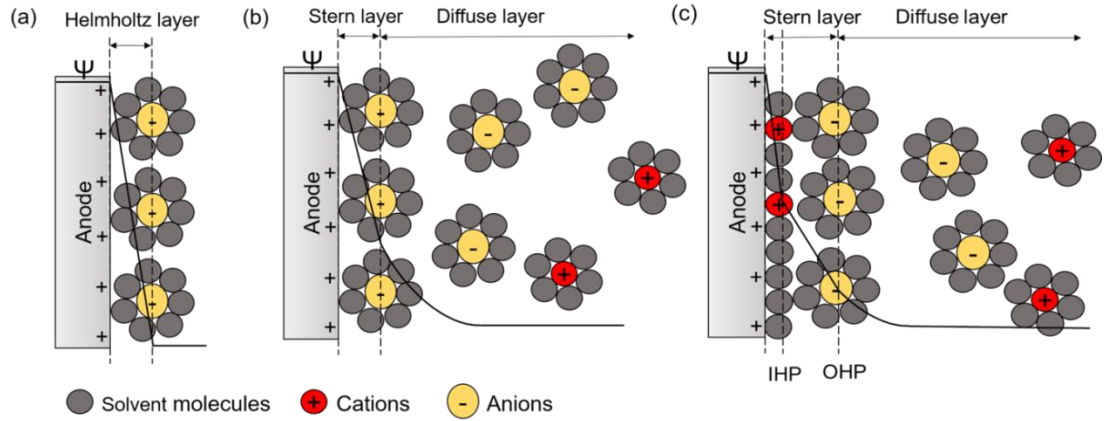
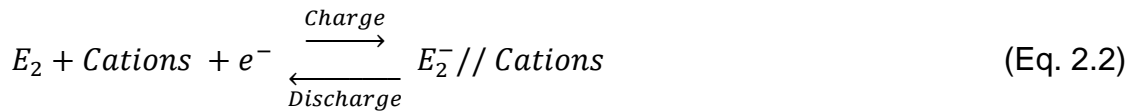
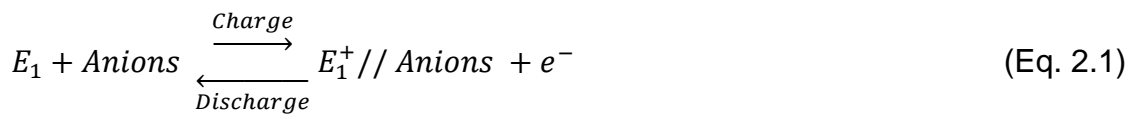


Figure 2.3 Illustration of double-layer models proposed by (a) Helmholtz, (b) Stern and (c) Grahame.  $\Psi$  represents electric potential.

## 2.2.2 Operating principle

As mentioned in section 2.2.1, a double-layer capacitor is generated at the electrode-electrolyte interface where electric charges are accumulated at the electrode surface whilst ions of opposite charge are built up close to the electrode surface in the electrolyte to meet electroneutrality. In an EDLC, the charge storage mechanism is purely electrostatic with no faradaic current (generated by reversible oxidation and reduction reactions) passing through the electrode-electrolyte interface and the electrode material is electrochemically inactive (mainly carbon-based) [4]. The electrochemical processes taking place at the electrode-electrolyte interface of an EDLC were expressed as follows by Zheng et al. in 1997 [18]:



where  $E_1$  and  $E_2$  represent the positive and negative electrodes of an EDLC cell, respectively and // expresses the electrode-electrolyte interface. As it is shown, the charge and discharge processes are in principle fully reversible.

## 2.3 Pseudocapacitors

### 2.3.1 Operating principle

In contrast to EDLCs, a series of redox reactions takes place within a pseudocapacitive electrode material. Transfer of charges across the double-layer results in a faradaic current passing through the cell. Conductive polymers and a number of metal oxides such as  $\text{RuO}_2$  [19,20] and  $\text{MnO}_2$  [21] (which undergo fast surface redox reactions) are good electrode material candidates for pseudocapacitors. It should be noted that the redox reactions take place together with the electrostatic charge adsorption on the electrode surface. Due to this additional charge storage mechanism, pseudocapacitors possess a higher specific capacitance and energy density compared to that of EDLCs [22,23]. Generally, faradaic (or redox) reactions take place at a slower rate compared to non-faradaic (or electrostatic) processes resulting in lower power density than that of EDLCs [24]. Figure 2.4 demonstrates the faradaic reaction taking place at the double-layer of a pseudocapacitor.

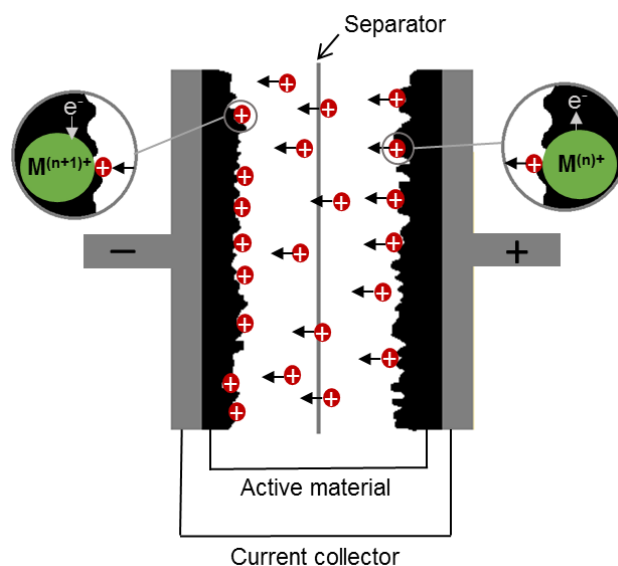


Figure 2.4 Schematic diagram of a pseudocapacitor in which the cations from the electrolyte participate in the redox reaction,  $M$  represents the metal atoms in the electrode active material.

### 2.3.2 Difference between rechargeable batteries and pseudocapacitors

It is important to elaborate on the difference between the operating mechanisms of rechargeable batteries and pseudocapacitors to provide a better understanding of what differentiates these energy storage devices.

In rechargeable batteries, charge is stored via intercalation/insertion of ions into and out of the crystalline electrode material coupled with oxidation and reduction of metal ions available in the electrode material. The capacitance of batteries is dependent on the diffusion of ions in the crystalline electrode [22]. During a charge and discharge cycle, the electrode material goes through a phase transformation which is characterised by sharp peaks in the current-vs-potential plot (also known as cyclic voltammetry profile, explained in detail in Chapter 3). Basically, ion insertion causes strain in the crystalline framework, which results in phase transformation to overcome the strain. This may result in some volume changes in the electrode which impacts the integrity of the crystalline material [25]. This phenomenon results in the poor cycling stability and short life-time of batteries compared to supercapacitors.

The electrochemical reactions taking place in a pseudocapacitor are very similar to those of rechargeable batteries. In terms of operating mechanism, a pseudocapacitor is in between a rechargeable battery and an EDLC; this means the charge storage takes place via both chemical and electrostatic means. The chemical means of charge transfer involves transfer of charge via reduction and oxidation reactions [7]. The charge storage in pseudocapacitors arises from adsorption and desorption of ions at the electrode-electrolyte interface as well as surface redox reactions which makes capacitance independent of diffusion process. There are no phase transformation taking place in the electrode material during charge/discharge cycles in pseudocapacitors and thus, a higher charge transfer rate is exhibited. In pseudocapacitors the capacitance is a function of the applied potential [25,26].

#### **2.4 Hybrid cells**

Hybrid cells are a combination of an EDLC and a pseudocapacitor or a battery (typically a lithium ion battery) where the electrodes have different charge storage mechanisms from each other [24]. This combination takes advantage of the higher energy density in batteries and high power density and durability of supercapacitors [25]. A comprehensive review on different types of battery-supercapacitor hybrid (BSH) devices was done recently by Zuo et al. [27]. They described the operating mechanism of BSH with the aid of the schematic shown in Figure 2.5 as follows: during charge/discharge cycles positive and negative

ions move toward one of the two electrodes, and redox reactions take place in the bulk of the battery-like electrode while ion accumulation and/or rapid charge transfer takes place at the interface of the opposite electrode.

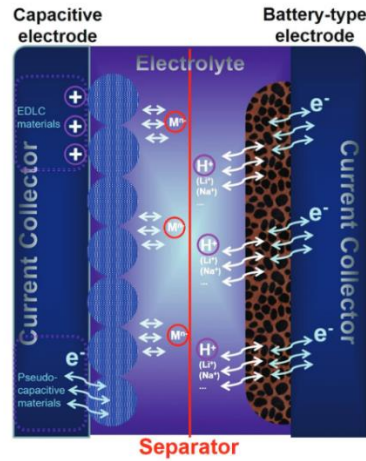


Figure 2.5 General structure and working mechanism of battery-supercapacitor hybrid cell (retrieved from [27]).

## 2.5 Fundamental characteristics of supercapacitors

### 2.5.1 Capacitance

Generally, within the operational range of the device, the amount of charge ( $Q$ ) stored within a capacitor (ranging from dielectric capacitors to supercapacitors) is proportional to the voltage ( $V$ ) built up across the two electrodes i.e. the strength of the electric field at the electrode-electrolyte interface. This proportion is called capacitance ( $C$ ) [5,28]:

$$C = \frac{Q}{V} = \frac{\epsilon_r \epsilon_0 A}{d} \quad (\text{Eq. 2.3})$$

where  $\epsilon_r$  is the relative permittivity of the dielectric material,  $\epsilon_0$  is the vacuum permittivity,  $A$  is the area of electrode-electrolyte interface and  $d$  is the thickness of the double layer. This thickness,  $d$ , is in the order of angstroms in supercapacitors with concentrated electrolytes and, due to porous nature of electrode materials used in these devices ( $A \sim 1000 \text{ m}^2 \text{ g}^{-1}$ ) [29], the capacitance of the cell becomes considerably larger than that of dielectric and electrolytic capacitors (between  $10^2 - 10^4 \text{ F}$  for commercial capacitors [5]).

The internal structure of a supercapacitor is equivalent to two capacitors ( $C_1$  and  $C_2$ ) connected in series (as shown in Figure 2.2). Each electrode-electrolyte

interface represents a single capacitor. Therefore, the total capacitance of the cell ( $C_T$ ) can be expressed as:

$$C_T = \frac{C_1 C_2}{C_1 + C_2} \quad (\text{Eq. 2.4})$$

where  $C_1$  and  $C_2$  are the capacitances of the two electrode-electrolyte interfaces. In the case of a symmetrical cell (where both electrodes are identical),  $C_T$  will be equal to half of the capacitance of either electrode, while in an asymmetric design, this value is dominated by the electrode material with smaller capacitance. Although capacitance is a key characteristic parameter for energy storage devices, it is not sufficiently informative with regards to supercapacitors, in which case this parameter is expressed as a gravimetric (mass-based) or a geometric (area or volume-based) value and is referred to as specific capacitance ( $C_{sp}$ ). The areal capacitance has a unit of Farads per square centimetre ( $\text{F cm}^{-2}$ ) in the context of the planar surface area of the electrode active material ( $A_{Planar}$ ). Gravimetric  $C_{sp}$  has a unit of Farads per gram ( $\text{F g}^{-1}$ ) and it incorporates the total mass of the active material on the electrodes. [7,30]. Two ways have been proposed to calculate the gravimetric  $C_{sp}$  [7,29,31,32]:

$$C_{sp} = \frac{C_T}{A_{Planar}} \times A_{BET} \quad (\text{Eq. 2.5})$$

$$C_{sp} = \frac{C_T}{m_T} \quad (\text{Eq. 2.6})$$

where  $A_{BET}$  is the total non-planar surface area of the porous electrode measured using Brunauer–Emmett–Teller (BET) surface area analysis technique (explained in Chapter 3) and  $m_T$  represents the total mass of the active material on the electrodes (typically in grams). The first route described in Eq. 2.5 assumes that the total BET surface area is accessible to the ions, which can be an overestimation since there may be some pores within the porous electrode that are inaccessible [7,32]. Gravimetric capacitance is the most often cited parameter in describing the performance of experimental supercapacitor [31], despite some researchers' belief that gravimetric value can be an inaccurate representation of cell performance when the mass of active material is negligible compared to other components of a cell [33,34]. For this reason, the specific capaci-

tance of commercial devices are usually normalised by the mass/size of the packaged device [31].

Due to the lack of a standard or an agreed method in describing supercapacitor performance, providing a clear and meaningful comparison between experimental work and reported works can be challenging. In addition, it is crucial to clarify whether the reported  $C_{sp}$  is associated with the full cell capacitance ( $C_{sp\ total}$ ) or a single electrode ( $C_{sp1}$ ). This is important as the difference between the two is a factor of 4 [29]. Assuming  $m_1 = m_2$  and  $C_1 = C_2$ :

$$C_{sp1} = C_{sp2} = \frac{C_1}{m_1} \quad (\text{Eq. 2.7})$$

$$C_{sp\ total} = \frac{C_T}{m_1 + m_2} = \frac{\frac{C_1}{2}}{2m_1} = \frac{C_{sp1}}{4} \quad (\text{Eq. 2.8})$$

### 2.5.2 Equivalent series resistance

The equivalent series resistance ( $R_{ESR}$ ) is the sum of various types of resistances present in a cell including contact resistance between the electrode active material and the current collector, intrinsic resistance of the active material, bulk resistance of the electrolyte and mass transfer resistance at the electrode-electrolyte interface [6,35].

### 2.5.3 Energy density and Power density

When a potential,  $V$ , is applied to a capacitor, a certain amount of work ( $dw$ ) is done to move an equivalent quantity of charges ( $dQ$ ) and accumulate at the electrode-electrolyte (or electrode-dielectric material) interface. If no heat is dissipated during this process, the amount of work done would be equivalent to the amount of energy stored in the capacitor [5,7] and can be expressed as:

$$\frac{dw}{dQ} = V = \frac{Q}{C} \quad (\text{Eq. 2.9})$$

$$W = \int_0^Q \frac{Q}{C} dQ = \frac{1}{C} \times \frac{Q^2}{2} = \frac{1}{C} \times \frac{(CV)^2}{2} = \frac{1}{2} CV^2 \quad (\text{Eq. 2.10})$$

$$E = \frac{1}{2} C_{sp} V^2 \quad (\text{Eq. 2.11})$$

where  $E$  is the specific energy and has a unit of Wh kg<sup>-1</sup>. Another key indicator of the performance of a capacitor is its specific power ( $P$ ) which describes how

fast the stored energy can be delivered to the external load ( $R_L$ ) per mass of the active material [5,36]:

$$P = \frac{E}{t} = \frac{i^2 \times R_L}{m_T} = \left( \frac{V}{R_{ESR} + R_L} \right)^2 \times \frac{R_L}{m_T} \quad (\text{Eq. 2.12})$$

Maximum specific power ( $P_{max}$ ) is achieved when  $R_L = R_{ESR}$ ,

$$P_{max} = \left( \frac{V}{2 \times R_{ESR}} \right)^2 \times \frac{R_{ESR}}{m_T} = \frac{V^2}{4 \times R_{ESR} \times m_T} \quad (\text{Eq. 2.13})$$

where  $i$  is the current going through the circuit,  $t$  is the full discharge time of the capacitor [5].

#### 2.5.4 Long-term stability

Application life-time is another performance indicator of an energy storage device. The end-life of supercapacitors has been defined as a 20-30% capacitance loss or doubling of  $R_{ESR}$  resistance by some researchers [29,37]. Different techniques have been used to evaluate the life-time of supercapacitors.

Cycle-life or cycling stability refers to the stability of a system after many charge-discharge cycles and it can reflect the duty cycle of the cell [37]. The analysis test procedure involves a single electrode or a complete cell undergoing continuous charge and discharge cycles whilst comparing the value of capacitance throughout the cycling process. Carbon-based EDLCs have shown very high cycling stability ( $\geq 10,000$  for activated carbon-based EDLCs [38]). However, pseudocapacitors possess a shorter cycle-life compared to that of double layer capacitors. This is due to the fact that pseudocapacitive electrode materials degrade over time by interacting with electrolyte ions and going through many redox reactions [25,39]. Cycling stability is also dependent on charge-discharge rate (also known as scan rate), electrolyte, potential window and operating temperature [6].

The cycling stability test can be highly time consuming and according to Weingarh et al., it is not sufficient as an indicator of long-term stability of a double-layer capacitor [37]. For instance, in applications where the cell is being utilised in an emergency or back-up system and is continuously kept at the charged state until an emergency event takes place, cycling stability would not

be meaningful. Okamura et al. [40] argued that during the cycling stability test only a “derated” voltage is applied to the capacitor which means that for the majority of the cycling test, the capacitor is exposed to potentials below the assumed potential limit or stability limit, and thus, the measured life-time of the cell becomes larger than the real value [37]. Another method utilised for long-term stability characterisation is the ‘constant voltage load’ or ‘float test’ [37,41,42] during which the capacitor is held at the nominal potential and the change in capacitance is recorded as a function of time by occasional charge-discharge cycles. Figure 2.6 represents the results reported by Weingarth’s team comparing the percentage of capacitance variation with time realised via both of the mentioned techniques [37]. Based on their results using float test, it only took 30 hours for the supercapacitor cell to reach a 30% capacitance drop while a total of ~350 hours of cycling test resulted in 30% drop of the initial capacitance value. Therefore, meaningful information about the long-term stability of supercapacitors can be achieved using the 'float test' technique in a less time-consuming manner compared to continuous cycling test.

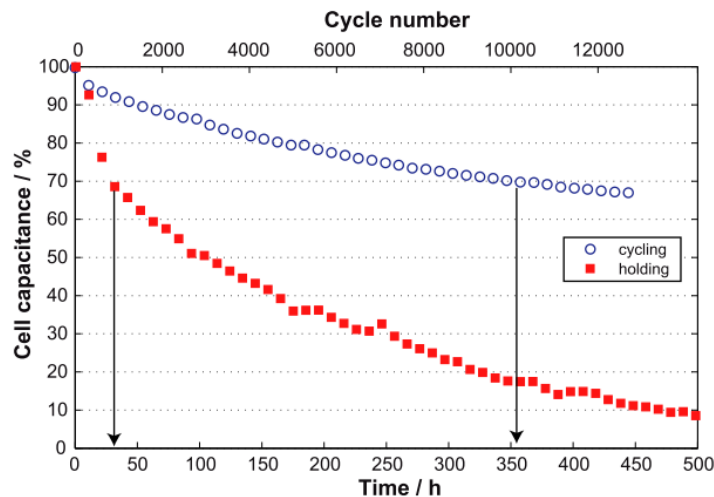


Figure 2.6 Float (or voltage hold) test and cycling test results as a function of real test time of a full supercapacitor cell using YP17 activated carbon and 1 M tetraethylammonium tetrafluoroborate (TEABF<sub>4</sub>) in acetonitrile. The hold voltage was set to 3.5 V while the lower and upper voltage limit for cycling test was set to 0.0 and 3.5 V, respectively [37].

## 2.6 Activated carbon as electrode material for EDLCs

Activated carbon (AC) is an assembly of defective graphene and graphite sheets resulting in a carbon material with high porosity and thus, high surface area [43,44]. H. Fritz Stoeckli described the structure of AC as a disorganised

microporous network and proposed the schematic displayed in Figure 2.7 for its structure which resembles a mixture of crumpled papers and wood shavings with gaps of various sizes and shapes in between [45]. Generally, any inexpensive material with high carbon and low inorganic content can be a suitable raw material for AC production. Activated carbon is manufactured by either thermal (or physical) or chemical activation process [44,46,47]. In the former method, the raw material is first carbonised by being heated (400-900°C) in the absence of oxygen. The product of this stage is referred to as char. The char is then heated between 350-1000°C in the presence of oxidising gases (CO<sub>2</sub>, steam, air, or a mixture of them). In the chemical route, the process of carbonisation and activation (at 450-900°C) is combined into one step by introducing activating agents to the raw material. Examples of these activating agents are ZnCl<sub>2</sub>, KOH and H<sub>3</sub>PO<sub>4</sub>.



Figure 2.7 schematic representation of activated carbon by H. F. Stoeckli [45].

As expressed in equation 2.3, capacitance is directly related to the area of the interface between active electrode material and the electrolyte. However, numerous studies have reported otherwise. For instance, Shi reported the specific surface area of 34 different activated carbons and their corresponding specific capacitances [48]. Table 2.1 provides examples of his work where the relation between  $C_{sp}$  and  $A_{BET}$  does not follow the theoretical trend. Another study was conducted a few years later by Qu and Shi and a similar observation was made, i.e. some ACs with larger  $A_{BET}$  had a smaller specific capacitance than those with smaller  $A_{BET}$  [43]. This phenomenon is thought to have two primary reasons; firstly, the specific surface area measured by the BET technique may not be fully accessible to the electrolyte charge carriers which creates a degree of

mismatch between experimental and theoretical values. This is very likely to be the case when large organic ions are present in the electrolyte. Secondly, the effect of pore size distribution and functional groups on the AC surface need to be taken into consideration as many publications have reported on their relation to specific capacitance [49–51].

*Table 2.1 Examples of different activated carbon electrodes and their corresponding EDLC specific capacitance (in aqueous electrolyte) and BET specific surface area. Retrieved from [48]. The M groups refer to activated carbon microbeads and the FD, FT and FU groups are activated carbon fibres.*

Activated carbon	$C_{sp}$ of single electrode / $Fg^{-1}$	$A_{BET}$ / $m^2g^{-1}$	Pore volume / $cm^3g^{-1}$
M20	378.8	2129.0	1.0
M30	272.5	2571.2	1.2
FD1	135.1	1851.0	1.0
FD2	160.0	1560.0	0.7
FT2A	140.0	1330.6	0.5
FT7A	140.0	2137.5	0.9
FU11B	147.4	2441.7	1.0
FU11C	249.2	2015.0	0.9

An interesting study was performed by Gryglewicz and co-workers on the influence of pore size distribution on the double-layer capacitance [50]. After investigating a series of activated carbons as the electrode active material for EDLC with  $A_{BET}$  ranging between 340-1270  $m^2g^{-1}$  and a wide range of mesopore content (16.7% to 86.9% of total pore volume) in both acidic and alkaline electrolytes, they concluded that sufficient specific surface area is equally as important as pore size distribution. This argument seems logical when looking at the main goal which is to increase ion accessibility to the electrode surface. Logically, due to its great sensitivity, an increase in  $A_{BET}$  can be associated with a rise in micropore ( $d < 2$  nm), mesopore ( $2 < d < 50$  nm) or macropore ( $> 50$  nm) volume or a combination of them. Depending on the size of the charge carriers, one of these cases is more favourable. Regarding Table 2.1 (results reported by Shi [48]), cells made with FT activated carbon, possess the same specific capacitance value ( $140.0 Fg^{-1}$ ) while FT7A possesses a larger  $A_{BET}$  and pore volume

compared to FT2A. This could be attributed to pore size distribution of the FT7A not agreeing with the size of the ionic species in the aqueous electrolyte.

Furthermore, several publications have shown an improvement in the capacitive performance of activated carbon-based EDLCs by modifying the surface function of the activated carbon electrode. Fang and Binder showed that the presence of the organic functional group  $-(\text{CH}_3\text{O})_2\text{SiCH}=\text{CH}_2$ , can increase the hydrophobicity of AC and thus increase its affinity to non-polar organic electrolytes such as propylene carbonate (PC) i.e. improving the wettability of the electrode by such electrolytes [51]. Another noteworthy example is the work done by Hsieh and Teng on the influence of oxygen treatment on the properties of AC supercapacitors [49]. As a result of the treatment, carbonyl and quinone-type groups were introduced to the surface of the AC causing Faradaic current to pass through the system during the charge and discharge cycles and increasing the capacitance by 25%.

Activated carbon is an attractive material for energy storage applications, specifically supercapacitors, due to their high surface area, low cost, abundance of its sources and well-established electrochemical properties. Some examples of carbon-rich precursors used to derive AC includes agricultural residue [46], coconut shell [52], Paulownia flower [53] and waste tea [54]. More details on the preparation of activated carbon-based electrodes are given in Chapter 3.

## 2.7 Ionic liquids

Ionic liquids (ILs) are salts with melting points below  $100^\circ\text{C}$  and are exclusively made of cation and anions; meaning this class of salts does not require a solvent in order to be dissociated [55]. Room temperature ionic liquids (RTILs) are salts with melting points below room temperature. Ionic liquids consist mostly of large organic cations and small (organic/inorganic) anions.

The first ionic liquid is believed to have been synthesised in 1914 by Walden [56]. He reported the synthesis of ethylammonium nitrate ( $\text{C}_2\text{NH}_8\text{NO}_3$ ) IL with a melting point of  $12^\circ\text{C}$  via the reaction between ethylamine and concentrated nitric acid. This was followed by Hurley and Weir's work in which they reported a room temperature synthesis route of an IL by mixing and heating 1-ethylpyridinium chloride with chloroaluminate ( $\text{AlCl}_3$ ) [57]. Subsequently, differ-

ent researchers extensively investigated the application of  $\text{AlCl}_3$  in IL fabrication [58–60]. However, the hygroscopic nature of fabricated ILs (including  $\text{AlCl}_3$ -based ILs) was the major influencer of a lack of scientific and industrial interest and progress in these materials. In 1992 the first air and water stable ILs were reported by Wilkes and Zaworotko, based on an organic cation (imidazolium) and two different inorganic anions (tetrafluoroborate and hexafluorophosphate) [61]. It was reported later that the application of more hydrophobic anions made the IL more stable towards moisture for a longer duration [62,63]. Figure 2.8a and 2.8b present the number of published documents relating to ionic liquids in terms of year of publication and subject area since 1914. As shown in Figure 2.8a, a limited number of publications per year in the early and mid-20<sup>th</sup> century has transformed into more than 6600 publications in 2017, and a multidisciplinary field of ILs. Around 7.5% of the publications (a total of ~5800 publications since 1914) in this field are reportedly dedicated to the application of ILs within the discipline of energy. Numerous publications have investigated the application of ionic liquids as the electrolyte for batteries and supercapacitors [64–67].

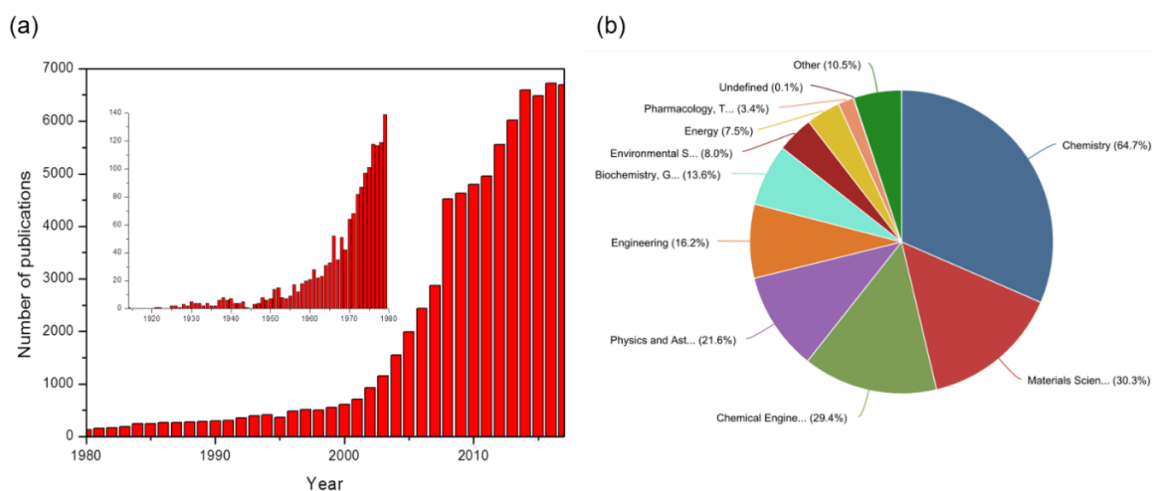


Figure 2.8 (a) Publications containing the phrase “ionic liquid” in the title, abstract and key words as a function of time and (b) subject area. The bar chart represents a total of 77307 publications between 1914 and 2017 (Determined by Scopus).

Electrolytes are a key component of an electrochemical system and they can greatly influence the properties and performance of a cell. An electrolyte resides inside the active material and the separator and provides ionic conductivity between the two electrodes. The most suitable electrolyte must ideally satisfy the following criteria [6]:

- a) Wide potential window
- b) High electrochemical stability
- c) High thermal stability
- d) Low to zero toxicity
- e) High ionic conductivity
- f) Low volatility and flammability
- g) Low viscosity
- h) Low cost

Liquid electrolytes used for supercapacitors are categorised into three major groups, namely (i) aqueous, (ii) organic and (iii) ionic liquids. Table 2.2 provides a comparison between the key physiochemical properties of the three major electrolyte groups. The physiochemical properties of ILs are highly temperature dependant. Generally, ILs have higher viscosity at room temperature (ranging between 10 and 500 mPa s) compared to other molecular solvents [68]. The viscosity is determined by the Van der Waals forces, hydrogen bonds and electrostatic forces present in the ionic system. For instance, it has been shown that ILs with fluorinated anions possess high viscosities due to the increased tendency of H-bond formation [68,69]. In addition, the presence of lengthy alkyl chains in the cation results in higher viscosity as stronger Van der Waals forces exists between cations [62].

Being made exclusively of positive and negative ions, ILs are expected to have high ionic conductivity. Generally, conductivity of a solution is dependent on the number of charge carriers and their mobility [68]. At room temperature, the ionic conductivity of ILs is lower than those of concentrated aqueous electrolytes which is mainly associated to large constituent ions, high viscosity and ion aggregation [68,70]. As the temperature of ILs is raised beyond room temperature, the overall viscosity is reduced and thus, the ionic conductivity increases [71].

Ionic liquids are mostly non-flammable (depending on the cation and anion combination) and possess low vapour pressure [70]. This property makes IL a safer candidate for the electrolyte in energy storage systems including batteries and supercapacitors [65]. In addition, ILs have a wide electrochemical potential window, defined as the potential range within which the electrolyte is not oxidised or reduced at the electrode surface [68]. As it is shown in equation 2.11 (section 2.5.3), the energy density is proportional to the capacitance and square of the potential window. Therefore, widening the potential window is more beneficial in terms of the amount of energy stored in the device compared to the influence of the specific capacitance.

Table 2.2 Examples of the key physiochemical properties of different ionic liquid, organic and aqueous electrolytes for supercapacitor applications. Abbreviations: AN= acetonitrile, PC= propylene carbonate, [Emim]= 1-Ethyl-3-methylimidazolium, [BF<sub>4</sub>]= tetrafluoroborate, TEABF<sub>4</sub>=Tetraethylammonium tetrafluoroborate

Electrolyte category	Operation temperature limit(s)	Viscosity at room temperature / mPa s	Ionic conductivity (at room temperature) / mS cm <sup>-1</sup>	Potential window with carbon-based electrodes	Comments	
Ionic liquid [6,65,68,72]	i) Aprotic ii) Protic (Cheaper and easier to synthesise than aprotic ILs)	Up to 450°C	10-500	Example: i) [Emim][BF <sub>4</sub> ]→ 14 ii) [Emim][TFSI]→ 11 (at 30°C)	i) >3 V ii) 3.4-3.5 V	Non-flammable, non-volatile, costly
	Typically, Conductive salts dissolved in AN or PC					

Electrolyte category	Operation temperature limit(s)	Viscosity at room temperature / mPa s	Ionic conductivity (at room temperature) / mS cm <sup>-1</sup>	Potential Window With carbon-based electrodes	Comments
Aqueous [6,73,74]	Acidic e.g. H <sub>2</sub> SO <sub>4</sub> Alkaline e.g. KOH	between 0- 100°C	Less than that of ionic liquid and organic electrolytes Example: i) 1 M H <sub>2</sub> SO <sub>4</sub> → 800 ii) 6 M KOH → 600	Typically: <1.2 V	Inexpensive and easy to handle. The water decomposition restricts potential window.

Ionic liquids mostly consist of a large irregular inorganic heterocyclic cation, such as imidazolium and pyrrolidinium, and an organic or inorganic anion including tetrafluoroborate, nitrate and trifluoromethanesulfonate. Figure 2.9 shows examples of some of the most commonly utilised cations and anions for electrochemical applications and their molecular structures. It is this large and antisymmetric ion structure that does not allow easy crystallisation (as occurs easily in inorganic salts like NaCl) that results in low melting points (<100°C) [75].

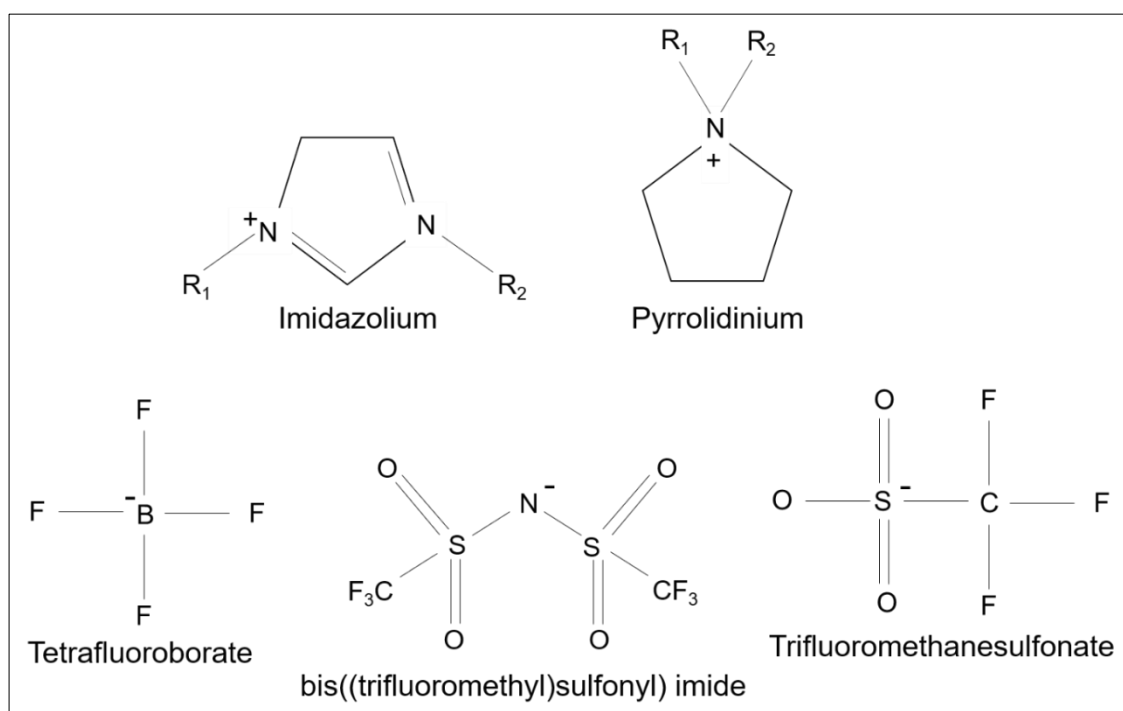


Figure 2.9 Examples of some common ionic liquid cations and anions.

High viscosity at room temperature is one of the major issues for ionic liquids as electrolytes in electrochemical devices. For this reason, some attempts have been made to resolve this issue. One commonly suggested method to overcome this problem is to use organic solvents such as propylene carbonate (boiling point of 242°C) [76,77], acetonitrile (boiling point of 82°C) [78,79], butyronitrile (boiling point of 117°C) [80] or 1,2-dichloroethane (DCE, boiling point of 83.5°C) [76] as a co-solvent. However, due to the flammable nature of organic solvents, their mixture with ionic liquids seems to be a counterproductive solution considering that the key purpose of IL application is the maintenance of safety.

Increasing the operating temperature is another suggested method to reduce IL electrolyte viscosity and thus, improve ionic conductivity. Operating temperature-dependency of the performance of electrochemical systems containing IL has been widely investigated [81–83]. Zheng et al. reported a ~90% drop in the electrode-electrolyte interface resistance (also known as charge transfer resistance,  $R_{ct}$ ) of a system containing a spinel  $\text{LiMn}_2\text{O}_4$  electrode and [TMHA][TFSI] (trimethylhexylammonium bis(trifluoromethane)sulfonylimide) ionic liquid electrolyte (containing 1M LiTFSI salt) when the temperature was increased from 20°C to 50°C [81]. This was attributed to the reduction of IL viscosity as a result of temperature increase. Similarly, Rodrigues et al. demonstrated a 50-fold decrease in the  $R_{ct}$  of a methoxymethyl)triethylphosphonium bis(trifluoromethylsulfonyl)imide-based lithium ion half cell (lithium titanate electrode) when the operating temperature was increased from 25 to 60°C [82]. Negre et al. reported that the ionic conductivity of an electrolyte containing a mixture of two bis(fluorosulfonyl)imide-based ionic liquids rises from ~5  $\text{mS cm}^{-1}$  at 20°C to ~11  $\text{mS cm}^{-1}$  at 80°C [83]. However, the application of supercapacitors and batteries are not limited to high operating temperatures. Thus, it is fair to conclude that high viscosity (and as a result, low ionic conductivity) of ILs at room temperature is an issue that remains problematic to this date.

## **2.8 Immobilisation of ionic liquids for electrochemical applications**

Although ionic liquids can overcome the major safety issues associated with the commercial electrolytes for energy storage devices (i.e. flammability and high vapour pressure), the problem of electrolyte leakage remains unresolved. Recently, ionogels have attracted the attention of many researchers as a unique and versatile type of electrolyte for batteries and supercapacitors. Ionogels are ionic liquids confined in a solid/quasi solid structure. Depending on the type and chemical composition of the ionogel, the physical appearance can vary from rigid and brittle to soft and compliant [84,85]. Being confined in a solid/quasi solid matrix helps prevent any problem associated with ionic liquid leakage while preserving its high ionic conductivity [86]. In addition, application of ionogels removes the need for the conventionally used rigid metal casings for safe containment of electrolyte and thus, can result in lighter, safer and more flexible

electronics [84]. This is very attractive to the wearable, printable and portable electronic industries [6]. In addition, other than a physical confinement for ionic liquids, ionogels act as separator inside electrical systems preventing short circuits. This eliminates the need for separators all together [87].

The properties of an ionogel are dependent on the nature of the utilised ionic liquid, the solid backbone and the interaction between them. The following sections aim to describe different types of ionogels and to provide an overview of the most recent literature, mainly in supercapacitor applications.

### **2.8.1 Different methods of ionic liquid confinement**

Depending on the type of the IL-encapsulating network, ionogels are classified into two main categories; organic and inorganic. Organic ionogels are synthesised using low molecular weight gelators (LMWGs) or polymers. The LMWGs are organic molecules that are added to ionic liquids at elevated temperatures and gelation takes place upon cooling of the system. In such ionogels, the gel network interacts with IL through H-bonding,  $\pi$ - $\pi$  and electrostatic interactions [70]. Polymer ionogels are fabricated through either swelling (or mixing) a polymer inside or (with) IL in the presence of a co-solvent, or by polymerising monomers while using IL as the solvent [88]. This type of ionogel combines the mechanical properties of polymers with the ionic conductivity of ILs. However, polymer-based systems have been shown to negatively impact the thermal stability of the gel electrolyte to the point of polymer degradation when compared to that of pristine IL [89].

Inorganic ionogels are classified into three groups; oxide networks based on sol-gel processing, gels arising from the dispersion of silica nanoparticles and carbon nanotube-based gels. In the latter, the gelation takes place through physical crosslinking of the nanotubes mediated by IL [70]. Similarly, the silica nanoparticles in the presence of an IL form a gel via weak intermolecular forces (Van der Waals and/or H-bonding) while sol-gel based ionogels are covalently bound [90]. Wang et al. published an interesting comparative study between ionogels derived from the last two named techniques. They fabricated EDLCs based on each of the ionogels with similar IL content sandwiched between acti-

vated carbon electrodes and both systems showed comparable thermal and electrochemical characteristics [90].

Unlike organic polymer-based ionogels, sol-gel derived gels have been shown to not impact the thermal stability of the resultant ionogels [89] and depending on the formulation, they can possess comparative ionic conductivity to that of pristine ILs [84,86]. For these reasons, this thesis is focused on this group of ionogels and to further explore this category of electrolytes for supercapacitor applications. Although sol-gel is a well-established field of chemistry, given the big family of ionic liquids and the recent growth of interest in ionogels, specifically in the world of electronics, many knowledge gaps still exist to this date. The following sections aim to highlight different areas that have been studied to this date to provide a clearer vision on where ionogels stand today and which areas require further investigation.

### 2.8.2 Ionogels through sol-gel processing

Sol-gel is a convenient method for ionogel fabrication in which the ionic liquid is confined in a solid network. The essence of sol-gel chemistry can be simply described as the transformation of (most commonly) a metal alkoxide precursor ( $[M]OR$ ) into a metal oxide ( $[M]O[M]$ ) network through a series of hydrolysis and condensation reactions. The hydrolysis reaction refers to the chemical reaction in which a hydroxyl group is linked to the metal atom [91]:



where  $[M]OR$ ,  $R$  and  $ROH$  represent the metal alkoxide (typically  $Si(OR)_4$ ), an organic functional group (typically alkyl groups) and an alcohol, respectively. Depending on the catalyst (if present) or the amount of water present in the reaction environment, the process of hydrolysis continues until partial or full hydrolysis of the precursor has taken place. The process of condensation involves (by definition) liberating a water and/or alcohol molecule [91]:



The product of the condensation reaction is called the 'sol' which is a dispersion of colloidal particles that connect together as the condensation proceeds further to create a three-dimensional structure called the 'gel'. This is followed by the drying and aging processes (prior to the formation of a stable solid network) where the volatile by-products and solvent(s) are extracted from the structure of the gel and may result in shrinkage. The resultant dried gels are referred to as xerogels (dried via evaporation) or aerogels (typically dried via supercritical extraction of the volatiles) [91,92]. For a gel network to be 'stable' (fully gelled), the number of [M]O[M] or metal oxide groups must be maximised while the number of [M]OH (metal hydroxides) and [M]OR groups must be minimised [92]. In the case of ionogel synthesis, although ionic liquid usually does not participate in the formation of the three-dimensional structure (as opposed to cases such as [93,94]), its low vapour pressure prevents solvent evaporation and thus inhibits collapsing of the sol-gel matrix while the gel prevents IL leakage [55]. Typically, no covalent bond is created between IL and silica [95]. The application of ILs as the solvent in a sol-gel process was first reported by Dai et al. in 2000 [96]. 1-ethyl-3-methylimidazolium bis((trifluoromethyl)sulfonyl) imide, [Emim][TFSI], ionic liquid was used in an acid-catalysed sol-gel process to stabilise the gel network during the aging process, after which the ionic liquid was removed from the gel (using acetonitrile, a polar solvent) to create a solid network. This innovative work initiated extensive investigations on the effects of IL on the sol-gel synthesis process and its possible applications in different disciplines. However, the application of sol-gels within this thesis is solely related to solid electrolytes for supercapacitors.

Ionogel preparation can be performed through either a hydrolytic [95,97,98] or a non-hydrolytic [84,85,99,100] (also known as acid solvolysis) sol-gel processing route. In the former technique, the hydrolysis reaction takes place in the presence of water or alcohol and in some cases a small volume of catalyst (e.g. 0.1 M HCl, [95]) is added to initiate the hydrolysis reaction. In the non-hydrolytic method, an acid is utilised both as the reactant and the solvent in the absence of water. The non-hydrolytic sol-gel route is more commonly reported in the literature for the fabrication of ionogel electrolytes which could be ascribed to the minimised volume of water in the electrolyte system. Another key difference be-

tween the two techniques is the rate of hydrolysis and condensation processes which are attributed to the pH dependency of these reactions. It has been shown that acidic conditions favour the hydrolysis of silicon alkoxides while the opposite is true for the condensation of silanol groups, Si–OH (as shown in Figure 2.10) [101]. Therefore, it is expected that under acidic conditions, the hydrolysis process takes place rapidly at first and slows down over time as more alcohol and water is produced [84].

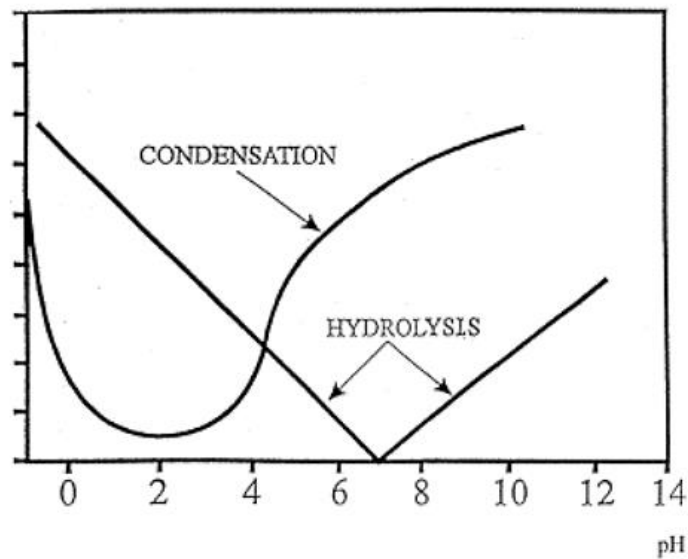
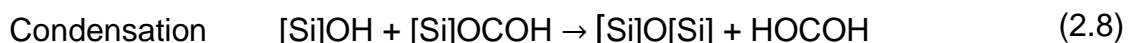
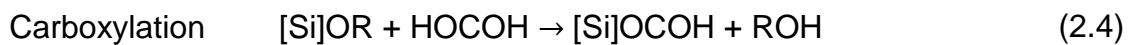


Figure 2.10 Schematic of relative hydrolysis and condensation kinetics of silicon alkoxide as a function of pH. Retrieved from [101].

Furthermore, reactions taking place in a non-hydrolytic sol-gel processing are slightly more complex than the hydrolytic route. This synthesis route that was first introduced by K. Sharp [102] using formic acid (FA) as solvent, involves carboxylation, esterification, hydrolysis and condensation reactions [103]:



where HOCOH and ROCOH represent FA and alkyl-formate, respectively. As can be seen, alkyl-formate is an additional volatile by-product of the non-

hydrolytic synthesis route which is expected to escape the gel structure during aging and drying stages.

Viau et al. provided a systematic comparison between these two synthesis approaches in terms of morphology, pore size, surface area and pore volume of various porous silica encapsulating different imidazolium and pyridinium-based ILs [103]. They argued that due to the reduced formation and release of volatile by-products in the hydrolytic method, a smaller degree of capillary tension and shrinkage occurs compared to the non-hydrolytic counterpart.

### **2.8.3 Influence of formulation on ionogels**

Generally, physical, chemical and electrical properties of the resultant ionogel produced via the sol-gel technique are dependent on the structure of the gel network, the ionic liquid itself and the interaction between the two.

As mentioned in the previous section, the application of a non-hydrolytic sol-gel route based on hydrolysis and condensation of silicon alkoxides is commonly employed for the synthesis of ionogels [84,87,104,105]. This is due to the simplicity, and versatile nature of this method. In addition, the presence of excess water in the ionogel produced via hydrolytic method can jeopardise the cathodic and anodic limits of the potential window (due to water splitting [106], explained in Chapter 7). The formulation of ionogels can determine the mechanical strength, degree of IL confinement, porous structure, surface functional groups and speed of gelation of the silica scaffold [84]. These characteristics are of paramount importance in the case of devices such as supercapacitors to ensure full encapsulation of the IL, to reduce IL diffusion resistance within the gel network, to increase the effective contact area at the electrode-electrolyte interface and finally to minimise the fabrication duration.

Horowitz et al. studied the influence of reactant formulation (precursor: acid catalyst: IL) on the mechanical characteristics, morphology and gelation time of [Emim][TFSI]-based ionogels [85]. Their work demonstrated that the reduction of FA: TMOS (tetramethylorthosilicate) molar ratio as well as increase in the percentage volume of IL, results in an increase in the gelation time. They reported gelation times ranging between 15 minutes (51% IL) to more than 12 hours (>70% IL) at ambient conditions. With the use of scanning electron mi-

croscopy (SEM), they showed that rapid gelation results in the formation of large voids (<5  $\mu\text{m}$  in diameter) in the silica scaffold while in a system with a slower gelation time, a denser silica structure was observed. Furthermore, they demonstrated that by reducing the silica content (or increasing the IL content), a more compliant/soft gel is produced rather than a brittle gel. The physical integrity of ionogels comes with great importance as very soft ionogels (usually with high IL loading) can easily deform in response to low mechanical forces while brittle ionogels as well as ionogels with significant shrinkage are unsuitable for electrolyte-based applications due to their possible loss of contact with the electrode. In a similar work published in 2012, Horowitz and Panzer approximated a 8-9% silica content (relative to the mass of the ionogel) to be the threshold between compliant and brittle ionogels [84].

Another interesting study on ionogels was conducted by Gupta et al. who reported extremely fast (~1 minute) gelation of 1-ethyl-3-methyl tetrafluoroborate-based ionogel using tetraethylorthosilicate (TEOS) and FA with a reactant molar ratio (TEOS:FA) of 1:8 and low ionic liquid content (0.25 to 0.35 mol%) [100]. However, this formulation may not be viable for electrochemical applications due to the low ionic liquid content which results in low ionic conductivity. Based on the results of a series of BET, thermogravimetric analysis (TGA) and transmission electron microscopy (TEM) characterisations, fast gelation resulted in 35-45% blind pores inside the silica scaffold which was mainly associated with the entrapment of the volatile by-products in the scaffold in the presence of the ionic liquid (compared to only 6% blind pores in the absence of the ionic liquid). Interestingly, by removing IL from the formulation, the gelation time increased to 5-6 days. Even though no explanation was given for this observation, it is clear that the presence of IL and the type of the IL can influence the gelation rate.

Sol-gel materials derived from alkoxy silane precursors can form various inorganic-organic hybrid structures via different combinations of precursors. A common formulation is to combine different silicon alkoxides to modify the mechanical characteristics and surface functional groups of the ionogels. One commonly reported combination is the mixture of a tetraalkoxy silane (typically TMOS or TEOS) and an alkyltrialkoxysilane (e.g. trimethoxymethylsilane, MTMS) [86,107,108]. The presence of  $[\text{Si}]\text{-R}$  bonds (where R represents a func-

tional alkyl group) in the sol mixture, results in a delay in gelation and a lower degree of shrinkage due to fewer crosslinks across the gel. In addition, depending on the alkyl group, its chain length, and the number of R groups available, the hydrophobicity of the gel scaffold can also vary. Neouze et al. reported a maximum gelation period of 36 hours for an ionogel synthesised via a non-hydrolytic sol-gel route using TMOS, MTMS and 1-butyl-3-methylimidazolium bis(trifluoromethylsulfonyl)imide ionic liquid at a 1:1:x molar ratio (TMOS:MTMS:IL, x=0.5, 1.0) [86]. By removing MTMS from the formulation the gelation period dropped to 1 hour. It has also been shown that gel scaffolds containing higher molar ratio of MTMS to TMOS, possess higher BET surface area [108]. This shows that the slight variations in the formulation can induce significant changes in the structure of the gel network. Furthermore, the presence of methyl groups can make the ionogel stable towards water [86,103] which is beneficial for electrochemical applications. It was also shown that the thermal stability of ionogels remained unaltered when a large number of methyl groups were incorporated in the gel network [86]. Therefore, in addition to the processing of ionogels, it is crucial to know whether the silica network can influence the electrochemical behaviour of the ionogels. However, this has not been explored extensively in the literature.

#### **2.8.4 Influence of ionic liquid on the structure of the solid network**

The presence of ionic liquid has been shown to influence the structure of the solid network [103,109,110]. Ionic liquids have been used as a 'drying control additive' to assist the silica network to relax the interface strain caused by the evaporation of volatiles and minimise the subsequent shrinkage of the solid network [109,111]. It has also been shown that the IL cation and anion combination, as well as the synthesis route (hydrolytic or non-hydrolytic), can greatly influence the porosity of the gel network and its gelation rate [103]. Furthermore, the type and degree of interaction between IL and the confining structure has been shown to be material dependent and it can influence the mobility of ions inside the gel network resulting in changes in ionic conductivity of the ionogel [98,101].

Table 2.3 highlights some additional studies performed on ionogels via the sol-gel technique. It is this wide range of possibilities and diversity of ionogels that

demands further investigation and research in this field to be able to create application specific systems. For these reasons, the work of this thesis is designed to further explore and study around (a) the influence of silica precursor on the physical properties and electrochemical performance of ionogels as electrolyte for EDLCs, (b) the strength of interactions between the chosen IL and pore walls of the confining silica matrix, and lastly, (c) the effect of curing process on the physical properties, electrochemical performance and degradation rate of the EDLCs. The latter objective is designed to address two of the key issues associated with sol-gel based ionogels which are slow gelation and poor performance at room temperature. The role of each chapter towards achieving the outlined objectives of this

Table 2.3 Some examples of ionogels synthesised through sol-gel processing. Abbreviations: CA=Citric Acid, VTES= Vinyltriethoxysilane, [Bmim]= 1-butyl-3-methylimidazolium, [PF<sub>6</sub>]= hexafluorophosphate, [Tf<sub>2</sub>N]= bis(trifluoromethyl-sulphonyl)imide, [PIP13]= N-methyl-N-propylpiperidinium, [PYR14]= N-butyl-N-methylpyrrolidinium [FSI]= bis(fluorosulfonyl)imide, [SiM-BIM]= 1-trimethylsilylmethyl-3-butylimidazolium.

Precursor(s) <sup>a</sup>	Synthesis route and catalyst (if any) <sup>b</sup>	Ionic liquid <sup>c</sup>	Reactant molar ratio a: b: c	Gelation duration	Aging duration and condition	Ref.
TMOS	Non-hydrolytic-FA in-situ	[Emim][TFSI]	1:6:6	21 hours	3 hours Under N <sub>2</sub> humidity <1%	[90]
TMOS	Non-hydrolytic-FA in-situ	[Emim][TFSI]	i) 1:6:6 (compliant) ii) 1:7.8:1 (brittle)	i) Within 24 hours ii) Within 2 hours	i) 12 days ii) 15 days (ambient conditions)	[84]
TMOS:TEOS 1:1	Non-hydrolytic-Methanolic acid in-situ	(PIP13-FSI): (PYR14-FSI) 50:50 (weight)	2:5:c IL→60% by volume	Within 24 hours (reactants were mixed for over 18 minutes at 40°C)	4 days at 50°C (argon atmosphere)	[83]
VTES:TMOS 1:1	Non-hydrolytic-FA ex-situ	[Bmim][BF <sub>4</sub> ]	2:5:c IL→72% by volume	3 hours (at 50°C)	50°C for 3 hours+100°C for 2 days	[104]

Precursor(s) <sup>a</sup>	Synthesis route and catalyst (if any) <sup>b</sup>	Ionic liquid <sup>c</sup>	Reactant molar ratio a: b: c	Gelation duration	Aging duration and condition	Ref.
TMOS	Hydrolytic- CA in-situ	[Bmim][BF <sub>4</sub> ] [Bmim][Tf <sub>2</sub> N] [Bmim][PF <sub>6</sub> ]	TMOS:ethanol:H <sub>2</sub> O:CA:l L 1:3:4:0.02:0.1	[BF <sub>4</sub> ] $\rightarrow$ 20 minutes [Tf <sub>2</sub> N] $\rightarrow$ 150 minutes [PF <sub>6</sub> ] $\rightarrow$ 30 minutes (at 70°C)	3 days (ambient conditions)	[110]
TMOS	Non-hydrolytic- FA in-situ	Li[TFSI] <sup>+</sup> [SiM-BIM][TFSI]	TMOS:FA:Li[TFSI]:[SiM-BIM][TFSI] 0.035:0.117:0.006:x x=10g	2 days in N <sub>2</sub> atmosphere	5 days (70°C, under vacuum)	[105]

## 2.9 References

- [1] F. Scholz, From the Leiden jar to the discovery of the glass electrode by Max Cremer, *J. Solid State Electrochem.* 15 (2011) 5–14.  
doi:10.1007/s10008-009-0962-7.
- [2] T.B. Greenslade, Discovery of Leiden jar, *Phys. Teach.* 32 (1994) 536–537. doi:10.1119/1.2344104.
- [3] J.Z. Buchwald, *Scientific credibility and technical standards in 19<sup>th</sup> and early 20<sup>th</sup> century Germany and Britain*, Kluwer Academic Publishers, 1996.
- [4] J. Mandapati, K. Balasubramanian, Simple capacitors to supercapacitors - An overview, *Int. J. Electrochem. Sci.* 3 (2008) 1196–1217.
- [5] G.Z. Chen, Understanding supercapacitors based on nano-hybrid materials with interfacial conjugation, *Prog. Nat. Sci. Mater. Int.* 23 (2013) 245–255. doi:10.1016/j.pnsc.2013.04.001.
- [6] C. Zhong, Y. Deng, W. Hu, J. Qiao, L. Zhang, J. Zhang, A review of electrolyte materials and compositions for electrochemical supercapacitors, *Chem. Soc. Rev.* 44 (2015) 7484–7539.  
doi:10.1039/C5CS00303B.
- [7] A. Yu, V. Chabot, J. Zhang, *electrochemical double-layer capacitors for energy storage and conversion*, 1<sup>st</sup> ed., CRC Press, Boca Raton, 2013.
- [8] Leyden Jar-FK 1152, Teylers · Museum Wonder. (n.d.).  
<https://www.teylersmuseum.nl/en/collection/instruments/fk-1152-leiden-jar>  
(accessed January 22, 2018).
- [9] H. Helmholtz, Studien über elektrische Grenzschichten, *Ann. Phys.* 243 (1879) 337–382. doi:10.1002/andp.18792430702.
- [10] H.I. Becker, Low voltage electrolytic capacitor, US2800616A, 1957.  
<https://www.google.com/patents/US2800616>.
- [11] R.A. Rightmire, Electrical energy storage apparatus, US3288641A, 1966.  
<https://www.google.co.uk/patents/US3288641>.

- [12] M. Gouy, Sur la constitution de la charge électrique à la surface d'un électrolyte, *J. Phys. Théorique Appliquée*. 9 (1910) 457–468.  
doi:10.1051/jphystap:019100090045700.
- [13] D.L. Chapman, A contribution to the theory of electrocapillarity, London, Edinburgh, Dublin *Philos. Mag. J. Sci.* 25 (1913) 475–481.  
doi:10.1080/14786440408634187.
- [14] O. Stern, Zur theorie der elektrolytischen doppelschicht, *Z. Elektrochem. Angew. Phys. Chem.* 30 (1924) 508–516.
- [15] D.C. Grahame, The nature of the electrical double layer, *J. Chem. Educ.* 20 (1943) 154. doi:10.1021/ed020p154.
- [16] J. Varghese, H. Wang, L. Pilon, Simulating electric double layer capacitance of mesoporous electrodes with cylindrical pores, *J. Electrochem. Soc.* 158 (2011) A1106–A1114. doi:10.1149/1.3622342.
- [17] R. Burt, G. Birkett, X.S. Zhao, A review of molecular modelling of electric double layer capacitors, *Phys. Chem. Chem. Phys.* 16 (2014) 6519–6538.  
doi:10.1039/C3CP55186E.
- [18] J.P. Zheng, J. Huang, T.R. Jow, The limitations of energy density for electrochemical capacitors, *J. Electrochem. Soc.* 144 (1997) 2026–2031.  
doi:10.1149/1.1837738.
- [19] S. Trasatti, G. Buzzanca, Ruthenium dioxide: A new interesting electrode material. Solid state structure and electrochemical behaviour, *J. Electroanal. Chem. Interfacial Electrochem.* 29 (1971) A1–A5.  
doi:10.1016/S0022-0728(71)80111-0.
- [20] R. Warren, F. Sammoura, F. Tounsi, M. Sanghadasa, L. Lin, Highly active ruthenium oxide coating via ALD and electrochemical activation in supercapacitor applications, *J. Mater. Chem. A*. 3 (2015) 15568–15575.  
doi:10.1039/C5TA03742E.

- [21] W. Wei, X. Cui, W. Chen, D.G. Ivey, Manganese oxide-based materials as electrochemical supercapacitor electrodes, *Chem. Soc. Rev.* 40 (2011) 1697–1721. doi:10.1039/C0CS00127A.
- [22] Y. Wang, Y. Song, Y. Xia, Electrochemical capacitors: mechanism, materials, systems, characterization and applications, *Chem. Soc. Rev.* 45 (2016) 5925–5950. doi:10.1039/C5CS00580A.
- [23] T. Brousse, O. Crosnier, D. Bélanger, J.W. Long, Capacitive and pseudocapacitive electrodes for electrochemical capacitors and hybrid devices, in: *Met. Oxides Supercapacitors*, Elsevier, 2017: pp. 1–24. doi:10.1016/B978-0-12-810464-4.00001-2.
- [24] G. Wang, L. Zhang, J. Zhang, A review of electrode materials for electrochemical supercapacitors, *Chem. Soc. Rev.* 41 (2012) 797–828. doi:10.1039/C1CS15060J.
- [25] M.R. Lukatskaya, B. Dunn, Y. Gogotsi, Multidimensional materials and device architectures for future hybrid energy storage, *Nat. Commun.* 7 (2016) 12647. doi:10.1038/ncomms12647.
- [26] P. Simon, Y. Gogotsi, B. Dunn, Where do batteries end and supercapacitors begin?, *Science* (6176). 343 (2014) 1210–1211. doi:10.1126/science.1249625.
- [27] W. Zuo, R. Li, C. Zhou, Y. Li, J. Xia, J. Liu, Battery-supercapacitor hybrid devices: recent progress and future prospects, *Adv. Sci.* 4 (2017) 1–21. doi:10.1002/advs.201600539.
- [28] S. Fletcher, V.J. Black, I. Kirkpatrick, A universal equivalent circuit for carbon-based supercapacitors, *J. Solid State Electrochem.* 18 (2014) 1377–1387. doi:10.1007/s10008-013-2328-4.
- [29] R. Kötz, M. Carlen, Principles and applications of electrochemical capacitors, *Electrochim. Acta.* 45 (2000) 2483–2498. doi:10.1016/S0013-4686(00)00354-6.

- [30] T. Chen, L. Dai, Flexible supercapacitors based on carbon nanomaterials, *J. Mater. Chem. A*. 2 (2014) 10756–10775. doi:10.1039/C4TA00567H.
- [31] R. Signorelli, D.C. Ku, J.G. Kassakian, J.E. Schindall, Electrochemical double-layer capacitors using carbon nanotube electrode structures, *Proc. IEEE*. 97 (2009) 1837–1847. doi:10.1109/JPROC.2009.2030240.
- [32] J. Biener, M. Stadermann, M. Suss, M.A. Worsley, M.M. Biener, K.A. Rose, T.F. Baumann, Advanced carbon aerogels for energy applications, *Energy Environ. Sci.* 4 (2011) 656–667. doi:10.1039/C0EE00627K.
- [33] Y. Gogotsi, P. Simon, True performance metrics in electrochemical energy storage, *Science* (6058). 334 (2011) 917–918. doi:10.1126/science.1213003.
- [34] M.F.L. De Volder, S.H. Tawfick, R.H. Baughman, A.J. Hart, Carbon nanotubes: Present and future commercial applications, *Science* (6119). 339 (2013) 535–539. <http://science.sciencemag.org/content/339/6119/535.abstract>.
- [35] L.L. Zhang, X.S. Zhao, Carbon-based materials as supercapacitor electrodes, *Chem. Soc. Rev.* 38 (2009) 2520–2531. doi:10.1039/b813846j.
- [36] A. Balducci, R. Dugas, P.L. Taberna, P. Simon, D. Plée, M. Mastragostino, S. Passerini, High temperature carbon–carbon supercapacitor using ionic liquid as electrolyte, *J. Power Sources*. 165 (2007) 922–927. doi:10.1016/J.JPOWSOUR.2006.12.048.
- [37] D. Weingarh, A. Foelske-Schmitz, R. Kötz, Cycle versus voltage hold – Which is the better stability test for electrochemical double layer capacitors?, *J. Power Sources*. 225 (2013) 84–88. doi:10.1016/J.JPOWSOUR.2012.10.019.
- [38] A. Borenstein, O. Hanna, R. Attias, S. Luski, T. Brousse, D. Aurbach, Carbon-based composite materials for supercapacitor electrodes: a review, *J. Mater. Chem. A*. 5 (2017) 12653–12672. doi:10.1039/C7TA00863E.

- [39] D. Yang, Application of nanocomposites for supercapacitors: Characteristics and properties, in: F. Ebrahimi (Ed.), *Nanocomposites - New Trends Dev.*, InTech, Rijeka, 2012: pp. 299–328. doi:10.5772/50409.
- [40] M. Okamura, K. Hayashi, H. Ohta, Status report 2006 on ECaSS and the nanogate-capacitors, in: *Proc. 16<sup>th</sup> Int. Semin. Double Layer Capacit. Hybrid Energy Storage Devices*, Deerfield Beach, FLorida, USA, 2006: pp. 149–158.
- [41] P.W. Ruch, D. Cericola, A. Foelske-Schmitz, R. Kötz, A. Wokaun, Aging of electrochemical double layer capacitors with acetonitrile-based electrolyte at elevated voltages, *Electrochim. Acta.* 55 (2010) 4412–4420. doi:10.1016/j.electacta.2010.02.064.
- [42] D. Cericola, P.W. Ruch, A. Foelske-Schmitz, D. Weingarh, R. Kötz, Effect of water on the aging of activated carbon based electrochemical double layer capacitors during constant voltage load tests, *Int. J. Electrochem. Sci.* 6 (2011) 988–996.
- [43] D. Qu, H. Shi, Studies of activated carbons used in double-layer capacitors, *J. Power Sources.* 74 (1998) 99–107. doi:10.1016/S0378-7753(98)00038-X.
- [44] H. Marsh, F. Rodrigues-Reinoso, *Activated Carbon*, Elsevier Science and Technology Books, 2006. doi:10.1016/0160-9327(81)90123-X.
- [45] H.F. Stoeckli, Microporous carbons and their characterization: The present state of the art, *Carbon N. Y.* 28 (1990) 1–6. doi:10.1016/0008-6223(90)90086-E.
- [46] O. Ioannidou, A. Zabaniotou, Agricultural residues as precursors for activated carbon production-A review, *Renew. Sustain. Energy Rev.* 11 (2007) 1966–2005. doi:10.1016/j.rser.2006.03.013.
- [47] M. Sevilla, R. Mokaya, Energy storage applications of activated carbons: supercapacitors and hydrogen storage, *Energy Environ. Sci.* 7 (2014) 1250–1280. doi:10.1039/C3EE43525C.

- [48] H. Shi, Activated carbons and double layer capacitance, *Electrochim. Acta.* 41 (1996) 1633–1639. doi:10.1016/0013-4686(95)00416-5.
- [49] C.-T. Hsieh, H. Teng, Influence of oxygen treatment on electric double-layer capacitance of activated carbon fabrics, *Carbon N. Y.* 40 (2002) 667–674. doi:10.1016/S0008-6223(01)00182-8.
- [50] G. Gryglewicz, J. Machnikowski, E. Lorenc-Grabowska, G. Lota, E. Frackowiak, Effect of pore size distribution of coal-based activated carbons on double layer capacitance, *Electrochim. Acta.* 50 (2005) 1197–1206. doi:10.1016/J.ELECTACTA.2004.07.045.
- [51] B. Fang, L. Binder, A novel carbon electrode material for highly improved EDLC performance, *J. Phys. Chem. B.* 110 (2006) 7877–7882. doi:10.1021/jp060110d.
- [52] E. Taer, W.S. Mustika, Agustino, Fajarini, N. Hidayu, R. Taslim, The flexible carbon activated electrodes made from coconut shell waste for supercapacitor application, *IOP Conf. Ser. Earth Environ. Sci.* 58 (2017) 12065. <http://stacks.iop.org/1755-1315/58/i=1/a=012065>.
- [53] J. Chang, Z. Gao, X. Wang, D. Wu, F. Xu, X. Wang, Y. Guo, K. Jiang, Activated porous carbon prepared from paulownia flower for high performance supercapacitor electrodes, *Electrochim. Acta.* 157 (2015) 290–298. doi:<https://doi.org/10.1016/j.electacta.2014.12.169>.
- [54] S.M. Holmes, I.G. Inal, A. Banford, Z. Aktas, The performance of supercapacitor electrodes developed from chemically activated carbon produced from waste tea, *Appl. Surf. Sci.* 357 (2015) 696–703. doi:10.1016/j.apsusc.2015.09.067.
- [55] M.P. Singh, R.K. Singh, S. Chandra, Ionic liquids confined in porous matrices: Physicochemical properties and applications, *Prog. Mater. Sci.* 64 (2014) 73–120. doi:10.1016/j.pmatsci.2014.03.001.

- [56] P. Walden, Ueber die Molekulargrösse und elektrische Leitfähigkeit einiger geschmolzenen Salze., Извѣтїя Императорской Академіи Наукъ, Bull. l'Académie Impériale Des Sci. St.-Pétersbourg. (1914). doi:10.14357/19922264150102.
- [57] F.H. Hurley, T.P. Wler, The electrodeposition of aluminum from nonaqueous solutions at room temperature, J. Electrochem. Soc. 98 (1951) 207–212. doi:10.1149/1.2778133.
- [58] R.J. Gale, B. Gilbert, R.A. Osteryoung, Raman spectra of molten aluminum chloride: 1-butylpyridinium chloride systems at ambient temperatures, Inorg. Chem. 17 (1978) 2728–2729. doi:10.1021/ic50188a008.
- [59] R.J. Gale, R.A. Osteryoung, Potentiometric investigation of dialuminum heptachloride formation in aluminum chloride-1-butylpyridinium chloride mixtures, Inorg. Chem. 18 (1979) 1603–1605. doi:10.1021/ic50196a044.
- [60] R.A. Carpio, L.A. King, R.E. Lindstrom, J.C. Nardi, C.L. Hussey, Density, electric conductivity, and viscosity of several n- alkylpyridinium halides and their mixtures with aluminum chloride, J. Electrochem. Soc. 126 (1979) 1644–1650. doi:doi: 10.1149/1.2128768.
- [61] J.S. Wilkes, M.J. Zaworotko, Air and water stable 1-ethyl-3-methylimidazolium based ionic liquids, J. Chem. Soc. Chem. Commun. (1992) 965–967. doi:10.1039/C39920000965.
- [62] P. Bonhôte, A.-P. Dias, N. Papageorgiou, K. Kalyanasundaram, M. Grätzel, Hydrophobic, highly conductive ambient-temperature molten salts, Inorg. Chem. 35 (1996) 1168–1178. doi:10.1021/ic951325x.
- [63] J.G. Huddleston, A.E. Visser, W.M. Reichert, H.D. Willauer, G.A. Broker, R.D. Rogers, Characterization and comparison of hydrophilic and hydrophobic room temperature ionic liquids incorporating the imidazolium cation, Green Chem. 3 (2001) 156–164. doi:10.1039/b103275p.

- [64] M. Watanabe, M.L. Thomas, S. Zhang, K. Ueno, T. Yasuda, K. Dokko, Application of ionic liquids to energy storage and conversion materials and devices, *Chem. Rev.* 117 (2017) 7190–7239. doi:10.1021/acs.chemrev.6b00504.
- [65] A. Eftekhari, Supercapacitors utilising ionic liquids, *Energy Storage Mater.* 9 (2017) 47–69. doi:10.1016/j.ensm.2017.06.009.
- [66] R. Prado, C.C. Weber, Application of ionic Liquids, in: O. Kuzmina, J. Hallett (Eds.), *Appl. Purification, Recover. Ion. Liq.*, 1st ed., Elsevier, 2016: pp. 1–58.
- [67] M. Mousavi, B.E. Wilson, S. Kashefolgheta, E.L. Anderson, S. He, P. Bühlmann, A. Stein, Ionic liquids as electrolytes for electrochemical double-layer capacitors: Structures that optimize specific energy, *ACS Appl. Mater. Interfaces.* 8 (2016) 3396–3406. doi:10.1021/acsami.5b11353.
- [68] F. Endres, S. Zein El Abedin, Air and water stable ionic liquids in physical chemistry, *Phys. Chem. Chem. Phys.* 8 (2006) 2101. doi:10.1039/b600519p.
- [69] P. Suarez, S. Einloft, Synthesis and physical-chemical properties of ionic liquids based on 1-n-butyl-3-methylimidazolium cation, *J. Chim.* 95 (1998) 1626–1639. doi:10.1051/jcp:1998103.
- [70] J. Le Bideau, L. Viau, A. Vioux, Ionogels, ionic liquid based hybrid materials, *Chem. Soc. Rev.* 40 (2011) 907–925. doi:10.1039/C0CS00059K.
- [71] Q. Zhu, Y. Song, X. Zhu, X. Wang, Ionic liquid-based electrolytes for capacitor applications, *J. Electroanal. Chem.* 601 (2007) 229–236. doi:10.1016/j.jelechem.2006.11.016.
- [72] H. Tokuda, S. Tsuzuki, M.A.B.H. Susan, K. Hayamizu, M. Watanabe, How ionic are room-temperature ionic liquids? An indicator of the physicochemical properties, *J. Phys. Chem. B.* 110 (2006) 19593–19600. doi:10.1021/jp064159v.

- [73] C. Zhong, Y. Deng, W. Hu, D. Sun, X. Han, J. Qiao, J. Zhang, *Electrolytes for electrochemical supercapacitors*, CRC Press, 2016.  
<https://books.google.co.uk/books?id=Wu0bDAAAQBAJ>.
- [74] K. Fic, G. Lota, M. Meller, E. Frackowiak, Novel insight into neutral medium as electrolyte for high-voltage supercapacitors, *Energy Environ. Sci.* 5 (2012) 5842–5850. doi:10.1039/C1EE02262H.
- [75] S. Zhang, J. Zhang, Y. Zhang, Y. Deng, Nanoconfined ionic liquids, *Chem. Rev.* 117 (2017) 6755–6833. doi:10.1021/acs.chemrev.6b00509.
- [76] H. Tokuda, S.-J. Baek, M. Watanabe, Room-temperature ionic liquid-organicsolvent mixtures: conductivity and ionic association, *Electrochemistry.* 73 (2005) 620–622.
- [77] A. Brandt, C. Ramirez-Castro, M. Anouti, A. Balducci, An investigation about the use of mixtures of sulfonium-based ionic liquids and propylene carbonate as electrolytes for supercapacitors, *J. Mater. Chem. A.* 1 (2013) 12669–12678. doi:10.1039/C3TA12737K.
- [78] F. Ghamouss, A. Brugère, J. Jacquemin, Physicochemical investigation of adiponitrile-based electrolytes for electrical double layer capacitor, *J. Phys. Chem. C.* 118 (2014) 14107–14123. doi:10.1021/jp5015862.
- [79] J. Vatamanu, M. Vatamanu, O. Borodin, D. Bedrov, A comparative study of room temperature ionic liquids and their organic solvent mixtures near charged electrodes, *J. Phys. Condens. Matter.* 28 (2016) 464002.  
<http://stacks.iop.org/0953-8984/28/i=46/a=464002>.
- [80] V. Ruiz, T. Huynh, S.R. Sivakkumar, A.G. Pandolfo, Ionic liquid-solvent mixtures as supercapacitor electrolytes for extreme temperature operation, *RSC Adv.* 2 (2012) 5591–5598. doi:10.1039/C2RA20177A.
- [81] H. Zheng, H. Zhang, Y. Fu, T. Abe, Z. Ogumi, Temperature effects on the electrochemical behavior of spinel  $\text{LiMn}_2\text{O}_4$  in quaternary ammonium-based ionic liquid electrolyte, *J. Phys. Chem. B.* 109 (2005) 13676–13684. doi:10.1021/jp051238i.

- [82] M.-T.F. Rodrigues, X. Lin, H. Gullapalli, M.W. Grinstaff, P.M. Ajayan, Rate limiting activity of charge transfer during lithiation from ionic liquids, *J. Power Sources*. 330 (2016) 84–91.  
doi:<https://doi.org/10.1016/j.jpowsour.2016.08.119>.
- [83] L. Negre, B. Daffos, V. Turq, P.L. Taberna, P. Simon, Ionogel-based solid-state supercapacitor operating over a wide range of temperature, *Electrochim. Acta*. 206 (2016) 490–495.  
doi:<https://doi.org/10.1016/j.electacta.2016.02.013>.
- [84] A.I. Horowitz, M.J. Panzer, High-performance, mechanically compliant silica-based ionogels for electrical energy storage applications, *J. Mater. Chem.* 22 (2012) 16534–16539. doi:10.1039/C2JM33496H.
- [85] A.I. Horowitz, K. Westerman, M.J. Panzer, Formulation influence on the sol-gel formation of silica-supported ionogels, *J. Sol-Gel Sci. Technol.* 78 (2016) 34–39. doi:10.1007/s10971-015-3918-7.
- [86] M.A. Néouze, J. Le Bideau, P. Gaveau, S. Bellayer, A. Vioux, Ionogels, new materials arising from the confinement of ionic liquids within silica-derived networks, *Chem. Mater.* 18 (2006) 3931–3936.  
doi:10.1021/cm060656c.
- [87] M. Brachet, T. Brousse, J. Le Bideau, All solid-state symmetrical activated carbon electrochemical double layer capacitors designed with ionogel electrolyte, *ECS Electrochem. Lett.* 3 (2014) A112–A115.  
doi:10.1149/2.0051411eel.
- [88] K. Põhako-Esko, Novel organic and inorganic ionogels: preparation and characterization, University of TARTU, 2013.  
[http://dspace.ut.ee/bitstream/handle/10062/31607/pohako\\_esko\\_kaija.pdf?sequence=1](http://dspace.ut.ee/bitstream/handle/10062/31607/pohako_esko_kaija.pdf?sequence=1).
- [89] M.A.B.H. Susan, T. Kaneko, A. Noda, M. Watanabe, Ion gels prepared by in situ radical polymerization of vinyl monomers in an ionic liquid and their characterization as polymer electrolytes, *J. Am. Chem. Soc.* 127 (2005) 4976–4983. doi:10.1021/ja045155b.

- [90] S. Wang, B. Hsia, J.P. Alper, C. Carraro, Z. Wang, R. Maboudian, Comparative studies on electrochemical cycling behavior of two different silica-based ionogels, *J. Power Sources*. 301 (2016) 299–305. doi:10.1016/J.JPOWSOUR.2015.09.121.
- [91] C.J. Brinker, G.W. Scherer, *Sol-gel science: The physics and chemistry of sol-gel processing*, 1990. doi:10.1186/1471-2105-8-444.
- [92] U. Schubert, Part one - Sol-gel chemistry and methods, in: *Sol-Gel Handb. Synth. Charact. Appl.*, 2015: pp. 1–28. doi:10.1002/9783527670819.ch01.
- [93] B. Orel, A. Šurca Vuk, V. Jovanovski, R. Ješe, L.S. Perše, S.B. Hočevar, E.A. Hutton, B. Ogorevc, A. Jesih, Structural and electrical studies of a sol-gel derived nanocomposite ionic liquid based on positively charged polysilsesquioxane and iodide, *Electrochem. Commun.* 7 (2005) 692–696. doi:https://doi.org/10.1016/j.elecom.2005.04.025.
- [94] E. Stathatos, V. Jovanovski, B. Orel, I. Jerman, P. Lianos, Dye-sensitized solar cells made by using a polysilsesquioxane polymeric ionic fluid as redox electrolyte, *J. Phys. Chem. C*. 111 (2007) 6528–6532. doi:10.1021/jp068812q.
- [95] O. Fontaine, A. Toudjine, M. Maréchal, C. Bonhomme, F. Ribot, B. Geffroy, B. Jousselme, C. Sanchez, C. Laberty-Robert, A one-pot route to prepare class II hybrid ionogel electrolytes, *New J. Chem.* 38 (2014) 2008–2015. doi:10.1039/C3NJ01272G.
- [96] S. Dai, Y.H. Ju, H.J. Gao, J.S. Lin, S.J. Pennycook, C.E. Barnes, Preparation of silica aerogel using ionic liquids as solvents, *Chem. Commun.* (2000) 243–244. doi:10.1039/a907147d.
- [97] R. Gobel, P. Hesemann, J. Weber, E. Moller, A. Friedrich, S. Beuermann, A. Taubert, Surprisingly high, bulk liquid-like mobility of silica-confined ionic liquids, *Phys. Chem. Chem. Phys.* 11 (2009) 3653–3662. doi:10.1039/B821833A.

- [98] R. Gobel, A. Friedrich, A. Taubert, Tuning the phase behavior of ionic liquids in organically functionalized silica ionogels, *Dalt. Trans.* 39 (2010) 603–611. doi:10.1039/B913482D.
- [99] F. Shi, Q. Zhang, D. Li, Y. Deng, Silica-gel-confined ionic liquids: A new attempt for the development of supported nanoliquid catalysis, *Chemistry (Easton)*. 11 (2005) 5279–5288. doi:10.1002/chem.200500107.
- [100] A.K. Gupta, M.P. Singh, R.K. Singh, S. Chandra, Low density ionogels obtained by rapid gellification of tetraethyl orthosilane assisted by ionic liquids, *Dalt. Trans.* 41 (2012) 6263–6271. doi:10.1039/C2DT30318C.
- [101] A.-M. Siouffi, Silica gel-based monoliths prepared by the sol–gel method: facts and figures, *J. Chromatogr. A*. 1000 (2003) 801–818. doi:https://doi.org/10.1016/S0021-9673(03)00510-7.
- [102] K.G. Sharp, A two-component, non-aqueous route to silica gel, *Sol-Gel Sci. Technol.* 2 (1994) 35–41.
- [103] L. Viau, M.-A. Néouze, C. Biolley, S. Volland, D. Brevet, P. Gaveau, P. Dieudonné, A. Galarneau, A. Vioux, Ionic liquid mediated sol-gel synthesis in the presence of water or formic acid: Which synthesis for which material?, *Chem. Mater.* 24 (2012) 3128–3134. doi:10.1021/cm301083r.
- [104] D. Membreno, L. Smith, K.-S. Shin, C.O. Chui, B. Dunn, A high-energy-density quasi-solid-state carbon nanotube electrochemical double-layer capacitor with ionogel electrolyte, *Transl. Mater. Res.* 2 (2015) 015001. doi:10.1088/2053-1613/2/1/015001.
- [105] Y. Li, C. Guo, L. Yue, W. Qu, N. Chen, Y. Dai, R. Chen, F. Wu, Organosilicon-group-derived silica-ionogel electrolyte for lithium ion batteries, *Rare Met.* 37 (2018) 504–509. doi:10.1007/s12598-018-1056-4.
- [106] M. He, K. Fic, E. Fr̄ckowiak, P. Novák, E.J. Berg, Ageing phenomena in high-voltage aqueous supercapacitors investigated by in situ gas analysis, *Energy Environ. Sci.* 9 (2016) 623–633. doi:10.1039/C5EE02875B.

- [107] N. Bengourna, L. Bonnet, R. Courson, F. Despetis, P. Solignac, H. Satha, Electrical , textural and structural characterization of EMIMAc silica ionogels and their corresponding aerogels 1 Introduction, Rapp. LAAS. (2013).
- [108] N. Bengourna, F. Despetis, L. Bonnet, R. Courson, P. Solignac, H. Satha, N. Olivi-Tran, Textural , structural and electrical characterizations of EMIMAc silica ionogels and their corresponding aerogels, Appl. Phys. Res. 6 (2014) 16–25.
- [109] M.A. Klingshirn, S.K. Spear, J.D. Holbrey, R.D. Rogers, Ionic liquids as solvent and solvent additives for the synthesis of sol-gel materials, J. Mater. Chem. 15 (2005) 5174. doi:10.1039/b508927a.
- [110] M. Ivanova, S. Kareth, E.T. Spielberg, A. V Mudring, M. Petermann, Silica ionogels synthesized with imidazolium based ionic liquids in presence of supercritical CO<sub>2</sub>, J. Supercrit. Fluids. 105 (2015) 60–65. doi:<https://doi.org/10.1016/j.supflu.2015.01.014>.
- [111] A. Vioux, L. Viau, S. Volland, J. Le Bideau, Use of ionic liquids in sol-gel; ionogels and applications, Comptes Rendus Chim. 13 (2010) 242–255. doi:<https://doi.org/10.1016/j.crci.2009.07.002>.

### **3. Methodology and characterisation techniques**

#### **3.1 Electrode fabrication**

The activated carbon (AC) electrodes were manufactured and supplied by WMG innovation centre at university of Warwick. Activated carbon ink was prepared by mixing YP50-F (Kuraray Chemical Co.), 8 wt% polyvinylidene fluoride binder (PVDF, Solvay) in n-methyl pyrrolidinone (NMP, Fisher Scientific) and carbon black (Imerys) as a conductivity enhancer, in the ratio 87:8:5 in NMP, in a high torque mixer (Buhler, Switzerland) for less than 4 hours. The mixed ink was then coated onto aluminium foil (current collector) using a reel to reel coater (Magtec, UK) with a three-stage dryer. The resultant electrode was further dried overnight under vacuum at 120°C before light calendaring. Electrode calendaring is a process in which the electrode sheets are passed under a series of high-pressure rollers to give a smooth finish and high coating density to the electrodes [1]. Two different sets of AC electrode sheets with different mass loadings (1.8 and 5.4 mg cm<sup>-2</sup>) were supplied by WMG for the duration of this project. The utilised AC electrode for different studies is indicated in each chapter.

#### **3.2 Coin cell assembly tools**

The received activated carbon electrode sheets had dimensions of 200 x 297 mm. Electrode disks of 15 mm diameter were cut using a compact precision disc cutter (MTI Corporation, USA). Separators (when applicable) were also cut using the same tool with a 20 mm die set. Separator sheets were cut slightly larger than the electrodes to prevent short circuit while assembling the cell. The electric double-layer capacitors (EDLCs) were assembled inside CR2032 coin cells using a digital pressure controlled electric crimper (MTI Corporation, USA). The CR2032 coin cell components (displayed in Figure 3.1) were purchased from PI-KEM, UK.

The CR2032 coin cell was 20 mm in diameter and 3.2 mm in thickness (when crimped). It was crucial that the pressure across various components was uniform from one cell to another in order to ensure good reproducibility in coin cell construction. In addition, one must ensure that enough pressure was applied

within the cell so that components stay in place after being crimped. For such coin cells, the thickness had to be less than 3.2 mm. Considering that the wavy spring had a thickness ranging between 0.35-2.50 mm depending on its compression level, the total thickness of the remaining components within each cell must range between 0.70-2.85 mm. Table 3.1 summarises the thickness of various components present in each cell and it can be observed that the total in cases with and without ionogel electrolyte was within the acceptable range. For the assembly reported here, two spacers were utilised.

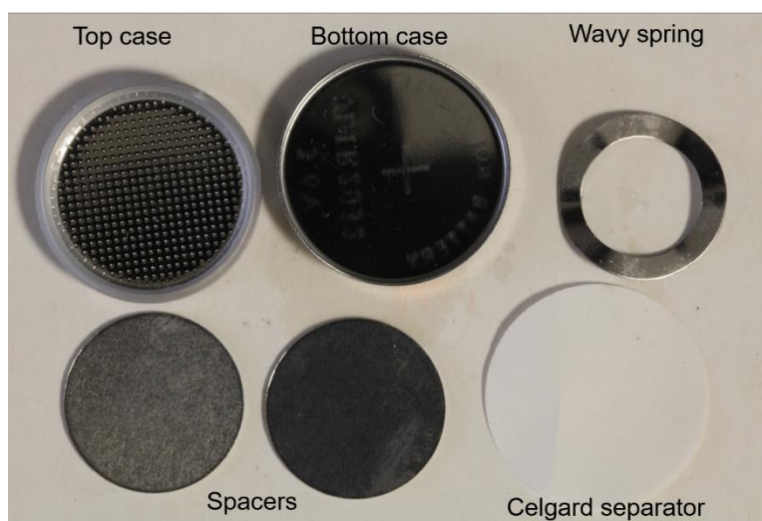


Figure 3.1 Different coin cell CR2032 components utilised for the EDLCs fabrication together with a Celgard separator. Application of this separator is discussed in Chapters 5 & 6.

Table 3.1 Thickness of various components inside each coin cell with and without ionogel electrolyte. Thickness of components marked with \* were measure using scanning electron microscopy. The total thickness of each cell without the spring must stay in 0.70-2.85 mm range.

Full Cell components	Thickness / mm	
	With Ionogel	Celgard separator
Top case	(0.28) x 1	(0.28) x 1
Spring (minimum-maximum)	(0.35-2.50) x 1	(0.35-2.50) x 1
Spacer	(0.50) x 2	(0.50) x 2
Electrode disk (Al + AC)*	(0.05-0.10) x 2	(0.05-0.10) x 2
Separator*	(0.04-0.20) x 2	(0.03) x 1
Bottom case	(0.25) x 1	(0.25) x 1
<b>Total (without spring) / mm</b>	<b>1.71-2.13</b>	<b>1.66-1.76</b>

### 3.3 Physical and chemical characterisation techniques

#### 3.3.1 Raman spectroscopy and multivariate curve resolution

Raman spectroscopy is a powerful technique that combines the spatial resolution of an optical microscope with spectroscopic analysis to obtain molecular information from micro-scaled space within a substance. Raman spectroscopy provides information about the vibrational frequencies of covalent bonds within a sample, which can be used to determine its composition and structure.

When a sample is illuminated with a monochromatic beam of light, molecules can be excited to a virtual energy state upon interacting with photons which are scattered elastically (Rayleigh scattering) and inelastically (Raman scattering). Figure 3.2 depicts the origin of Rayleigh and Raman scattering. The arrows demonstrate the change in the molecule energy level as it interacts with the excitation photon. When a photon is scattered to lower energy than that of the excitation photon, it is referred to as Stokes scattering and conversely, when the excitation photon gains energy upon collision/interaction with the molecule, it is referred to as anti-Stokes scattering. The latter is of lower intensity compared to Stokes scattering since it requires the molecule to be in an excited state (i.e. unstable state) prior to collision with the photon and most molecules reside in the ground state at standard temperature and pressure.

The energy difference between the excitation photon ( $E_{ex}$ ) and the scattered photon ( $E_{sc}$ ) must be equal to the energy difference between the two allowed vibrational states of the molecule [2]. Based on Planck's law, the change in the vibrational energy of the molecule ( $\Delta E$ ) can be calculated according to:

$$\Delta E = |E_{ex} - E_{sc}| = h\nu_v \quad (\text{Eq. 3.1})$$

where  $h$  is the Planck's constant ( $6.63 \times 10^{-34} \text{ m}^2 \text{ kg s}^{-1}$ ) and  $\nu_v$  is the vibrational frequency of the molecule. In cases where the excitation photon has the appropriate energy, it can cause excitation of the molecule to a higher electronic state rather than a virtual energy state. The molecule then relaxes back to the ground state emitting photons which can mask Raman scattering and for this reason it should be avoided. This phenomenon is called fluorescence and the most effective way to eliminate/reduce this defect is to utilise a suitable laser source with longer wavelength (i.e. lower excitation energy) [2].

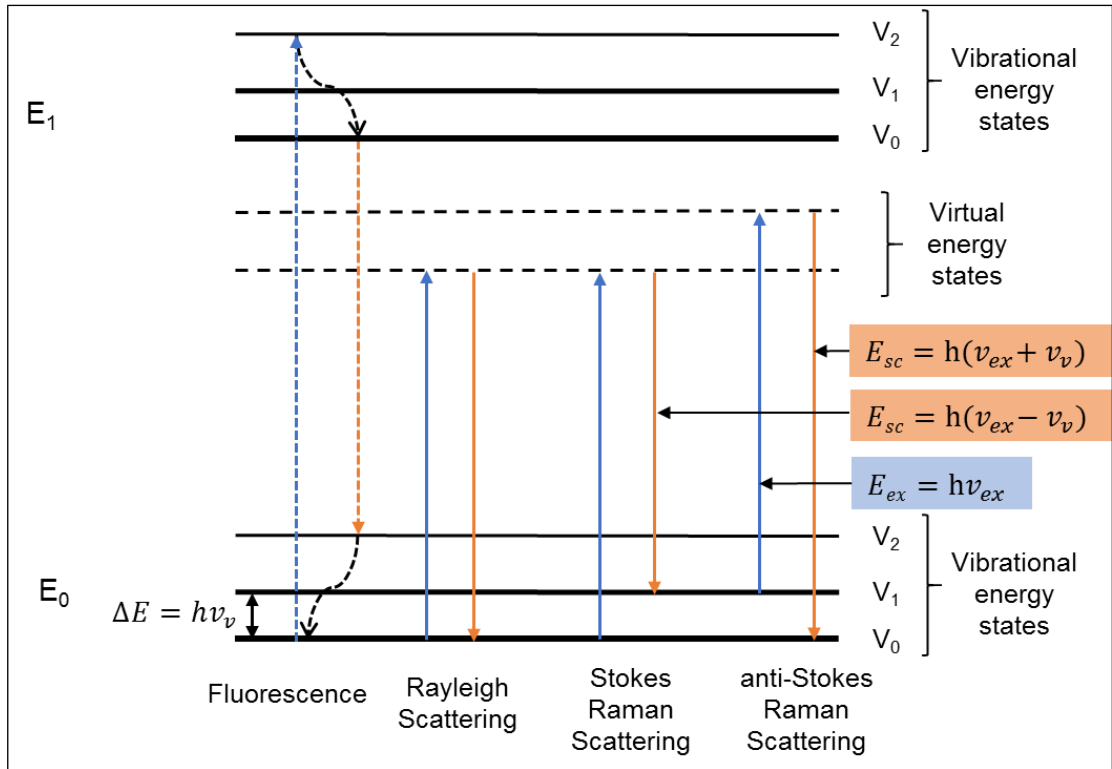


Figure 3.2 Modified Jablonski diagram illustrating molecular transition between energy levels via Rayleigh and Raman scattering. If the exciting photon has sufficient energy, fluorescence can take place which involves transition of the molecule to an excited electronic state (represented here by  $E_1$ ) which then decays back to the ground energy state ( $E_0$ ) emitting a strong radiation.

A Raman spectrum is a plot of Raman intensity of the scattered radiation versus vibrational frequency ( $\bar{\nu}_v$ ) or Raman shift which refers to the difference between Raman scattering frequency and the excitation frequency traditionally expressed in wavenumbers (waves per unit length,  $\text{cm}^{-1}$ ):

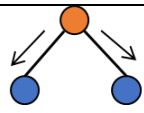
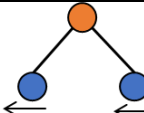
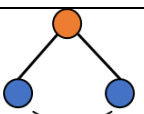
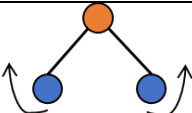
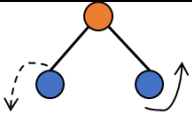
$$\bar{\nu}_v (\text{cm}^{-1}) = \frac{10^{-7}}{\lambda_{ex}(\text{nm})} - \frac{10^{-7}}{\lambda_{sc}(\text{nm})} \quad (\text{Eq. 3.2})$$

$$\bar{\nu}_v (\text{cm}^{-1}) = \frac{\nu_v (\text{Hz})}{c} = \frac{1}{\lambda} \quad (\text{Eq. 3.3})$$

where  $\lambda_{ex}$  and  $\lambda_{sc}$  represent excitation and scattered wavelengths, respectively and  $c$  represents the speed of light ( $3 \times 10^8 \text{ m s}^{-1}$ ). In order for a vibration of a molecule to be Raman active, there must be a change in its polarizability during the vibration [2,3]. Polarizability is defined as the ease at which the electron cloud of a molecule is distorted when placed in an electric field. The number of vibrational modes of a molecule is dependent on its linearity and number of atoms in the molecule ( $n$ ) where a linear molecule has  $3n-5$  and a nonlinear mol-

ecule has  $3n-6$  vibrational modes [4]. Some examples of the molecular vibrational modes are provided in Table 3.2.

Table 3.2 Examples of common vibrational modes and their corresponding symbols and schematic representation [5,6].

Mode of vibration		Symbol	Schematic illustration
Stretching (in-plane)		$\nu$	
Bending ( $\delta$ )	Rocking (in-plane)	$\rho$	
	Scissoring (in-plane)	$\delta_s$	
	Wagging (out-of-plane)	$\omega$	
	Twisting (out-of-plane)	$\tau$	

The position of each band in the Raman spectrum is governed by Hooke's law principle where a covalent bond can be represented by a spring as shown in Figure 3.3.

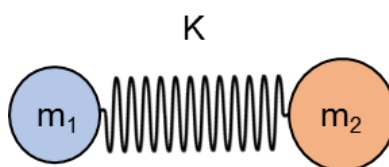


Figure 3.3 A diatomic molecule with masses  $m_1$  and  $m_2$  connected by a spring. The term  $K$  represents strength of the spring (spring constant) i.e. strength of the covalent bond.

The vibrational frequency ( $\bar{\nu}$ ) of a diatomic molecule is expressed as [4]:

$$\bar{\nu} = \frac{1}{2\pi c} \sqrt{K \left( \frac{1}{m_1} + \frac{1}{m_2} \right)} \quad (\text{Eq. 3.4})$$

where  $m_1$  and  $m_2$  are the masses of atoms involved in the covalent bond. Based on the equation 3.4, the position of a Raman band or the frequency of vibration of a band is influenced by the strength of the covalent bond and the mass of the atoms involved in the bond.

The design of the Raman instrumentation is shown in Figure 3.4. A laser source capable of emitting radiations at the desired wavelength is used. The radiation is first passed through a collimator which ensures uniform intensity of the laser beam. The uniform radiation is then focussed on the sample using a microscope. The scattered light is then collected by the microscope optics and directed by mirrors onto an edge filter which is responsible for blocking Rayleigh and anti-Stokes scattering. The Stokes scattering is then passed through a slit onto a grating that separates the radiation into its constituent frequencies, which are collected using a charged-couple device (CCD) detector connected to a computer with appropriate operating software generating a Raman spectrum in the pre-set spectral range.

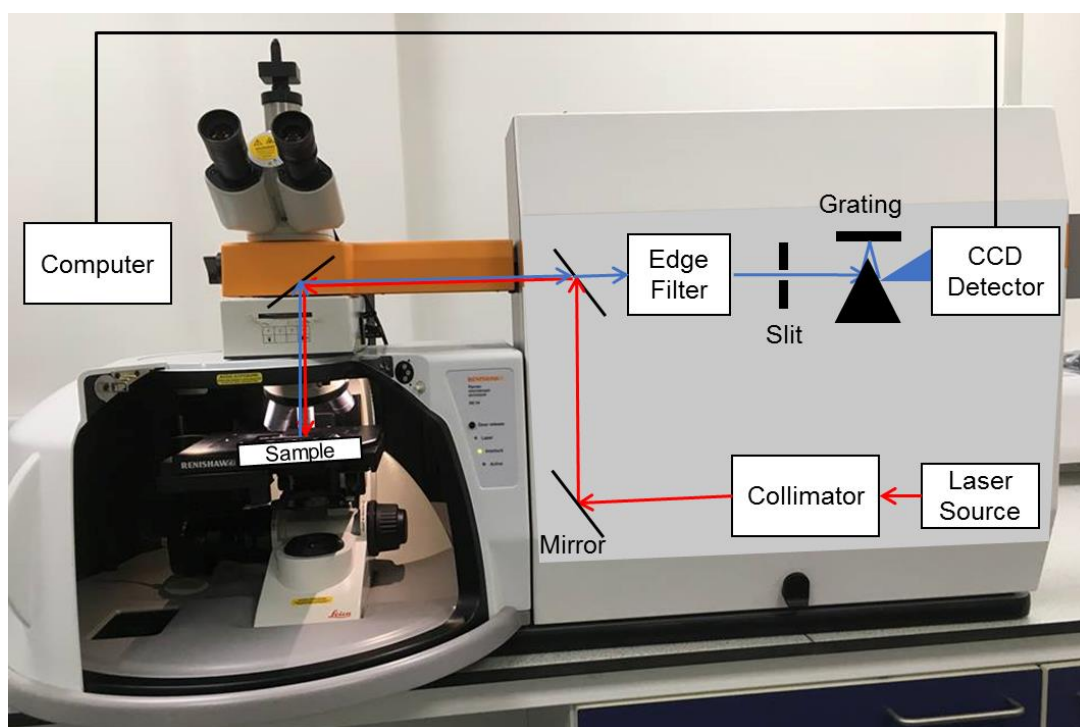


Figure 3.4 A schematic illustration of the key components of Raman instrumentation superimposed on an image of the inVia Raman instrument (Renishaw, UK) utilised in this work. The red and blue arrows represent the incoming and scattered beams, respectively.

Depending on the study, Raman mapping can be used to acquire spectral information in 1 to 2 physical dimensions. For this, laser is focused on one spot

and the sample is moved (automatically or manually) using a motorised stage at the desired or pre-set step size. A series of spectra is then generated for each sampling point which contains information about each and every component/material present in the scanned region. The Raman technique does not facilitate separation of spectral information, so if there is more than one component/material within the sampled region, then the spectrum produced will show features for all components, leading to ambiguity of signal and making the determination of the distribution of each material at each sampling point challenging. One of the strategies that can be applied to extract discrete information from mixed signals is multivariate curve resolution (MCR), which uses a number of algorithms including non-linear iterative partial least squares (NIPALS) and alternating least squares (ALS) to decompose mixed spectroscopic matrices into pure component (factors) and pure concentration (loadings) matrices. The concentration of each of the pure components can then easily be determined by solving the following equation [7–9].

$$D = CS^T + E \quad (\text{Eq. 3.5})$$

where  $D$  is the data matrix containing data acquired from the spectroscopic monitoring (e.g. Raman mapping spectra),  $S^T$  and  $C$  are matrices representing pure components and contribution/concentration of each component, respectively. Matrix  $E$  represents the residual data that the mathematical model does not explain and ideally should be close to experimental error [7]. As can be seen from the above equation, MCR is capable of solving the complex equation described when raw data is presented as a matrix. Thus, it is necessary to convert the raw data into a data matrix prior to the MCR analysis. In cases where a number of data sets containing the same components/factors are being investigated and/or compared, a data matrix can be generated that combines different sets of data. By generating a single matrix of all of the samples, a single model will be used for the whole data set resulting in a reliable and comparable output. This can be facilitated by ISys® software which requires the user to input the dimensions of the required matrix depending on the number of data sets and data points. A summary of this process is displayed in Figure 3.5.

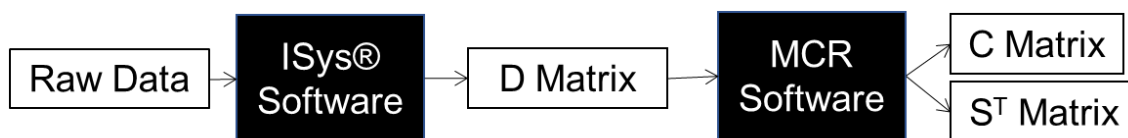


Figure 3.5 A summary of the steps involved in deconvolution of raw data using MCR analysis. Raw data is first converted into a data matrix which is then fed into MCR software to generate matrices of different components ( $S^T$ ) and their concentrations ( $C$ ).

In this work, Raman spectra were collected using an inVia Raman spectrometer equipped with an automated stage (Renishaw, UK) using 785 nm diode laser excitation (10% laser power, unless stated otherwise) and x5 objective (spot size  $\sim 8 \mu\text{m}$ ). Spectra were collected between 200 and 3200  $\text{cm}^{-1}$  (unless stated otherwise) utilising the WiRE software (version 3.4) with exposure time and number of accumulations set to 10 seconds and 1, respectively. Prior to the collection of data set, the device was calibrated using a silicon wafer (provided by Renishaw) in order to ensure accuracy of the spectral data. Deconvolution of the Raman line-map data was executed using ISys® (version 5.0.0.14) and MCR (version 1.6) analysis software.

### 3.3.2 Scanning electron microscopy and energy dispersive X-ray analysis

Scanning electron microscope (SEM) is an instrument that utilises a finely focused beam of electrons to observe and analyse the surface microstructure of samples. Electron microscopes are capable of providing a higher resolution and depth of field compared to optical microscopes [10]. A schematic illustration of a typical SEM instrumentation is provided in Figure 3.6. The main components of an SEM are: an electron source, a series of electromagnetic lenses, sample chamber, detectors, vacuum system and a control and display system. The electron source generates a beam of electrons via heat (thermionic source), an electric field (field-emitter source) or a combination of both (hybrid source). The generated electrons are attracted to the anode away from the electron source and then directed onto the sample using electromagnetic condenser and objective lenses. Accumulation of electrons on the sample or charging effect will result in a number of imaging defects as well as deflection of the incoming electron beam and thus it must be avoided. Good electrical contact between the sample and the stage is a key requirement for SEM imaging. For non-conductive samples a thin layer (a few nanometers) of conductive material (typically gold or carbon) must be coated to ensure an electrical path is provided for

electron beam. There are a number of mechanisms with which the electron beam interacts with the sample. Loosely bound electrons from the outer shell of the sample molecule/atom can be ejected upon interacting with the primary electron beam. They are labelled as secondary electrons (SEs) and possess low levels of energy (0-50 eV). Due to their low energy, only the SE produced at the very top surface can escape and reach the positively charged grid in front of an SE detector (typically an Everhart-Thornley detector or ETD). Therefore, the secondary electrons can provide information about the surface topography of the sample. The primary electron beam can also be deflected as back-scattered electrons (BSEs) upon interacting with a sample. A back-scattered detector is typically placed above the sample which means it is capable of collecting BSEs, scattered at 180°. The BSEs are more energetic than SEs and thus they can travel and be emitted from a deeper volume within the sample providing compositional information (the higher the atomic number, the more BSEs can escape) [10].

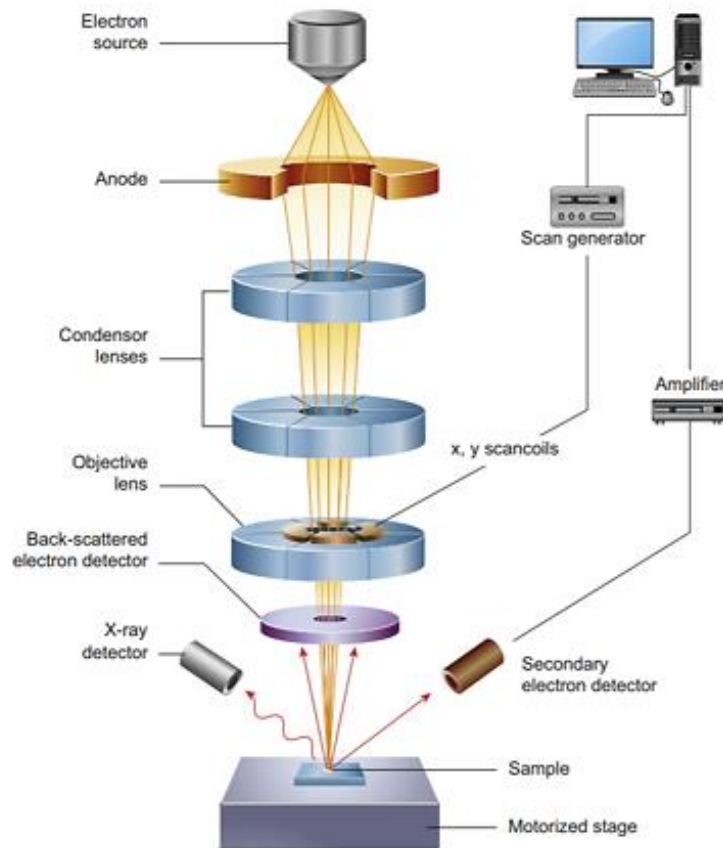


Figure 3.6 Schematic diagram of basic components of an SEM, retrieved from [11].

Finally, when the primary beam knocks an electron out of the inner shell in an atom, and a subsequent electron from a higher energy level fills the created vacancy, a characteristic X-ray is emitted which is equivalent to the energy difference between the two energy levels and is unique to the atom. Energy dispersive x-ray analysis or EDX relies on this phenomenon. An EDX detector converts the energy of an individual X-ray to a characteristic electrical voltage signal. Figure 3.7 demonstrates the three main radiation types emitted upon primary beam-sample interactions on the surface and volume of the sample.

In this work, a Quanta 650 (FEI, USA) with a tungsten thermionic electron source was utilised for EDX characterisations and a combination of NOVA NanoSEM 200 (FEI, USA) and a Quanta 3D FEG (FEI, USA) with the same hybrid electron source (thermally assisted Schottky Emitter, single crystal tungsten) were used for electron imaging. All samples were coated with 20 nm of gold (unless stated otherwise) using a Q300T T Quorum sputter coater at 60 mA sputtering current (Quorum Technologies, UK) prior to SEM imaging.

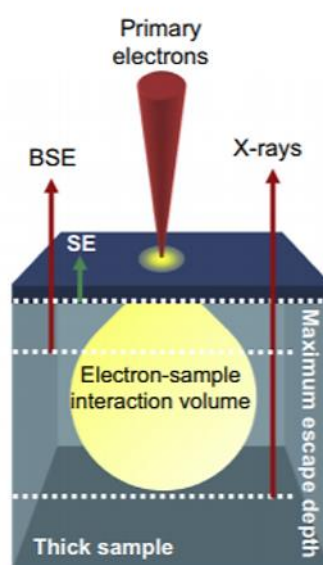


Figure 3.7 Three main types of radiations as a result of the primary beam of electron interacting with the sample. Retrieved from [11].

### 3.3.3 Thermogravimetric analysis

Thermogravimetric analysis (TGA) enables monitoring of the mass of a sample as a function of temperature and/or time in a controlled atmosphere [3]. A commercial TGA instrument consists of a sensitive balance, a furnace, a purge gas

system and computer system for instrumentation control. The acquired data are typically presented in mass or percentage mass of the sample as a function of temperature or time.

The thermogravimetric measurements in this work were collected using a METTLER TOLEDO TGA/DSC 1 STAR® system (USA) in air between 35 to 800°C at a ramping rate of 20°C min<sup>-1</sup>. Solid samples of 30-35 mg and liquid samples of 25 µL were heated in alumina crucibles.

### 3.3.4 Contact angle measurements

Contact angle ( $\theta$ , also referred to as three-phase contact angle) of a liquid droplet resting on a solid surface is geometrically defined as the angle formed between the intersection of the solid-liquid interface and the liquid-vapour interface. Contact angle can give information about the degree of wetting when a solid and a liquid interact; a small contact angle ( $\theta < 90^\circ$ ) represents high wettability while a contact angle above 90° represents low wettability [12]. Figure 3.8 represents a static contact angle where the liquid droplet is resting on the solid surface and the three-phase boundary does not move. Young's equation describes the relationship between contact angle and surface tension of the liquid ( $\sigma_{lv}$ ), surface energy of the solid ( $\sigma_{sv}$ ) and the interfacial tension between liquid and solid ( $\sigma_{ls}$ ) [13]:

$$\sigma_{sv} = \sigma_{ls} + \sigma_{lv} \cos \theta \quad (\text{Eq. 3.6})$$

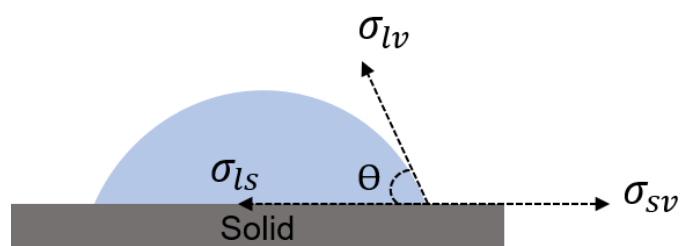


Figure 3.8 schematic representation of sessile drop technique where  $\theta$  is the three phase contact angle and  $\sigma_{lv}$ ,  $\sigma_{sv}$  and  $\sigma_{ls}$  represent the surface tension of the liquid, surface energy of the solid, and the interfacial tension between liquid and solid phases, respectively.

In this work, static contact angles were measured with an OCA30 drop shape analyser (DataPhysics Instruments, Germany) using a standard 500 µL syringe (1750 Hamilton, USA) and a 25 µL syringe with polytetrafluoroethylene coated needle (80250 Hamilton, USA) for water and the ionic liquid, respectively. The

contact angle between the activated carbon surface and a 2- $\mu$ L ionic liquid/water droplet was recorded at five different locations and the contact angles were analysed and calculated using the SCA 20 software (version 3.50.1) and the sessile drop technique.

### 3.3.5 Surface tension measurement

Surface tension is defined as the tendency of a liquid/fluid surface to acquire the least surface area possible and is determined by the interactions between its molecules [14]. Each molecule inside a liquid is equally pulled in every direction by its neighbouring molecules. This does not apply to the molecules at the surface of the liquid as they are not surrounded by molecules in every direction. This results in attractive forces acting on the molecules at the surface of the liquid pulling the surface molecules inward. One of the commonly utilised methods for surface tension measurements is the Wilhelmy method, in which a platinum plate (an inert material with high free surface energy) connected to a precise balance, is vertically suspended and placed in contact with the surface of a liquid. In such case, a force ( $F$ ) acts on the plate which correlates with the surface tension of the liquid (as shown in equation 3.7) [15].

$$\sigma = \frac{F}{l \cos \theta} = \frac{mg}{l \cos \theta} \quad (\text{Eq. 3.7})$$

where  $m$  is the mass of the liquid sample measured by the balance,  $g$  is the acceleration of gravity ( $9.8 \text{ m s}^{-2}$ ),  $l$  is the wetted length of the plate and  $\theta$  is the contact angle between the plate and the liquid which is generally equal to  $0^\circ$  due to the high surface free energy of the platinum plate [15]. Figure 3.9 demonstrates the set-up for Wilhelmy plate technique. Based on this technique, surface tension of the selected ionic liquid was measured using a DCAT25 tensiometer equipped with TEC250 temperature control chamber (DataPhysics Instruments GmbH, Germany). The standard platinum plate PT8 was used as the probe. The surface tension measurements reported in this work were conducted by Dr. Matrin Grüßer.

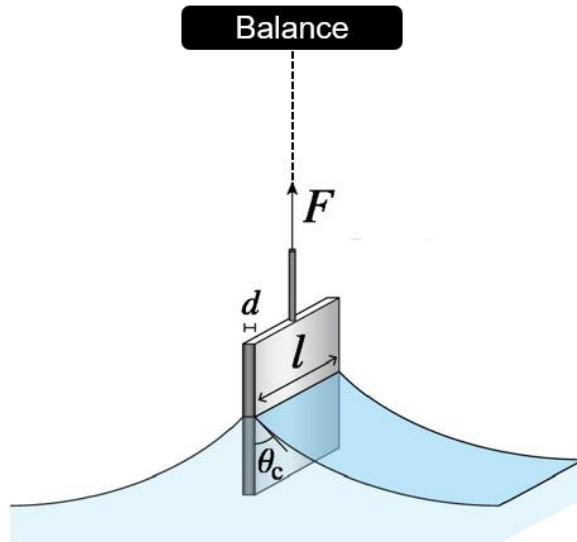


Figure 3.9 Schematic illustration of Wilhelmy plate set-up. Retrieved from [16] with modification.

### 3.3.6 Viscosity measurements

Viscosity is the measure of resistance of a fluid to flow caused by the internal frictional forces between fluid molecules [17]. In this work, the viscosity of the ionic liquid was measured using a MCR301 Rheometer (Anton Paar, UK) equipped with a 'bob and cup' setup as illustrated in Figure 3.10. In this setting, the bob is in motion at a pre-set rotational speed (shear rate) while the cup is stationary. Based on the input shear rate, the electronic controller applies the appropriate current to the motor to produce the necessary torque. Subsequently, a resistive torque caused by the fluid acts on the motor torque which results in a change in the rotational speed. This is detected by the position sensor and it sends a signal to the controller. The controller then calculates and applies the necessary current to the motor in order to maintain the pre-set rotational speed. The shear stress (the component of the torque acting parallel to the bob) and viscosity ( $\eta$ ) can then be calculated based on the following equation [17]:

$$\eta = \frac{\text{Shear Stress}}{\text{Shear rate}} = \frac{M/A}{\text{Shear rate}} \quad (\text{Eq. 3.8})$$

where  $M$  is the resultant torque and  $A$  is the contact area (area of the bob).

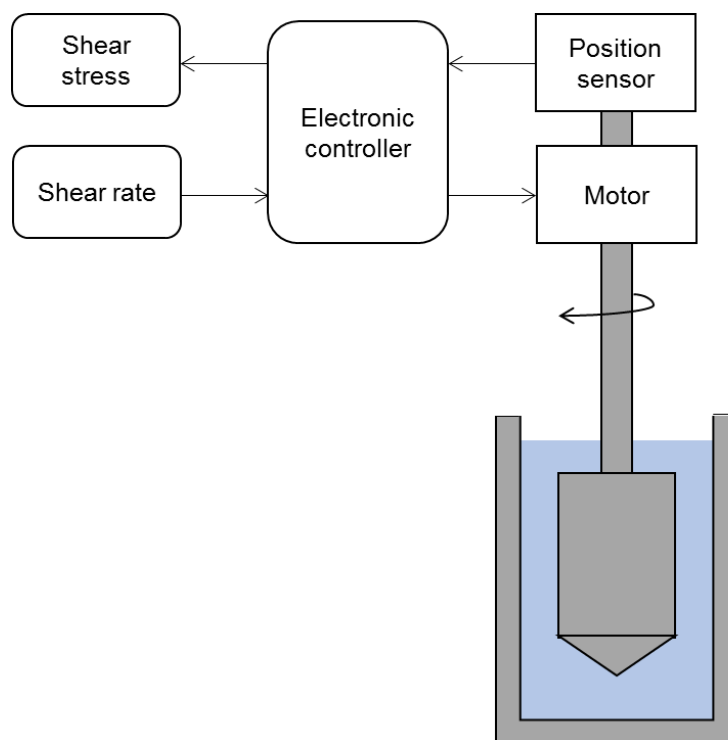


Figure 3.10 Schematic illustration of the 'cup and bob' setting for viscosity measurements.

In this work, the variation of viscosity was measured against temperature. A shear rate of  $10 \text{ s}^{-1}$  was utilized while the temperature was nominally raised from 25-200°C at  $2^\circ\text{C min}^{-1}$  ramping rate (using a C-LTD 180 temperature control chamber). These measurements were repeated 3 times and the mean value was reported. Due to limitations of the instrumentation, the actual maximum temperature achieved during measurement was 188°C. Viscosity at 200°C was therefore estimated by extrapolating the viscosity vs. temperature curve.

### 3.3.7 Brunauer–Emmett–Teller

Naderi [18] described surface area of a solid as the external surface area of the object including that attributed to its pores. Brunauer–Emmett–Teller (BET) technique which was first introduced in 1938 [19], enables the determination of surface area of a sample by measuring the amount of the physically adsorbed gas molecules (typically nitrogen) on the solid surface. Physical adsorption is governed by weak Van der Waals attraction between the solid surface and the adsorbate [18]. The generalised BET equation is provided below [19]:

$$v = \frac{v_m c p}{(p_0 - p) \left[ 1 + (c - 1) \left( \frac{p}{p_0} \right) \right]} \quad (\text{Eq. 3.9})$$

where  $v$  is the volume of adsorbed gas,  $v_m$  is the adsorbed monolayer volume,  $c$  is the BET constant,  $p$  is the equilibrium gas pressure and  $p_0$  is the saturation pressure. Rearranging the terms in the above equation gives:

$$\frac{p}{v(p_0 - p)} = \frac{1}{v_m c} + \frac{c - 1}{v_m c} \frac{p}{p_0} \quad (\text{Eq. 3.10})$$

The equation above suggests that the plot of  $\frac{p}{v(p_0 - p)}$  versus  $\frac{p}{p_0}$  should form a straight line. The value of  $v_m$  can then be derived from the slope of the BET plot ( $\frac{c-1}{v_m c}$ ). The average pore size ( $r_p$ ) can then be evaluated based on the  $v_m$  value [20,21]:

$$r_p = \frac{2Mv_l}{v_m NA} = \frac{2v_l}{A_{BET}} \quad (\text{Eq. 3.11})$$

where  $N$  is the Avogadro's number ( $6.023 \times 10^{23} \text{ mol}^{-1}$ ),  $M$  is the molar volume of the adsorbate at standard temperature and pressure,  $v_l$  is the volume of liquid nitrogen in the pores and  $A$  is the adsorbate cross sectional area.

Prior to the BET measurements, it is necessary to remove contaminants (mainly gasses) that may be chemically/physically adsorbed onto the surface of the sample. This can be achieved by applying a vacuum at an elevated temperature to remove the chemical/physical contaminants [18]. This is referred to as the outgassing or degassing process. In this work the BET measurements (using  $\text{N}_2$ ,  $-196^\circ\text{C}$ ) were conducted by Dr. Alexander Kulak at Leeds University using a volumetric adsorption analyser (Micrometrics ASAP2020, USA). The degassing process was done under high vacuum at  $120^\circ\text{C}$  for 3 hours.

### 3.3.8 Karl Fischer titration

This characterisation technique is a quantitative method for water determination which was first introduced in 1935 by a German chemist Karl Fischer [22]. This technique is based on Bunsen reaction between iodine and sulfur dioxide in aqueous media [22]:



Fischer discovered that by modifying the above reaction, it can be used to determine the amount of water present in a non-aqueous system in the presence of excess sulfur dioxide. In coulombic Karl Fischer, iodine is generated at the

anode of the titration cell to stoichiometrically react with water [23]. When water content in the system is consumed, an excess of iodine is generated which is detected by a double platinum pin indicator electrode, and subsequently, the reaction is stopped by the control system. Water content is then determined based on the amount of current passed through the anode to produce the required iodine [22]:

$$Q(C) = i(A) \times t(s) \quad (\text{Eq. 3.12})$$

where  $Q$  is the total charge,  $i$  is the current and  $t$  is time. Generally, 1 mg of  $\text{H}_2\text{O}$  is equivalent to consumption of 10.71 C of electrical current [24]. In this work, measurement of ionic liquid water content was conducted at Warwick University using a Karl Fischer Coulometer (Mettler Toledo, UK).

### 3.4 Electrochemical characterisation techniques

The electrochemical characteristic of the EDLCs in this work were analysed using a combination of cyclic voltammetry (CV), galvanostatic charge-discharge (GCD) and electrochemical impedance spectroscopy (EIS) techniques. The CV and EIS measurements were collected using a PARSTAT 2273 potentiostat (Princeton Applied Research, USA) equipped with PowerSuite (version 2.58) software. The GCD measurements were executed using a MACCOR automated battery tester (series 4000, USA). All of the tests were performed at room temperature ( $22 \pm 2^\circ\text{C}$ ). The potentiostat was set up in a two-electrode mode in which one terminal is connected to the working electrode (WE) and the opposite terminal is connected to the counter electrode (CE) and reference electrode (RE) as shown in Figure 3.11b. Alternatively a three-electrode setup can be used to study the performance of an electrochemical cell in the connection setting shown in Figure 3.11a. For EIS and CV measurements, the connections between the potentiostat and the coin cells were made using CR2032 cell holders, jumper wires and breadboards. Ideally, coin cell holders with thumbscrew terminal on one end and a spring-loaded terminal on the opposite end should be utilised for consistent electrical conductivity. The MACCOR instrumentation (in Warwick University) was equipped with such connections.

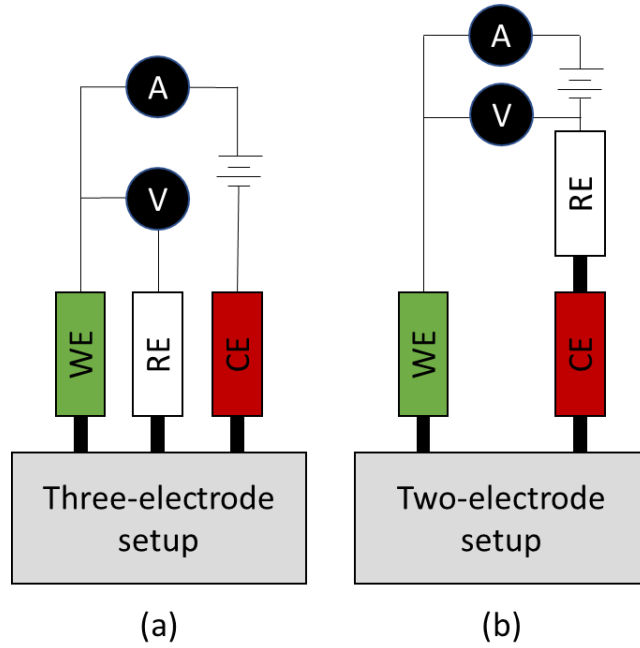


Figure 3.11 A schematic illustration of the connections between the working, counter and reference electrodes in the (a) three-electrode and (b) two-electrode setups.

### 3.4.1 Cyclic voltammetry

Cyclic voltammetry is an electrochemical characterization technique in which a cell is charged and discharged within a fixed potential window at a pre-set scan rate ( $v$ ) and the current response of the cell is recorded. The linear change in potential ( $V$ ) can be represented by [25]:

$$V = V_{\min} + vt - iR \quad (0 \leq t \leq \frac{V_{\max}}{v}) \quad (\text{Eq. 3.13})$$

$$V = V_{\max} - vt - iR \quad (\frac{V_{\max}}{v} < t \leq \frac{2V_{\max}}{v}) \quad (\text{Eq. 3.14})$$

where  $t$  represents time and  $V_{\min}$  and  $V_{\max}$  are the lower and upper potential limits, respectively. The term  $iR$  reflects the potential drop across the electrochemical cell due to an internal resistance,  $R$ . For an ideal supercapacitor,  $iR$  is equal to zero. In CV tests, the potentiostat applies and maintains a linear potential ramp between the RE and the WE while simultaneously the current flowing between WE and CE is measured. A CV scan consists of variation of current or current density (normalised to surface area or mass of the electrode(s)) as a function of the applied potential. In both capacitors and supercapacitors, the amount of charge ( $Q$ ) stored in the cell is proportional to the strength of the electric field or the potential across the positive and negative electrodes [26].

Rearranging Eq. 2.3 (given in Chapter 2) gives:

$$Q = CV \quad (\text{Eq. 3.15})$$

where  $C$  is the capacitance. This equation can be differentiated against time to give an understanding of the cyclic voltammetry output:

$$\frac{dQ}{dt} = C \frac{dV}{dt} + V \frac{dC}{dt} \xrightarrow{C \text{ is a constant}} \frac{dQ}{dt} = C \frac{dV}{dt} \quad (\text{Eq. 3.16})$$

The terms  $\frac{dQ}{dt}$  and  $\frac{dV}{dt}$  represent current and scan rate, respectively which gives [26]:

$$i = Cv \quad (\text{Eq. 3.17})$$

This equation shows that current is linearly proportional to the scan rate. Thus, upon changing the direction of the voltage scan, the direction of current changes. This results in a rectangular CV curve as shown in Figure 3.12. A quasi-rectangular shaped CV curve (for a double-layer supercapacitor) indicates fast charge propagation in the electrodes and good capacitive behaviour [27,28] and for this reason, CV is utilised as a qualitative measure of the capacitive nature of a cell/electrode [26]. On the other hand, when a cell has high internal resistance, the current response of the cell becomes dominated by the resistive component. This phenomena can result in an elliptical CV curve which reflects a poor current response and a high internal resistance of the cell [25,29,30].

The total specific capacitance of a supercapacitor can be calculated from the enclosed area in a CV curve using the following equation [31–33]:

$$C_{sp \text{ total}} = Q / (V_{\max} - V_{\min})S = \int_{V_{\min}}^{V_{\max}} I(V)dV / 2(V_{\max} - V_{\min})Sv \quad (\text{Eq. 3.18})$$

where  $C_{sp \text{ total}}$  is the total specific areal capacitance in  $\text{mF cm}^{-2}$ ,  $\int_{V_{\min}}^{V_{\max}} I(V)dV$  is the integral of the CV curve,  $(V_{\max} - V_{\min})$  is the potential window and  $S$  is the total planar surface area of the electrode disks in  $\text{cm}^2$ . The term  $S$  can be replaced by the total mass of the active material in the cell to determine the grav-

imetric specific capacitance value. In this work, all of the CV measurements were conducted between 0.0-2.5 V at a scan rate of 50 mV s<sup>-1</sup>.

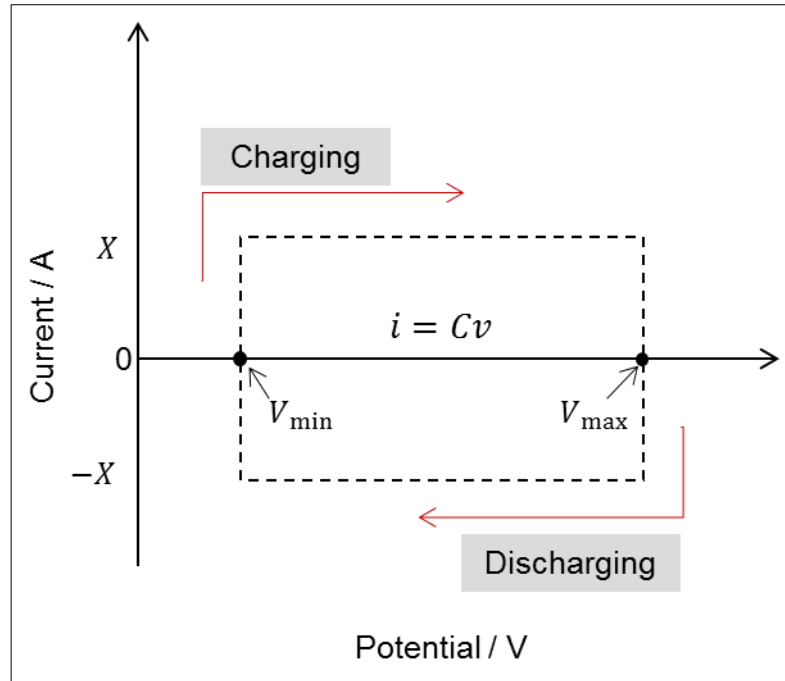


Figure 3.12 A schematic illustration of the rectangular CV curve response of an ideal EDLC. The difference between  $V_{max}$  and  $V_{min}$  determines the potential window.

### 3.4.2 Galvanostatic charge-discharge

Galvanostatic charge-discharge, also known as constant current charge-discharge, technique involves applying a constant current to charge and discharge an electrochemical cell and recording the potential-time response of the cell. Based on Eq. 3.17, once a constant current is applied to charge or discharge a supercapacitor, a constant rate of potential increase is expected. Thus, the potential versus time plot consists of linear charge and discharge regions as shown in Figure 3.13a. These regions are represented by [26,34]:

$$V = \frac{it}{C} + iR \quad (\text{Charging, } t < t_{max}) \quad (\text{Eq. 3.19})$$

$$V = V_{max} - \frac{i(t - t_{max})}{C} - iR \quad (\text{Discharging, } t > t_{max}) \quad (\text{Eq. 3.20})$$

where  $i$ ,  $t_{max}$  and  $V_{max}$  represent the constant charge/discharge current, current reversal time, and the pre-set potential limit, respectively. In the presence of resistive effects ( $iR > 0$ ), the galvanostatic charge-discharge profile of an EDLC

becomes non-symmetrical about the  $t_{max}$  [25]. This phenomenon is shown in Figure 3.13b. The resistance  $R$ , which is the internal resistance of the cell, is often referred to as the equivalent series resistance (ESR) and based on the drop of potential ( $V_{drop}$ ) in GCD plot, it can be calculated as follows [34]:

$$ESR = \frac{V_{drop}}{i} \quad (\text{Eq. 3.21})$$

The total specific capacitance can be evaluated from GCD plot via [35]:

$$C_{sp\ total} = \frac{i\Delta t}{S(\Delta V - V_{drop})} \quad (\text{Eq. 3.22})$$

where  $\Delta t$  and  $\Delta V$  represent the discharge time ( $t_1 - t_{max}$ ) and the change in potential, respectively.

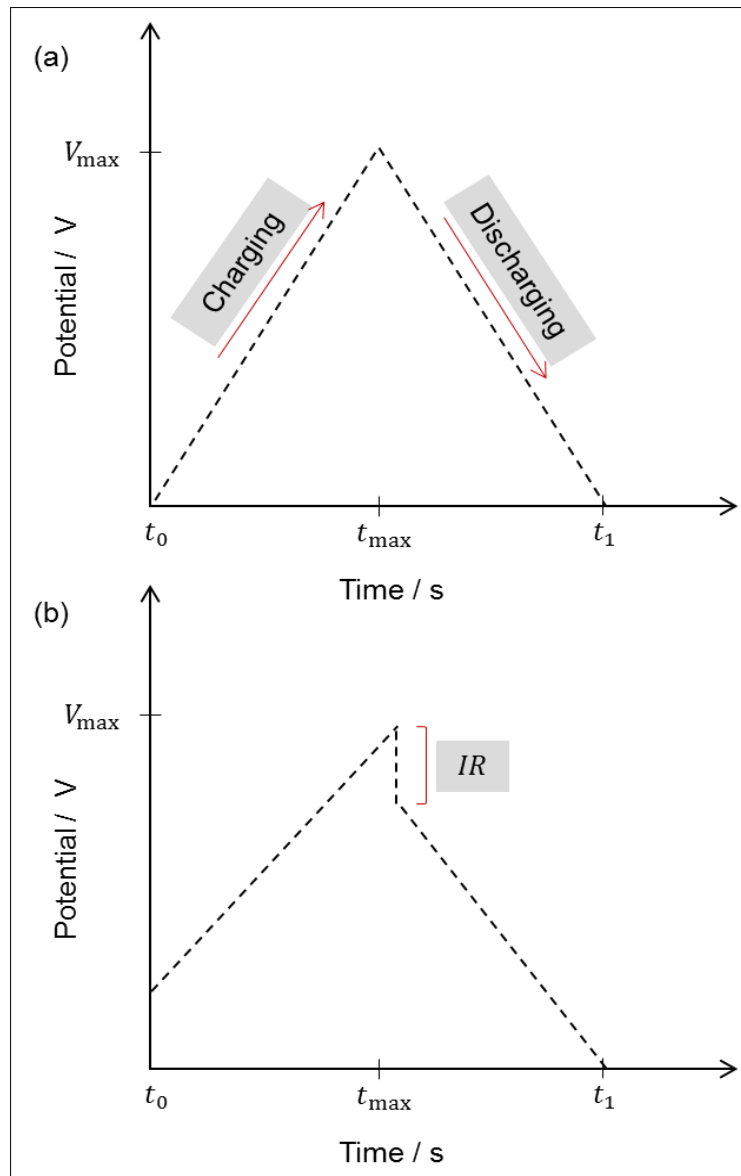


Figure 3.13 (a) GCD profile of an ideal supercapacitor in the absence of any IR effect and (b) GCD profile with IR effect.

### 3.4.3 Electrochemical impedance spectroscopy

Electrochemical impedance spectroscopy is an effective electrochemical characterisation technique that operates in frequency domain rather than time domain (as opposed to CV and GCD), which enables this technique to provide information about the contribution of different electrochemical processes towards the overall impedance of the electrochemical cell. In a potentiostatic EIS, an alternating-current (ac) potential with a small amplitude is applied to the supercapacitor over a wide range of frequencies while the current response of the system is recorded. The potential and current signals can be expressed as below [34]:

$$V(\omega) = V_s + \delta V \sin(\omega t) \quad (\text{Eq. 3.23})$$

$$i(\omega) = i_s + \delta i \sin(\omega t + \varphi) \quad (\text{Eq. 3.24})$$

where  $V_s$ ,  $\delta V$ ,  $i_s$ ,  $\delta i$ ,  $\omega$  and  $\varphi$  are steady state potential, ac potential amplitude, steady state current, ac current amplitude, angular frequency and phase angle, respectively. Phase angle represents the degree by which the current signal is out of phase with respect to the potential signal. Probing of an ac signal to an electrochemical cell, results in a complex impedance term represented by  $Z(\omega)$  which possesses a magnitude at each frequency. Based on Ohm's law, the complex impedance can be expressed as [34,36]:

$$Z(\omega) = \frac{V(\omega)}{i(\omega)} = Z' + jZ'' \quad (\text{Eq. 3.25})$$

$$|Z(\omega)| = \sqrt{Z'^2 + Z''^2} \quad (\text{Eq. 3.26})$$

where  $Z'$ ,  $Z''$  and  $|Z(\omega)|$  are the real component, imaginary component, and the magnitude of impedance, respectively. A Nyquist plot, generated from EIS measurements, shows the real and imaginary components of the cell impedance (x- and y-axis, respectively) as a function of frequency. Figure 3.14 shows the typical Nyquist plot of an EDLC with porous active material [37].

A Nyquist plot is divided into 3 main regions of high, mid-range and low frequency which carry valuable information about the electrochemical system being investigated. The high frequency x-axis intercept is referred to as intercept resistance ( $R_i$ ). At this point in an EIS measurement, the frequency is too high

for any mass transfer to take place. Therefore, intercept resistance is a representation of the bulk electrolyte resistance [38,39] although in some cases this resistance has also been attributed to electrolyte-electrode-current collector contact resistance [40]. This is followed by the mid-range frequency semicircle which has been assigned to a number of ionic and electrical components inside an EDLC; Yoo et al. attributed the mid-range semicircle to the ion migration across the electrolyte-electrode interface. They showed that small increase in the solvated ionic diameter can result in an increase in the charge transfer resistance ( $R_{ct}$ , given by the diameter of the mid-range frequency semicircle) implying in an increase in the ionic transport resistance [39].

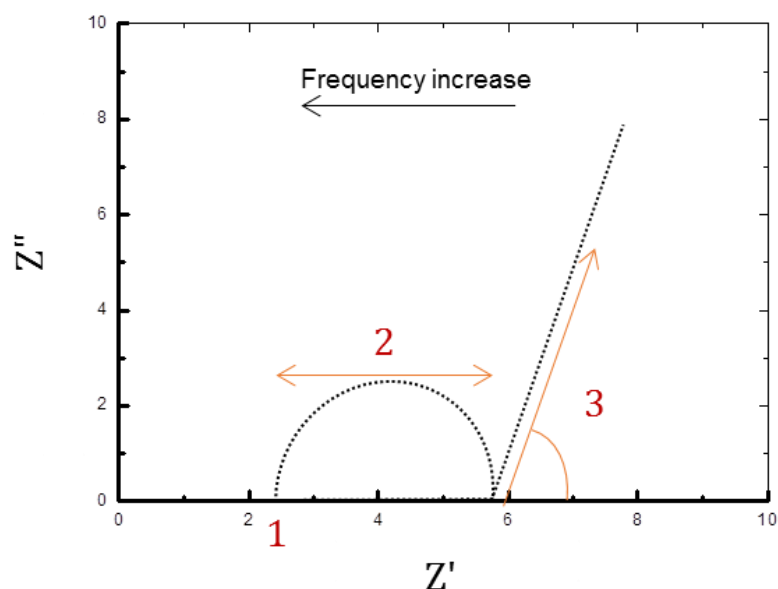


Figure 3.14 A Schematic illustration of a typical Nyquist plot for EDLCs with a porous electrode (as explained in [37]), consisting of 3 main regions of high, mid-range and low frequency regions, respectively.

Yang et al. investigated the effect of carbon aerogel pore size on  $R_{ct}$  [41]. Based on their work, the EDLC cell with the largest electrode pore size (and surface area) showed the lowest  $R_{ct}$ . This suggests a close relation between  $R_{ct}$  and the mobility of electrolyte ions inside the ‘textural’ pores of the electrode. It can be inferred that larger pore size imposes less resistance to the electrolyte ions. Subsequently, the same group reported a similar study that contradicted their previous conclusion [42]. They investigated another set of carbon aerogel based EDLCs containing an organic electrolyte (1 M tetraethylammonium tetrafluoroborate in acetonitrile). The EIS analysis showed that as the electrode average pore diameter raised from 2 to 10 nm (and the specific surface area

raised from  $\sim 163$  to  $847 \text{ m}^2 \text{ g}^{-1}$ ), the corresponding  $R_{ct}$  increased by  $\sim 300\%$ . They reported that the increase in  $R_{ct}$  is associated with high electronic resistance of the active material. These studies conclude that depending on the investigating system, electrical or ionic component of  $R_{ct}$  can have a dominating effect. An et al. demonstrated that the contact resistance between active material (single walled carbon nanotubes) and current collector (nickel foil) can influence the  $R_{ct}$  [43]. Pell et al. investigated the influence of tetraethylammonium tetraborate electrolyte concentration (ranging between 0.08 and 1.00 M) on the performance of EDLC containing porous carbon electrodes [44]. A depressed semicircle appeared at higher frequency ranges for cells with lowest electrolyte concentration and the diameter of this semicircle increased as the potential window was raised. They explained this observation by the 'electrolyte starvation' phenomena, which refers to the reduction of electrolyte conductance as the double-layer is formed, when the device is being charged. These studies demonstrate that the dominating components influencing the  $R_{ct}$  are dependent on the system being investigated. Systems containing ionic liquids are expected to have dominating ionic resistances influencing the mid-frequency semicircle due to high viscosity and relatively large size ions of ionic liquids. However, the influence of electrical resistances should not be neglected. It is important to note that the nature of  $R_{ct}$  in EDLCs with porous electrodes [38,42] is different from that in pseudocapacitors which is mainly associated with the Faradaic processes taking place in the cell [45].

Finally, the low frequency region (straight line) in a Nyquist plot is associated with the intra-particle diffusion of electrolyte ions and double-layer formation ( $Z_{dl}$ ) [39,40]. When the frequency becomes low enough, the overall impedance of the cell increases linearly at an angle with x-axis of  $45^\circ$  to  $90^\circ$ . A large inclining angle (i.e. sharp increase in imaginary impedance,  $Z''$ ) or a nearly vertical line at low frequencies represents facile ion diffusion [40] and a capacitive behaviour [29]. For EIS measurements of the EDLCs, a 10 mV rms potential was applied oscillating around 0 V bias voltage over a frequency range of 10 m to 100 kHz.

### 3.5 References

- [1] C. Meyer, H. Bockholt, W. Haselrieder, A. Kwade, Characterization of the calendring process for compaction of electrodes for lithium-ion batteries, *J. Mater. Process. Technol.* 249 (2017) 172–178. doi:10.1016/J.JMATPROTEC.2017.05.031.
- [2] C.N. Banwell, E.M. McCash, *Fundamentals of molecular spectroscopy*, 4th editio, McGraw-Hill Publishing Company, Maidenhead, 1994.
- [3] D.A. Skoog, F.J. Holler, S.R. Crouch, Raman spectroscopy, in: *Princ. Instrum. Anal.*, 7<sup>th</sup> ed., CENGAGE Learning, Boston, 2007: pp. 437–452.
- [4] P. Larkin, Chapter 2 – Basic Principles, in: *Infrared Raman Spectrosc.*, 2011: pp. 7–25. doi:10.1016/B978-0-12-386984-5.10002-3.
- [5] D. Tuschel, Practical group theory and Raman spectroscopy, Part I: Normal vibrational modes, *Spectrosc. (Solutions Mater. Anal.* 29 (2014) 14.
- [6] Z. Liu, S.Z. El Abedin, F. Endres, Raman and FTIR spectroscopic studies of 1-ethyl-3-methylimidazolium trifluoromethylsulfonate, its mixtures with water and the solvation of Zinc ions, *ChemPhysChem.* 16 (2015) 970–977. doi:10.1002/cphc.201402831.
- [7] J. Jaumot, R. Gargallo, A. de Juan, R. Tauler, A graphical user-friendly interface for MCR-ALS: A new tool for multivariate curve resolution in MATLAB, *Chemom. Intell. Lab. Syst.* 76 (2005) 101–110. doi:https://doi.org/10.1016/j.chemolab.2004.12.007.
- [8] M. Garrido, F.X. Rius, M.S. Larrechi, Multivariate curve resolution-alternating least squares (MCR-ALS) applied to spectroscopic data from monitoring chemical reactions processes, *Anal. Bioanal. Chem.* 390 (2008) 2059–2066. doi:10.1007/s00216-008-1955-6.
- [9] K.R. Fega, D.S. Wilcox, D. Ben-Amotz, Application of Raman multivariate curve resolution to solvation-shell spectroscopy, *Appl. Spectrosc.* 66 (2012) 282–288. <http://as.osa.org/abstract.cfm?URI=as-66-3-282>.

- [10] R.F. Egerton, Physical principles of electron microscopy: An introduction to TEM, SEM, and AEM, second edition, 2nd editio, Springer US, 2016. doi:10.1007/978-3-319-39877-8.
- [11] B.J. Inkson, Scanning electron microscopy (SEM) and transmission electron microscopy (TEM) for materials characterization, in: Mater. Charact. Using Nondestruct. Eval. Methods, Woodhead Publishing, 2016: pp. 17–43. doi:10.1016/B978-0-08-100040-3.00002-X.
- [12] Y. Yuan, T.R. Lee, Contact angle and wetting properties, in: G. Bracco, B. Holst (Eds.), Surf. Sci. Tech., Springer Berlin Heidelberg, Berlin, Heidelberg, 2013: pp. 3–34. doi:10.1007/978-3-642-34243-1\_1.
- [13] T. Young, An eEssay on the cohesion of fluids, Philos. Trans. R. Soc. London. 95 (1805) 65–87. doi:10.1098/rstl.1805.0005.
- [14] J.G. Speight, Chapter 5: Properties of organic compounds, in: Environ. Org. Chem. Eng., 2017: pp. 203–261. doi:10.1016/B978-0-12-804492-6.00005-8.
- [15] L.A. Wilhelmy, Ueber die abh angigkeit der capillaritats-constanten des alkohol con substanz und gestalt des benetzten festen korpers, Ann. Phys. 119 (1863) 177–217. doi:10.1002/andp.18631950602.
- [16] J.D. Berry, M.J. Neeson, R.R. Dagastine, D.Y.C. Chan, R.F. Tabor, Measurement of surface and interfacial tension using pendant drop tensiometry, J. Colloid Interface Sci. 454 (2015) 226–237. doi:10.1016/J.JCIS.2015.05.012.
- [17] T.G. Mezger, The rheology handbook: for users of rotational and oscillatory rheometers, 2<sup>nd</sup> ed., Vincentz Network, Hannover, 2006.
- [18] M. Naderi, Surface area: Brunauer-Emmett-Teller (BET), in: Prog. Filtr. Sep., Academic Press, 2014: pp. 585–608. doi:10.1016/B978-0-12-384746-1.00014-8.

- [19] S. Brunauer, P.H. Emmett, E. Teller, Adsorption of gases in multimolecular layers, *J. Am. Chem. Soc.* 60 (1938) 309–319. doi:10.1021/ja01269a023.
- [20] N. Leddy, Surface area and porosity, *C. Anal. Work.* -Trinity Coll. Dublin. (2012). [https://www.tcd.ie/CMA/misc/Surface\\_area\\_and\\_porosity.pdf](https://www.tcd.ie/CMA/misc/Surface_area_and_porosity.pdf) (accessed December 11, 2018).
- [21] M.F. De Lange, T.J.H. Vlugt, J. Gascon, F. Kapteijn, Adsorptive characterization of porous solids: Error analysis guides the way, *Microporous Mesoporous Mater.* 200 (2014) 199–215. doi:10.1016/J.MICROMESO.2014.08.048.
- [22] K. Fischer, Neues verfahren zur maßanalytischen bestimmung des wassergehaltes von flüssigkeiten und festen körpern, *Angew. Chemie.* 48 (1935) 394–396. doi:<https://doi.org/10.1002/ange.19350482605>.
- [23] E. Scholz, Karl fischer titration (determination of water), 1<sup>st</sup> ed., Springer-Verlag Berlin Heidelberg, 1984. doi:10.1007/978-3-642-69989-4.
- [24] H.J. Muhr, R. Rohner, Good titration practise in Karl Fischer titration, Mettler Toledo, METTLER TOLEDO, 2011.
- [25] W.G. Pell, B.E. Conway, Voltammetry at a de Levie brush electrode as a model for electrochemical supercapacitor behaviour, *J. Electroanal. Chem.* 500 (2001) 121–133. doi:10.1016/S0022-0728(00)00423-X.
- [26] G.Z. Chen, Understanding supercapacitors based on nano-hybrid materials with interfacial conjugation, *Prog. Nat. Sci. Mater. Int.* 23 (2013) 245–255. doi:10.1016/j.pnsc.2013.04.001.
- [27] M.F. El-Kady, R.B. Kaner, Scalable fabrication of high-power graphene micro-supercapacitors for flexible and on-chip energy storage, *Nat. Commun.* 4 (2013) 1475–1479. doi:10.1038/ncomms2446.

- [28] L. Negre, B. Daffos, V. Turq, P.L. Taberna, P. Simon, Ionogel-based solid-state supercapacitor operating over a wide range of temperature, *Electrochim. Acta.* 206 (2016) 490–495.  
doi:<https://doi.org/10.1016/j.electacta.2016.02.013>.
- [29] R. Signorelli, D.C. Ku, J.G. Kassakian, J.E. Schindall, Electrochemical double-layer capacitors using carbon nanotube electrode structures, *Proc. IEEE.* 97 (2009) 1837–1847. doi:10.1109/JPROC.2009.2030240.
- [30] O. Fontaine, A. Toudjine, M. Maréchal, C. Bonhomme, F. Ribot, B. Geffroy, B. Jousselme, C. Sanchez, C. Laberty-Robert, A one-pot route to prepare class II hybrid ionogel electrolytes, *New J. Chem.* 38 (2014) 2008–2015. doi:10.1039/C3NJ01272G.
- [31] W. Chen, Z. Fan, L. Gu, X. Bao, C. Wang, Enhanced capacitance of manganese oxide via confinement inside carbon nanotubes, *Chem. Commun.* 46 (2010) 3905–3907. doi:10.1039/C000517G.
- [32] Q. Chen, X. Li, X. Zang, Y. Cao, Y. He, P. Li, K. Wang, J. Wei, D. Wu, H. Zhu, Effect of different gel electrolytes on graphene-based solid-state supercapacitors, *RSC Adv.* 4 (2014) 36253–36256.  
doi:10.1039/C4RA05553E.
- [33] K.L. Van Aken, J.K. McDonough, S. Li, G. Feng, S.M. Chathoth, E. Mamontov, P.F. Fulvio, P.T.C. Yury, S. Dai, Y. Gogotsi, Effect of cation on diffusion coefficient of ionic liquids at onion-like carbon electrodes, *J. Phys. Condens. Matter.* 26 (2014) 284104–284114.  
<http://stacks.iop.org/0953-8984/26/i=28/a=284104>.
- [34] P.-L. Taberna, P. Simon, *Electrochemical Techniques*, in: F. Beguin (Ed.), *Supercapacitors Mater. Syst. Appl.*, Wiley-VCH Verlag GmbH & Co. KGaA, 2013: pp. 111–130.
- [35] A. Balducci, R. Dugas, P.L. Taberna, P. Simon, D. Plée, M. Mastragostino, S. Passerini, High temperature carbon–carbon supercapacitor using ionic liquid as electrolyte, *J. Power Sources.* 165 (2007) 922–927.  
doi:10.1016/J.JPOWSOUR.2006.12.048.

- [36] Eliezer Gileadi, *Physical Electrochemistry (Fundamentals, Technique and Applications)*, 3<sup>rd</sup> ed., Wiley-VCH Verlag GmbH & Co. KGaA, Weinheim, 2011.
- [37] S. Fletcher, V.J. Black, I. Kirkpatrick, A universal equivalent circuit for carbon-based supercapacitors, *J. Solid State Electrochem.* 18 (2014) 1377–1387. doi:10.1007/s10008-013-2328-4.
- [38] C. Lei, F. Markoulidis, Z. Ashitaka, C. Lekakou, Reduction of porous carbon/Al contact resistance for an electric double-layer capacitor (EDLC), *Electrochim. Acta.* 92 (2013) 183–187. doi:10.1016/J.ELECTACTA.2012.12.092.
- [39] H.D. Yoo, J.H. Jang, J.H. Ryu, Y. Park, S.M. Oh, Impedance analysis of porous carbon electrodes to predict rate capability of electric double-layer capacitors, *J. Power Sources.* 267 (2014) 411–420. doi:10.1016/J.JPOWSOUR.2014.05.058.
- [40] N.H. Basri, M. Deraman, M. Suleman, N.S.M. Nor, B.N.M. Dolah, M.I. Sahri, S.A. Shamsudin, Energy and power of supercapacitor using carbon electrode deposited with nanoparticles nickel oxide, *Int. J. Electrochem. Sci.* 11 (2016) 95–110.
- [41] I. Yang, S.G. Kim, S.H. Kwon, J.H. Lee, M.S. Kim, J.C. Jung, Pore size-controlled carbon aerogels for EDLC electrodes in organic electrolytes, *Curr. Appl. Phys.* 16 (2016) 665–672. doi:10.1016/j.cap.2016.03.019.
- [42] I. Yang, S.-G. Kim, S.H. Kwon, M.-S. Kim, J.C. Jung, Relationships between pore size and charge transfer resistance of carbon aerogels for organic electric double-layer capacitor electrodes, *Electrochim. Acta.* 223 (2017) 21–30. doi:10.1016/J.ELECTACTA.2016.11.177.
- [43] K.H. An, W.S. Kim, Y.S. Park, J.M. Moon, D.J. Bae, S.C. Lim, Y.S. Lee, Y.H. Lee, Electrochemical properties of high-power supercapacitors using single-walled carbon nanotube electrodes, *Adv. Funtional Mater.* 11 (2001) 387–392. doi:10.1002/1616-3028(200110)11:5<387::AID-ADFM387>3.0.CO;2-G.

- [44] W.G. Pell, B.E. Conway, N. Marincic, Analysis of non-uniform charge/discharge and rate effects in porous carbon capacitors containing sub-optimal electrolyte concentrations, *J. Electroanal. Chem.* 491 (2000) 9–21. doi:10.1016/S0022-0728(00)00207-2.
- [45] T. Gu, B. Wei, Fast and stable redox reactions of MnO<sub>2</sub>/CNT hybrid electrodes for dynamically stretchable pseudocapacitors, *Nanoscale*. 7 (2015) 11626–11632. doi:10.1039/c5nr02310f.

## **4. Comparative studies of the gelation kinetics and structure of TEOS, TMOS, MTMS and MTES based silica gels synthesised through a non-hydrolytic sol-gel route**

### **4.1 Introduction**

Being one of the main fabrication routes for ionogels, sol-gel processing has provided researchers with diversity and simplicity. As indicated in Chapter 2, various formulations have been suggested for the encapsulating solid-skeleton of ionogels. In some cases, two or more precursors are combined to create the three dimensional structure, while the choice of the formulation is key in tuning the properties of the gel network (e.g. enhancing the mechanical strength) [1,2]. One must understand the possible effects that the metal alkoxide precursor can have on the properties of the resultant gel in order to gain the ability to design a task-specific formulation. This requires investigation of the sol-gel system with and without ionic liquids. Martinelli studied the non-hydrolytic sol-gel process pathway of a TMOS-based formulation in the presence and absence of ionic liquid [3]. Examples of such works are limited in the literature as most of the studies are focused on the physiochemical properties of the ionogels [1,4,5] after preparation and/or the effect of precursor-to-IL ratio on the electrochemical performance of ionogels [6–8]. This knowledge gap has left two key questions: (1) Can the alkoxide precursor influence the properties and performance of ionogels and (2) If so, how?

An *in situ* investigation of the initial stages of hydrolysis and polymerisation of various silica alkoxide precursors was conducted in the presence of formic acid (FA) using Raman spectroscopy. This powerful characterisation technique has been used in the past to monitor the time evolution of various systems. For example, Mulder and Damen employed Raman spectroscopy to monitor the time evolution of hydrolysis and condensation reactions of tetraethoxysilane (TEOS) in the presence of ethanol [9]. Lee and Jen investigated the influence of formamide ( $\text{CH}_3\text{NO}$ ) concentration on the gelation kinetic of tetramethoxysilane (TMOS) via an acid-catalysed hydrolytic sol-gel route [10]. Marino et al. utilised Raman spectroscopy to monitor the reaction of TEOS in the presence of vari-

ous acids during a series of hydrolytic sol-gel processes [11]. However, there is limited information in the literature regarding the comparison of physical properties such as morphology and gelation mechanism of silica gels synthesised by different precursors.

In this regard, this chapter systematically investigates a series of silica alkoxides to determine the influence of different precursors (in terms of the number of alkoxy groups and the chain length of the functional groups) on the (a) process kinetics and (b) structure of the resultant silica gel, in the absence of ionic liquid.

The four precursors chosen in the present work are TMOS, TEOS, methyltrimethoxysilane (MTMS) and methyltriethoxysilane (MTES) which are commonly utilised precursors for the formation of ionogels. These chemicals share a very similar molecular structure as shown in Figure 4.1. MTMS and MTES molecules contain a non-hydrolysable methyl group attached to the silicon atom.

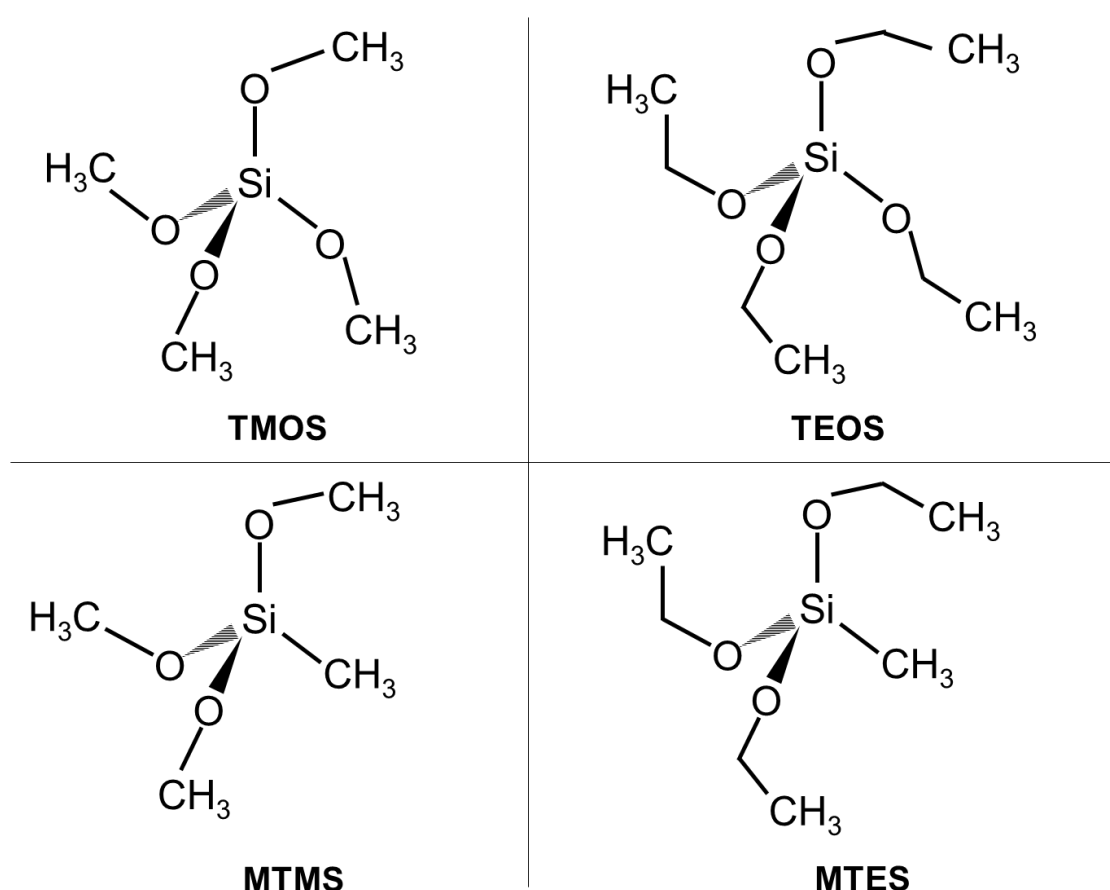


Figure 4.1 Molecular structures of the silica alkoxides investigated in the present work.

## 4.2 Materials

The four different silica gels were synthesised using a simple non-hydrolytic sol-gel route. Each precursor (as listed in Table 4.1) was mixed with formic acid in a glass vial at 600 rpm using a magnetic stirrer. The duration of mixing of the two reactants varied between 3 to 10 minutes as required depending on the subsequent characterisation (Raman and SEM imaging, respectively). The precursor: FA molar ratio was kept constant at 2:7 for all samples. All of the chemicals were used as received. The instrumentation settings for Raman and SEM techniques were as described in Chapter 3 sections 3.3.1 and 3.3.2.

Table 4.1 Detailed summary of the chemicals utilised for silica gels preparation.

	Material	Supplier	%Purity	Volume utilised
1	TMOS	Sigma Aldrich	≥98%	296 μL
2	TEOS	Aldrich	≥99%	446 μL
3	MTMS	Sigma Aldrich	≥98%	286 μL
4	MTES	Aldrich	≥99%	398 μL
5	FA	Aldrich	≥96%	264 μL
6	Methanol	Prime Chemicals	≥99.8%	1 mL
7	Ethanol	Fisher Scientific	≥99.5%	1 mL

## 4.3 *In situ* reaction monitoring

### 4.3.1 Experimental procedure

In order to monitor the chemical processes taking place in each sol-gel formulation, Raman spectra of each of the mixtures were collected at regular intervals. The first spectrum was collected after 3 minutes of mixing the precursor and formic acid. To do so, a 500 μL of the mixture was transferred into a 304 stainless steel container using a micropipette. The subsequent spectra were collected at 10 minutes intervals for 2 hours. The focus of the laser beam was manually adjusted prior to each measurement. The kinetics of the hydrolysis reaction for each precursor was then determined based on the evolution of peak height at selected wavenumbers. The justification for the peak selection is discussed briefly in the following section (4.3.2).

### **4.3.2 Results and discussion**

As a primary step, Raman spectra for each of the reactants were collected and are displayed in Figure 4.2. The background from the steel container has been subtracted from each spectrum using available tools in Omnic software (version 9.6.238). In order to successfully monitor the reaction evolution over time, it is necessary to observe the original spectrum of each reactant prior to the reaction and to determine the unequivocal signatures of each material. Table 4.2, summarises the characteristic peaks of each of the chemicals and their corresponding assignments based on spectra displayed in Figure 4.2 and data available in the literature.

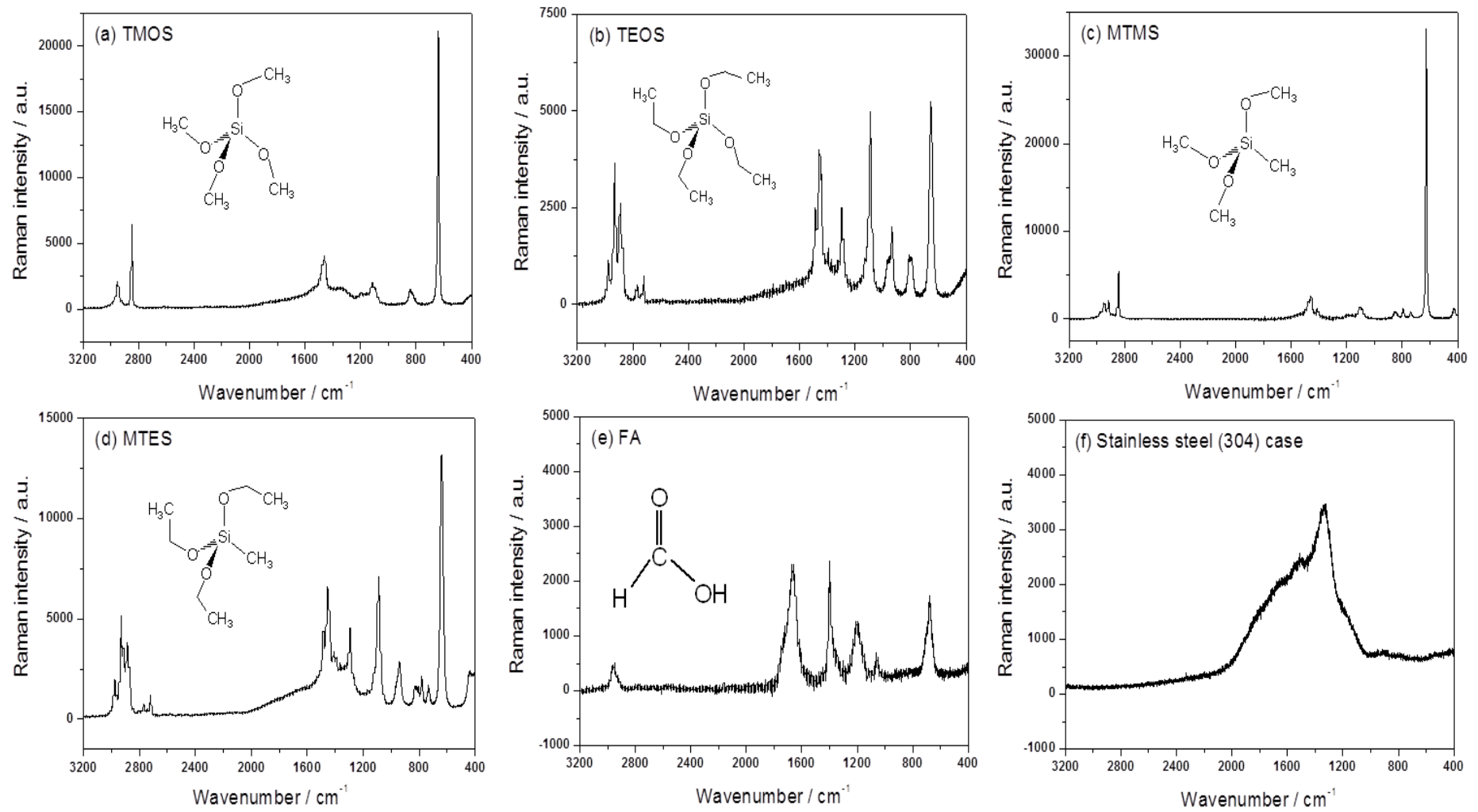


Figure 4.2 Raman spectra of (a) TMOS, (b) TEOS, (c) MTMS, (d) MTES, (e) FA and (f) 304 stainless steel container between 3200 and 400  $\text{cm}^{-1}$  wavenumbers.

Figure 4.2a displays the Raman spectrum of pristine TMOS. Starting from highest wavenumbers, the bands at 2951 and 2849  $\text{cm}^{-1}$  are assigned to antisymmetric and symmetric stretching vibrations of C–H bonds, respectively [12]. Assignments for TMOS bands in the 900-1600  $\text{cm}^{-1}$  region (also known as fingerprint region) have been scarcely reported in the literature. Bands attributed to vibrations of C–O bonds as well as deformation vibration of C–H bonds are included in this region (inferred from the references listed in Table 4.2 based on similarity of chemistry). Furthermore, the weak band at 843  $\text{cm}^{-1}$  and the strong band at 639  $\text{cm}^{-1}$  correspond to the antisymmetric and symmetric stretching mode of Si–OCH<sub>3</sub> bonds, respectively [12,13]. As it is shown in both Figures 4.1 and 4.2, MTMS has a very similar molecular structure to TMOS. Having common functional groups between TMOS and MTMS, leads to Raman bands located at similar positions. The TMOS and MTMS precursors are referred to as methyl-based precursors in this work. As can be seen, MTMS has its C–H stretching modes located at 2845 and 2948  $\text{cm}^{-1}$  and its signature Raman band associated with Si–OCH<sub>3</sub> bonds located at 627  $\text{cm}^{-1}$ . A small red shift is detected in these bands compared to those of TMOS (3-4  $\text{cm}^{-1}$  for C–H stretching modes and 12  $\text{cm}^{-1}$  for stretching mode of Si–OCH<sub>3</sub> bond). As discussed in Chapter 3 section 3.3.1, the frequency of vibration depends on the masses of the atoms involved in the covalent bond and the strength of the bond. For instance, due to the substitution of a methyl group (in replacement of a methoxy group), the electron cloud around silicon atom is altered. The –CH<sub>3</sub> groups have less electronegativity compared to that of –OCH<sub>3</sub> groups [14]. This results in a decrease on the partial charge on Si atom in MTMS compared to that in TMOS molecules which in turn reduces the Si–OCH<sub>3</sub> strength in MTMS and results in the small red shift of peaks in MTMS spectrum compared to that of TMOS. An additional C–H stretch is detected in Figure 4.2c at 2916  $\text{cm}^{-1}$  which is associated with the methyl group directly connected to Si atom [15]. The weak bands appearing at 854 and 739  $\text{cm}^{-1}$  correspond to the rocking vibrations of CH<sub>3</sub> group in Si–CH<sub>3</sub> [15].

Furthermore, Figure 4.2b and d demonstrate the Raman spectra of as-received TEOS and MTES, respectively. These two precursors are referred to as ethyl-based precursors in this work. Because of their similar molecular structure, they

also have similar Raman spectra. The presence of new bands in the 2800-3100  $\text{cm}^{-1}$  and 900-1600  $\text{cm}^{-1}$  regions in the Raman spectrum of TEOS are associated with the additional C–H vibrational modes in the  $-\text{CH}_2\text{CH}_3$  groups available in this precursor. The detailed band assignments of this precursor can be found in Table 4.2. As can be seen in Figure 4.2b and d, the C–H stretch regions of both TEOS and MTES are much more complex compared to that of methyl-based precursors (4.2a and c) as there are more different types of CH bonds available in their molecule. The C–H stretch band located at 2914  $\text{cm}^{-1}$  in figure 4.2d corresponds to the methyl group available in MTES molecule. The strong Raman peaks attributed to the symmetric stretching vibration of  $\text{Si}-\text{OC}_2\text{H}_5$  bonds in TEOS and MTES spectra are located at 653 and 640  $\text{cm}^{-1}$ , respectively. Once again a red shift is observed in the band position of the methyl substituted precursor which can be explained by the Raman principle explained earlier.

All of the alkoxide molecules have a strong Raman peak in the 627-653  $\text{cm}^{-1}$  region which corresponds to the vibration of the Si–O bond where an oxygen atom is bonded to a carbon atom. The stronger Raman intensity of this peak in TMOS and MTMS relative to that of TEOS and MTES are ascribed to the higher polarizability of Si–O bonds in the methyl-based precursors [16].

The molecular structure of formic acid and its Raman spectrum are displayed in Figure 4.2e. Formic acid is commonly utilised as both the catalyst and the solvent in the non-hydrolytic sol-gel route and the Raman bands associated with this material have been reported in the past [10,12,13]. Similar to the Raman spectra of the alkoxides discussed earlier, the weak band at 2958  $\text{cm}^{-1}$  in formic acid Raman spectrum is assigned to the C–H stretching vibration. The bands located at 1667 and 1203  $\text{cm}^{-1}$  correspond to the stretching modes of C=O and C–O, respectively. Lastly, the deformational vibrations of H–C–O and O–C=O bonds are located at 1399 and 676  $\text{cm}^{-1}$ , respectively.

The two characteristic bands at 1330 and 1531  $\text{cm}^{-1}$  in the stainless steel spectrum (shown in Figure 4.2f) originate from the D- and G-bands of the carbon content (0.07%) in the steel [17–19]. More detailed peak assignments are provided in Table 4.2 based on similar works referenced in the Table.

Table 4.2 Summary of selected vibrational modes and their corresponding assignments. The starred C–H bonds represent the case where C atom is directly connected to Si atom.

Compound	Wavenumber in this work (cm <sup>-1</sup> )	Wavenumber in other works (cm <sup>-1</sup> )	Assignment
TMOS	639	643 [3,5], 642 [12]	$\nu_s(\text{Si}-\text{O})$
	843	845 [10,12]	$\nu_{as}(\text{Si}-\text{O})$
	2849	2845 [12]	$\nu_s(\text{C}-\text{H})$
	2951	2946 [12]	$\nu_{as}(\text{C}-\text{H})$
TEOS	653	654[9], 656 [11]	$\nu_s(\text{Si}-\text{O})$
	801	790[9]	$\nu_{as}(\text{Si}-\text{O})$
	933	933[9]	$\nu_s(\text{C}-\text{C})$
	962	960 [9]	$\delta(\text{C}-\text{H})$
	1089	1090[9]	$\nu(\text{C}-\text{O})$
	2892	-	$\nu(\text{C}-\text{H})$
	2935	-	$\nu(\text{C}-\text{H})$
MTMS	627	628 [15]	$\nu_s(\text{Si}-\text{O})$
	2845	2836 [15]	$\nu_s(\text{C}-\text{H})$
	2916	2916 [15]	$\nu(\text{C}-\text{H})^*$
	2948	2948 [15]	$\nu_{as}(\text{C}-\text{H})$
MTES	640	-	$\nu_s(\text{Si}-\text{O})$
	2885	-	$\nu(\text{C}-\text{H})$
	2914	-	$\nu(\text{C}-\text{H})^*$
	2931	-	$\nu(\text{C}-\text{H})$
	2976	-	$\nu(\text{C}-\text{H})$
FA	676	677 [12]	$\delta(\text{O}-\text{C}=\text{O})$
	1203	1230 [12]	$\nu(\text{C}-\text{O})$
	1399	1382 [12]	$\delta(\text{H}-\text{C}-\text{O})$
	1667	1667 [5,12]	$\nu(\text{C}=\text{O})$
	2958	-	$\nu(\text{C}-\text{H})$
304 stainless steel	1330	1320[19], 1350 [17]	<i>D-band</i>
	1531	1594 [19], 1580[17]	<i>G-band</i>

As mentioned in Chapter 2, in non-hydrolytic sol-gel processing, acid acts as both the solvent and the catalyst. K. Sharp who introduced the non-hydrolytic sol-gel route, summarised the reactions taking place between an alkoxide and FA as follows [20]:



Where R, ROH and ROCOH groups represent alkyl, alcohol and alkyl formate groups, respectively. In some works reactions (4.7) and (4.8) are expressed as equilibria [21,22] since these reactions are reversible. Since various reactions can take place simultaneously in the investigated system, one must elucidate the formation and/or consumption kinetics of various compounds in the system as a function of time.

Figures 4.3 to 4.6 show the reaction evolution in all four formulations within the first ~2 hours of mixing the alkoxides and FA. The arrow in each Figure demonstrates the direction of time. The evolution of the highlighted peaks is investigated during the experimental window in this work and will be discussed in detail later in this section. As can be seen in Figure 4.3, as the reaction proceeds the following changes are observed in the TMOS-based mixture:

- (i) The intensity of the strong band at  $639 \text{ cm}^{-1}$  (symmetric stretching vibration of  $\text{Si}-\text{OCH}_3$ ), which corresponds to the consumption of TMOS, reduces quickly.

This precursor contains four  $-\text{OCH}_3$  branches in each molecule and the reaction of one or more of these bonds, results in a reduction of the corresponding Raman peak intensity. According to the reactions listed by Sharp, the alkoxide can be consumed in four different routes listed earlier as reactions (4.1), (4.4), (4.8) and (4.9) [20]. Consumption of TMOS marks the start of the sol-gel process.

(ii) Peak variations in the  $650\text{-}720\text{ cm}^{-1}$  region are mainly attributed to the vibrations of  $\text{Si}-\text{OCH}_3$  bonds in partially hydrolysed TMOS (as summarised by Winter et al. [23]) formed as a result of hydrolysis reactions (reactions no. (4.4) and (4.5)). Consumption of FA partially contributes to the variations of Raman intensity in this region (i.e.  $\delta(\text{O}-\text{C}=\text{O})$  at  $676\text{ cm}^{-1}$  as shown in Table 4.2).

(iii) Formation of a weak band at  $489\text{ cm}^{-1}$  which is attributed to the formation of  $\text{Si}-\text{O}-\text{Si}$  bonds or silica particles [3,12] marks the start and progress of the condensation process (reactions (4.6)-(4.9)).

(iv) Formation of  $\text{Si}-\text{O}-\text{Si}$  bridges in the intermediate species (e.g.  $\text{Si}_2\text{O}(\text{OCH}_3)_6$  or  $\text{Si}_3\text{O}_2(\text{OCH}_3)_8$ ) gives rise to the detection of stretching vibrations of  $\text{Si}-\text{O}$  in the  $500\text{-}610\text{ cm}^{-1}$  region [9,24].

(v) The vibrations in the  $780\text{-}880\text{ cm}^{-1}$  correspond to a combination of antisymmetric stretching vibrations of  $\text{Si}-\text{OCH}_3$  in TMOS and the  $\text{Si}-\text{O}$  vibrations in the intermediate species (partially hydrolysed monomers) [3,9,24].

(vi) Relatively weak bands at  $910$  ( $\nu(\text{O}-\text{CH}_3)$ ) and  $1018$  ( $\nu(\text{C}-\text{O})$ )  $\text{cm}^{-1}$  appear in the spectra within the 2-hour experimental period which are unequivocal signatures of methyl formate and methanol, respectively [3,12]. These are the volatile by-products of the sol-gel process. Generally, methyl formate is formed via both the esterification and the condensation reactions (i.e. reactions no. (4.3) and (4.9)) while methanol is either formed or consumed in all of the four stages of sol-gel process. The kinetics of formation and consumption of these two species are studied in this work and will be discussed later.

(vii) Depletion of various Raman peaks in the  $1350\text{-}1450\text{ cm}^{-1}$  and  $1600\text{-}1800\text{ cm}^{-1}$  region are related to the consumption of formic acid as a result of carboxy-

lation and esterification reactions listed precisely as reactions (4.1) to (4.3) [3,12,13]. In addition, the bending vibrations of CH<sub>3</sub> bonds present in methyl formate contribute to the Raman peaks in the 1440-1470 cm<sup>-1</sup> region [3].

(vii) Gradual intensity reduction of C–H stretching modes in the 2800-3000 cm<sup>-1</sup> region can be observed. The positions of the two existing bands agree well with C–H stretching modes of CH<sub>3</sub> in TMOS as shown in Figure 4.2a. However, the evolution of these bands does not follow the same trend as that of 639 cm<sup>-1</sup> over time. This observation is discussed later in this chapter.

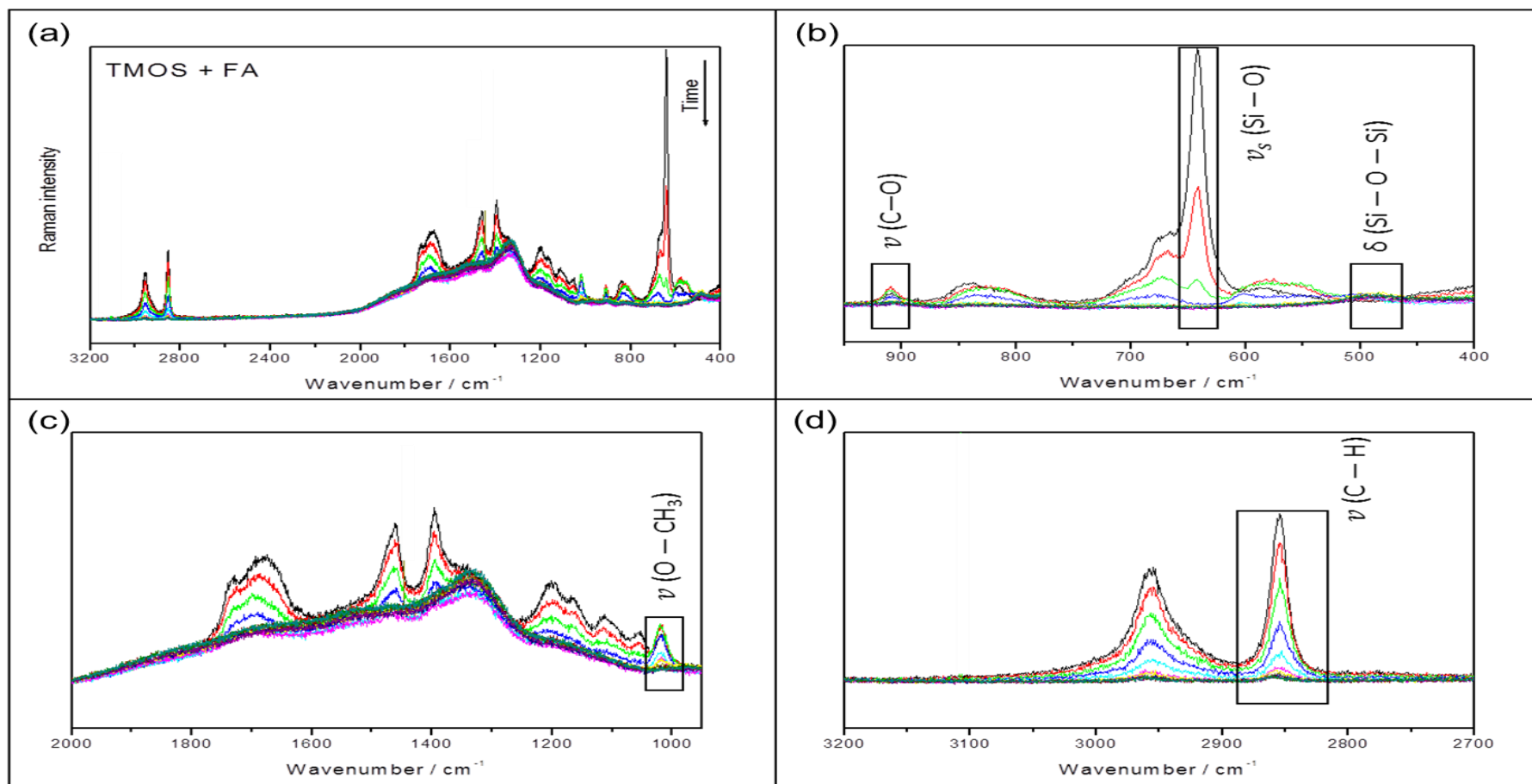


Figure 4.3 Raman spectra evolution with time of TMOS and FA mixtures in the (a) 400-3200  $\text{cm}^{-1}$ , (b) 400-950  $\text{cm}^{-1}$ , (c) 950-2000  $\text{cm}^{-1}$ , and (d) 2700-3200  $\text{cm}^{-1}$  regions. The intensity evolution of bands associated with  $\nu_s(\text{Si-O})$ ,  $\nu(\text{C-O})$ ,  $\nu(\text{O-CH}_3)$ ,  $\delta(\text{Si-O-Si})$  and  $\nu(\text{C-H})$  vibrations as a function of time can be found in Figures 4.8, 4.9, 4.10, 4.11 and 4.12, respectively.

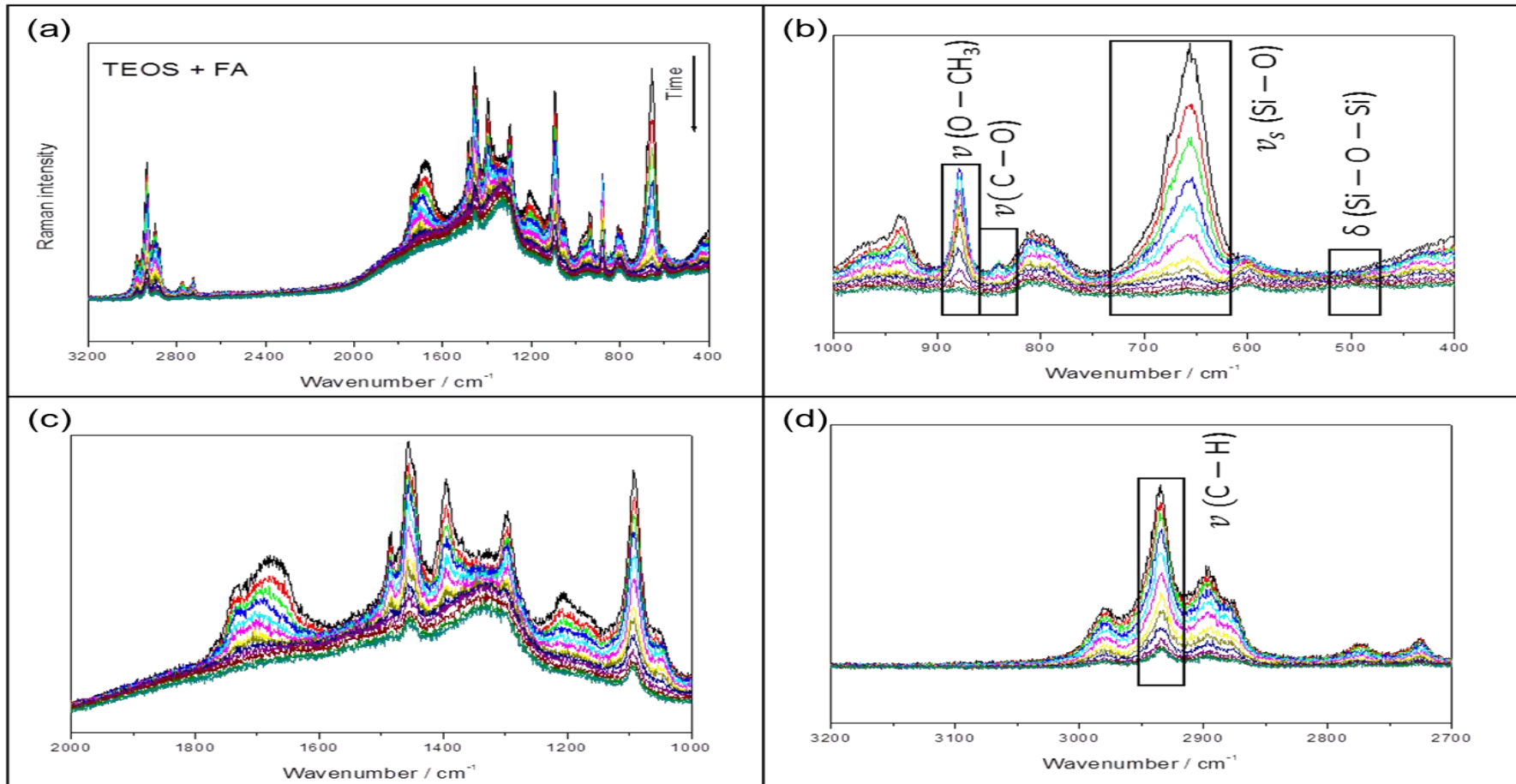


Figure 4.4 Raman spectra evolution with time of TEOS and FA mixtures in the (a) 400-3200  $\text{cm}^{-1}$ , (b) 400-1000  $\text{cm}^{-1}$ , (c) 1000-2000  $\text{cm}^{-1}$ , and (d) 2700-3200  $\text{cm}^{-1}$  regions. The intensity evolution of bands associated with  $\nu_s(\text{Si}-\text{O})$ ,  $\nu(\text{C}-\text{O})$ ,  $\nu(\text{O}-\text{CH}_3)$ ,  $\delta(\text{Si}-\text{O}-\text{Si})$  and  $\nu(\text{C}-\text{H})$  vibrations as a function of time can be found in Figures 4.8, 4.9, 4.10, 4.11 and 4.12, respectively.

Figure 4.4 demonstrates the evolution of the TEOS precursor with time, shortly after being mixed with formic acid. As can be seen, the unequivocal signature of TEOS located at  $653\text{ cm}^{-1}$  dissipated gradually over the 2 hours experimental window. This happened at a much slower rate compared to that of TMOS (Figure 4.3). Simultaneously, a weak band was formed at  $600\text{ cm}^{-1}$  which Mulder and Damen [9] interpreted as the Si–O stretching vibrations of TEOS dimer ( $\text{Si}_2\text{O}(\text{OC}_2\text{H}_5)_6$ ). These observations demonstrate the start of sol-gel process which entails consumption of the TEOS precursor and formation of intermediates as a result of reactions (4.1) and (4.4). The detectable peaks in  $400\text{--}450\text{ cm}^{-1}$  region represent the Si–OC<sub>2</sub>H<sub>5</sub> deformation vibrations while the very weak peak at  $474\text{ cm}^{-1}$  corresponds to the formation of Si–O–Si bridges in the mixture [9]. As the reaction progressed, the intensity of TEOS characteristic Raman peak dropped while the peak spread in a wider region of  $650\text{--}720\text{ cm}^{-1}$ . Similar to TMOS mixtures, this observation is assigned to the formation of partially hydrolysed TEOS molecules [9,23]. As shown in Table 4.2, the Raman peaks located at  $801$ ,  $933$  and  $962\text{ cm}^{-1}$  also correspond to TEOS precursor and are assigned to antisymmetric stretching of Si–O, symmetric stretching vibration of C–C and deformation vibration of C–H in the CH<sub>3</sub> groups, respectively.

In contrast to TMOS and MTMS, the volatile by-products of ethyl-based precursors undergoing the FA-based non-hydrolytic sol-gel process are ethanol and ethyl formate. The unequivocal signatures of ethanol and ethyl formate ( $\nu(\text{C–O})$  in both cases) are highlighted in Figure 4.4 and are located at  $877$  and  $841\text{ cm}^{-1}$  [11,25], respectively. Variations of peaks in the  $1000\text{--}1800\text{ cm}^{-1}$  region are mainly attributed to the consumption of formic acid via carboxylation and esterification reactions (no. (4.1)–(4.3)) and the formation of ethyl formate. Lastly, additional bands in the  $2700\text{--}3100\text{ cm}^{-1}$  region correspond to various vibrational modes of C–H bonds in TEOS ethyl groups.

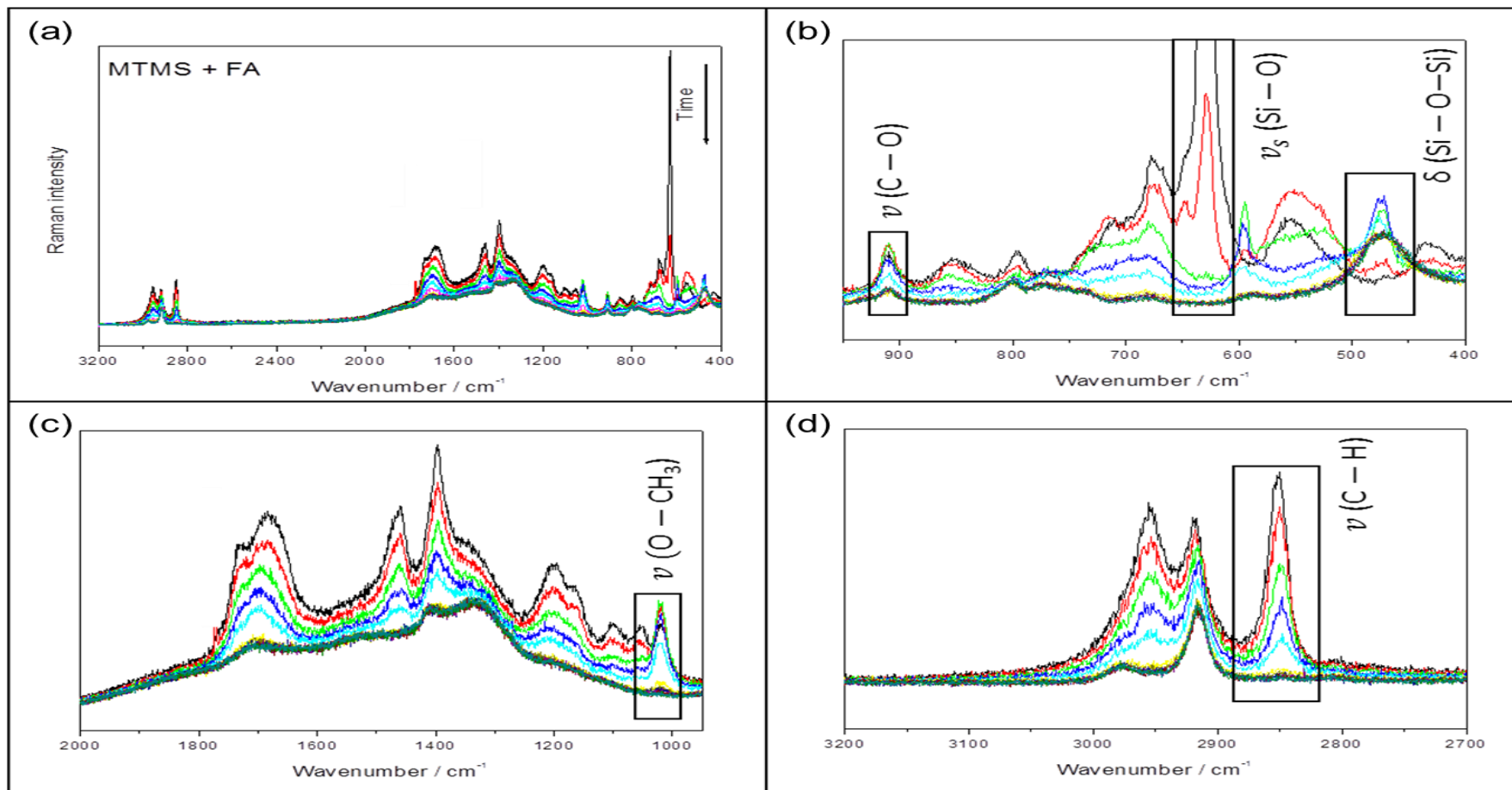


Figure 4.5 Raman spectra evolution with time of MTMS and FA mixtures in the (a) 400-3200  $\text{cm}^{-1}$ , (b) 400-950  $\text{cm}^{-1}$ , (c) 950-2000  $\text{cm}^{-1}$ , and (d) 2700-3200  $\text{cm}^{-1}$  regions. The intensity evolution of bands associated with  $\nu_s(\text{Si}-\text{O})$ ,  $\nu(\text{C}-\text{O})$ ,  $\nu(\text{O}-\text{CH}_3)$ ,  $\delta(\text{Si}-\text{O}-\text{Si})$  and  $\nu(\text{C}-\text{H})$  vibrations as a function of time can be found in Figures 4.8, 4.9, 4.10, 4.11 and 4.12, respectively.

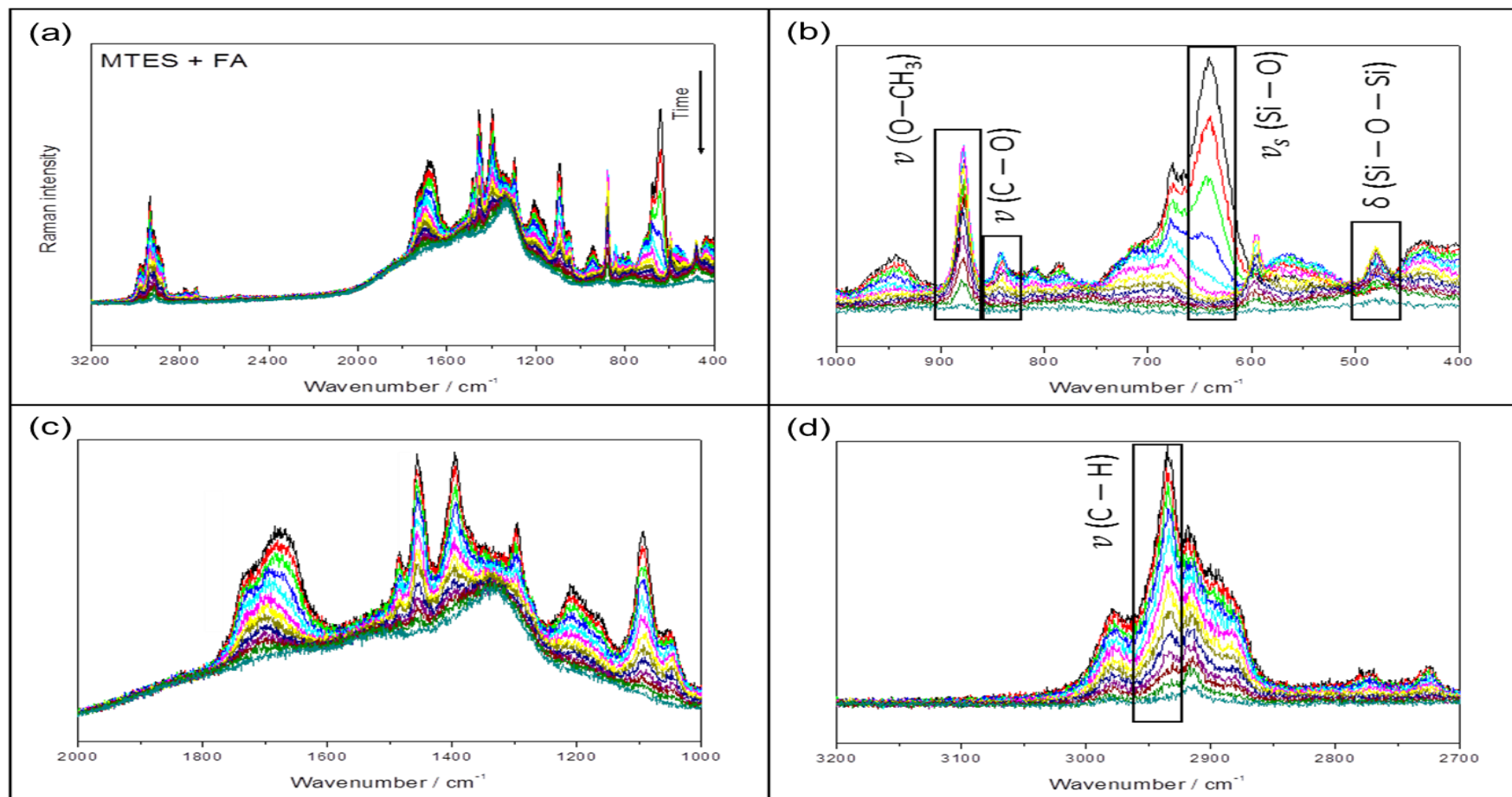


Figure 4.6 Raman spectra evolution with time of MTES and FA mixtures in the (a) 400-3200  $\text{cm}^{-1}$ , (b) 400-1000  $\text{cm}^{-1}$ , (c) 1000-2000  $\text{cm}^{-1}$ , and (d) 2700-3200  $\text{cm}^{-1}$  regions. The intensity evolution of bands associated with  $\nu_s(\text{Si}-\text{O})$ ,  $\nu(\text{C}-\text{O})$ ,  $\nu(\text{O}-\text{CH}_3)$ ,  $\delta(\text{Si}-\text{O}-\text{Si})$  and  $\nu(\text{C}-\text{H})$  vibrations as a function of time can be found in Figures 4.8, 4.9, 4.10, 4.11 and 4.12, respectively.

Figures 4.5 and 4.6 represent the variation in the Raman spectra of MTMS and MTES mixtures with FA, respectively. The reaction evolution of MTMS-based mixture follows a close trend to that of TMOS. This is also true for the ethyl-based mixtures. The main difference between the spectra of corresponding tetraalkoxysilane and alkyltrialkoxysilane-based mixtures is the presence of additional C–H stretching vibration bands at 2916 and 2914  $\text{cm}^{-1}$  that originate from the non-hydrolysable methyl group available in MTMS- and MTES-based acid mixtures, respectively. It is clear that Si–CH<sub>3</sub> bonds remain in the system after the 2 hours experimental duration, as they do not participate in the sol-gel process. In addition, the position of some of the characteristic peaks varies from one tetraalkoxysilane to its alkyltrialkoxysilane counterpart. As can be observed from Figure 4.5, the bending vibrations of the Si–O–Si bridge appears at 474  $\text{cm}^{-1}$  while the stretching vibrations of Si–O, C–O (in methyl formate), O–CH<sub>3</sub> (in methanol) and C–H (in CH<sub>3</sub> groups) in the MTMS-based acid mixtures appear at 627, 909, 1020 and 2845  $\text{cm}^{-1}$ , respectively.

A similar observation is made in the ethyl-based samples. As shown in Figure 4.6, the bending vibrations of the Si–O–Si bridge appears at 481  $\text{cm}^{-1}$  while the stretching vibrations of Si–O, O–C in ethyl formate, O–C in ethanol and C–H (in CH<sub>3</sub> groups) in the MTES-based acid mixtures appear at 640, 840, 877 and 2931  $\text{cm}^{-1}$ , respectively. The shifts in the peak positions corresponding to the bending vibrations of Si–O bonds in all four mixtures are attributed to structural difference between the final 3-dimensional silica networks.

The *in situ* monitoring of the sol-gel process in each formulation was performed by following the variations in the characteristic Raman intensity of key components in the mixture from  $t_0 = 3$  minutes. These include: (a) the Si–O and C–H stretching modes of the silica alkoxide located in the 627-653 and 2845-2935  $\text{cm}^{-1}$  regions, respectively, (b) characteristic peaks of volatile by-products including ethyl and methyl formates ( $\nu(\text{C–O})$ ) located in 840-841 and 909-910  $\text{cm}^{-1}$  regions, respectively (c) ethanol and methanol ( $\nu(\text{O–C}_x\text{H}_{2x+1})$ ) located at 877 and in 1018-1020  $\text{cm}^{-1}$  region, respectively and finally (d) the deformation of Si–O bond in silica located between 474 and 489  $\text{cm}^{-1}$ .

The reaction kinetic information was extracted from data by plotting the Raman intensity of the selected peaks as a function of time. Changes in Raman intensity provide information on the relative concentration of the components available in sample window (spot size  $\sim 8 \mu\text{m}$ ) being exposed to the monochromatic light. A meaningful interpretation of data requires appropriate normalisation procedures to account for differences in the surface properties and quality of focus during collection. As the first step, all data points were divided by a 'reference peak'. During the 2 hours monitoring, the mixture evolves into a solid gel. Thus, throughout the experiment the liquid phase and solid phase compete until full gelation takes place. Because of this biphasic condition, the optical transmittance of the solution drops during gelation. In addition, an unknown volume of the reaction by-products evaporates during the course of the experiment, which jeopardises the focus of the laser on the sample surface. Both of these events influence the depth of laser penetration, which causes the signal/noise ratio to fall. Therefore, it is necessary to normalise the obtained data with respect to a peak that does not go through any changes during the reaction process, to eliminate the influence of the reduction in signal/noise ratio. This is straightforward for the formulations containing methyl and ethyl bonds directly connected to Si atom i.e. the ones containing MTMS and MTES. These bonds do not participate in the sol-gel process (due to their non-hydrolysable nature) and thus, their corresponding C–H stretches (at  $2916$  and  $2914 \text{ cm}^{-1}$ , respectively) were utilised for the initial stage of normalisation. Data normalisation for TMOS and TEOS precursors are slightly more complicated as all of the covalent bonds available in the mixture go through transformation. This issue has been resolved in different ways in the past. Mulder and Damen studied a low-rate hydrolysis reaction of TEOS in ethanol and water and postulated that the rocking mode of the  $\text{CH}_3$  group at  $960 \text{ cm}^{-1}$  does not undergo significant changes over time [9]. Other studies have been conducted in the presence of a non-reactive chemical (e.g. toluene [11] or ionic liquid [3]) to enable normalisation. In this work, the strong band at  $1330 \text{ cm}^{-1}$  attributed to the carbon content in 304 stainless steel container was utilised for normalisation. This was done through precise peak fitting using Omnic software (version 9.6.238) to evaluate the correct peak intensity at  $1330 \text{ cm}^{-1}$ . The validity of this approach was examined by plotting the peak height variation of bands at  $1330$  and  $2916 \text{ cm}^{-1}$  over time. This process was

repeated in duplicate for two different MTMS-based samples and the results are shown in Figure 4.7. As can be seen, both bands share a similar trend for each sample confirming that either of the peaks can be utilised for normalisation of data points.

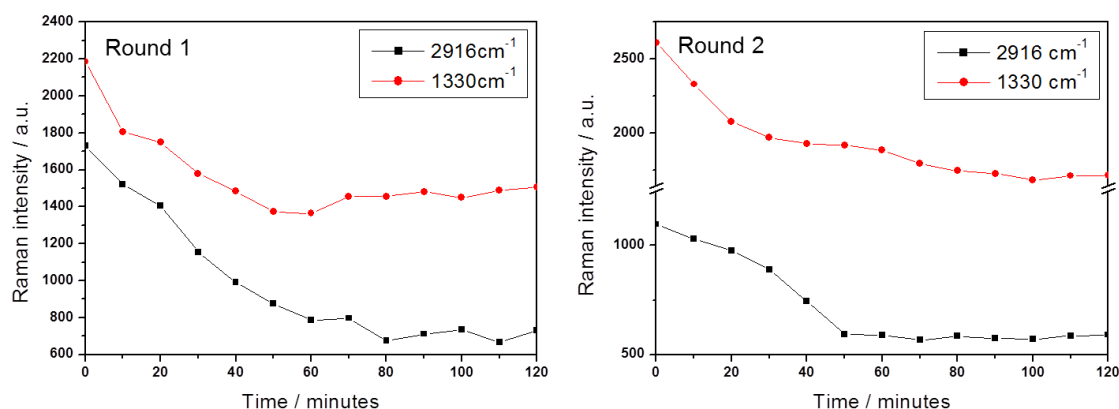


Figure 4.7 Demonstration of Raman intensity variations of 2916 ( $C-H$  stretch in methyl groups of MTMS) and  $1330\text{ cm}^{-1}$  ( $D$ -band in steel container) bands over time in two rounds of nominally identical MTMS-based formulations.

As the second and last step of normalisation, the maximum ( $Raman\ intensity$ ) / ( $Reference\ Peak\ intensity$ ) value in every data set was identified and every data point in the same series was divided by this value. This resulted in all series having a maximum value of 1. To demonstrate repeatability, every measurement was performed in duplicate, and both were plotted as round 1 and 2 in the same graph.

Figure 4.8 displays the rate of precursor consumption in all four samples within two hours of being mixed with acid. In order to quantify the difference in the reaction rate, zero order kinetics was assumed and therefore, a linear fit was plotted for each round of measurements (for the linear region), the results of which are recorded in Table 4.3. Examples of typical linear fits are provided as insets in Figure 4.8a and b.

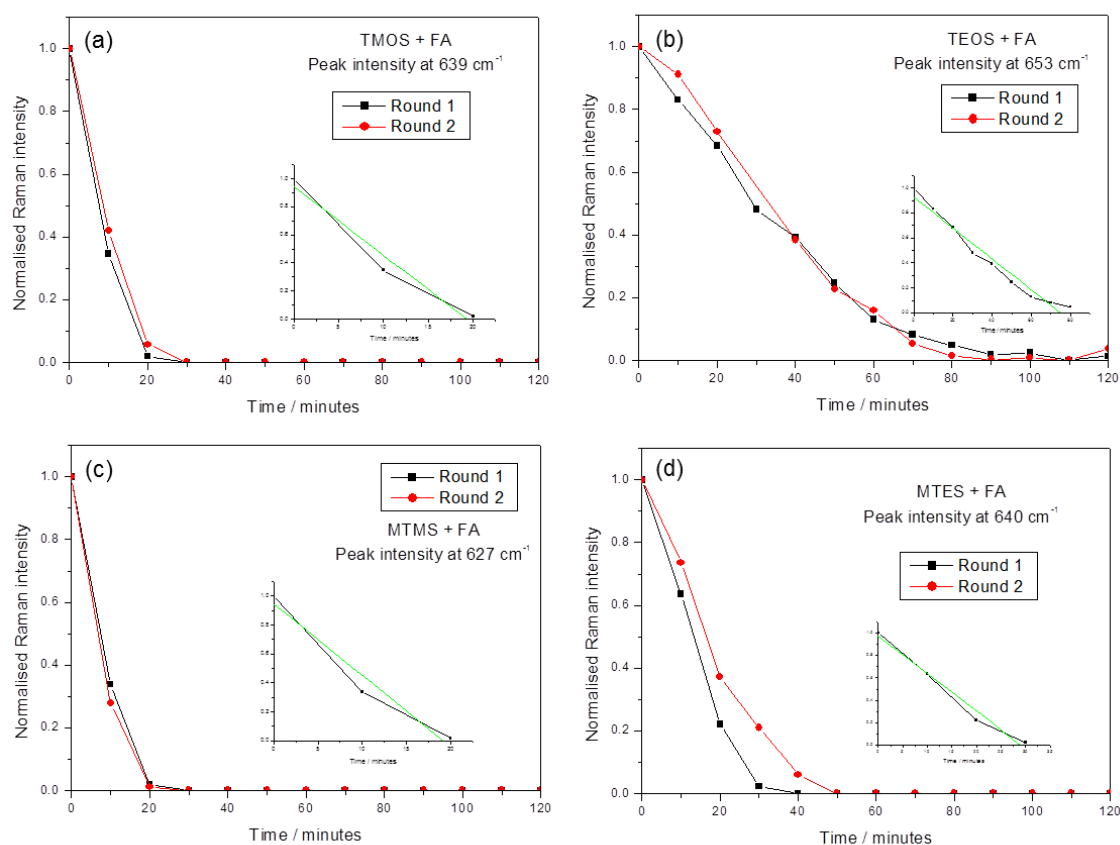


Figure 4.8 Time evolution of Si–O symmetric stretching mode in four different systems namely, (a) TMOS-, (b) TEOS-, (c) MTMS- and (d) MTES-based mixtures. Examples of linear fits are provided in the insets.

Table 4.3 Linear fitting ( $Y = A + BX$ ) information using Origin (version 6.0) software for time evolution of Si–OC<sub>x</sub>H<sub>2x+1</sub> band for each mixture.

Sample		B / minute <sup>-1</sup>	Order of kinetics	R <sup>2</sup>
TMOS+ FA	Round 1	$(-49.04 \pm 9.44)E-3$	0	0.96
	Round 2	$(-47.12 \pm 6.26)E-3$	0	0.98
TEOS+ FA	Round 1	$(-12.33 \pm 0.88)E-3$	0	0.97
	Round 2	$(-13.35 \pm 0.87)E-3$	0	0.98
MTMS+ FA	Round 1	$(-49.12 \pm 9.88)E-3$	0	0.96
	Round 2	$(-49.44 \pm 13.18)E-3$	0	0.93
MTES+ FA	Round 1	$(-33.45 \pm 3.27)E-3$	0	0.98
	Round 2	$(-24.08 \pm 2.45)E-3$	0	0.97

As can be seen from Table 4.3, Si–OCH<sub>3</sub> is consumed at a higher rate than Si–OC<sub>2</sub>H<sub>5</sub>. At the starting point of reaction monitoring (t<sub>0</sub>=3 minutes) these bands can undergo two distinct chemical reactions (as indicated by Sharp [20]):



Simultaneous to the carboxylation (reaction (4.1)), hydrolysis reaction (reaction (4.4)) can take place due to the presence of small volume of water (~4%) in commercial FA. At the start of the sol-gel process, reaction (4.4) is unlikely to take place as the alkoxide precursors are immiscible in water and require alcohol as a co-solvent [26]. This is due to the hydrophobic nature of the alkyl groups [27]. During the course of the reaction and as more water-soluble groups are formed, hydrolysis through reaction (4.4) becomes more likely. Since the hydrophobicity increases with the size of the alkyl chain, ethyl-based precursors require a larger volume of alcohol to solubilise in water. Therefore, consumption of ethyl-based precursors is expected to accelerate once enough ethanol is produced in the reaction environment and TEOS/MTES can participate in reaction (4.4) as well as reaction (4.1). Subsequently, the precursor participates in condensations reactions ((4.8) and (4.9)) and can be consumed in a wider range of routes.

Thus, reaction (4.1) can be considered as the main route of precursor consumption in the initial stages of sol-gel process. During the non-hydrolytic sol-gel route, the oxygen atom in the alkoxy group undergoes protonic attack. This is the rate-determining step of the non-hydrolytic sol-gel process and is related to the electronegativity of the oxygen atom. Table 4.4 is extracted from the work done by Kanamori et al. [14] in which they calculated the partial charge of various alkoxy silanes using the 'partial charge model'. This model, proposed by Livage and Henry [28], suggests that the partial charge ( $\delta$ ) of an element can be calculated by considering the electronegativity of all of the elements present in the molecule (in neutral state). As it is shown in the Table 4.4, the partial charge on oxygen atom ( $\delta_{\text{O}}$ ) in TMOS (-0.44) is slightly lower than that of TEOS (-0.46). The same is true for the case of MTMS (-0.46) and MTES (-0.47). This observation suggests that TMOS should have the slowest rate for reactions 4.1 and 4.4

while MTES should have the fastest rate. This does not agree with the observation made from Figure 4.8 and Table 4.3. This can be explained by considering the other influential factor in the protonic attack, steric hindrance. This phenomenon explains that due to the arrangement of atoms in a molecule, a longer alkyl chain hinders the protonic attack to the oxygen atom in the alkoxy chain. For this reason, the rate of TMOS consumption is faster (~4 times) than that of TEOS and similarly, rate of MTMS consumption is faster than that of MTES (by a factor of ~1.7).

Based on Table 4.3, the rate of precursor consumption in MTMS-based system ( $B_{\text{Average}} = -49.28\text{E-}3$ ) is only slightly higher than that of TMOS-based mixture ( $B_{\text{Average}} = -48.08\text{E-}3$ ). This difference is much more noticeable for the MTES and TEOS precursors. The substitution of an ethoxy group with an ethyl group is not expected to induce a reduction in the steric hindrance around the oxygen atoms in the remaining ethoxy groups. However, the partial charge on the oxygen atoms in MTES is slightly higher than that in TEOS as shown in Table 4.4. This is due to weaker electron withdrawing power of ethyl groups compared to ethoxy groups [14,29]. The higher electron density at oxygen atoms in MTES molecules makes this precursor more susceptible to protonic attack.

Table 4.4 Partial charges value of various silica alkoxides calculated using the partial charge model [14].

	Si(OR) <sub>4</sub>	CH <sub>3</sub> Si(OR) <sub>3</sub>	C <sub>2</sub> H <sub>5</sub> Si(OR) <sub>3</sub>
$\delta_{\text{O}}$ values			
R = CH <sub>3</sub>	-0.44	-0.46	-0.47
R = C <sub>2</sub> H <sub>5</sub>	-0.46	-0.47	-0.48
R = C <sub>3</sub> H <sub>7</sub>	-0.47	-0.48	-0.48
$\delta_{\text{Si}}$ values			
R = CH <sub>3</sub>	+0.35	+0.33	+0.32
R = C <sub>2</sub> H <sub>5</sub>	+0.32	+0.31	+0.31
R = C <sub>3</sub> H <sub>7</sub>	+0.31	+0.30	+0.30

Another factor influencing this considerable difference in the reaction kinetics among tetraalkoxysilanes and alkyltrialkoxysilanes is the stoichiometry of the carboxylation reaction. For every 1 mole of tetraalkoxysilane, 4 moles of FA is

required for reaction (4.1) to take place while the precursor:FA molar ratio for alkyltrialkoxysilanes is 1:3:



Because of the precursor:FA molar ratio used in this work (1:3.5), there is a stoichiometric imbalance for the case of TMOS and TEOS, while excess FA is present when MTMS and MTES are used. This mismatch contributes to the rate of the carboxylation process, which facilitates the alkoxide consumption.

Based on Figure 4.8, after ~20 minutes of the sol-gel process, Si–OR stretching vibration disappears in methyl-base precursor and acid mixtures while it takes between 40-100 minutes for this band to no longer be discernible from Raman spectra of the ethyl-based mixtures. As mentioned before, this band is attributed to the symmetric stretching vibration of Si–OR and its intensity is reduced when one or more of these bonds are broken [9]. Thus, its disappearance cannot be regarded as the absence of Si–OR bonds in the sol mixture. The results shown in this work confirm that the initial sol-gel processes have progressed further in the case of methyl-based precursors compared to ethyl-based ones and follows the following order: MTMS~TMOS>MTES>TEOS.

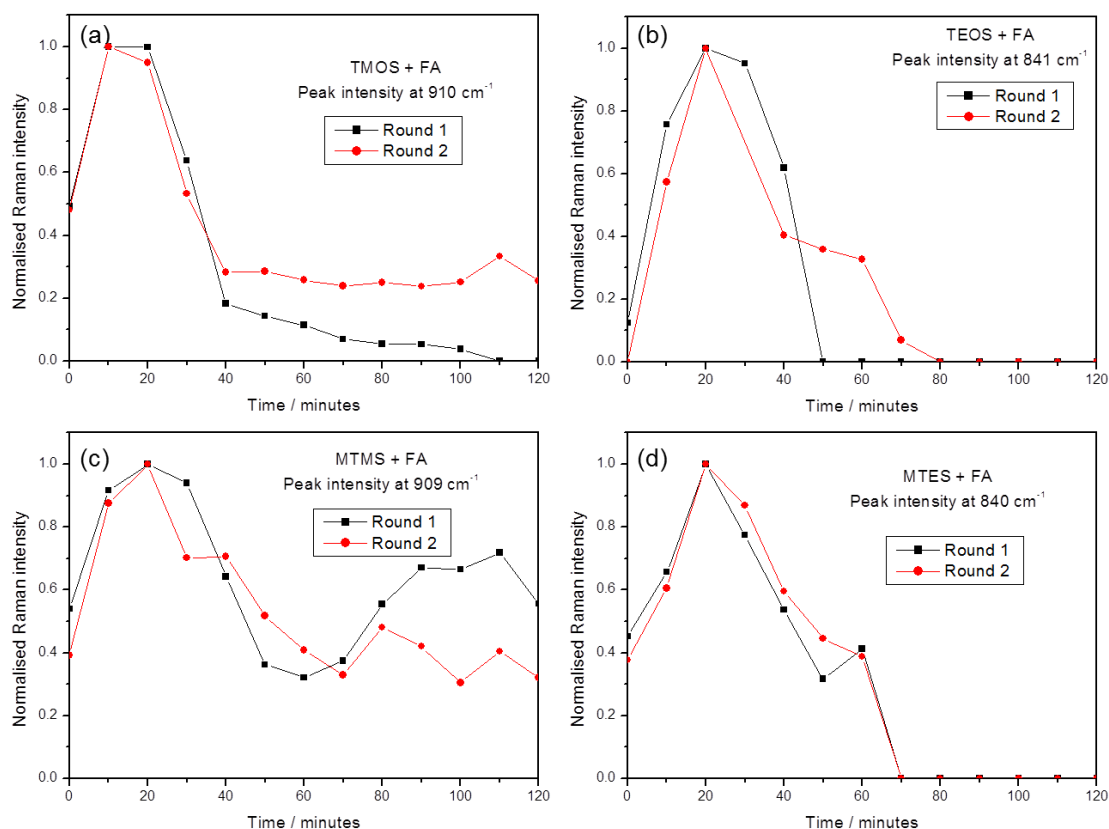


Figure 4.9 Formation and consumption of methyl formate (in (a) TMOS- and (c) MTMS-based samples) and ethyl formate (in (b) TEOS- and (d) MTES-based mixtures).

Figure 4.9 represents the consumption of the alkyl formate characteristic peak over time in each mixture. Generally, the methyl/ethyl formate is produced via two chemical routes:



Alcohol and/or [Si]OCOH are required for the production of ROCOH groups. As the sol-gel process proceeds over time, more alcohol is introduced into the system disturbing the equilibrium of esterification reaction (no. (4.3)). Based on Le Chatelier's principle, the system will then adjust itself to counteract the excess ROH groups present in the system by producing more yield (water and ethyl/methyl formate) and establishing a new equilibrium. Therefore, simultaneous to the esterification reaction, some condensation takes place in each sys-

tem resulting in rapid formation of ROCOH. The results shown in Figure 4.9 demonstrate a peak maximum in the formation of both methyl formate and ethyl formate after 20 minutes post mixing acid with the precursor. After 20 minutes, the production of methyl formate dissipates slowly while the Raman band associated with ethyl formate reaches zero intensity after ~70 minutes. In order to understand this observation, the alcohol production must first be investigated.

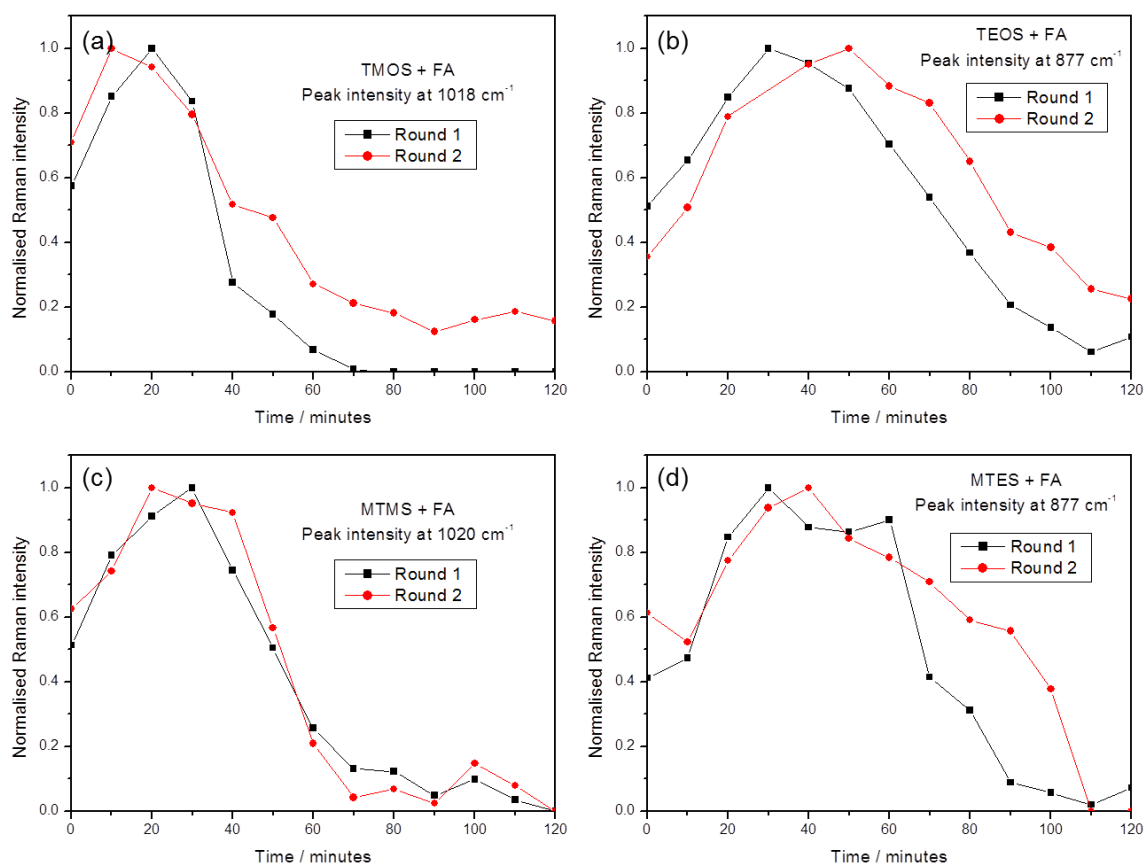
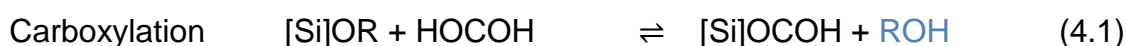


Figure 4.10 Formation and consumption of methanol in (a)TMOS and (c) MTMS mixtures and ethanol in (b) TEOS and (d) MTES mixtures as a function of time.

Figure 4.10 displays the rate of formation and consumption of methanol (for TMOS and MTMS) and ethanol (in TEOS and MTES-based samples). As can be seen, alcohol production reaches its peak after 20-50 minutes of the reaction monitoring period. The slower production of ethanol compared to methanol can be explained by the reduced rate of the carboxylation step (reaction (4.1)). As discussed previously, consumption rate of methyl-based precursors is higher than that of ethyl-based precursors. This means that methanol is produced at a higher rate in methyl-based mixtures compared to ethanol in ethyl-based mix-

tures as a result of reactions (4.1) and (4.4). It can be seen in Figure 4.10 that the production of methanol reaches a maximum at ~20 minutes post precursor and FA mixing while this maximum is reached after ~50 minutes for ethyl-based mixtures.

Generally, alcohol can either be consumed through esterification (reaction (4.3)) or leave the structure via evaporation. Methanol and ethanol have vapour pressures of 55.5 and 29.4 kPa at 50°C [30], respectively and thus, methanol is more volatile and more likely to leave the sol-gel mixture via evaporation compared to ethanol. On the other hand, as more methanol is formed in the system, the reaction equilibrium in all of the reactions listed below becomes disturbed. In other words, while esterification reaction (reaction 4.3) yields more methyl formate to counterbalance the excess methanol, reactions (4.1) and (4.4) introduce more acid and alkoxide into the system. Due to the complex nature of the reactions, it is hard to confidently describe what takes place in the system at each point of time. However, based on Figure 4.10, one can confidently state that methanol leaves the sol-gel system and/or is consumed at a higher rate compared to ethanol.



Based on the formation and consumption patterns of alkyl formates and alcohols, one can presume that within the first hour of reaction monitoring, methyl formate is produced via both esterification (reaction (4.3)) and condensation (reaction (4.9)) routes. After this, due to the reduction in methanol concentration in the methyl-based systems, the methyl formate is mainly produced via the condensation reaction (4.9) and its rate of production drops quickly.

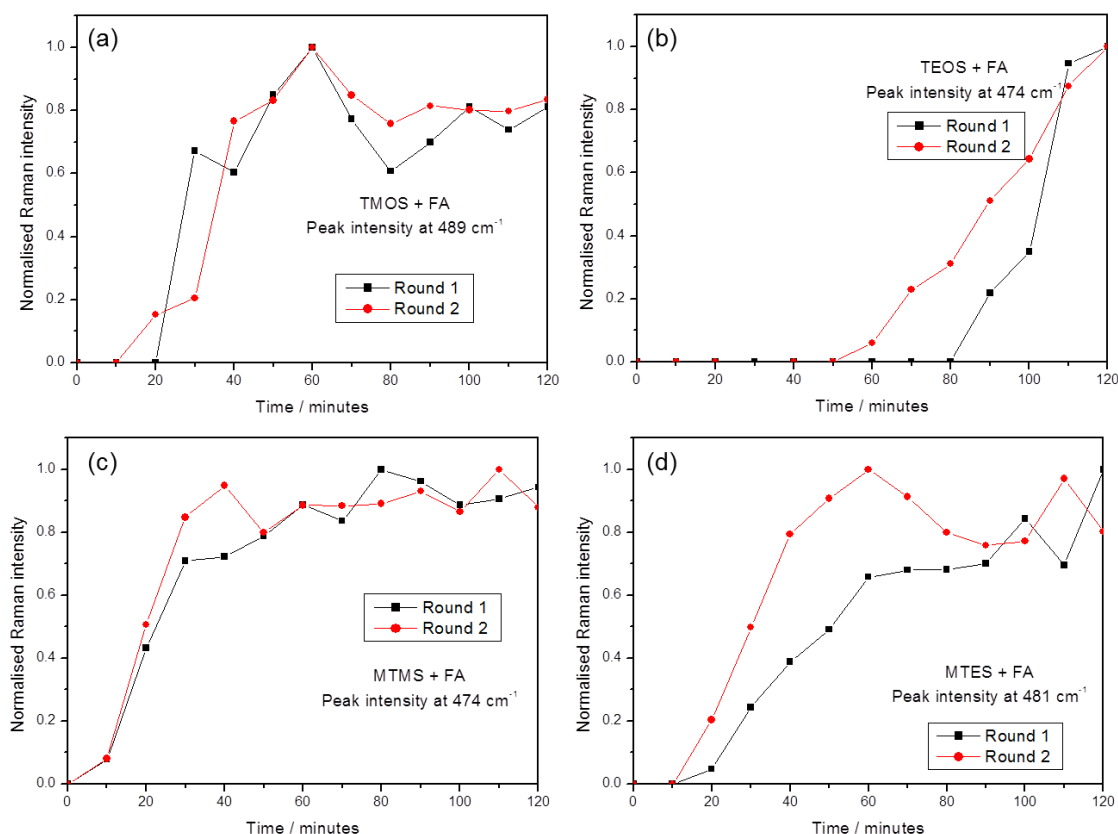
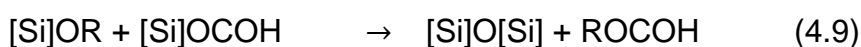


Figure 4.11 Formation of Si–O deformation band located between 474–489  $\text{cm}^{-1}$ . This band represents the initial stages of condensation process in (a) TMOS, (b) TEOS, (c) MTMS and (d) MTES mixtures.

Formation of the Si–O–Si bridges, characterised by deformation vibration of Si–O bond (located in the 474–489  $\text{cm}^{-1}$  region), marks the start of the condensation process. This band is weak, and its intensity is increasingly obscured by the reduced signal to noise ratio as the reaction proceeds. This effect may not have been fully removed by the normalisation process. This could explain the scatter in its intensity shown in Figure 4.11.

Generally, condensation in these systems can take place in multiple ways:



As soon as carboxylation of Si–OR takes place, condensation is initiated via reaction (4.9). As the reaction proceeds and the hydrolysis reaction takes place (producing Si–OH groups), condensation is facilitated in the other chemical routes listed as reactions (4.6-4.8) which results in a rapid increase in the intensity of  $\delta(\text{Si–O})$  band. Therefore, rate of condensation is dependent on the rate of both carboxylation and hydrolysis reactions. The results shown in Figure 4.11 agree well with the kinetics of the precursor consumption process in all four samples as shown in Figure 4.8.

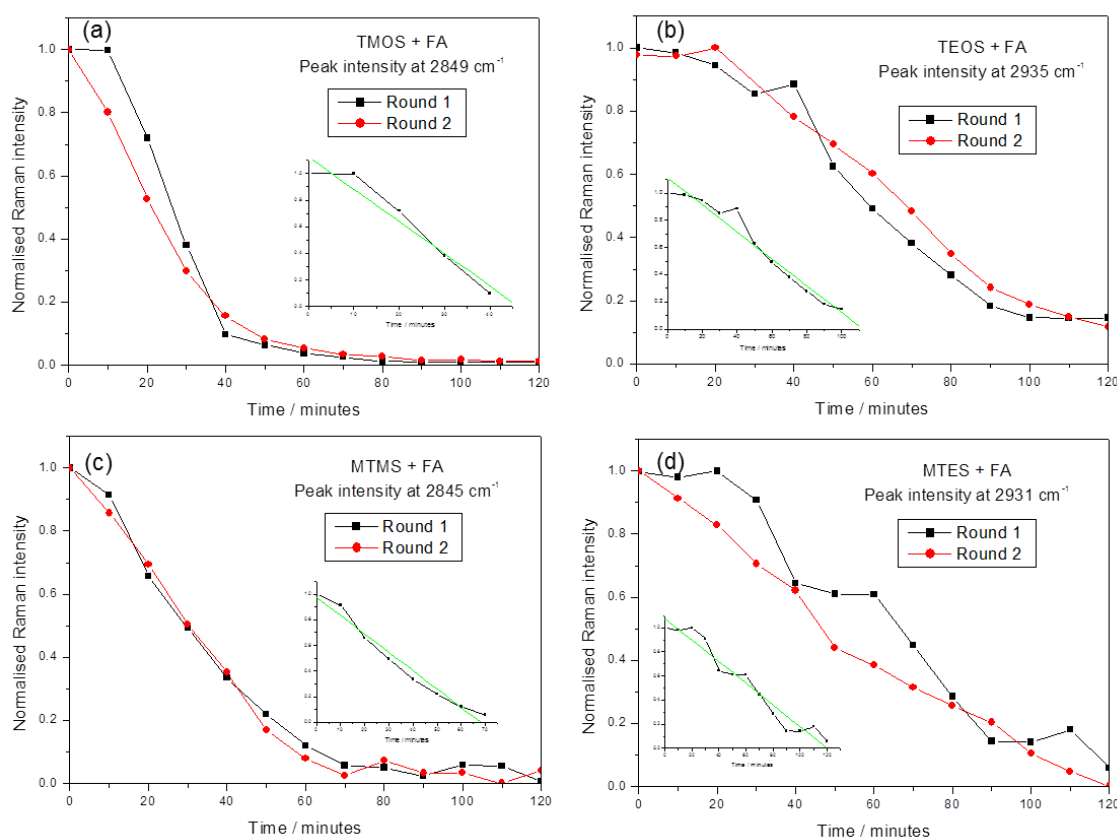


Figure 4.12 variation of Raman intensity in the selected C–H stretching vibrations in each sample, (a) TMOS, (b) TEOS, (c) MTMS and (d) MTES mixtures. The insets represent typical fitting utilised to calculate the rate of Raman band-intensity drop.

Figure 4.12 represents the time evolution of C–H stretching vibration bands at 2849, 2935, 2845 and 2931  $\text{cm}^{-1}$  in TMOS-, TEOS-, MTMS- and MTES-based mixtures, respectively during the 2 hours experimental window. The position of these bands agree well with the C–H vibrations of the corresponding precursor in each mixture as demonstrated in Figure 4.2 and Table 4.2. Zero order kinetics was chosen to plot the linear fittings using Origin software (version 6.0).

Examples of these fittings are shown in Figure 4.12 insets. The kinetic rates obtained from fittings are recorded in Table 4.5. Theoretically, the consumption of each precursor reduces the concentration of SiOC–H bonds in the system and as a result, the intensity of the corresponding C–H vibrational band drops in Raman spectra. As illustrated in Table 4.5, the average rate of C–H stretching evolution differs from that of Si–O bands located at 639, 627 and 640  $\text{cm}^{-1}$  for TMOS-, MTMS- and MTES-based FA mixtures (mentioned in Table 4.3).

*Table 4.5 Linear fitting ( $Y = A + BX$ ) information using Origin (version 6.0) software for time evolution of the selected C–H band for each mixture. The selected vibrational bands are 2849, 2935, 2845 and 2931  $\text{cm}^{-1}$  in TMOS-, TEOS-, MTMS- and MTES-based acid mixtures, respectively.*

Sample		B / $\text{minute}^{-1}$	Order of kinetics	$R^2$
TMOS+ FA	Round 1	$(-24.24 \pm 3.61)\text{E-3}$	0	0.94
	Round 2	$(-19.32 \pm 1.72)\text{E-3}$	0	0.97
TEOS+ FA	Round 1	$(-9.82 \pm 0.71)\text{E-3}$	0	0.95
	Round 2	$(-8.44 \pm 0.46)\text{E-3}$	0	0.97
MTMS+ FA	Round 1	$(-14.34 \pm 0.98)\text{E-3}$	0	0.97
	Round 2	$(-14.81 \pm 0.78)\text{E-3}$	0	0.98
MTES+ FA	Round 1	$(-8.93 \pm 0.60)\text{E-3}$	0	0.95
	Round 2	$(-8.56 \pm 0.36)\text{E-3}$	0	0.98

Although careful peak fitting tools were utilised to remove the effect of neighbouring peaks on the intensity of investigated bands, it is clear that other bands have contributed to the intensity of C–H band associated with each precursor due to superimposition. Figures 4.13 demonstrates the Raman spectra of methanol, ethanol, methyl formate and ethyl formate. As can be seen, C–H stretching vibrations of methyl formate ( $2844 \text{ cm}^{-1}$ ) contributes to the intensity of methyl-based mixtures at 2849 and 2845  $\text{cm}^{-1}$ . Similarly, C–H stretching vibrations of ethanol ( $2933 \text{ cm}^{-1}$ ) contributes to the intensity of MTES-based mixture at 2931  $\text{cm}^{-1}$ .

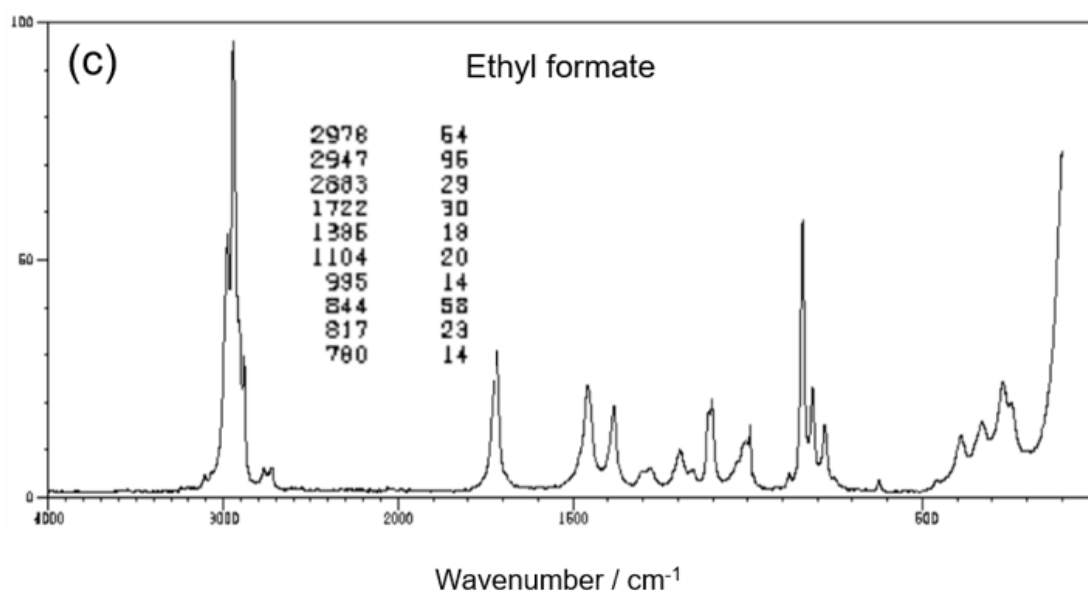
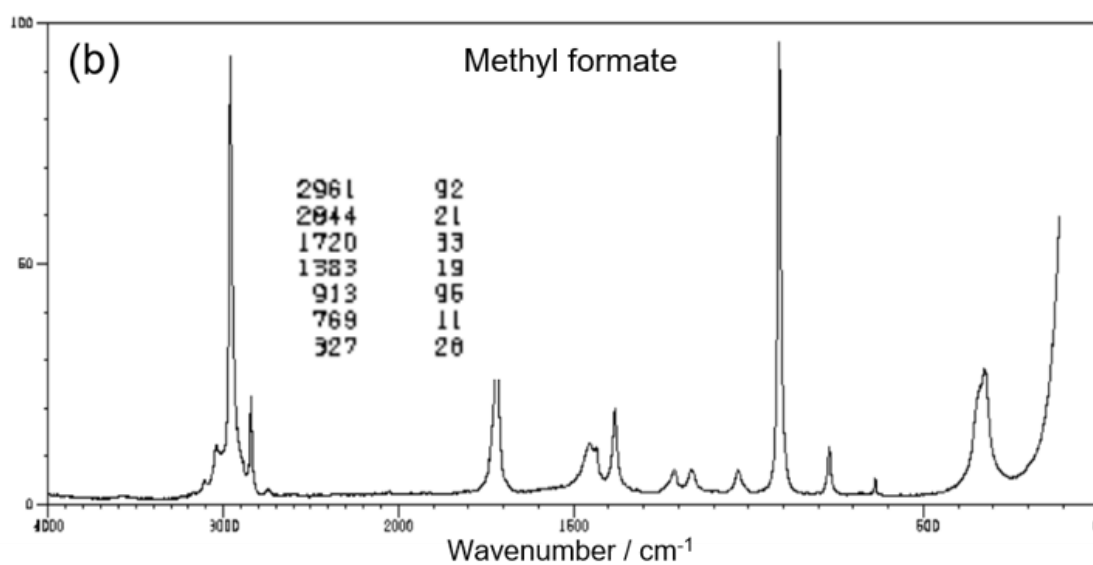
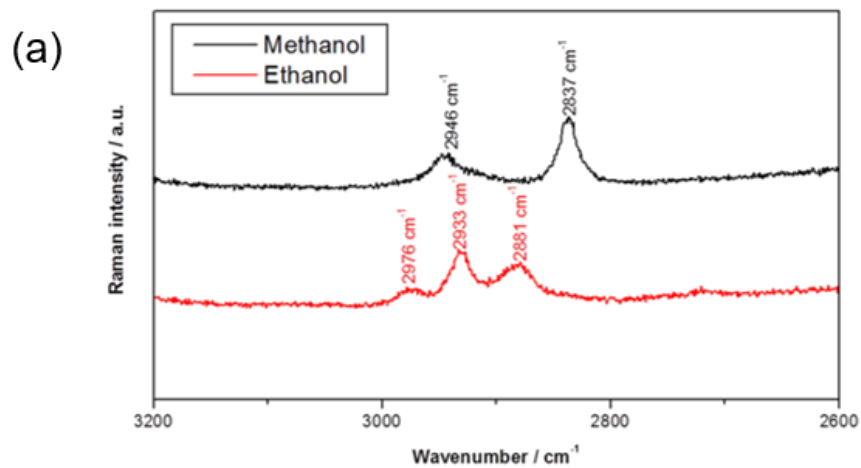


Figure 4.13 Raman spectra of (a) methanol and ethanol, (b) methyl formate (retrieved from [31] with modifications) and (c) ethyl formate (retrieved from [32] with modifications).

Counterintuitively, the TEOS-based mixture showed relatively close kinetic rates for bands at 653 and 2935  $\text{cm}^{-1}$  (average values of  $-12.84\text{E-}3$  and  $-9.13\text{E-}3$   $\text{minutes}^{-1}$ , respectively). One possible explanation for this observation could be the slow rate of TEOS consumption as shown in Figure 4.8b. The slower rate of TEOS consumption results in slower formation of ethanol in the system. Therefore, a lower volume of ethanol is formed in the TEOS mixture during the experiment and its corresponding band at 2933  $\text{cm}^{-1}$  does not influence the peak intensity of the precursor band at 2935  $\text{cm}^{-1}$  extensively.

#### **4.4 Morphology of silica network**

##### **4.4.1 Experimental procedure**

Scanning electron microscopy was used to compare the morphologies of the four synthesised silica networks. Each silica alkoxide was mixed with FA (with the formulation described in section 4.2) for 10 minutes in a glass vial at 600 rpm using a magnetic stirrer. Since early stage monitoring was not required in this study, the reactants were mixed for additional 7 minutes (compared to the *in situ* reaction monitoring study) to allow the sol to reach a more homogenous state. After the 10 minutes mixing period, 500  $\mu\text{L}$  of each mixture was transferred into a stainless steel container using a micropipette. After two hours of aging under ambient conditions (humidity and temperature were monitored during this period using an RS 1260 humidity temperature meter), the wet gels were transferred to a Genlab oven (Model MINO/40) and were heated at  $110\pm 5^\circ\text{C}$  for 12 hours. Once dried, the xerogels were coated with gold to minimise the charging effects caused by the electron beam during SEM imaging (Quanta 3D FEG, FEI, USA).

##### **4.4.2 Results and discussion**

As mentioned previously, the sol-gel mixtures are kept at ambient conditions for two hours prior to being dried at  $110^\circ\text{C}$ . Table 4.6 provides a comparison between the points of time at which each sol turns into a gel, where  $t$  represents the time passed from the mixing point of precursors with acid. The point of gelation, referred to as sol-gel transition point, was determined by mildly agitating each sample, every 10 minutes by applying a light force using a spatula on the sample surface. Once no flowing behaviour was observed upon agitation, the

sample was considered gelled. The quickest silica gel was formed with TMOS precursor followed by MTMS, TEOS, and lastly MTES. Based on the results of *in situ* monitoring of hydrolysis and condensation processes taking place in each mixture (shown in section 4.3.2), TMOS, and MTMS showed very similar reaction kinetics throughout the first 2 hours of the sol-gel process. Interestingly, formation of the Si–O–Si bridges characterised by deformation vibrations of Si–O bonds (corresponding bands located at 489 and 474  $\text{cm}^{-1}$  for TMOS and MTMS, respectively) have a very similar profile as shown in Figure 4.11a and c. A similar observation is made by comparing the ethyl-based precursors. Based on Figure 4.11b and d, the Si–O–Si bridges are formed at earlier stages of sol-gel process in MTES mixture compared to TEOS. However, according to the data in Table 4.6, TEOS mixture showed to gel quicker than MTES. These observations can be explained by the mechanism of gelation in sol-gel process. Formed silica particles (primary particles) aggregate to form secondary particles or clusters and finally these particles link together in a 'pearl necklace' morphology [33]. Presence of methyl groups in MTES and MTMS retards the formation of primary and secondary particles due to steric hindrance effect [29].

*Table 4.6 Gelation timeline determined visually for TMOS, TEOS, MTMS and MTES based gels. The 'X' symbol describes a not-gelled state while the '✓' symbol represents a gelled silica network.*

	t / minutes				
	10'	30'	60'	90'	120'
Humidity	39.0%	42.3%	44.4%	44.3%	44.8%
Temperature (°C)	24.2	24.2	24.2	24.4	24.3
TMOS	X	X	~40'	✓	✓
TEOS	X	X	X	~80'	✓
MTMS	X	X	X	~70'	✓
MTES	X	X	X	X	~100'

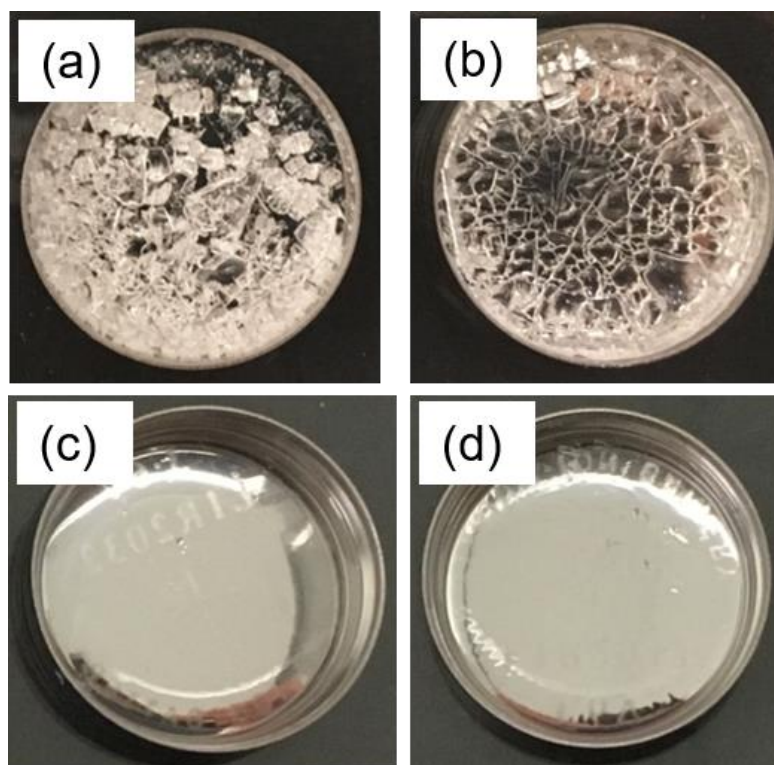


Figure 4.14 Optical images of (a) TMOS, (b) TEOS, (c) MTMS and (d) MTES based wet gels after 2 hours of sol-gel process under ambient conditions.

Figure 4.14 demonstrates the physical structure of the synthesised gels after 2 hours of hydrolysis and condensation processes under ambient conditions. As can be seen, the tetraalkoxysilane-based gels have extensively fractured into small pieces, which suggest that the TMOS- and TEOS-based gels have brittle structures. On the other hand, the trialkoxysilane-based gels have a smooth surface with no apparent signs of shrinkage or fractures. As discussed previously and shown in Figures 4.9 and 4.10, ROH and ROCOH groups formed during the carboxylation, esterification, hydrolysis, and condensation reactions are removed from the mixture either through consumption in another reaction or through evaporation. As the volatile by-products leave the silica network, capillary pressure is exerted on the porous silica structure. This is overcome by compressive stress on the gel structure, which results in shrinkage of the gels [34,35]. In addition, a typical porous silica network contains pores of various sizes and therefore, as evaporation of by-products takes place, a high pressure-gradient is created inside the network, which can result in mechanical damage such as fracturing. The presence of Si-CH<sub>3</sub> groups in the MTMS and MTES based gels reduces the surface tension of the alcohol and water within the

pores of the gels preventing the capillary collapse [35]. In addition, the presence of the non-hydrolysable groups inside the network results in a lower crosslinking density in the silica network, which increases the flexibility of the porous network.

Generally, silica gels have pearl-necklace microstructures in which primary particles consist of well-connected and agglomerated silica particles that are connected through a few Si–O–Si bonds together to create secondary silica particles [36]. Figure 4.15 demonstrates a schematic description of this structure. It can be seen that the weak mechanical points are the neck regions between secondary particles. Based on controlled aggregation mechanism, once secondary particles reach a certain size, colloidal stability is reached inside the sol due to surface charges [22].

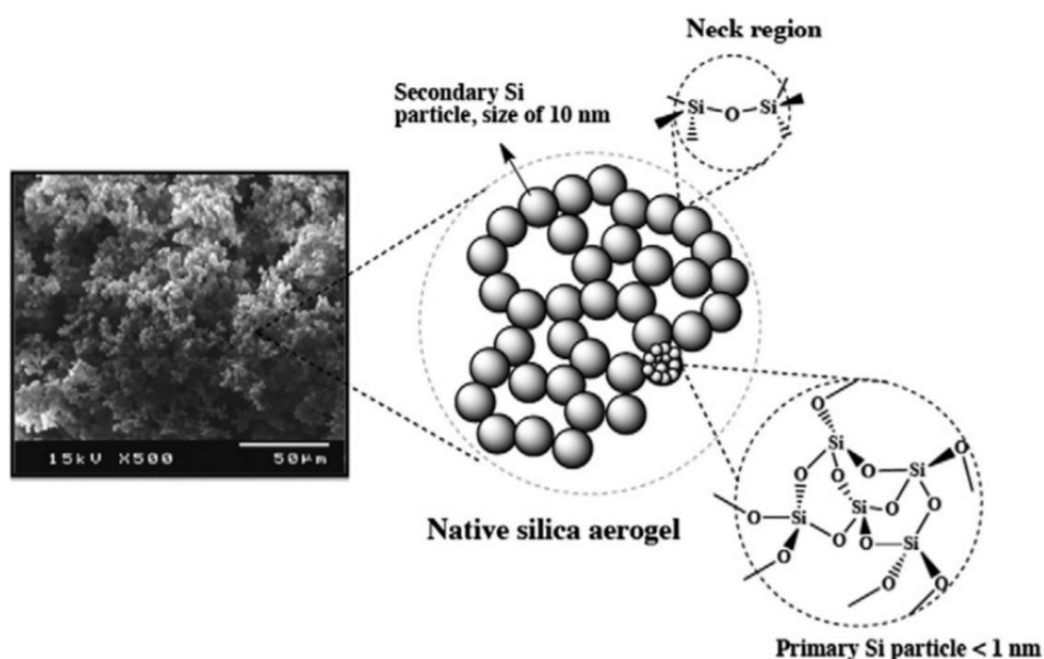


Figure 4.15 A typical SEM image and schematic demonstration of porous silica which is constructed of primary and secondary particles. Retrieved from [36].

Figures 4.16 to 4.19 demonstrate the SEM images of all four of the xerogels after being dried at 110°C for 12 hours. Electron microscopy images of each sample were taken from four arbitrary regions within the sample. The SEM images shown here are representative of the porous structure of each silica network. During the heating process, the water content and the residual volatiles

are expected to leave the structure of the gel, causing an increase in the capillary pressure as a result of which the network is pulled inwards and the gel shrinks [34]. The SEM images for all samples show a dense structure for the xerogels, which is a result of extensive shrinkage.

Furthermore, the secondary silica particles can be detected in all SEM images. These particles are smaller in size and are more uniformly distributed in tetraalkoxide-based xerogels compared to trialkoxide-based xerogels. The inter-particle boundaries are less defined in TMOS- and TEOS-based xerogels, which can be translated into smaller inter-particle pore sizes in these samples. The highly brittle nature of these xerogels supports this observation since the smaller the pore sizes, the less permeable the gel is to the fluid flow rate which results in the formation of cracks and fractures in the silica xerogel [35]. Permeability is the ease with which fluid flows through a porous structure [37].

In addition, the sizes of the secondary silica particles are larger in MTMS- and MTES-based xerogels compared to TMOS and TEOS xerogels. Zhang et al. reported a similar observation while investigating the influence of MTES/TEOS molar ratio on the morphology of the resultant silica particles [38]. Based on their study, as the MTES/TEOS ratio was increased, the size of secondary silica particles, formed by aggregation of primary particles, increased. They explained that as the amount of MTES in the mixture increases, the charge balance of the colloid is disturbed and for this reason, the colloid particles continue to grow in size. This explanation seems relevant to the work reported here as well. Presence of non-hydrolysable and hydrophobic methyl groups in MTMS and MTES sol mixtures retarded the colloidal balance, which led to the formation of larger secondary particles.

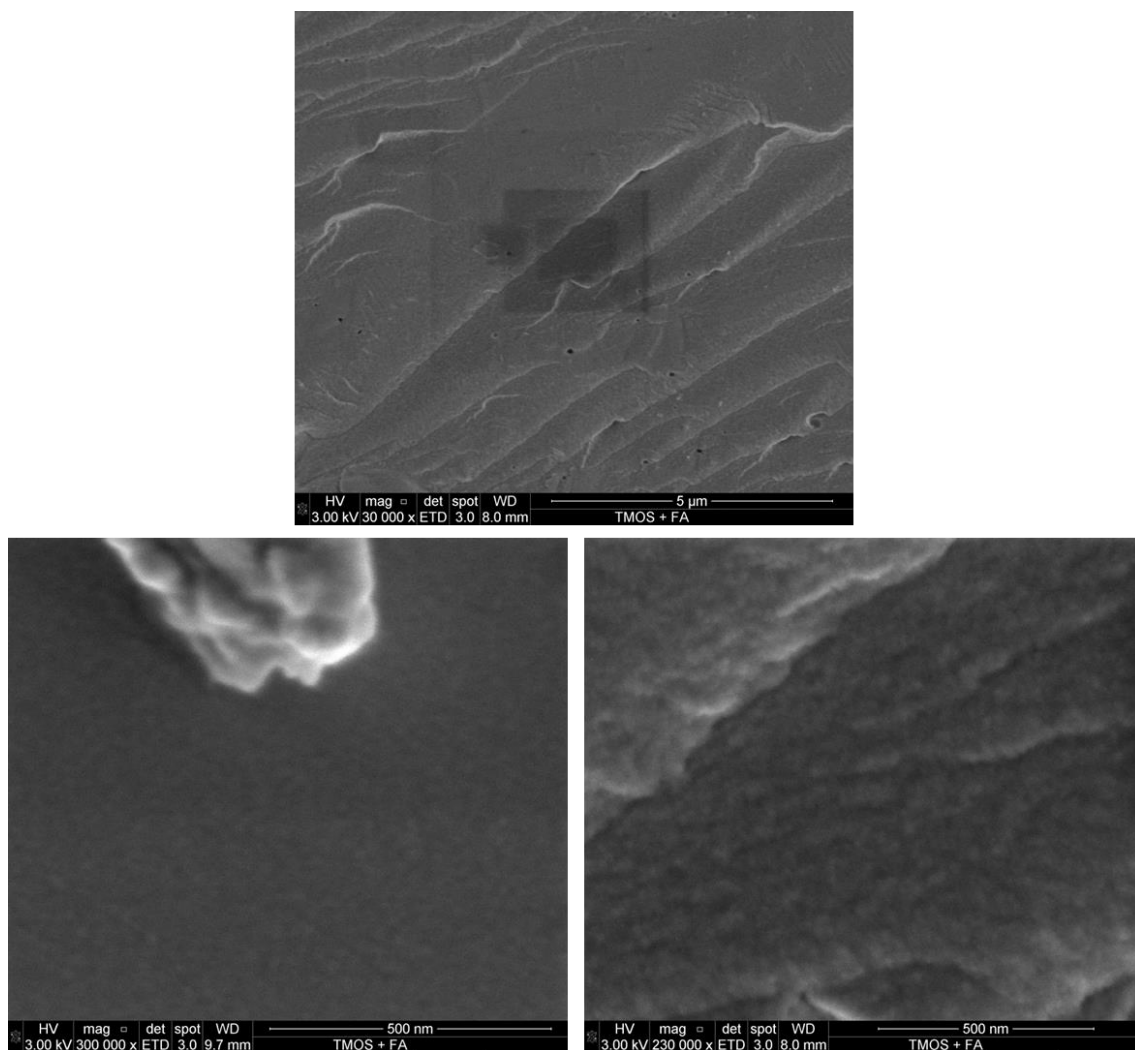


Figure 4.16 SEM images of TMOS-based xerogels after being dried at 110°C for 12 hours.

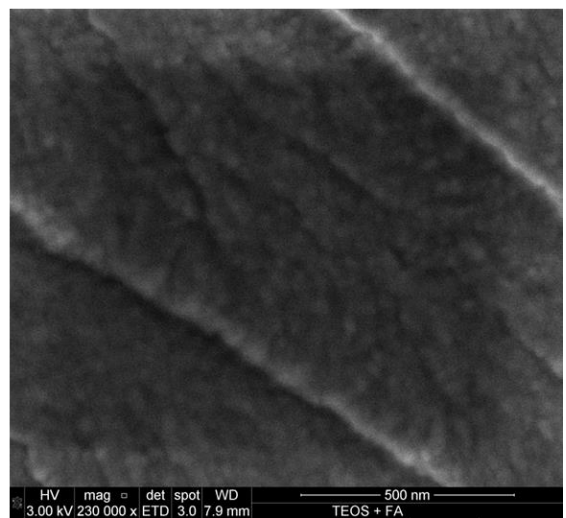
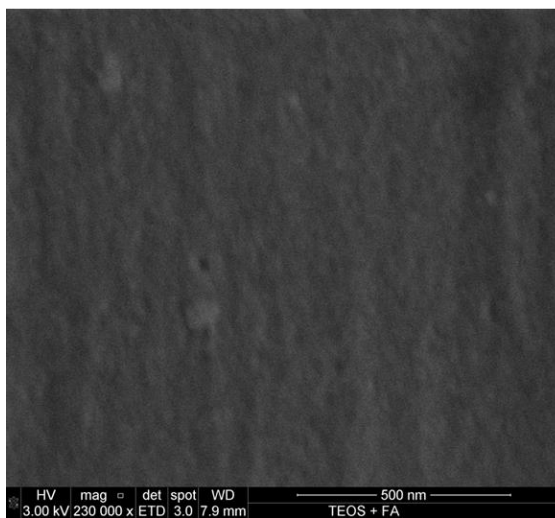
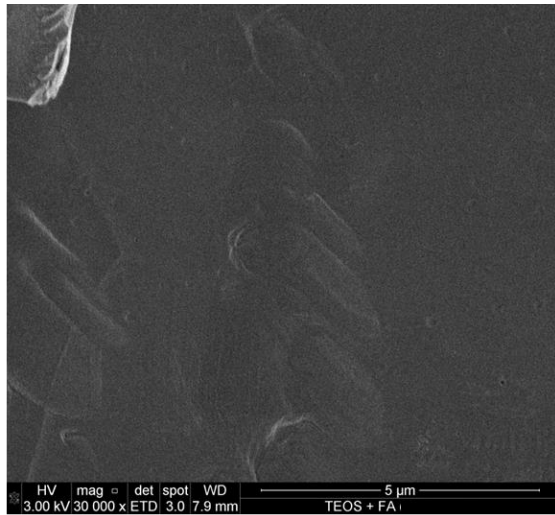


Figure 4.17 SEM images of TEOS-based xerogels after being dried at 110°C for 12 hours.

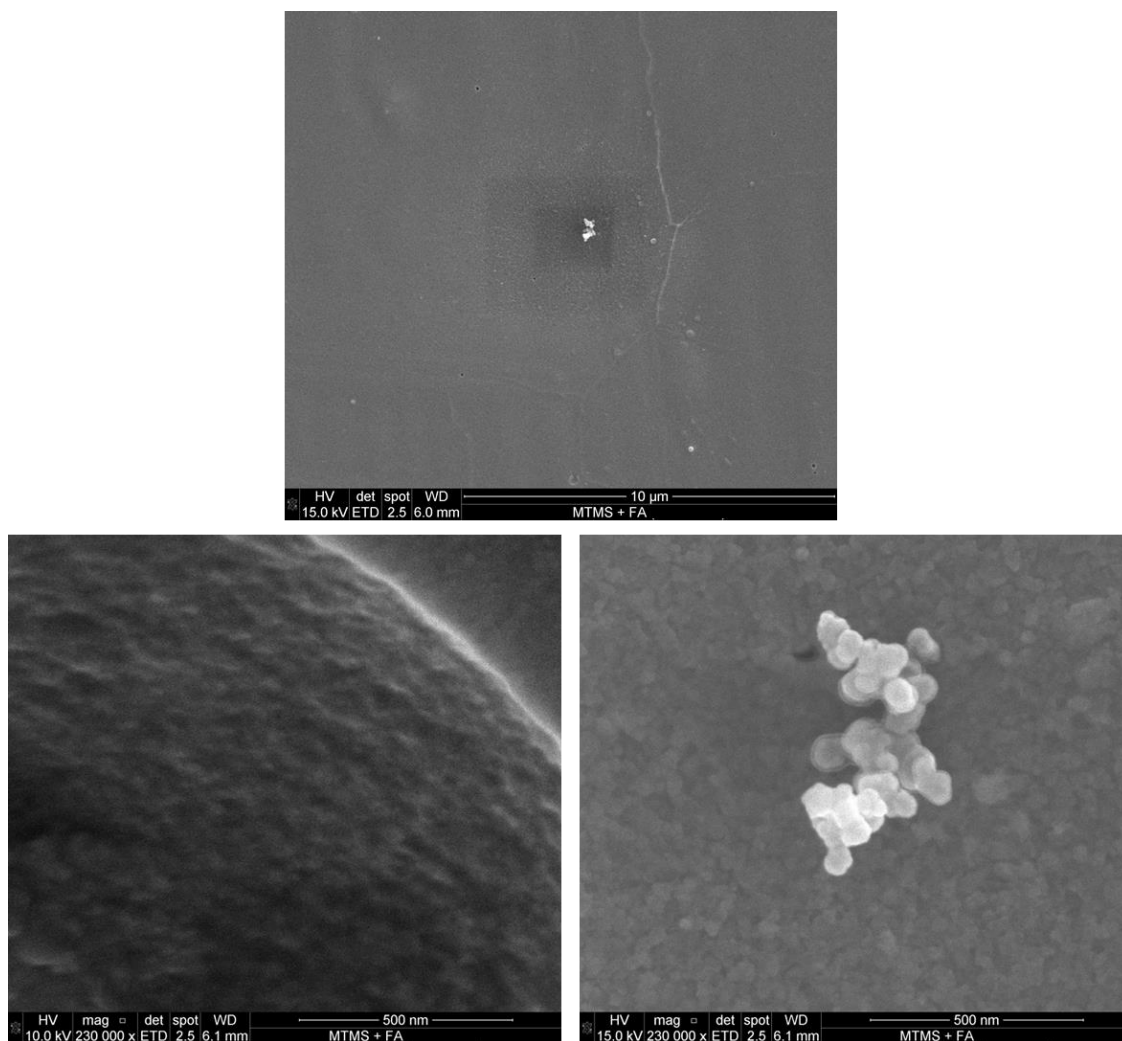
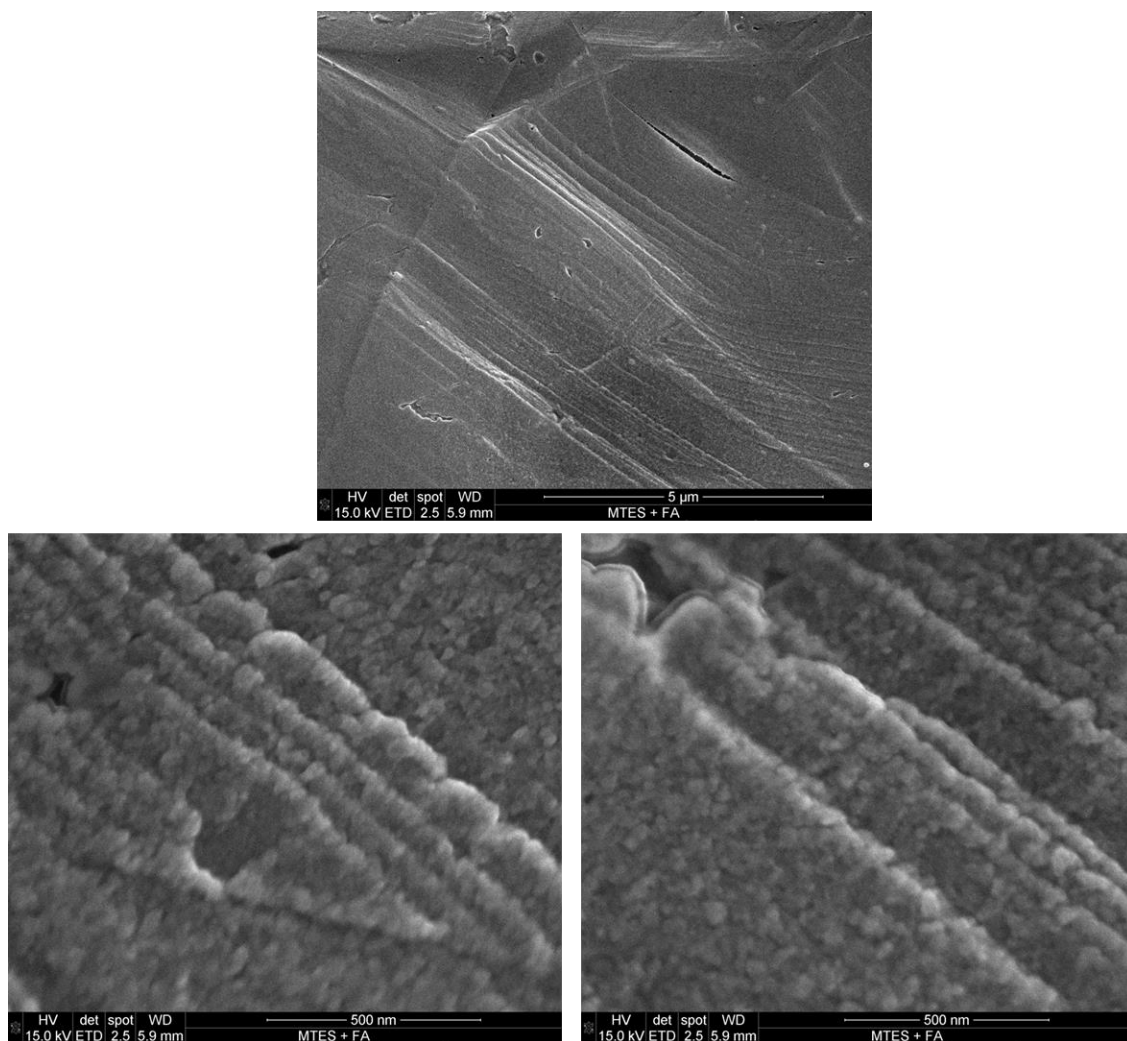


Figure 4.18 SEM images of MTMS-based xerogels after being dried at 110°C for 12 hours.



*Figure 4.19 SEM images of MTES-based xerogels after being dried at 110°C for 12 hours.*

## 4.5 Conclusions

Four different precursors (TMOS, TEOS, MTMS and MTES) have been selected to elucidate the effect of gradual modification in organic substitution of the precursor on the non-hydrolytic sol-gel process kinetics and the morphology of the resultant silica structure. Figure 4.20a provides a summary of the reactions involved in the formation of methanol/ethanol (ROH) and methyl/ethyl formate (ROCOH).

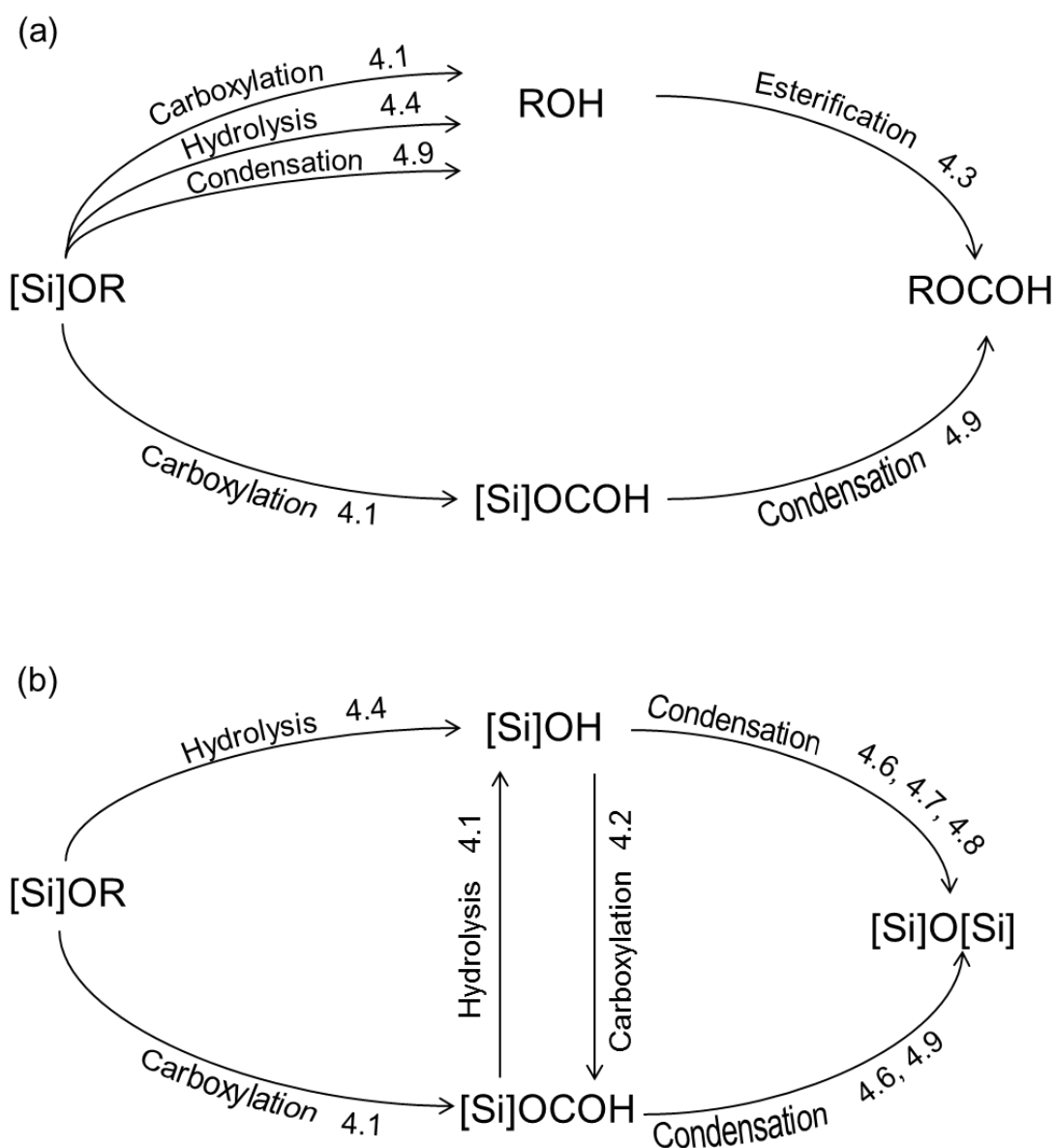


Figure 4.20 Summary of the reactions taking place in a non-hydrolytic sol-gel route based on the reactions listed by Sharp [20] (numbers represent the reaction number as listed in section 4.3.2). The illustration shows the reactions involved in the (a) formation of methanol/ethanol (ROH) and methyl/ethyl formate (ROCOH), (b) formation of  $[\text{Si}]\text{O}[\text{Si}]$ .

The *in situ* Raman analysis demonstrated that the rate of alkoxide ([Si]OR) consumption, has the following order amongst the precursors: MTMS~TMOS>MTES>TEOS. This was attributed to a number of reasons:

- a) At the early stages of being mixed with FA, TMOS and MTMS are consumed through reactions 4.1 and 4.4 while for MTES and TEOS, reaction 4.4 is less likely (TEOS and MTES are not as miscible in water as MTMS and TMOS).
- b) Due to steric hindrance effect, the methoxy-based precursors undergo protonic attack faster than their counterpart ethoxy-based precursors.
- c) Based on the utilised formulation, the precursor: FA ratio is not stoichiometrically satisfied in the carboxylation reaction (reaction (4.1)) for TMOS and TEOS precursors causing the carboxylation kinetics to be lower than MTMS and MTES mixtures.

Faster consumption of [Si]OR in TMOS and MTMS manifests into faster formation of methanol and methyl formate compared to ethanol and ethyl formate through the reactions shown in Figure 4.20a.

As can be seen from Figure 4.20b, rate of formation of the [Si]O[Si] bridges is dependent on the rate of the hydrolysis (4.4) and carboxylation (4.1) reactions. It was shown that the rate of gelation had the following order: TMOS>MTMS>TEOS>MTES. This trend was associated with the presence of methyl groups in the MTMS and MTES mixtures, which retards the formation of primary and secondary silica particles due to steric hindrance effect and delays their gelation with respect to the TMOS and TEOS, respectively.

The two precursors having the fastest hydrolysis and condensation processes were shown to be TMOS and MTMS in this work. Mixing various precursors together is often a way to improve mechanical properties and create unique structures appropriate for specific applications. Attention must be paid to the compatibility of the precursors as poor choice can result in heterogeneity in the gel (the more reactive precursor forms silica network in shorter time). Based on the reaction kinetics investigated in this work, TMOS and MTMS have shown to be the most compatible precursors amongst all four investigated precursors.

#### 4.6 References

- [1] M.A. Néouze, J. Le Bideau, P. Gaveau, S. Bellayer, A. Vioux, Ionogels, new materials arising from the confinement of ionic liquids within silica-derived networks, *Chem. Mater.* 18 (2006) 3931–3936. doi:10.1021/cm060656c.
- [2] N. Bengourna, F. Despetis, L. Bonnet, R. Courson, P. Solignac, H. Satha, N. Olivi-Tran, Textural, structural and electrical characterizations of EMIMAc silica ionogels and their corresponding aerogels, *Appl. Phys. Res.* 6 (2014) 16–25.
- [3] A. Martinelli, Effects of a protic ionic liquid on the reaction pathway during non-aqueous sol–gel synthesis of silica: A Raman spectroscopic investigation, *Int. J. Mol. Sci.* 15 (2014) 6488–6503. doi:10.3390/ijms15046488.
- [4] A.K. Gupta, Y.L. Verma, R.K. Singh, S. Chandra, Studies on an ionic liquid confined in silica nanopores: Change in  $T_g$  and evidence of organic-inorganic linkage at the pore wall surface, *J. Phys. Chem. C.* 118 (2014) 1530–1539. doi:10.1021/jp408142a.
- [5] M. Nayeri, M.T. Aronson, D. Bernin, B.F. Chmelka, A. Martinelli, Surface effects on the structure and mobility of the ionic liquid  $C_6C_1ImTFSI$  in silica gels, *Soft Matter.* 10 (2014) 5618–5627. doi:10.1039/C4SM00642A.
- [6] A.I. Horowitz, M.J. Panzer, High-performance, mechanically compliant silica-based ionogels for electrical energy storage applications, *J. Mater. Chem.* 22 (2012) 16534–16539. doi:10.1039/C2JM33496H.
- [7] A. Taubert, R. Löbbicke, B. Kirchner, F. Leroux, First examples of organosilica-based ionogels: synthesis and electrochemical behavior, *Beilstein J. Nanotechnol.* 8 (2017) 736–751. doi:10.3762/bjnano.8.77.
- [8] A.I. Horowitz, K. Westerman, M.J. Panzer, Formulation influence on the sol-gel formation of silica-supported ionogels, *J. Sol-Gel Sci. Technol.* 78 (2016) 34–39. doi:10.1007/s10971-015-3918-7.

- [9] C.A.M. Mulder, A.A.J.M. Damen, Raman analysis of the initial stages of the hydrolysis and polymerization of tetraethylorthosilicate, *J. Non. Cryst. Solids*. 93 (1987) 169–178. doi:10.1016/S0022-3093(87)80036-4.
- [10] Y.T. Lee, H.H. Jen, A Raman study of the effect of formamide on the tetramethoxysilane sol–gel process, *J. Non. Cryst. Solids*. 342 (2004) 39–45. doi:10.1016/J.JNONCRY SOL.2004.07.009.
- [11] I.-G. Marino, P.P. Lottici, D. Bersani, R. Raschellà, A. Lorenzi, A. Montenero, Micro-Raman monitoring of solvent-free TEOS hydrolysis, *J. Non. Cryst. Solids*. 351 (2005) 495–498. doi:10.1016/J.JNONCRY SOL.2004.11.023.
- [12] A. Martinelli, L. Nordstierna, An investigation of the sol-gel process in ionic liquid-silica gels by time resolved Raman and <sup>1</sup>H NMR spectroscopy, *Phys. Chem. Chem. Phys.* 14 (2012) 13216–13223. doi:10.1039/C2CP41914A.
- [13] M. Nayeri, K. Nygård, M. Karlsson, M. Maréchal, M. Burghammer, M. Reynolds, A. Martinelli, The role of the ionic liquid C<sub>6</sub>C<sub>1</sub>ImTFSI in the sol–gel synthesis of silica studied using in situ SAXS and Raman spectroscopy, *Phys. Chem. Chem. Phys.* 17 (2015) 9841–9848. doi:10.1039/C5CP00709G.
- [14] K. Kanamori, K. Nakanishi, Controlled pore formation in organotrialkoxysilane-derived hybrids: From aerogels to hierarchically porous monoliths, *Chem. Soc. Rev.* 40 (2011) 754–770. doi:10.1039/C0CS00068J.
- [15] A. Baatti, F. Erchiqui, P. Bébin, F. Godard, D. Bussièrès, A two-step sol-gel method to synthesize a ladder polymethylsilsesquioxane nanoparticles, *Adv. Powder Technol.* 28 (2017) 1038–1046. doi:10.1016/j.ap t.2017.01.009.
- [16] P. Larkin, Chapter 2 – Basic Principles, in: *Infrared Raman Spectrosc.*, 2011: pp. 7–25. doi:10.1016/B978-0-12-386984-5.10002-3.

- [17] H.-P. Feng, C.-H. Hsu, J.-K. Lu, Y.-H. Shy, Effects of PVD sputtered coatings on the corrosion resistance of AISI 304 stainless steel, *Mater. Sci. Eng. A.* 347 (2003) 123–129. doi:10.1016/S0921-5093(02)00578-6.
- [18] M. Esteves, A. Ramalho, F. Ramos, Fretting behavior of the AISI 304 stainless steel under different atmosphere environments, *Tribol. Int.* 88 (2015) 56–65. doi:10.1016/J.TRIBOINT.2015.02.016.
- [19] A. Janković, S. Eraković, M. Mitrić, I.Z. Matić, Z.D. Juranić, G.C.P. Tsui, C. Tang, V. Mišković-Stanković, K.Y. Rhee, S.J. Park, Bioactive hydroxyapatite/graphene composite coating and its corrosion stability in simulated body fluid, *J. Alloys Compd.* 624 (2015) 148–157. doi:10.1016/J.JALLCOM.2014.11.078.
- [20] K.G. Sharp, A two-component, non-aqueous route to silica gel, *Sol-Gel Sci. Technol.* 2 (1994) 35–41.
- [21] C.J. Brinker, Hydrolysis and condensation of silicates: Effects on structure, *J. Non. Cryst. Solids.* 100 (1988) 31–50. doi:10.1016/0022-3093(88)90005-1.
- [22] G.H. Bogush, C.F. Zukoski IV, Studies of the kinetics of the precipitation of uniform silica particles through the hydrolysis and condensation of silicon alkoxides, *J. Colloid Interface Sci.* 142 (1991) 1–18. doi:10.1016/0021-9797(91)90029-8.
- [23] R. Winter, J. Chan, R. Frattini, J. Jonas, The effect of fluoride on the sol-gel process, *J. Non. Cryst. Solids.* 105 (1988) 214–222.
- [24] J.L. Lippert, S.B. Melpolder, L.M. Kelts, Raman spectroscopic determination of the pH dependence of intermediates in sol-gel silicate formation, *J. Non. Cryst. Solids.* 104 (1988) 139–147. doi:10.1016/0022-3093(88)90193-7.
- [25] J.-C. Panitz, A. Wokaun, Characterization of the sol-gel process using Raman spectroscopy organically modified silica gels prepared via the formic acid-alkoxide route, *J. Sol-Gel Sci. Technol.* 9 (1997) 251–263. doi:10.1007/BF02437188.

- [26] J. Gnado, P. Dhamelincourt, C. Pélégri, M. Traisnel, A. Le Maguer Mayot, Raman spectra of oligomeric species obtained by tetraethoxysilane hydrolysis-polycondensation process, *J. Non. Cryst. Solids*. 208 (1996) 247–258. doi:10.1016/S0022-3093(96)00526-1.
- [27] G. Wheeler, Alkoxysilanes and the consolidation of stone, C. Hudson, 2005. doi:10.1007/s13398-014-0173-7.2.
- [28] J. Livage, M. Henry, Ultrastructure processing of advanced ceramics, John Wiley and Sons, New York (US), 1988. <https://www.osti.gov/servlets/purl/7250006>.
- [29] B. Tan, S.E. Rankin, Study of the effects of progressive changes in alkoxysilane structure on sol-gel reactivity, *J. Phys. Chem. B*. 110 (2006) 22353–22364. doi:10.1021/jp060376k.
- [30] P. Moilanen, P. Uusi-Kyyny, J.-P. Pokki, M. Pakkanen, J. Aittamaa, Vapor-liquid equilibrium for butane + methanol, + ethanol, + 2-propanol, + 2-butanol, and + 2-methyl-2-propanol (TBA) at 323 K, *J. Chem. Eng. Data*. 53 (2008) 83–88. doi:10.1021/je7003947.
- [31] Methyl formate (107-31-3) Raman, *Chem. B.* (2016). [https://www.chemicalbook.com/SpectrumEN\\_107-31-3\\_Raman.htm](https://www.chemicalbook.com/SpectrumEN_107-31-3_Raman.htm) (accessed May 24, 2018).
- [32] Ethyl formate (109-94-4) Raman related products, *Chem. B.* (2016). [https://www.chemicalbook.com/SpectrumEN\\_109-94-4\\_Raman.htm](https://www.chemicalbook.com/SpectrumEN_109-94-4_Raman.htm) (accessed May 24, 2018).
- [33] G. Zhang, A. Dass, A.-M.M. Rawashdeh, J. Thomas, J.A. Counsil, C. Sotiriou-Leventis, E.F. Fabrizio, F. Ilhan, P. Vassilaras, D.A. Scheiman, L. McCorkle, A. Palczer, J.C. Johnston, M.A. Meador, N. Leventis, Isocyanate-crosslinked silica aerogel monoliths: preparation and characterization, *J. Non. Cryst. Solids*. 350 (2004) 152–164. doi:10.1016/J.JNONCRY SOL.2004.06.041.
- [34] C.J. Brinker, G.W. Scherer, Sol-gel science: The physics and chemistry of sol-gel processing, 1990. doi:10.1186/1471-2105-8-444.

- [35] A.A. Pisal, A.V. Rao, Comparative studies on the physical properties of TEOS, TMOS and Na<sub>2</sub>SiO<sub>3</sub> based silica aerogels by ambient pressure drying method, *J. Porous Mater.* 23 (2016) 1547–1556. doi:10.1007/s10934-016-0215-y.
- [36] H. Maleki, L. Durães, A. Portugal, An overview on silica aerogels synthesis and different mechanical reinforcing strategies, *J. Non. Cryst. Solids.* (2014). doi:10.1016/j.jnoncrysol.2013.10.017.
- [37] J.P. Harrison, J.A. Hudson, J.P. Harrison, J.A. Hudson, 9 – Permeability, in: *Eng. Rock Mech. Part II*, 2000: pp. 141–158. doi:10.1016/B978-008043010-2/50010-1.
- [38] Y. Zhang, C. Zhao, P. Wang, L. Ye, J. Luo, B. Jiang, A convenient sol–gel approach to the preparation of nano-porous silica coatings with very low refractive indices, *Chem. Commun.* 50 (2014) 13813–13816. doi:10.1039/C4CC05397D.

## **5. Comparative studies of the gelation kinetics and the physical and electrochemical properties of TEOS, TMOS, MTMS and MTES based ionogels synthesised through a non-hydrolytic sol-gel route**

### **5.1 Introduction**

As indicated in Chapter 4, one of the aims of this thesis is to answer two key questions in the field of sol-gel synthesised ionogel electrolytes: (1) Can the alkoxide precursor influence the properties and performance of ionogels and (2) If so, how? The previous chapter provided insights about the sol-gel process kinetics for the four different precursors, and the microstructure of each xerogel. This chapter aims to:

1. Provide a comparison between TMOS, TEOS, MTMS and MTES-based ionogels as solid skeleton encapsulating 1-ethyl-3-methylimidazolium trifluoromethanesulfonate ionic liquid in terms of sol-gel process kinetics, microstructure and thermal stability.
2. Evaluate the presence and the strength of interactions between the ionic liquid and pore walls of the confining silica matrix and provide a comparison between the four ionogels. This is of a crucial importance for applications where ionic mobility can be jeopardised.
3. Examine the electrochemical performance of each ionogel as the electrolyte for activated carbon-based EDLCs.

To achieve these goals, a series of characterisation techniques, including Raman spectroscopy, TGA, SEM, EDX and a combination of electrochemical analysis tools (CV and EIS) were utilised to provide an understanding of each system.

### **5.2 Materials**

The choice of ionic liquid was made based on the fulfilment of certain criteria. A suitable ionic liquid electrolyte for supercapacitors must possess a wide potential window, high thermal stability, low viscosity, high ionic conductivity at room temperature and low cost. Generally, imidazolium and pyrrolidinium-based ionic

liquids are most commonly employed for supercapacitors [1–4]. The general structures of these cations are provided in Figure 5.1.

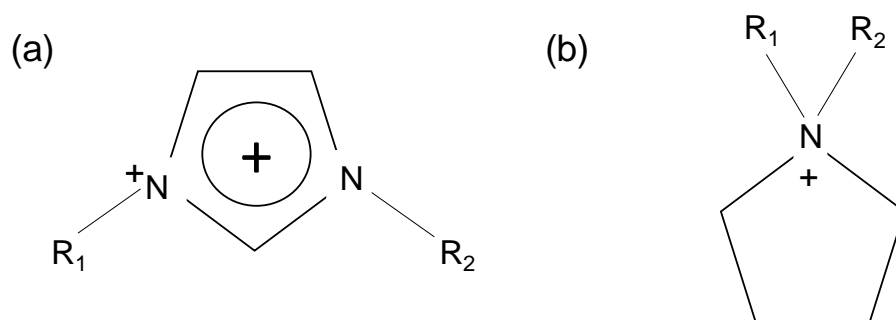


Figure 5.1 General molecular structure of (a) imidazolium and (b) pyrrolidinium cations.

Neat imidazolium-based ionic liquids have been shown to have higher ionic conductivity compared to their equivalent pyrrolidinium-based ionic liquid [1]. This observation was attributed to the planar molecular structure of the imidazolium cations whereas presence of substituents below or above the pyrrolidinium plane restricts the ion mobility of these types of ionic liquids. Similarly, having smaller substituent groups (e.g. H, CH<sub>3</sub>, C<sub>2</sub>H<sub>5</sub>) attached to the imidazolium cation ring is generally preferred as longer chains can hinder ionic mobility. In addition, ionic conductivity of ionic liquids containing imidazolium cations have been shown to be more stable compared to pyrrolidinium-based ionic liquids [1,4] due to the stable aromatic structure of the imidazolium ring.

Chloride [Cl], tetrafluoroborate [BF<sub>4</sub>], hexafluorophosphate [PF<sub>6</sub>], bis(trifluoromethylsulfonyl)imide [TFSI] and trifluoromethanesulfonate [TfO] are examples of some common ionic liquid anions for energy storage applications. Eftekhari attributed this popularity in the field of electrochemistry to their 'acceptable' viscosity and ionic conductivity at room temperature when combined with certain imidazolium and pyrrolidinium cations [4]. Disappointingly, the vague nature of the term 'acceptable' was not clarified. In this investigation, choosing an anion with a single conformer (and reasonable pricing) was favourable to reduce the complexity of *in situ* investigation using Raman spectroscopy.

Based on these requirements, 1-ethyl-3-methylimidazolium trifluoromethanesulfonate was chosen as the ionic liquid for the entire project and its molecular structure is shown in Figure 5.2. This ionic liquid which is also referred to as 1-

ethyl-3-methylimidazolium triflate has a variety of abbreviations in the literature: (a) [Emim][TfO], (b) [Emim][OTf], (c) [C<sub>6</sub>H<sub>11</sub>N<sub>2</sub>][OTf], (d) [C<sub>2</sub>MIm][TfO], and (e) EMITf. This ionic liquid has a conductivity of 8.6 mS cm<sup>-1</sup> (at room temperature) and a potential window of 4.3 V (manufacturer specification) [5]. At room temperature an average viscosity of 44 mPa s has been reported for this ionic liquid [6]. A pH of 6.6±0.1 has recently been reported for pristine [Emim][TfO] ionic liquid [7]. The molecular dimensions (length x width x height) of [Emim] and [TfO] ions are 7.8 x 5.8 x 3.3 Å and 4.4 x 4.4 x 3.3 Å, respectively [8].

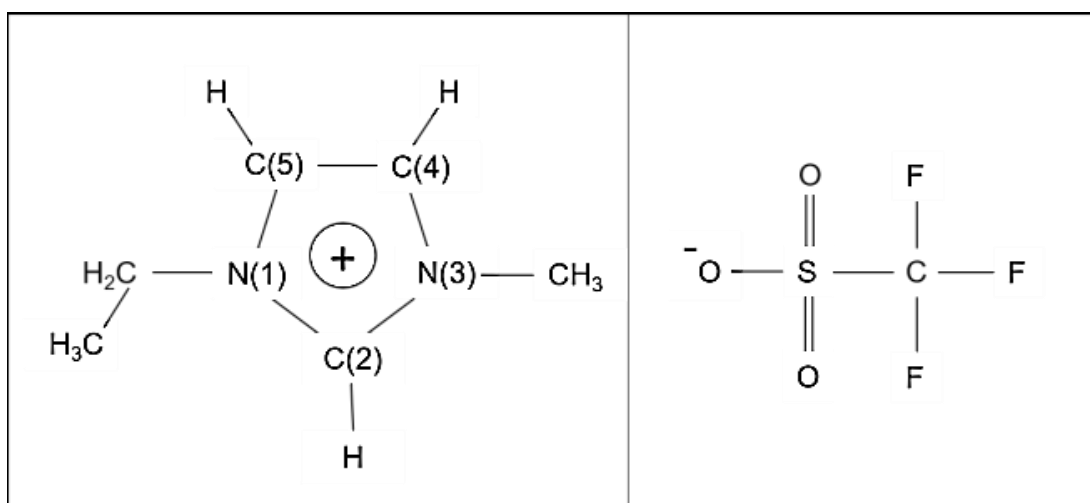


Figure 5.2 Molecular structure of 1-ethyl-3-methylimidazolium cation (left) and trifluoromethanesulfonate anion (right).

The four different ionogels were synthesised using the non-hydrolytic sol-gel route described in Chapter 4. Each precursor (as listed in Table 5.1) was used as received.

Table 5.1 Detailed summary of the chemicals utilised for the silica ionogels preparation.

	Material	Supplier	%Purity	Volume utilised
1	TMOS	Sigma Aldrich	≥98%	296 µL
2	TEOS	Sigma Aldrich	≥99%	446 µL
3	MTMS	Sigma Aldrich	≥98%	286 µL
4	MTES	Sigma Aldrich	≥99%	398 µL
5	FA	Aldrich	≥96%	264 µL
6	[Emim][TfO] ionic liquid	Sigma Aldrich	≥98% (≤0.1% water)	400 µL

### 5.3 *In situ* reaction monitoring

#### 5.3.1 Experimental procedure

Each ionogel was prepared by mixing the specified volume of silica precursor in Table 5.1 with 400  $\mu\text{L}$  [Emim][TfO] ionic liquid in a glass vial for 10 minutes at 600 rpm using a magnetic stir bar. After this mixing stage, 398  $\mu\text{L}$  of FA was added to the mixture and was allowed 3 minutes to react with the silica precursor. The precursor: ionic liquid: FA molar ratio was kept constant at 2:2:7 for all samples. In order to monitor the chemical processes taking place in each ionogel formulation, a Raman spectrum of each mixture was collected at regular intervals similar to the process described in Chapter 4 section 4.3.1. The first spectrum was collected after 3 minutes of mixing the precursor, ionic liquid and FA. To do so, 500  $\mu\text{L}$  of the mixture was transferred into a 304 stainless steel container using a pipette. The subsequent spectra were collected at 10 minutes intervals for the first 2 hours and then after 6 and 12 hours of the experiment. The kinetics of the hydrolysis reaction for each precursor was then determined based on the evolution of peak height at selected wavenumbers. The justification for the peak selection is discussed briefly in the following section (5.3.2).

#### 5.3.2 Results and discussion

As a primary step, Raman spectrum of the 'as-received' ionic liquid (500  $\mu\text{L}$  inside a 304 stainless steel container) was collected. The collected spectrum is displayed in Figure 5.3. Due to presence of a key ionic liquid vibrational band ( $\nu_s(\text{CS})$ ) located at  $313\text{ cm}^{-1}$ , the Raman spectra of samples were collected between  $300\text{-}3200\text{ cm}^{-1}$  as opposed to  $400\text{-}3200\text{ cm}^{-1}$  in xerogels discussed in Chapter 4. Raman spectroscopic investigations of 1-Ethyl-3-methylimidazolium trifluoromethane-sulfonate have been reported in the past. For example, Liu et al. investigated the interaction between water and [Emim][TfO] ionic liquid using Raman and Fourier transform infrared spectroscopy [9]. They conducted this investigation by increasing the water/ionic liquid volume ratio from 0 to 80%. Singh et al. studied the molecular structure and the cation-anion interactions in [Emim][TfO] using quantum chemical calculations and vibrational spectroscopic characterisations [10]. They achieved good agreement between the theoretical and experimental results. Based on the mentioned reports and the experimental results achieved in the present work, the assignments corresponding to charac-

teristic peaks of the ionic liquid have been realised and the summary of the key peak assignments are provided in Table 5.2.

From the lowest wavenumber, the vibrational bands at 313 and 348  $\text{cm}^{-1}$  correspond to symmetric stretching vibrations of the C–S bond and the rocking mode of  $\text{SO}_3$  of the anion [9]. Bands at 573, 756 and 597  $\text{cm}^{-1}$  are associated with the antisymmetric and symmetric deformation vibrations of  $\text{CF}_3$  and the oscillating vibrations of SO in the [TfO] anion, respectively [9,10].

The strong band at 1033  $\text{cm}^{-1}$  is assigned to the symmetric stretching of S–O while its corresponding antisymmetric vibrational band is located at 1257  $\text{cm}^{-1}$  [9,10]. The bands at 1169 and 1227  $\text{cm}^{-1}$  correspond to the antisymmetric and symmetric stretching vibrations of C–F bonds in the anion, respectively [9]. The bands in the 1300-1600  $\text{cm}^{-1}$  region are attributed to various vibrations within the imidazolium cation which are listed in Table 5.2 [10]. The 2700-3050  $\text{cm}^{-1}$  and 3050-3200  $\text{cm}^{-1}$  regions are associated with the C–H stretching modes of alkyl chains (methyl and ethyl groups) and the C–H bonds within the ring (C(2)H, C(4)H, C(5)H) of the imidazolium cation [9,10].

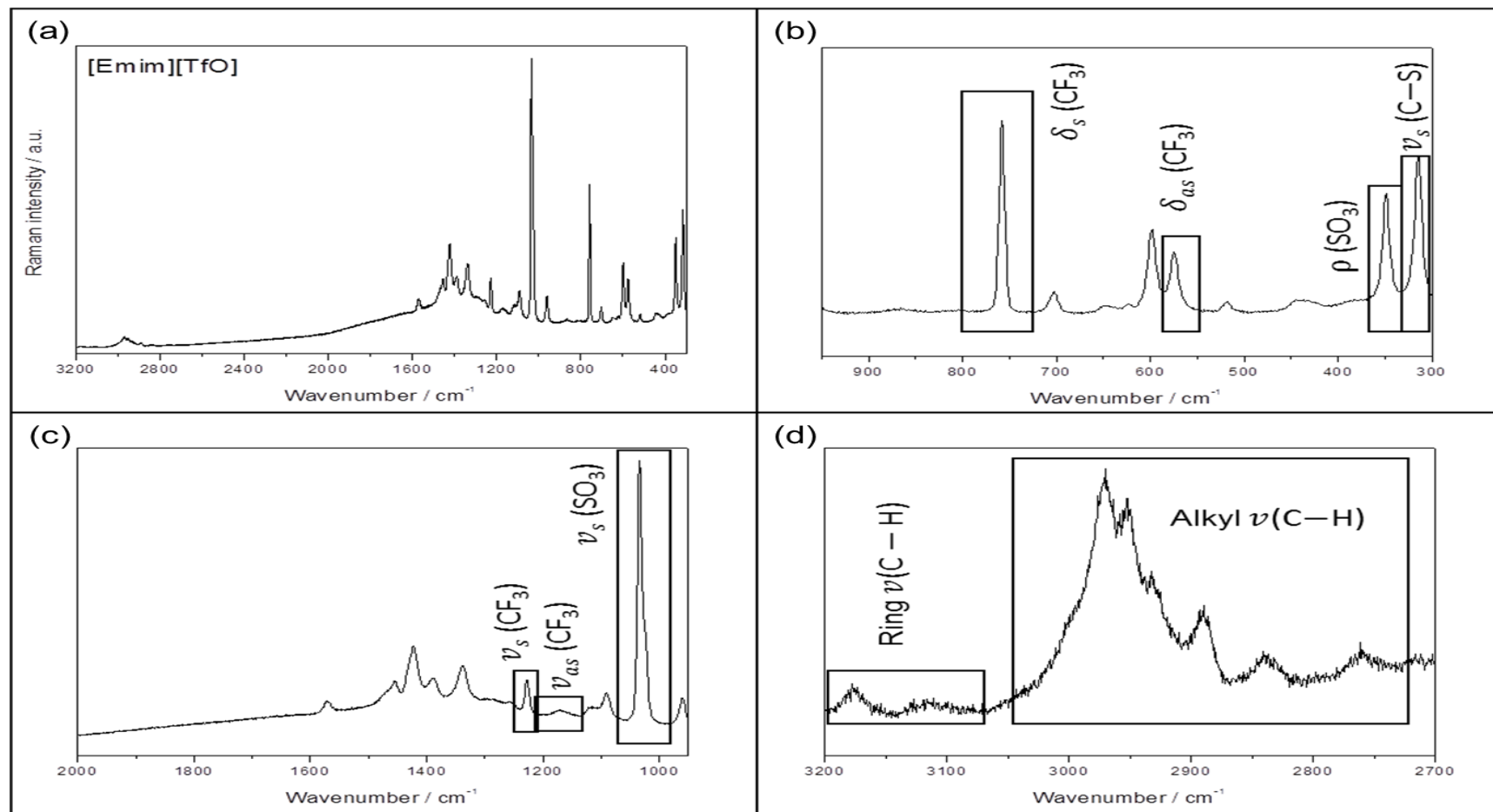


Figure 5.3 Raman spectrum of [Emim][TfO] ionic liquid in the (a) 300-3200  $\text{cm}^{-1}$ , (b) 300-950  $\text{cm}^{-1}$ , (c) 950-2000  $\text{cm}^{-1}$ , and (d) 2700-3200  $\text{cm}^{-1}$  regions. Some of the key vibrational bands of the ionic liquid cation and anion are highlighted (exact locations of the highlighted bands can be found in Table 5.2) [9,10].

Table 5.2 Summary of selected vibrational modes of [Emim][TfO] and their corresponding assignments based on the results of the current investigation and the referenced works.

Wavenumber in this work / cm <sup>-1</sup>	Wavenumber in other works / cm <sup>-1</sup>	Assignment
313	315 [9]	$\nu_s(\text{CS})$
348	350 [9]	$\rho(\text{SO}_3)$
573	573 [9]	$\delta_{as}(\text{CF}_3)$
597	600 [10]	$\delta(\text{SO})$
756	757 [9]	$\delta_s(\text{CF}_3)$
960	960 [10]	$\omega(\text{NC}(2)\text{H})$
1033	1034 [9], 1033 [10]	$\nu_s(\text{SO}_3)$
1169	1173 [9]	$\nu_{as}(\text{CF}_3)$
1227	1230 [9]	$\nu_s(\text{CF}_3)$
1257	1260 [9]	$\nu_{as}(\text{SO}_3)$
1338	1337 [10]	$\rho(\text{NCH}), \tau(\text{HC}(7)\text{H})$
1423	1424 [10]	$\nu(\text{C}(5)\text{N}), \delta(\text{HC}(6)\text{H})$
1570	1570 [10]	$\nu(\text{C}(2)\text{N}), \nu(\text{C}=\text{C}),$ $\rho(\text{C}(2,4)\text{H})$
2768	2770 [10]	$\nu_s(\text{CH}_3)$
2889 & 2839	2890 & 2837 [10]	$\nu_s(\text{C}_2\text{H}_5)$
2931	2930 [10]	$\nu_{as}(\text{C}_2\text{H}_5)$
2971 & 2952	2971 & 2951 [10]	$\nu_{as}(\text{CH}_3)$
3118	3117 [9], 3116 [10]	$\nu_s(\text{C}(2)\text{H})$
3177	3157 [9], 3171 [10]	$\nu_s(\text{C}(4,5)\text{H})$

Figures 5.4 to 5.7 show the evolving Raman spectra during reaction for all four formulations within the first ~12 hours of mixing the reactants. The arrows demonstrate the direction of time. Similar to xerogels, an ionogel was considered fully gelled (i.e. reached sol-gel transition point) when no flowing behaviour was observed upon agitation (using a spatula). Under ambient conditions, TMOS- and TEOS-based ionogels reach sol-gel transition point after 12 hours of synthesis while it takes 4 days for full gelation to be achieved for MTMS- and MTES-based ionogels. Therefore, the reactions taking place inside all four mix-

tures were followed for the first 12 hours of the synthesis. As mentioned before in Chapter 4, section 4.3.2, Sharp [11] who introduced the non-hydrolytic sol-gel route for the first time, summarised the chemical process taking place between an alkoxide and FA in 9 reactions. The overall reactions can be summarised as follows:



where R, ROH and ROCO groups represent alkyl, alcohol and alkyl formate groups, respectively. As the reaction proceeds the intensity of the strong band at  $642 \text{ cm}^{-1}$  (symmetric stretching vibration of Si–OCH<sub>3</sub>), which corresponds to the consumption of TMOS, is reduced quickly (Figure 5.4). As mentioned previously, this precursor contains four –OCH<sub>3</sub> branches on each molecule and the breaking of one or more of these bonds, results in a reduction of the corresponding Raman peak intensity. The peak variations in the  $650\text{--}690 \text{ cm}^{-1}$  region are mainly attributed to the vibrations of Si–OCH<sub>3</sub> bonds in partially hydrolysed TMOS [12] and consumption of the FA ( $\delta(\text{O}=\text{C}=\text{O})$  at  $676 \text{ cm}^{-1}$ ) [13]. The vibrations in the  $780\text{--}880 \text{ cm}^{-1}$  region correspond to a combination of antisymmetric stretching vibrations of Si–OCH<sub>3</sub> in TMOS and the Si–O vibrations of the intermediate species [14–16].

Based on the spectrum of 'as-received' [Emim][TfO] ionic liquid (Figure 5.3) and that of TMOS-based ionogel, one can conclude that ionic liquid does not participate in the sol-gel process. However, Raman signals from ionic liquid dominate and interfere with the silica-related bands to some extent. As shown in Chapter 4, unequivocal signatures of methyl formate and methanol are located at  $910 \text{ cm}^{-1}$  ( $\nu(\text{O}-\text{CH}_3)$ ) and  $1018 \text{ cm}^{-1}$  ( $\nu(\text{C}-\text{O})$ ), respectively [13,16] which are the volatile by-products of sol-gel processes. However, these bands are relatively weak to begin with and in the case of ionogels, they cannot be detected. Similarly, the band associated with deformation of the Si–O–Si bonds located at  $490 \text{ cm}^{-1}$  [13,16], cannot be detected in the Raman spectra of TMOS-based ionogel. These can be associated with a combination of low signal/noise ratio and/or

change in the symmetry of the Si–O bonds within the structure of this ionogel due to interactions with ionic liquid. The latter is discussed in section 5.3.3. Depletion of various Raman peaks in the 1350-1450  $\text{cm}^{-1}$  and 1600-1800  $\text{cm}^{-1}$  regions are partially related to the consumption of FA as a result of carboxylation and esterification reactions [13,16,17]. In addition, the bending vibrations of  $\text{CH}_3$  bonds present in methyl formate contribute to the Raman peaks in the 1440-1470  $\text{cm}^{-1}$  region [16]. Finally, the intensity of the band at 2855  $\text{cm}^{-1}$  is reduced gradually over the duration of the experiment. This band is mainly associated with C–H stretching modes of  $\text{CH}_3$  in TMOS. However, as shown in Chapter 4, C–H stretching vibrations of methyl formate and (in this case) imidazolium cation contribute to the intensity of this band.

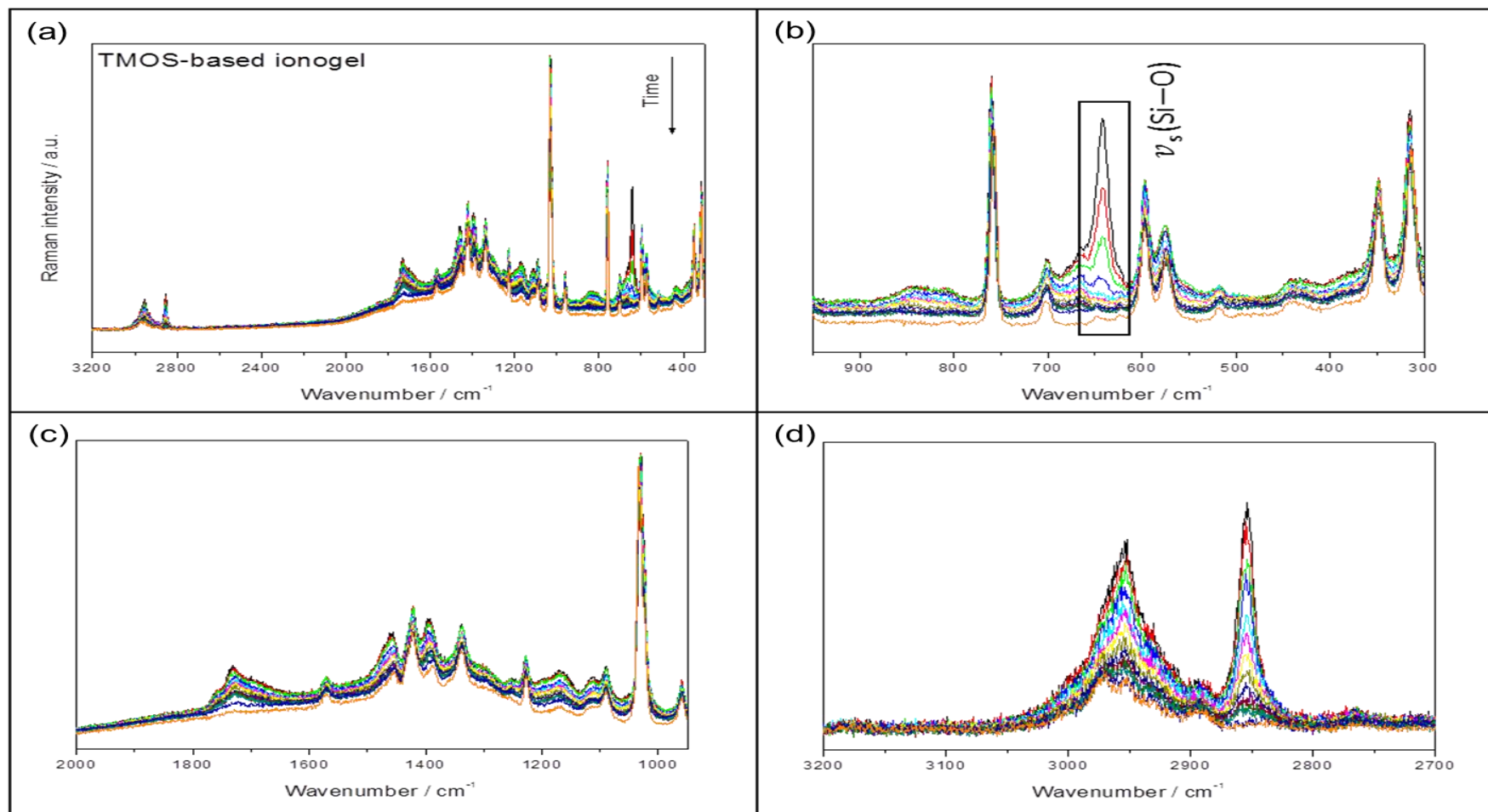


Figure 5.4 Raman spectra evolution with time of TMOS-based ionogel over 12 hours in the in the (a) 300-3200  $\text{cm}^{-1}$ , (b) 300-950  $\text{cm}^{-1}$ , (c) 950-2000  $\text{cm}^{-1}$ , and (d) 2700-3200  $\text{cm}^{-1}$  regions. Kinetics of peak height variation of the highlighted band is discussed later in this section and its evolution with time can be found in Figure 5.8.

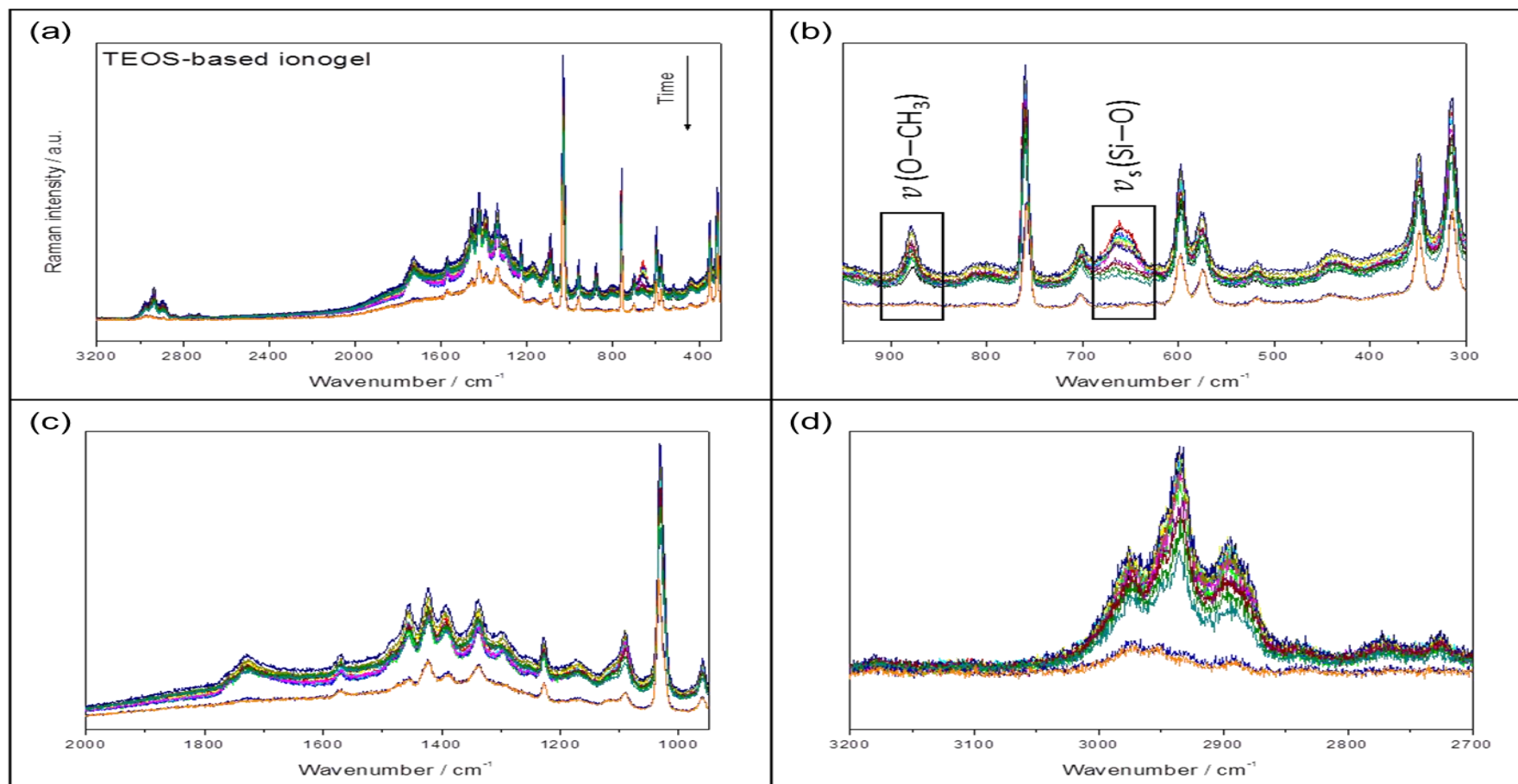


Figure 5.5 Raman spectra evolution with time of TEOS-based ionogel over 12 hours in the (a) 300-3200  $\text{cm}^{-1}$ , (b) 300-950  $\text{cm}^{-1}$ , (c) 950-2000  $\text{cm}^{-1}$ , and (d) 2700-3200  $\text{cm}^{-1}$  regions. Kinetics of peak height variations of the highlighted bands are discussed later in this section. The time evolution of the intensity of  $\nu_s(\text{Si-O})$  and  $\nu(\text{O-CH}_3)$  bands can be found in Figures 5.8 and 5.9, respectively.

Figure 5.5 represents the evolution of the TEOS-based ionogel mixture with time shortly after being mixed with FA. The most substantial change is observed in 600-670  $\text{cm}^{-1}$  region of the spectrum. The unequivocal signature of TEOS located at 662  $\text{cm}^{-1}$  disappeared within the first 2 hours of the experiment at a reduced rate compared to that of TMOS-based ionogel (Figure 5.4). Similar to TMOS ionogel, the band associated with the deformation vibrations of Si–O–Si bond is not detectable in the Raman spectrum of this ionogel even after 12 hours. Once again this could be attributed to low signal/noise ratio and/or change in the symmetry of this bond within the structure of the ionogel resulting in the bond becoming Raman inactive.

The bands located at 801 and 933  $\text{cm}^{-1}$  which correspond to antisymmetric stretching of Si–O and symmetric stretching vibration of C–C in TEOS, respectively [14] gradually disappear from the Raman spectra as the precursor is consumed. Due to low signal/noise ratio the unequivocal signature of ethyl formate ( $\nu(\text{C–O})$ ) located at 841  $\text{cm}^{-1}$  cannot be detected [18,19]. The C–O stretching vibrations assigned to ethanol at 877  $\text{cm}^{-1}$  depletes within the first 2 hours of the experiment and cannot be detected after 6 hours of the experiment which suggests that the majority of alcohol within the structure has either been consumed and/or evaporated. Variations of peaks in the 1000-1800  $\text{cm}^{-1}$  are partly attributed to the consumption of FA via carboxylation and esterification reactions and the formation of ethyl formate. Lastly, the strong C–H stretch band located at 2935  $\text{cm}^{-1}$  drops in intensity over time. This band mainly corresponds to TEOS but the alkyl groups in the imidazolium ring contribute to the intensity of this band.

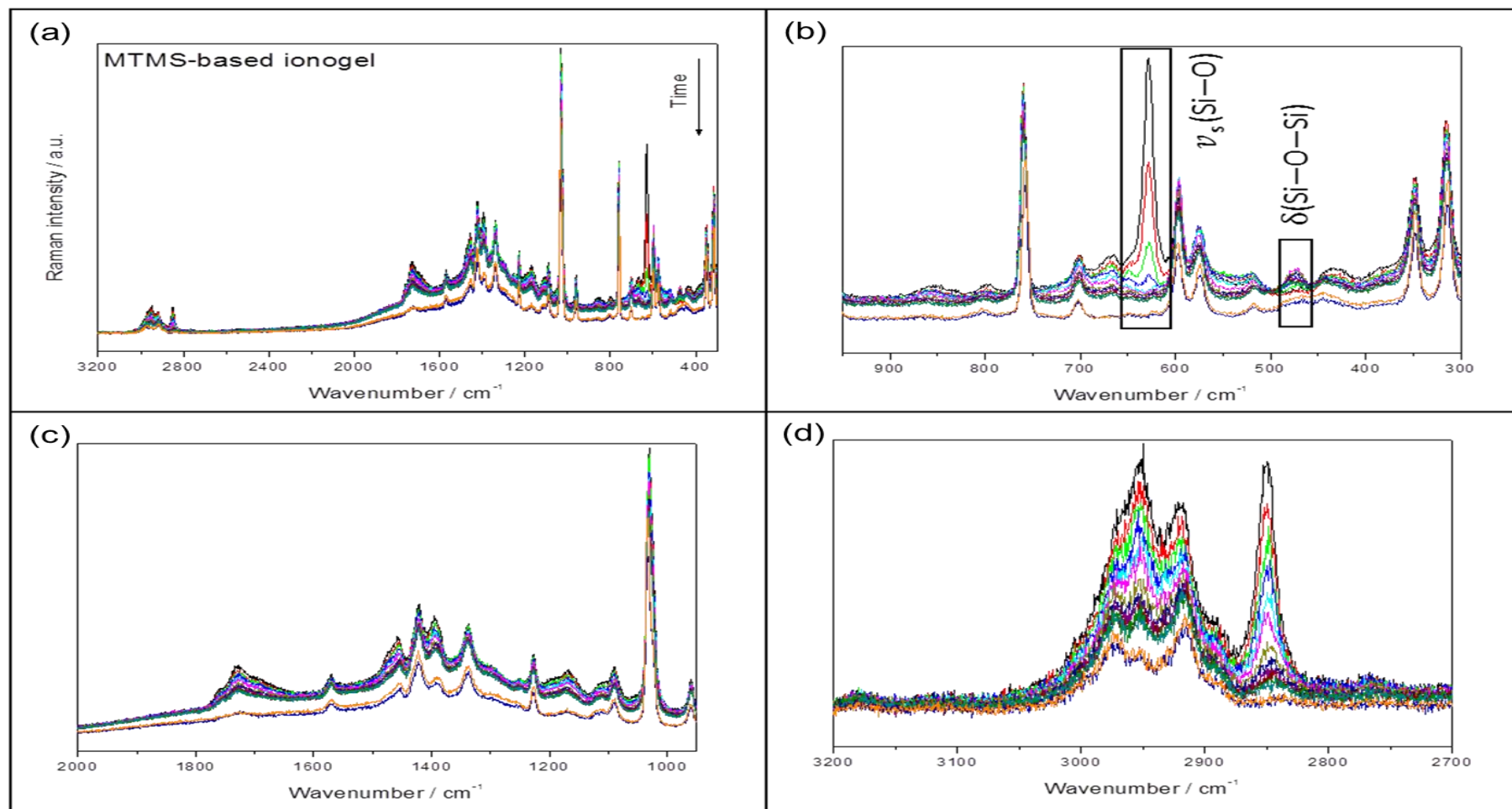


Figure 5.6 Raman spectra evolution with time of MTMS-based ionogel over 12 hours in the (a) 300-3200 cm<sup>-1</sup>, (b) 300-950 cm<sup>-1</sup>, (c) 950-2000 cm<sup>-1</sup>, and (d) 2700-3200 cm<sup>-1</sup> regions. The evolution of the intensity of  $\nu_s(\text{Si-O})$  band with time can be found in Figure 5.8.

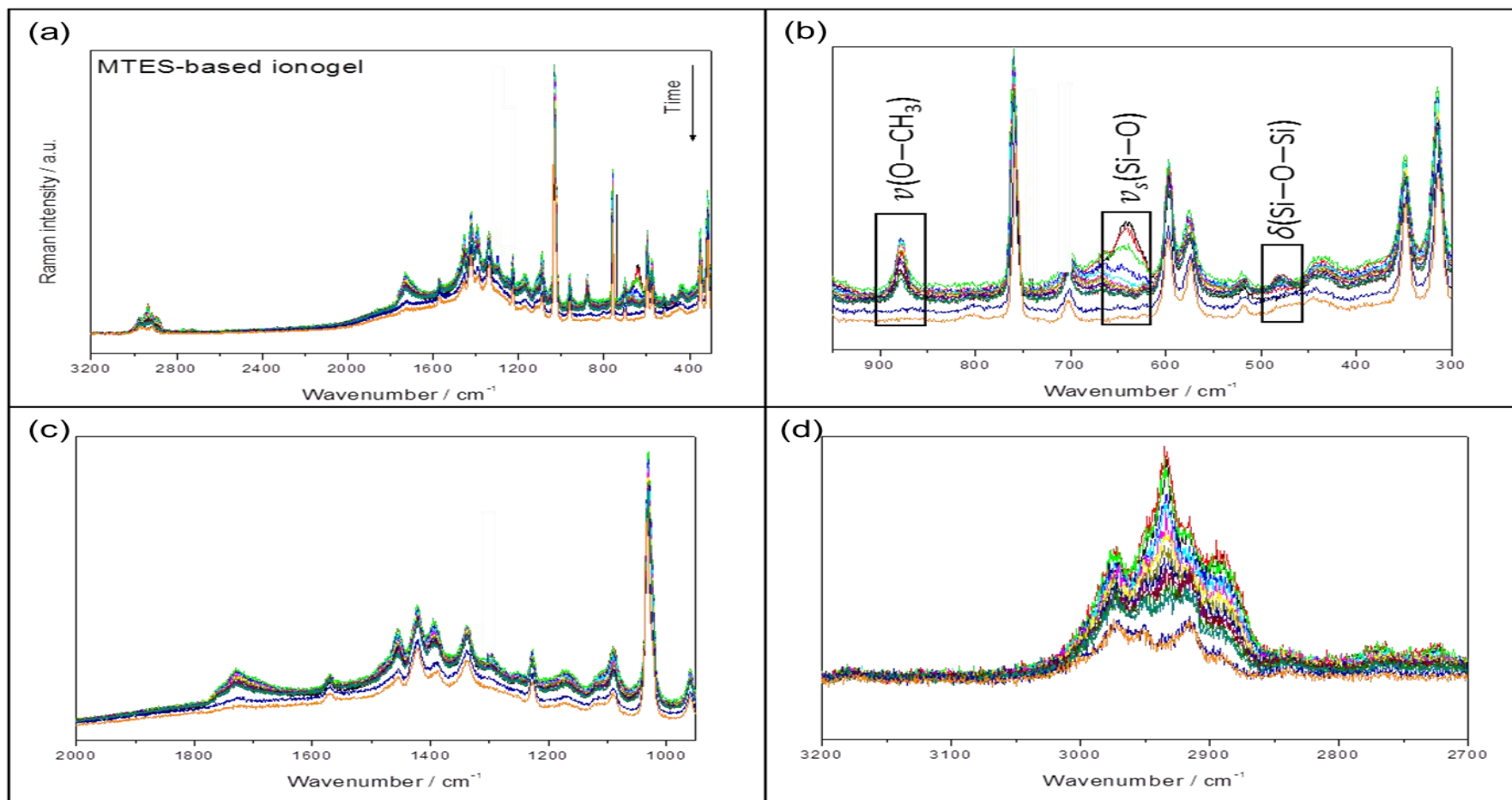


Figure 5.7 Raman spectra evolution with time of MTES-based ionogel over 12 hours in the (a) 300-3200  $\text{cm}^{-1}$ , (b) 300-950  $\text{cm}^{-1}$ , (c) 950-2000  $\text{cm}^{-1}$ , and (d) 2700-3200  $\text{cm}^{-1}$  regions. Kinetics of peak height variations of the highlighted bands are discussed later in this section. The time evolution of the intensity of  $\nu_s(\text{Si-O})$  and  $\nu(\text{O-CH}_3)$  bands can be found in Figures 5.8 and 5.9, respectively.

Figures 5.6 and 5.7 represent the variation in the Raman spectra of MTMS and MTES-based ionogels, respectively. Unlike ionogels with tetraalkoxide silica precursors, the deformation vibrations of the Si–O–Si can be clearly detected in the Raman spectra of MTMS and MTES-based ionogels (located between 470 and 480  $\text{cm}^{-1}$ ). As observed for xerogels, ethyl-based ionogels show a similar trend to one another while the same is accurate for methyl-based ionogels. The main difference between the spectra of corresponding tetraalkoxysilane and alkyltrialkoxysilane-based mixtures is the presence of an additional C–H stretching vibration band at 2915 and 2914  $\text{cm}^{-1}$  (according to their position after 2 hours) that originates from the non-hydrolysable methyl group available in MTMS- and MTES-based ionogels, respectively. The stretching vibrations of Si–O and C–H (in  $\text{CH}_3$  groups) of MTMS appear at 628 and 2850  $\text{cm}^{-1}$ , respectively. On the other hand, the stretching vibrations of C–O in methyl formate (located at 909  $\text{cm}^{-1}$ ) and O– $\text{CH}_3$  in methanol (located at 1020  $\text{cm}^{-1}$ ) are undetectable in the MTMS-based ionogel spectrum similar to that in TMOS.

The band associated with the stretching vibrations of C–O in ethyl formate, is not detectable for MTES-based ionogels (located at 840  $\text{cm}^{-1}$ ) while the  $\nu(\text{O–CH}_3)$  band in ethanol appears at 877  $\text{cm}^{-1}$  similar to TEOS ionogel. Lastly, the  $\nu(\text{Si–O})$  and  $\nu(\text{C–H})$  bands which correspond to the stretching vibrations within MTES precursor are located at 640 and 2931  $\text{cm}^{-1}$ , respectively.

As described in Chapter 4, the *in situ* monitoring of the sol-gel process for each formulation was done by following the variations in the characteristic peak height of key components available in the mixture from  $t_0 = 3$  minutes. This includes: (a) the Si–O stretching mode of the silica alkoxide located in the 628–662  $\text{cm}^{-1}$  region and (b) characteristic peak of ethanol ( $\nu(\text{O–C}_2\text{H}_5)$ ) located at 877  $\text{cm}^{-1}$ .

The reaction kinetic information was extracted from the data by plotting the peak height or Raman intensity of selected peaks as a function of time. Peak height variations or changes in Raman intensity provide information on the relative concentration of the components available in sample window. As the first step of normalisation, all data points were divided by a 'reference peak' to account for the loss of optical transmittance throughout the experiment. Since ion-

ic liquid does not participate in the sol-gel process, the strong peak at  $756\text{ cm}^{-1}$  associated with  $\delta_s(\text{CF}_3)$  was used as the 'reference peak'. As the second and last step of normalisation, the maximum value ( $(\text{Raman intensity}) / (\text{Reference Peak intensity})$ ) in every data set was identified and every data point in the same series was divided by this value. This resulted in all series having a maximum value of 1. To demonstrate repeatability, every measurement was performed in duplicate, and both were plotted as round 1 and 2 in the same graph.

Figure 5.8 displays the rate of precursor consumption in all four samples within 12 hours of being mixed with acid. In order to quantify the difference in the reaction rate, 0 order kinetics was assumed and therefore, a linear fit was plotted for each round of measurement the results of which are recorded in Table 5.3. Examples of typical linear fits are provided as insets in Figure 5.8.

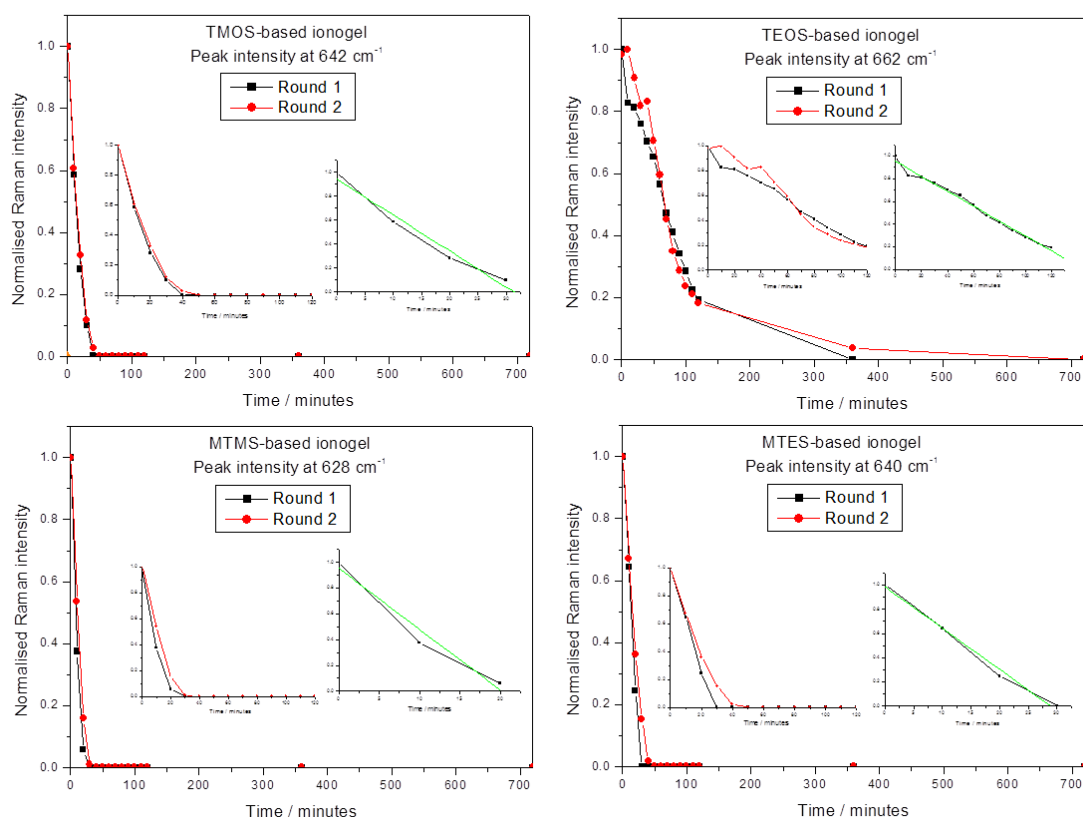


Figure 5.8 Time evolution of Si–O symmetric stretching mode in TMOS-, TEOS-, MTMS- and MTES-based ionogel mixtures. Examples of linear fits utilised for calculation of reaction kinetics (in green) and expanded graphs of the intensity variations within the first two hours are provided in the insets.

Table 5.3 Linear fitting ( $Y= A + BX$ ) information using Origin (version 6.0) software for time evolution of  $Si-OC_xH_{2x+1}$  band for each mixture. For comparison purposes, the kinetics of the same process calculated previously for xerogels in Chapter 4 are displayed here once again.

Sample		B / minute <sup>-1</sup>		Order of kinetics	R <sup>2</sup>
		Ionogel	Xerogel		
TMOS + FA	Round 1	(-30.02±3.67)E-3	(-49.04 ± 9.44)E-3	0	0.97
	Round 2	(-29.26±2.95)E-3	(-47.12 ± 6.26)E-3		0.98
TEOS+ FA	Round 1	(-6.59±0.21)E-3	(-12.33 ± 0.88)E-3	0	0.99
	Round 2	(-7.82±0.42)E-3	(-13.35 ± 0.87)E-3		0.97
MTMS + FA	Round 1	(-47.11±8.89)E-3	(-49.12 ± 9.88)E-3	0	0.97
	Round 2	(-33.47±5.07)E-3	(-49.44 ± 13.18)E-3		0.96
MTES + FA	Round 1	(-33.98±2.23)E-3	(-33.45 ± 3.27)E-3	0	0.99
	Round 2	(-24.83±2.42)E-3	(-24.08 ± 2.45)E-3		0.97

As it was concluded from Chapter 4, the following reaction is the main route for alkoxide precursor consumption in the early stages of sol-gel process:



Based on the fitting results recorded in Table 5.3, the rate at which the band associated with  $Si-OC_xH_{2x+1}$  stretching mode becomes indiscernible, drops when [Emim][TfO] ionic liquid is introduced to the sol-gel system for all mixtures except that of MTES. The process kinetics in the first 3 systems drops by 20-40% while no apparent change occurs in the initial consumption rate of MTES in its ionogel mixture. As described previously, and as shown in the Raman spectra of all samples, ionic liquid does not participate in the sol-gel process. However, its presence dilutes the sol mixture, changes the environmental pH and retards the rate of protonic attack. In addition, ionic liquids have been suggested as a non-volatile drying control additive for sol-gel process to help control the rate of hydrolysis and condensation processes and reduce the mechanical stress exerted on the gel network during the drying stage [20,21]. The overall kinetic rate of all four formulations has the following rank order: MTMS>TMOS~MTES>TEOS. As mentioned in Chapter 4, the stoichiometry of the reaction, steric hindrance of the alkoxy chains and the difference in partial

charge on the oxygen atom among the precursors contribute to the overall rate kinetics. It is perhaps a balance of all 3 phenomena that resulted in essentially no variation in the initial kinetics of precursor consumption in MTES ionogel mixture.

Based on Table 5.3, the degree of repeatability in the B values is low for MTMS ionogel and MTES ionogel as well as xerogel. A possible explanation for this observation is poor dispersion of the reactants in the named mixtures which results in the sol-gel process not taking place homogeneously within each sample, and the Raman results, being position sensitive, may not easily detect this. To confirm this speculation, more measurements are required which, due to time constraint, were not conducted.

Figure 5.9 represents the variations in C–O stretching vibrations (located at  $877\text{ cm}^{-1}$ ) associated with the formation and consumption/evaporation of ethanol in TEOS and MTES ionogels. Formation of ethanol in the MTES mixture reaches a maximum after 30-40 minutes, which is very similar to the case of the MTES xerogel where ionic liquid is absent. However, concentration of ethanol in the TEOS mixture only peaks after 60-70 minutes of the monitoring process and by taking into account the results obtained from the initial sol-gel process kinetics (associated with precursor consumption), this is a result of an overall delay in the sol-gel processes in the presence of [Emim][TfO] ionic liquid.

The bands associated with C–O stretching vibrations in methanol formed in the TMOS and MTMS ionogel mixtures were not detectable due to overlapping with strong ionic liquid bands in the same region. Figure 5.10 displays the peak fitting results of the ionic liquid in the  $1700\text{--}990\text{ cm}^{-1}$  region. The strong band at  $1033\text{ cm}^{-1}$  is associated with  $\nu_s(\text{SO}_3)$  while the slightly weaker band at  $1024\text{ cm}^{-1}$  corresponds to the same vibration shifted due to H-bonding [9]. The area and intensity of this band vary as the water content in the system changes and for this reason, even using precise peak fitting tools in Omnic (version 9.6.238), it is impossible to generate reliable information about the time evolution of C–O stretching in methanol that is located at  $1018$  and  $1020\text{ cm}^{-1}$  for TMOS and MTMS mixtures, respectively. Bond intensities will not be equivalent due to changes in polarisability.

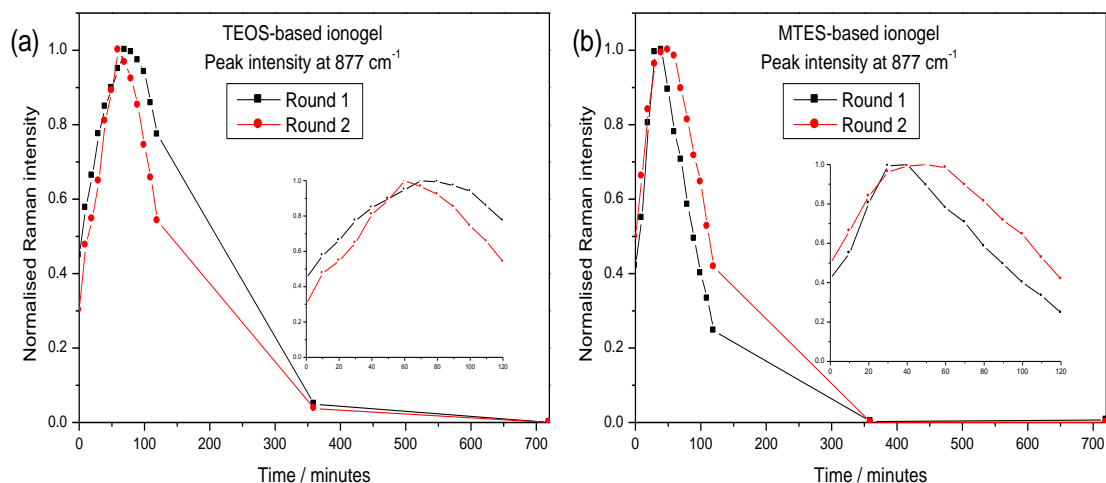


Figure 5.9 The time evolution of C–O stretching vibrations assigned to ethanol at 877 cm<sup>-1</sup> in (a) TEOS and (b) MTES ionogels. The insets show the variations of the Raman intensity within the first two hours.

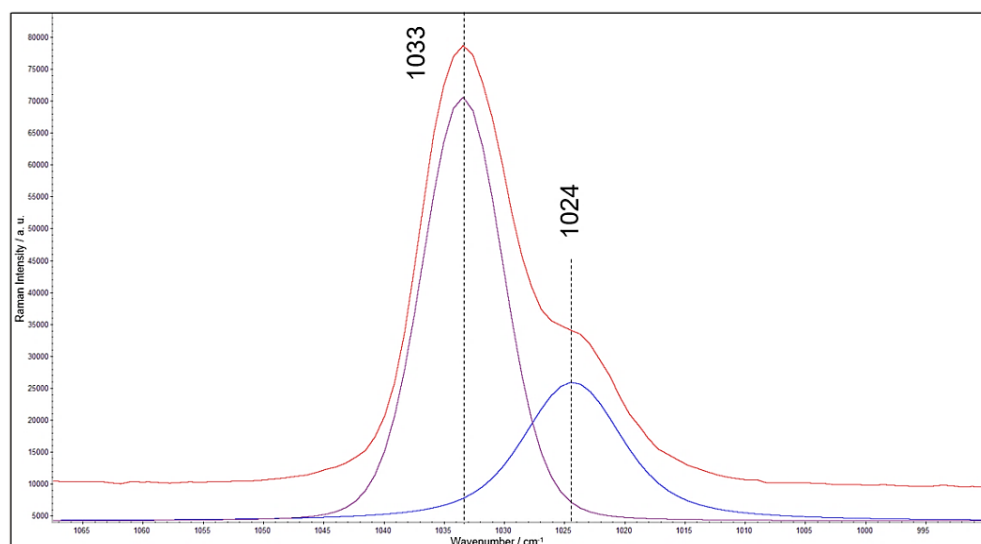


Figure 5.10 Peak fitting of 'as-received' [Emim][TfO] ionic liquid bands in the 1700-990 cm<sup>-1</sup> region using Voigt function in Omnic software (version 9.6.238).

### 5.3.3 Ionic liquid-pore wall interactions

Figure 5.11 demonstrates the physical appearance of the four ionogels after 4 days of aging under ambient conditions. Similar to xerogels (Figure 4.14), the TMOS and TEOS ionogels have fractured, which suggests that these two samples have brittle structures. The MTMS and MTES ionogels possess smooth, fracture-free and compliant structures, which is due to lowered capillary pressure caused by the presence of Si–CH<sub>3</sub> groups [22]. Upon removal of the ionogel films from the steel casing, traces of ionic liquid were observed inside the

casing for TMOS ionogel. This was observed for TEOS ionogel to a smaller degree. This observation is attributed to a fraction of ionic liquid being pushed out of the ionogel network due to extensive shrinkage. However, no traces of ionic liquid were observed in the case of MTMS and MTES ionogels which suggests that the ionic liquid is fully encapsulated within their gel networks.

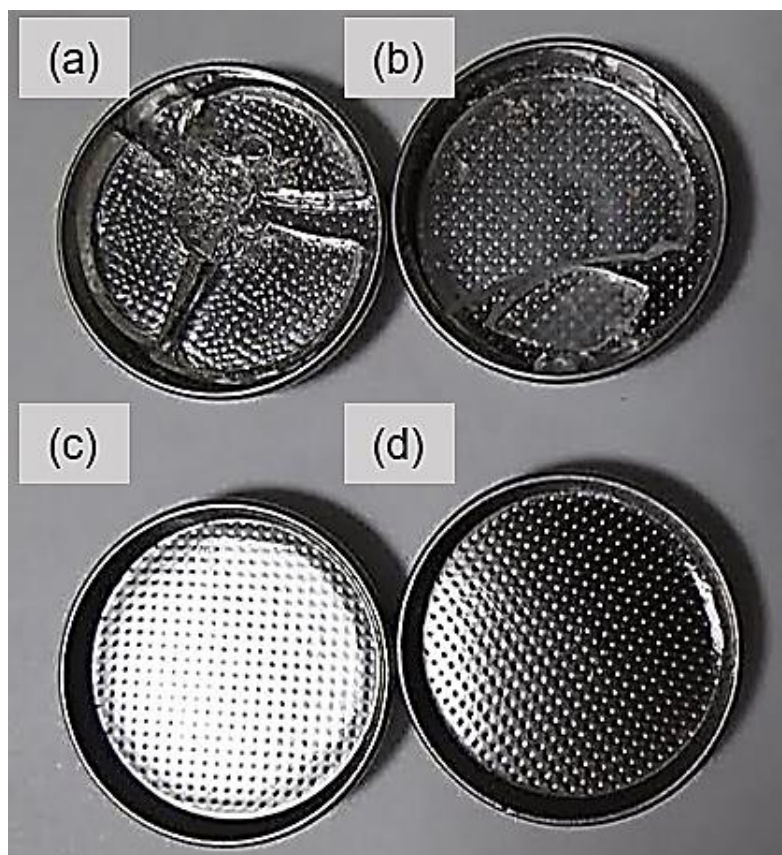


Figure 5.11 Optical images of (a) TMOS-, (b) TEOS-, (c) MTMS- and (d) MTES-ionogels after 4 days of aging at ambient conditions. The fractured structure of tetraalkoxy-based ionogels suggests that these ionogels are brittle while presence of the methyl group has led to fracture-free MTMS and MTES-ionogels.

Understanding the degree of interaction between ionic liquid and pore walls of the confining silica matrix is of crucial importance for applications where ionic mobility can be jeopardised. Generally, any  $X - Y \cdots Z$  interaction results in an elongation or contraction of the  $X - Y$  bond which causes  $X - Y$  stretching vibrations to shift to a higher or lower wavenumber [23]. The degree of the Raman shift is indicative of the strength of the  $X - Y \cdots Z$  interaction.

Olivier-Bourbigou et al. gave a summary of the possible interactions present in imidazolium-based ionic liquids and provided a schematic of them which is reproduced in Figure 5.12 [24]. The complex structure of imidazolium cations

leads into the possibility of H-bonding and Van der Waals interactions between cations and other species available in the reaction environment. The amphiphilic nature of the cation can also influence the arrangement of the imidazolium ions depending on the hydrophobicity of the neighbouring species.

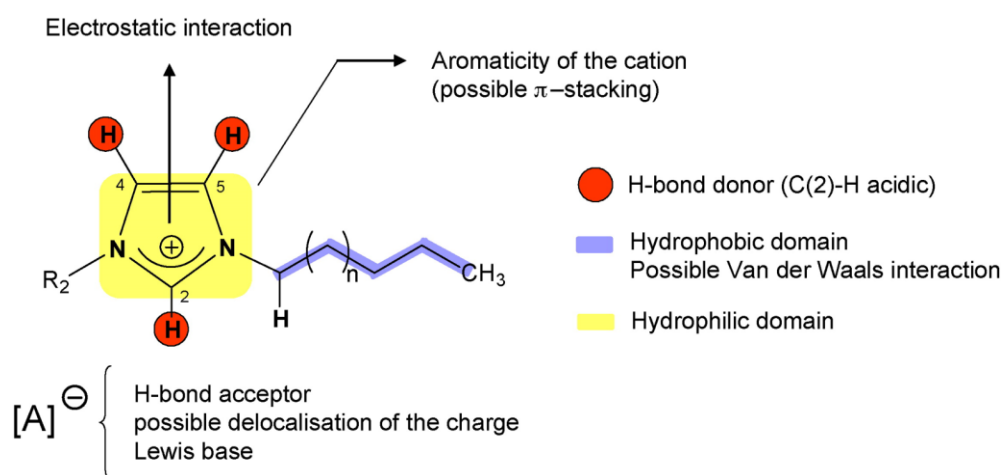


Figure 5.12 Schematic representation of different types of interaction present in imidazolium-based ionic liquids. Reproduced from [24].

The surface of the silica porous network can contain Si–O and Si–OH groups, Si atoms and in the case of trialkoxysilane precursors, Si–CH<sub>3</sub> groups. The ionic liquid cations and anions may interact with one or more of these groups when confined within the silica matrix. The possibility and the degree of these interactions have been investigated in the past. Gupta et al. [25] employed a series of quantum mechanical calculations and Fourier-transform infrared spectroscopy (FTIR) to predict and confirm the types of interactions present between 1-ethyl-3-methylimidazolium ethylsulfate, [Emim][EtSO<sub>4</sub>], and TEOS-based silica network. The combination of the characterisations confirmed that the two most probable interactions are (i) Si atoms interaction with the S–O groups of the anion and (ii) interaction of H atoms from the imidazolium ring with the Si–O groups on the pore wall. In another study done by Martinelli et al. presence of interaction between anion in 1-hexyl-3-methylimidazolium bis(trifluoromethanesulfonyl)imide ionic liquid, [Hmim][TFSI], and a silica network (TMOS-based) was confirmed using Raman spectroscopy [13]. Although the nature of this interaction was not specified, they reported a stronger interaction upon reduction of ionic liquid loading or increasing the ionic liquid confinement. In addition to interacting with the pore walls, ionic liquid ions can interact

with the intermediate materials such as water, alcohol, and ester formed during the sol-gel process. Liu et al. explored the interaction between [Emim][TfO] and water at different volumetric ratios (5-80% v/v) using vibrational spectroscopy techniques and indicated that the [TfO] anion can form strong H-bonds with water molecules through  $\text{SO}_3 \cdots \text{H}_2\text{O}$  [9]. In another interesting work by Nayeri et al., it was postulated that higher degree of ionic liquid confinement can increase the ion-ion interaction [26].

In this work, the peak position of bands associated with the C–H stretch of alkyl chains in the imidazolium cation and the S–O and C–S stretching modes in [TfO] anion were investigated after 2 and 12 hours of synthesis. An additional Raman scan was collected after 30 days of aging the ionogels in ambient conditions to obtain the same information well beyond the point of sol-gel transition. Furthermore, the position of Raman bands associated with the C–H stretching mode of the methyl groups in MTMS and MTES ionogels were elucidated. The positions of these peaks were determined using precise peak fitting (utilising Omnic software, version 9.6.238) in three different regions of: i)  $3028\text{-}2871\text{ cm}^{-1}$ , ii)  $1065\text{-}981\text{ cm}^{-1}$  and iii)  $336\text{-}295\text{ cm}^{-1}$  and using a Voigt function with a FWHM of 1.568. A summary of this investigation is provided in Table 5.4 with the degree and direction of the Raman shifts provided with respect to the original peak positions. For stretching vibrations, a red-shift (shift to lower wavenumbers, represented by a negative sign in Table 5.4) corresponds to lengthening/weakening of the covalent bond whereas a blue-shift (shift to higher wavenumbers, represented by a positive sign in Table 5.4) corresponds to a shortening/strengthening of the covalent bond [9]. Due to the spectral resolution of the Raman instrumentation utilised (0.5 wavenumbers) and the signal/noise ratio of the measurements, Raman shifts between  $-0.8$  and  $+0.8$  wavenumbers are assumed unjustifiable. In addition, it should be noted that the data tabulated in Table 5.4 are associated with one of the Raman spectra collected for each sample and a single location on each sample. Thus, the data may not be representative of all samples and every location on each sample.

As can be seen in Table 5.4, the Raman frequencies associated with the stretching vibrations of the [Emim] cation alkyl chains and anion S–O and C–S

bonds in all ionogels are different from that of 'as-received' ionic liquid after 2 hours of synthesis. This is attributed to strong ionic liquid-silica precursor and ionic liquid-by-products interactions at the early stages of sol-gel process. As described by Liu et al., it is likely that the small red shifts in  $\nu_s(\text{SO}_3)$  position is associated with elongation of S–O covalent bond due to formation of H-bonds [9]. This in turn causes shortening of the C–S bonds (due to Coulombic forces) and consequently, a blue-shift in the  $\nu_s(\text{CS})$  band.

Furthermore, it is reasonable to assume that the dispersion of ionic liquid inside the precursor and FA mixture can disturb the ion-ion interaction in the pristine/'as-received' ionic liquid which can include Van der Waals interactions between the [Emim] alkyl chains. The blue shifts observed for the  $\nu_{\text{as}}(\text{CH}_3)$  and  $\nu_s(\text{C}_2\text{H}_5)$  bands can be ascribed to a reduction in the Van der Waals interactions between the alkyl groups in the ionic liquid upon being dispersed in the sol mixture. For the case of MTMS and MTES ionogels, the  $\nu_s(\text{C}_2\text{H}_5)$  band of the ionic liquid demonstrates smaller Raman shifts compared to those in TMOS and TEOS ionogels after two hours from the ionogel synthesis. One can speculate that the difference in the extent of Raman shift is due to the counterbalancing effect of additional interactions with the methyl groups in the MTMS and MTES-based gel networks. However, MTES ionogel demonstrated a red shift of  $-1.2 \text{ cm}^{-1}$  for this band after 2 hours which disagrees with this speculation. As can be seen from the Raman spectra displayed in Figures 5.6 and 5.7, the neighbouring  $\nu(\text{C–H})$  band associated with the non-hydrolysable methyl groups in MTMS and MTES (located at  $2914.5$  and  $2914.2 \text{ cm}^{-1}$ , respectively) has a higher intensity compared to that of  $\nu_s(\text{C}_2\text{H}_5)$  in the ionic liquid. Therefore, the difference in the overall degree and direction of the Raman shift (red or blue) for the  $\nu_s(\text{C}_2\text{H}_5)$  band (associated with the ionic liquid) in MTMS and MTES ionogels is presumed to have been due to fitting errors caused by the presence of an overlapping  $\nu(\text{C–H})$  band.

Table 5.4 Summary of Raman shifts in the selected ionic liquid peak bands as well as that of the C–H stretch in non-hydrolysable methyl groups (in MTMS and MTES mixtures) after 2 hours, 12 hours and 30 days of ionogels synthesis and 2 hours after xerogels synthesis with respect to the original position of these bands in the corresponding pristine reactants.

Time of scan	Scanned material	Peak shift / cm <sup>-1</sup>				
		$\nu_{as}(CH_3)$	$\nu_s(C_2H_5)$	$\nu_s(SO_3)$	$\nu_s(CS)$	$\nu(C-H)$
-	'As-received' ionic liquid	2970.7	2888.9	1033.4	312.8	-
120 minutes	TMOS-ionogel	+1.5	+4.0	-0.8	+2.1	-
720 minutes		< 0.8	+3.6	< 0.8	< 0.8	-
30 days		< 0.8	+1.4	< 0.8	+0.9	-
120 minutes	TEOS-ionogel	+3.9	+2.1	-1.4	+2.1	-
720 minutes		+2.1	+2.4	< 0.8	+1.1	-
30 days		< 0.8	+2.2	< 0.8	< 0.8	-
120 minutes	MTMS-ionogel	+1.4	+0.9	-1.2	+1.6	-2.1
720 minutes		+0.8	< 0.8	< 0.8	< 0.8	-2.2
30 days		+0.8	+0.9	< 0.8	< 0.8	-2.6
120 minutes	MTMS-xerogel	-	-	-	-	< 0.8
-	Pristine MTMS	-	-	-	-	2916.6
120 minutes	MTES-ionogel	+2.8	-1.2	-1.3	+1.9	-0.8
720 minutes		+1.9	+2.5	< 0.8	+0.8	< 0.8
30 days		+0.9	+1.3	< 0.8	< 0.8	< 0.8
120 minutes	MTES-xerogel	-	-	-	-	< 0.8
-	Pristine MTES	-	-	-	-	2915.0

As time reaches 30 days, the degree of Raman shift in  $\nu_{as}(\text{CH}_3)$  band is minimised (to less than 1 wavenumbers) and this vibrational band shifts closer to its position in the 'as-received' ionic liquid, indicating weak interactions or a low density of interactions between this methyl chain in the ionic liquid and the silica network and/or the volatiles (water, alcohol and ester) remaining in the ionogel network. No clear difference can be seen amongst the four ionogels at the end of the 30 days aging period in terms of the degree of interaction with  $\nu_{as}(\text{CH}_3)$  band. This is also true for the bands associated with  $\nu_s(\text{CS})$  and  $\nu_s(\text{SO}_3)$  in the ionic liquid anions.

Between MTMS and MTES ionogels, the former sample showed a larger red shift (-2.6 wavenumbers compared to -0.8 wavenumbers) in the position of  $\nu(\text{C-H})$  band of the non-hydrolysable methyl groups after 30 days from synthesis. Due to the hydrophobic nature of this group, one can predict that the source of this red shift is interaction with another hydrophobic group such as the alkyl chains in the imidazolium cation. However, the blue shifts in the [Emim] alkyl chains do not support this hypothesis. Another possibility is that the methyl groups in the gel network are interacting with a different group such as other methyl groups in the gel network.

It is interesting that this behaviour is not seen in the MTES ionogel which is expected to have a very similar structure to MTMS ionogel. Difference in the porous structure can be a possible explanation for this observation. As mentioned previously, it is necessary to conduct more studies to examine the reproducibility of the obtained results.

## **5.4 thermal stability and microstructure of the ionogels**

### **5.4.1 Experimental procedure**

As described previously, each ionogel was prepared by mixing the silica precursor with [Emim][TfO] ionic liquid in a glass vial for 10 minutes at 600 rpm using a magnetic stir bar. After this mixing stage, FA was added to the mixture and was allowed 10 minutes to react with the silica precursor. The utilised volumes of the reactants are listed in Table 5.1. The precursor: ionic liquid: FA molar ratio was kept constant at 2:2:7 for all samples. After 20 minutes mixing, 500  $\mu\text{L}$  of each mixture was pipetted into a stainless steel container. After 4 days of aging

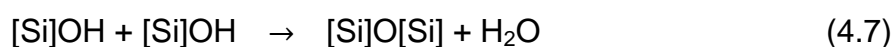
under ambient conditions, thermogravimetric analyses (TGA) of the ionogels were conducted and repeated 3 times for each sample including the 'as-received' [Emim][TfO] ionic liquid to examine the consistency of the results. Portions of the samples remaining after the TGA measurements (after ionic liquid decomposition and subsequent removal from the gel network) were utilised for SEM characterisation (NOVA NanoSEM 200 (FEI, USA)). Since the heating procedure introduces stress to the mechanical structure of the silica scaffold [27], the remaining samples tend to be very brittle. This introduces a challenge to fully gold coat the silica particles and avoid charging effects. For this reason, a thick layer of gold (40 nm) was sputtered while the samples were tilted by  $\sim 30^\circ$  in an effort to fully coat the small silica particles in all dimensions and ground them to the carbon tab on the steel stage. The sample preparation procedure was repeated in duplicate and four random locations in each sample were investigated using SEM. The images provided in the following section are representative of the morphology of each silica network.

#### 5.4.2 Results and discussion

Thermal stability is a critical requirement for electrolytes utilised in supercapacitors (and other forms of energy storage devices). Figure 5.13 provides the thermogravimetric behaviour of 'as-received' [Emim][TfO] as well as the formulated ionogels. The TGA curves of the ionic liquid show three-step mass loss processes where the first step (35-300°C) corresponds to the loss of water traces and other impurities including halides and residual solvents remained from the ionic liquid synthesis process [28,29] which based on Figure 5.13a makes up to  $\sim 2.0\% \pm 0.6$  of the total mass of the as-received [Emim][TfO] ionic liquid. Between 300 and 475°C a significant mass loss of  $88.2\% \pm 0.3$  is observed which is assigned to the decomposition of the ionic liquid. The final mass loss of  $\leq 10\%$  between 475 and 700°C is attributed to the complete decomposition of the ionic liquid. A similar three-step mass loss TGA pattern for [Emim][TfO] ionic liquid in air was reported previously by Göbel et al. [30]. The onset temperature (the temperature at which the weight loss begins) for the second region (i.e. the ionic liquid decomposition) was evaluated to be  $418^\circ\text{C} \pm 4$  based on the intersection of tangent lines after the initial drying process (from 300°C) using

STARe software (version 10.0). This process was repeated for every sample. The results of these evaluations are recorded in Table 5.5.

As can be seen in Figure 5.13b-e, all four ionogels show a similar TGA pattern to that of the ionic liquid. The first stage mass loss in all four ionogels ranges between 2.3-3.3% of the total ionogel mass which is attributed to the loss of ionic liquid impurities as well as release of physically bound water and the residual volatile by-products formed during the sol-gel process. It is worth noting that during the heating process, some of the unreacted Si–OH groups undergo condensation forming siloxane groups and water molecules [11]:



This is followed by major mass loss (ranging between -75.8 to -89.4%) mainly due to decomposition of ionic liquid. Meanwhile, the methyl groups in the MTMS and MTES ionogels are expected to decompose between 375 and 550°C according to Darmawan et al. [31] and oxidise to CO<sub>2</sub> via the following reaction:



Finally and as described by Brinker and Scherer [27], beyond 550°C, the xerogels are expected to undergo structural relaxation which entails removal of excess volume through diffusive motion of the solid network and it does not accompany weight loss. Based on the ionogel TGA curves shown in Figure 5.13, no further mass loss occurs beyond 700°C. Thus, the remaining mass at the end of the heating process of the ionogels corresponds to the mass of the silica xerogels.

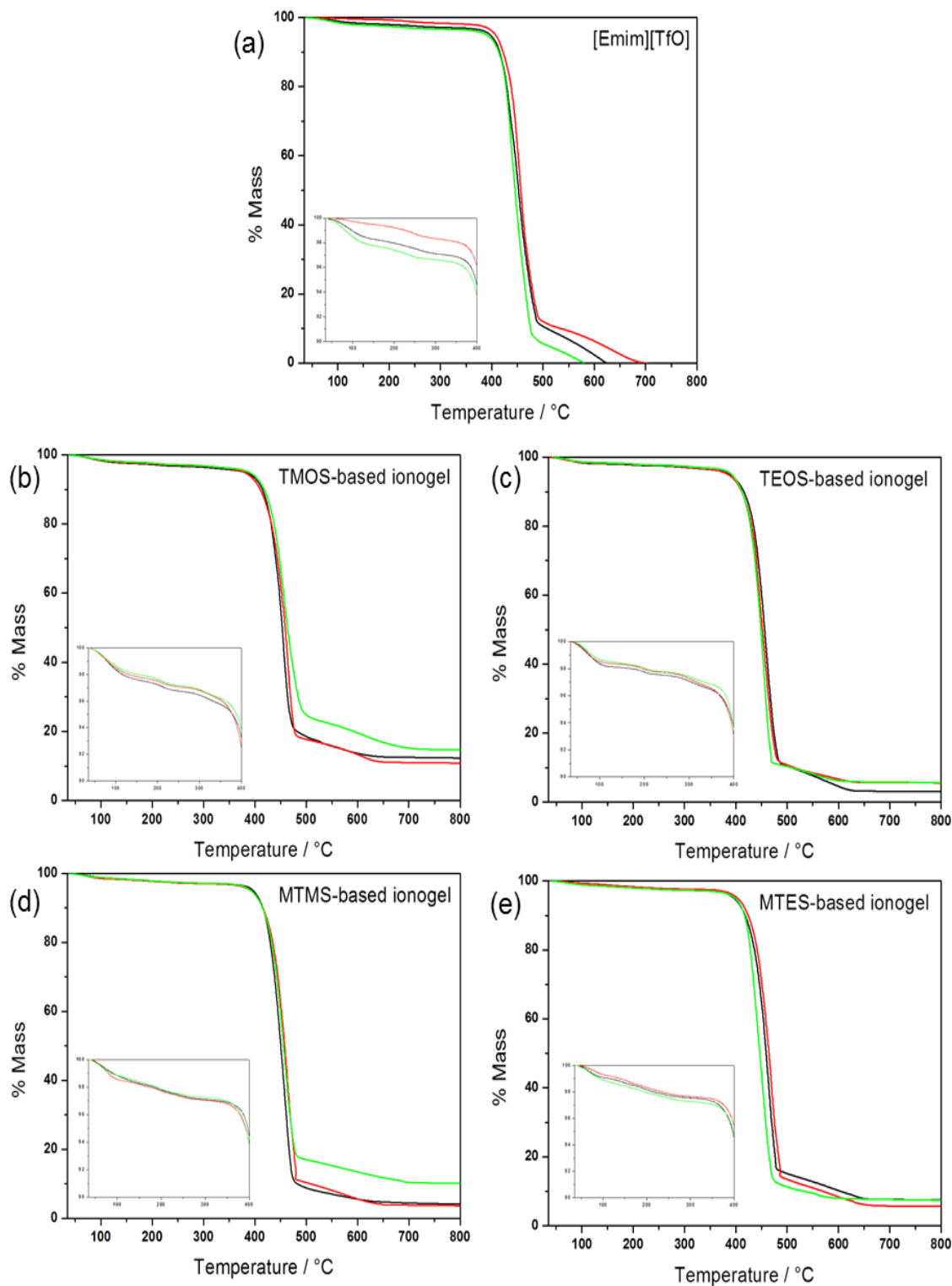


Figure 5.13 Thermogravimetric analysis results of (a) 'as-received' [Emim][TfO], (b) TMOS-, (c) TEOS-, (d) MTMS- and (e) MTES-ionogels between 35 to 800°C at 20°C min<sup>-1</sup>. A total of 3 samples were tested for each system and their TGA patterns are displayed here in black, red and green

Based on Table 5.5, the onset temperature (for stage II) which is mainly associated with decomposition of the ionic liquid, is shifted to higher temperatures when the ionic liquid is encapsulated inside a silica network. This shows that confinement within the silica network has improved the thermal stability of the [Emim][TfO] ionic liquid. This is an advantage over polymer-based ionogels where the thermal stability is greatly influenced by the compositional ratio of polymer to ionic liquid [32].

The resultant silica content for each formulation was calculated to be  $12.6\% \pm 1.6$ ,  $4.9\% \pm 1.4$ ,  $6.0\% \pm 2.9$  and  $6.9\% \pm 0.9$  on average for TMOS-, TEOS-, MTMS- and MTES-based ionogels, respectively. For TMOS-based ionogel this mass is slightly higher than that of the other ionogels. This is attributed to some of the ionic liquid being pushed out of the TMOS ionogel network during the process of aging resulting in higher silica-to-ionic liquid mass ratio. This is confirmed by the comparatively lower mass loss ( $75.8\% \pm 2.3$ ) over the second region of the heating process for TMOS ionogels.

*Table 5.5 A summary of the information extracted from the TGA graphs shown in Figure 5.13 including percentage mass loss for stage I and II of the heating process and the onset temperature of the second region. The recorded values are an average between the three TGA tests conducted for each sample.*

Sample	Stage I mass loss (35-300°C)	Stage II mass loss (300-475°C)	Onset temperature (300-475°C region)
Ionic liquid	$-2.0\% \pm 0.6$	$-88.2\% \pm 0.3$	$418^{\circ}\text{C} \pm 4$
TMOS-ionogel	$-3.3\% \pm 0.7$	$-75.8\% \pm 2.3$	$442^{\circ}\text{C} \pm 2$
TEOS-ionogel	$-2.3\% \pm 0.2$	$-89.4\% \pm 0.8$	$428^{\circ}\text{C} \pm 4$
MTMS-ionogel	$-2.7\% \pm 0.1$	$-82.0\% \pm 2.1$	$430^{\circ}\text{C} \pm 3$
MTES-ionogel	$-2.5\% \pm 0.2$	$-84.1\% \pm 1.6$	$425^{\circ}\text{C} \pm 6$

Figures 5.14-17 show the SEM images of the four ionogels after the removal of ionic liquid using TGA heating process. Although the heating process prior to the SEM imaging (35-800°C at 20°C min<sup>-1</sup>) effectively removes the ionic liquid content, it causes shrinkage and densification in the silica network [27]. However, in micrometer scale or smaller, the process of shrinkage can be presumed to occur isotropically meaning that although pore sizes may not be representative of those of ionogels, the microstructure as a whole is still representative of the ionogel morphology. Due to challenges in setting an even conductive coating, there is evidence of charging in some of the images. Since the ionic liquid has been removed, these samples cannot be regarded as ionogels and for this reason, they are referred to as 'heated-xerogels' within the text. As can be observed, all of the 'heated-xerogels' have porous structures with pores ranging between micro and sub-micro sizes. Evidently, the presence of ionic liquid has introduced macropores (> 50 nm in diameter) into the solid structures as such large pores are absent in the structure of xerogels shown in Chapter 4 (Figures 4.16-4.19). Ionic liquid acts as a barrier during the growth of silica clusters and shapes the microstructure of silica, which results in the formation of a porous network rather than a dense film. This is schematically demonstrated in Figures 5.18 a and c.

The porous structure of TMOS 'heated-xerogels' shown in Figure 5.14 appears to be uniform throughout the scaffold. Figure 5.14a shows presence of a dense 'skin' layer in the structure of this 'heated xerogel'. Skin formation in silica gels has been briefly discussed in the past [27,33–35]. It is believed that due to faster gelation of the top surface of the gel, a dense layer is formed. The water vapour in the air can be adsorbed on the surface of the sol mixture and participate in the hydrolysis reaction:



This speeds the process of hydrolysis and subsequently condensation on the top surface of the sol while the volatiles produced, as a result of hydrolysis and condensation processes, can escape the structure top surface more rapidly (compared to the bulk) resulting in more shrinkage on the drying surface and the formation of a dense 'skin' layer [27,33–35]. From SEM images it is clear

that formation of the skin layer is not unique to TMOS-based 'heated xerogel' and it does appear in all four of the samples.

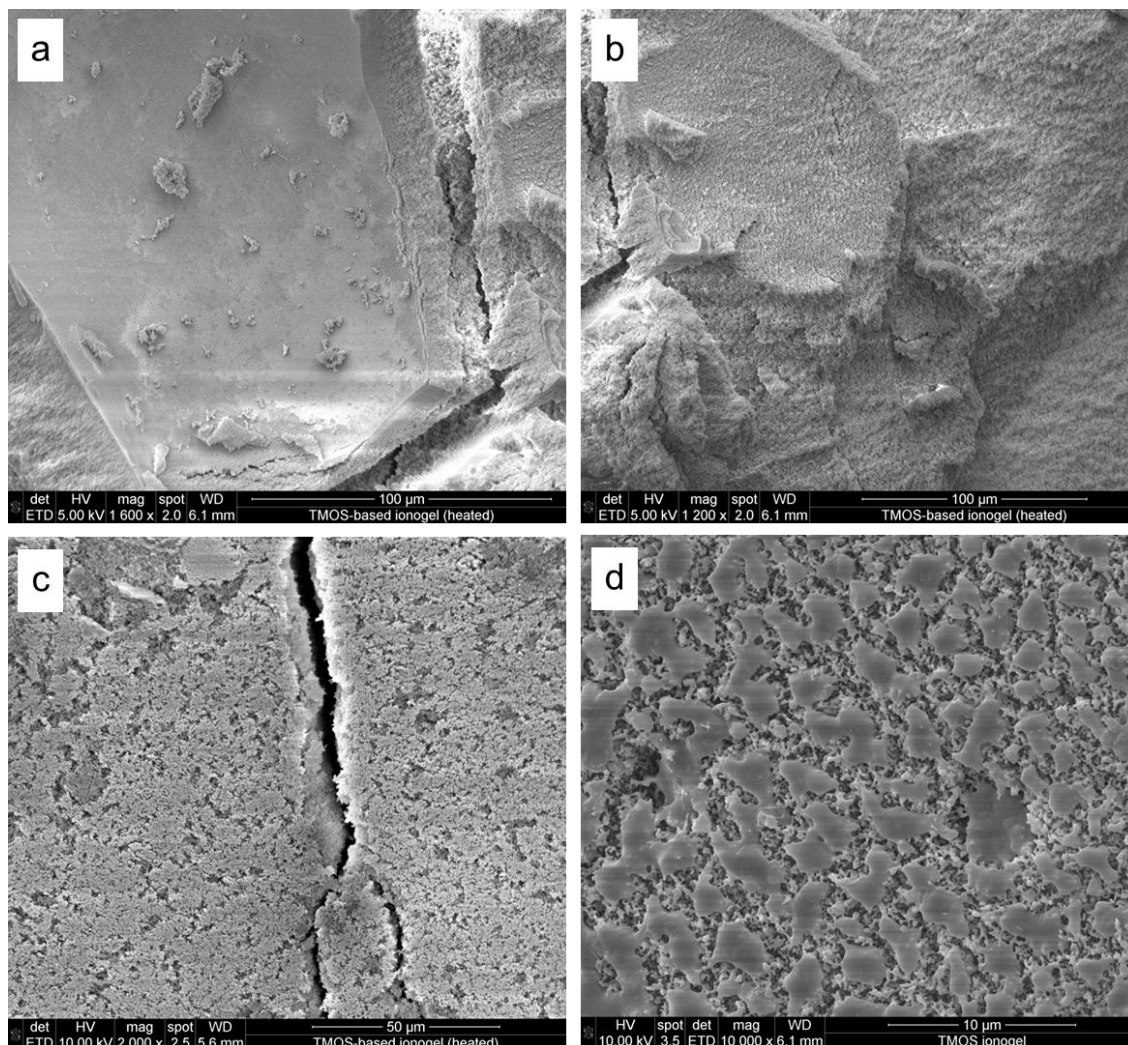


Figure 5.14 SEM images of TMOS -based 'heated-xerogel' at various magnifications: (a) x1600, (b) x1200, (c) x2000 and (d) x10000. The ionic liquid was removed by evaporation to reveal the silica network structure.

The porous structure of the TEOS 'heated xerogel' shown in Figure 5.15 is similar to its TMOS counterpart in terms of the size of the pores. Based on the reaction kinetics discussed earlier, initial consumption of the precursor takes place almost 3 times slower in the TEOS mixture compared to TMOS, whilst the sol-gel transition point is achieved after 12 hours for both of the mixtures. This could mean that the hydrolysis and condensation processes compete for the majority of the 12 hours; silica clusters formed at the beginning of the gelation period have more chance to grow in size through aggregation compared to the clusters formed towards the end of the gelation process, resulting in an inho-

mogeneous structure. Comparing the SEM images of the TMOS (Figure 5.14) and TEOS 'heated xerogels' a greater degree of heterogeneity was observed in the latter system.

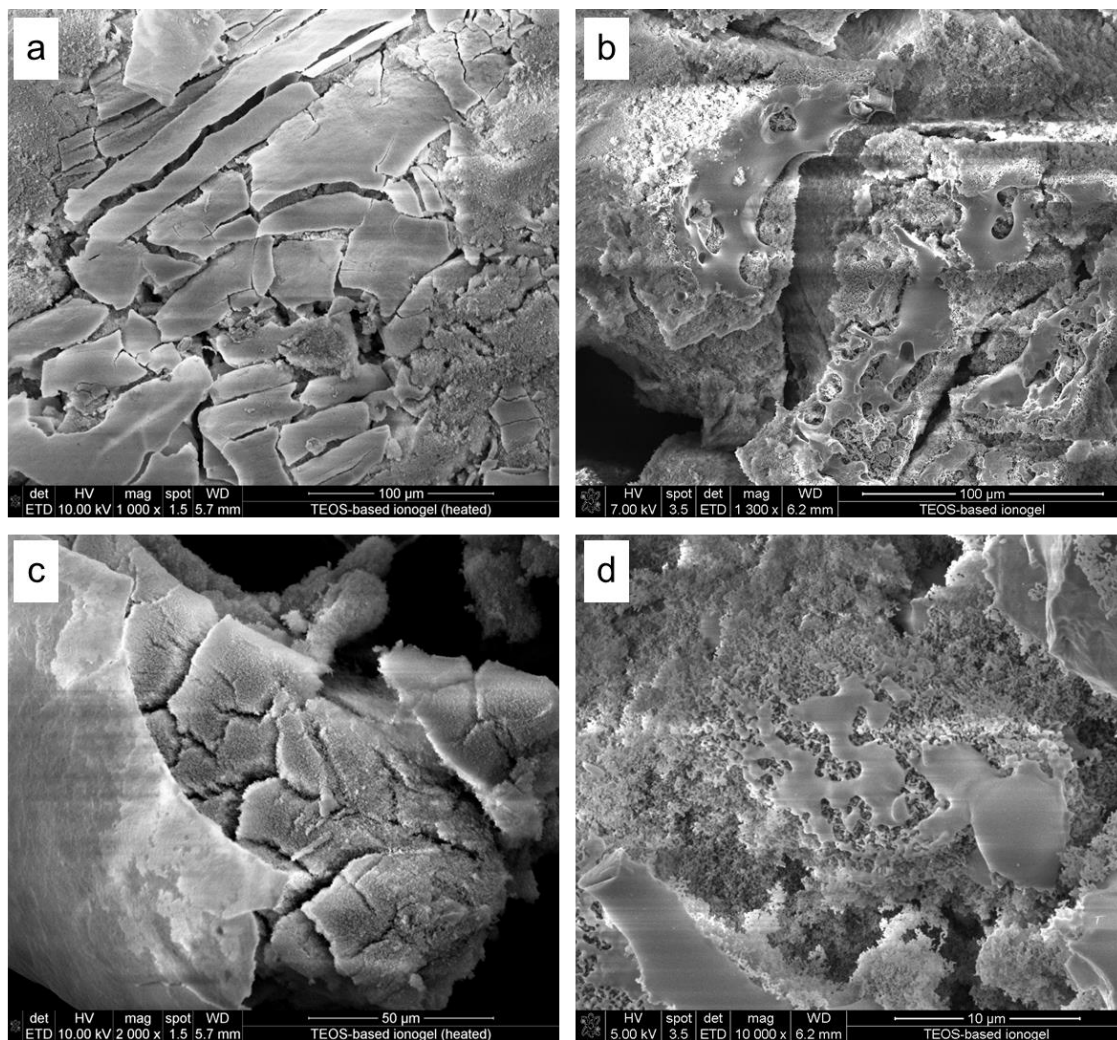


Figure 5.15 SEM images of TEOS -based 'heated-xerogel' at various magnifications: (a) x1000, (b) x1300, (c) x2000 and (d) x10000. The ionic liquid was removed by evaporation to reveal the silica network structure.

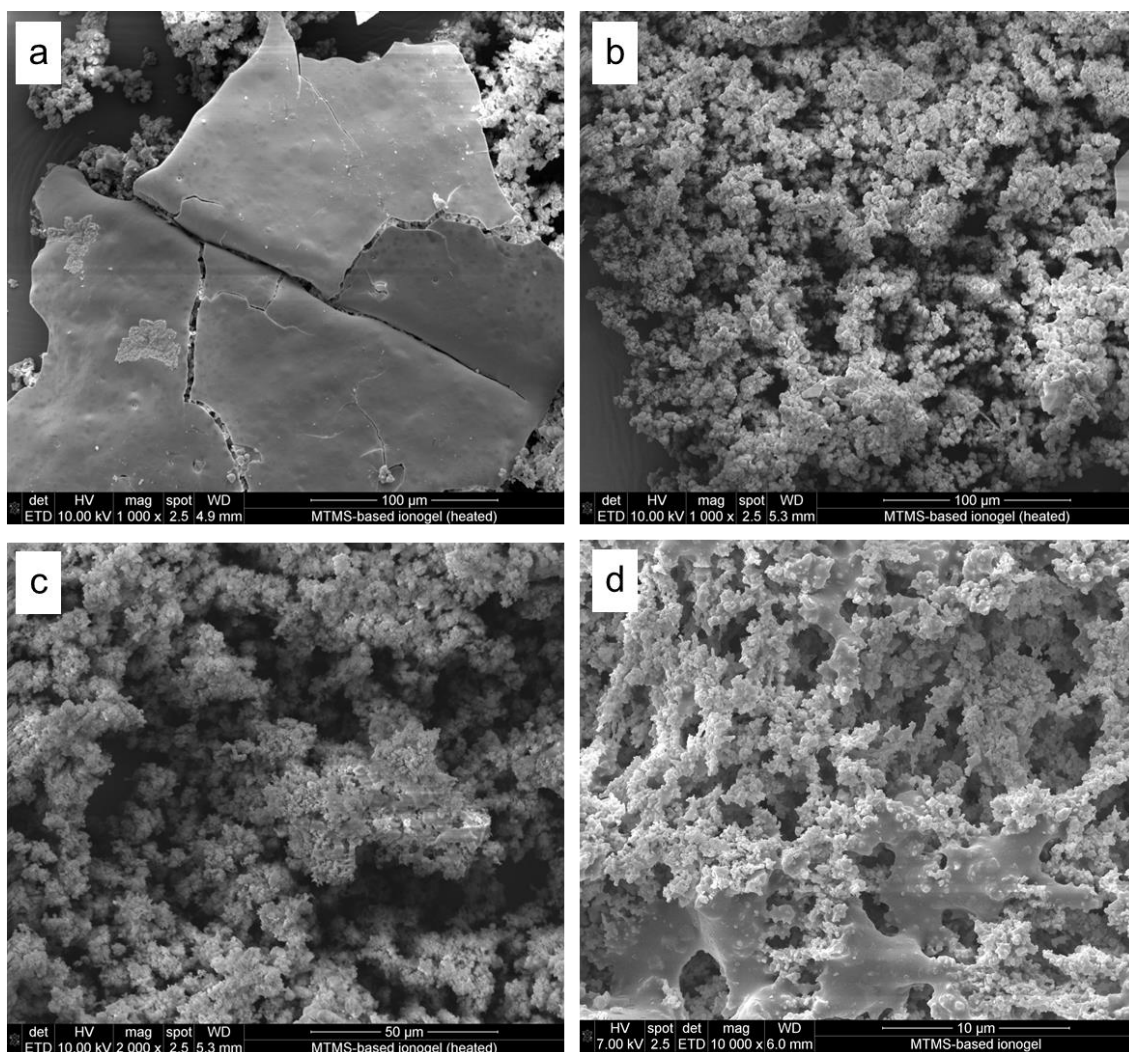


Figure 5.16 SEM images of MTMS -based 'heated-xerogel' at various magnifications: (a) and (b) x1000, (c) x2000 and (d) x10000. The ionic liquid was removed by evaporation to reveal the silica network structure.

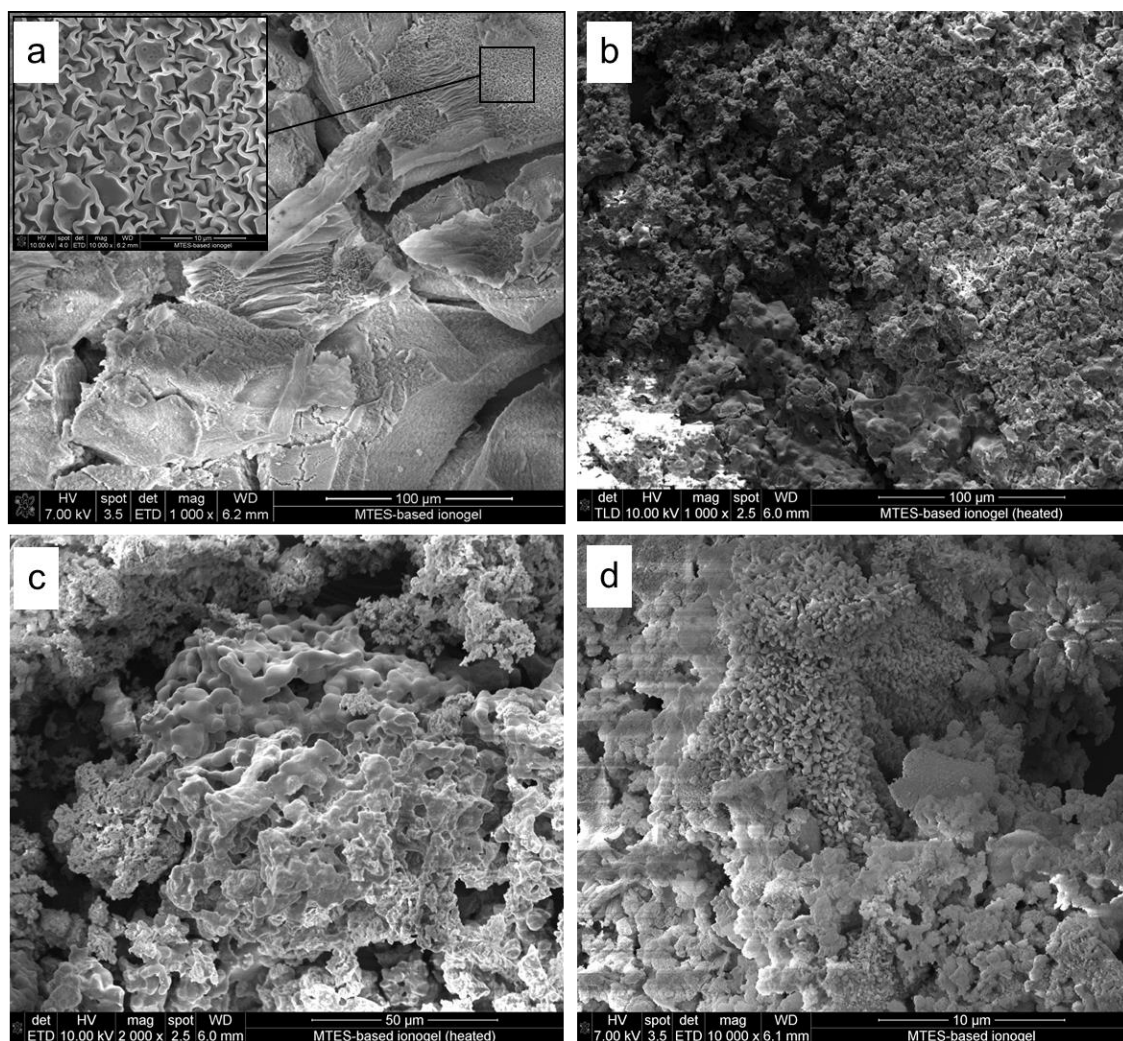


Figure 5.17 SEM images of MTES -based 'heated-xerogel' at various magnifications: (a) and (b) x1000, (c) x2000 and (d) x10000. The ionic liquid was removed by evaporation to reveal the silica network structure.

The porous networks of the MTMS and MTES 'heated-xerogels' (shown in Figures 5.16 and 5.17) possess larger macropores compared to the two TMOS and TEOS xerogel structures (Figures 5.14 and 5.15). Among the initial sol-gel process kinetics discussed earlier, TMOS, MTMS and MTES mixtures showed to have similar reaction kinetics to each other while it was visually determined that the sol-gel transition point is reached after 4 days for the trialkoxy-based ionogel mixtures and only after 12 hours for the TMOS ionogel. Based on the Raman analysis, the siloxane groups (Si–O–Si) are formed at early stages of the synthesis of both MTMS and MTES ionogels and thus, the slow gelation can be attributed to the slow formation of 'Neck region' between silica clusters. This is a result of the steric hindrance effect caused by the Si–CH<sub>3</sub> groups and the solid phase separation induced by the ionic liquid.

In addition, the presence of methyl groups results in the formation of larger silica clusters due to the disturbance caused by these groups to the colloidal stability of silica particles [36,37]. This combined with the steric hindrance effect associated with Si-CH<sub>3</sub> groups [37] results in formation of larger pores within the ionogel matrix as shown schematically in Figure 5.18d.

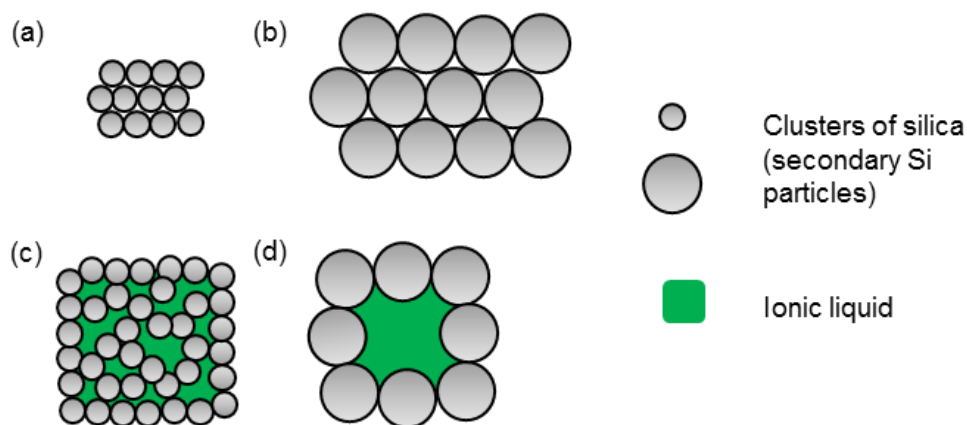


Figure 5.18 Schematic illustration of silica particles arranged in (a) tetraalkoxy-based xerogels, (b) alkyltrialkoxo-based xerogels, (c) tetraalkoxy-based ionogels and (d) alkyltrialkoxo-based ionogels. Presence of alkyl groups in the trialkoxo-based gels increases the cluster size [37] and generates larger pores within the ionogel network.

Formation of a skin layer is clearly seen in MTMS and MTES 'heated xerogels'. This skin layer has wrinkle-like features for MTES sample (as shown in Figure 5.17a) which could be due to flexibility of this layer. One possible explanation for this behaviour is the presence of methyl groups which introduce a degree of flexibility to the silica film. It is not known why this layer did not show the same degree of flexibility in the MTMS sample despite the presence of methyl groups. As shown in Table 5.3, MTMS and MTES ionogels showed very similar precursor consumption kinetics and according to the collected Raman spectra, in both ionogels the band associated with the deformation of Si-O bond in Si-O-Si (located between 470 and 480 cm<sup>-1</sup>) appears after 20 minutes of reaction monitoring. This creates the expectation that the two silica networks encapsulating the ionic liquid have similar microstructures which is not the case based on the SEM images. The microstructure of the MTES heated xerogel is inhomogeneous and clusters of various shapes and sizes (ranging between hundreds of nanometers to tens of micrometers) can be seen throughout its network. This is similar to that of TEOS 'heated xerogel' microstructure in comparison to its

TMOS counterpart seen in Figures 5.15 and 5.14, respectively. Therefore, one can speculate that the origin of this heterogeneity for the ethoxy-based samples is inhomogeneous dispersion of ionic liquid in the TEOS- and MTES-based mixtures.

## **5.5 Application of the ionogels as EDLC electrolytes**

### **5.5.1 EDLC fabrication**

In order to examine and compare the electrochemical performance of each ionogel as the electrolyte for EDLC supercapacitors, the ionogels were coated on activated carbon (AC) electrode disks. As described in Chapter 3, the activated carbon electrodes were fabricated by WMG international manufacturing centre using the procedure described in Chapter 3, section 3.1. After the 20 minutes mixing time described in section 5.4.1, 86, 100, 86 and 96  $\mu\text{L}$  volume of TMOS-, TEOS-, MTMS- and MTES-ionogel, respectively was transferred onto circular AC disks (1.5 cm in diameter) with a mass loading of  $1.8 \text{ mg cm}^{-1}$  using a micropipette. The transferred volume of each ionogel corresponds to 36  $\mu\text{L}$  of [Emim][TfO] on each electrode. The coated electrodes were then aged under ambient conditions until the sol-gel transition point of the ionogel is reached i.e. 12 hours for TMOS- and TEOS-ionogels and 4 days for the MTMS- and MTES-ionogels. Two coated electrodes were crimped and tested immediately once the sol-gel transition point was reached.

### **5.5.2 Electrochemical experiment design**

A combination of cyclic voltammetry (CV) and electrochemical impedance spectroscopy (EIS) were utilised for performance analysis. It is a common practice to heat ionic liquids (at  $\geq 70^\circ\text{C}$ ) inside a vacuum oven for a minimum of 12 hours prior to application to minimise the water content [38–40]. For the experiments reported in this chapter, ionic liquid was utilised as received due lack of suitable instrumentation (including a vacuum oven and a Karl Fischer titrator) to sufficiently reduce and control the water content in the ionic liquid. From the TGA results (Table 5.5), it was shown that the contribution of the gel network to the overall volatile impurity content (which includes water) in the ionogels is negligible (2.3-3.3%) compared to the ionic liquid itself (2%). Generally, presence of water can reduce the potential window of an electrochemical cell to 1.2 V due to

the water splitting effect above this potential window and its influence on the long-term stability of the cell [41]. In a similar system designed by Horowitz and Panzer, the electrochemical performance of ionogel electrolytes with less than 2 weight% volatile content (including water) was investigated in a 2.5 V potential window without an ionic liquid drying stage [42]. Using CV, they showed that the 2.5 V potential window is within the stability window of the ionogel electrolyte meaning that the ionogel does not contain enough water to cause a significant influence on the electrochemical performance. It must be noted that in their work, only 3 CV cycles were conducted which is not indicative of long-term influence of the water content on the electrochemical performance of the system. In this work, cyclic voltammetry was conducted in a reduced potential window of 2.5 V (compared to the 4.3 V potential window limit reported for this ionic liquid [5]) and at  $50 \text{ mV s}^{-1}$ . Since long-term stability of the cells (typically >500,000 cycles) was not being studied at this point in the project, only 1000 CV cycles were recorded. Chapter 7 is dedicated to the long-term stability of EDLCs and the influence of volatile impurity content (including water) on the performance of the ionogels. In addition, to gain better understanding of the electrochemical behaviour of each EDLC cell, the electrochemical impedance spectroscopy were conducted before and after the 1000 CV cycles as shown in the diagram below (Figure 5.19). The EIS settings are specified in Chapter 3, section 3.4.3. The gravimetric and planar areal capacitances were calculated based on the integration of enclosed area in the CV curves using the equation 3.18 provided in Chapter 3. The described experiments were conducted in duplicate and the results are provided in section 5.5.4 as set 1 and set 2.

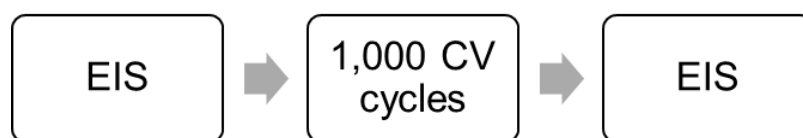


*Figure 5.19 The schematic illustration of the conducted electrochemical study discussed in this section.*

For comparison purposes, the electrochemical performance of the 'as-received' [Emim][TfO] ionic liquid was examined using the same techniques described above. A filter paper (2 cm in diameter, Whatman plc) was soaked with 200  $\mu\text{L}$  of the ionic liquid and was sandwiched between two activated carbon electrodes

to create a full EDLC cell. All activated carbon electrodes were utilised as received.

### 5.5.3 Characterisation of the activated carbon

The activated carbon electrodes were characterised using a variety of techniques. The microstructure of the AC was characterised using SEM microscopy (NOVA NanoSEM 200 (FEI, USA)). The hydrophobicity of the AC and the wettability of the electrode by [Emim][TfO] ionic liquid were examined using a drop shape analyser. The contact angle between a 2- $\mu$ L deionized water/[Emim][TfO] ionic liquid droplet and AC was recorded at five different locations and the average value is reported here. Surface area, pore volume and average pore size of AC were measured using the Brunauer-Emmett-Teller (BET) technique.

### 5.5.4 Results and discussion

Figure 5.20a shows an SEM image of the AC electrode surface demonstrating its microstructure. Presence of voids, i.e. inter-particle pores, with dimensions of a few micrometres facilitates electrolyte penetration. Although the microstructure is not uniform throughout the surface, small carbon black particles provide good electrical connection within the surface and bulk of the electrode. Based on the BET results, this electrode has a surface area of  $1169.61 \text{ m}^2 \text{ g}^{-1}$  and a pore volume of  $0.57 \text{ cm}^3 \text{ g}^{-1}$ . The average pore size was shown to be 2.01 nm, which originates from the intra-particle pores present on the carbon particles.

As can be seen in Figure 5.20b, the activated carbon electrode has a hydrophobic nature [43] with an average contact angle of  $124^\circ \pm 8.2$  with D.I. water. This characteristic makes the AC electrodes more resistant towards water contamination. In order to examine the wettability of this electrode by the ionic liquid chosen for this work, the contact angle between the two was examined and the results are demonstrated in Figures 5.20c and d. The first image corresponds to the moment of contact and the second image is 8 seconds after the initial contact. As can be seen, the ionic liquid has fully infiltrated into the AC after 8 seconds which proves great wettability.

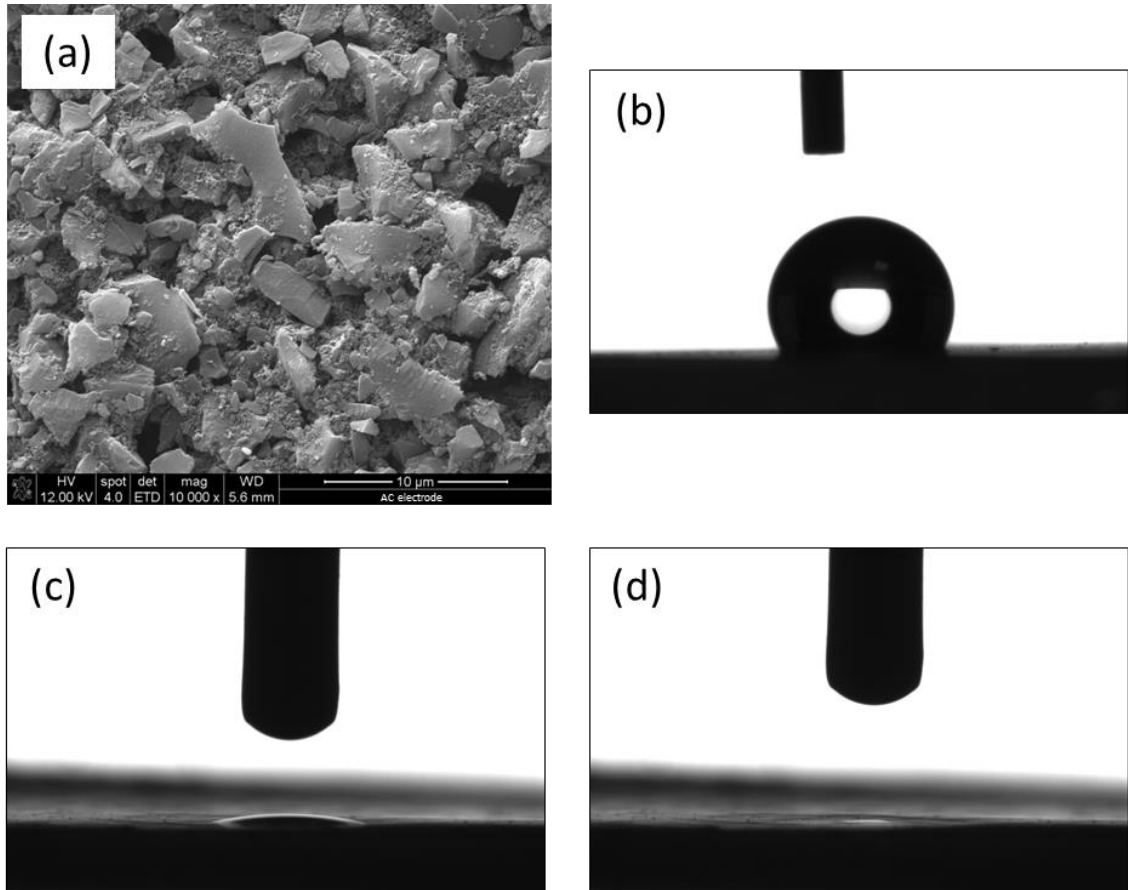


Figure 5.20 (a) SEM image showing the surface microstructure of the AC electrode, (b) contact angle of  $\sim 124^\circ$  between activated carbon and 2- $\mu\text{L}$  deionised water droplet, (c) and (d) contact angle between 2- $\mu\text{L}$  [Emim][TfO] ionic liquid droplet and activated carbon electrode at  $t=0$  s and  $t=8$  s, respectively.

Figure 5.21a shows the CV curves of EDLC with liquid electrolyte (pristine [Emim][TfO] ionic liquid) after 50, 250, 500, 750 and 1000 cycles. As it is shown, the CV curves have quasi-rectangular shape that is consistent throughout the 1000 charge-discharge cycles. As explained in Chapter 3 (section 3.4.1), a quasi-rectangular shaped CV curve indicates fast charge propagation in the electrodes and good capacitive behaviour [44,45]. It is necessary to note that the performance of this cell was examined immediately after being fabricated without allowing enough aging time for the electrolyte to fully wet the electrode through capillary forces (this phenomenon is studied and explained in Chapter 6). The areal and gravimetric capacitances calculated for the full EDLC cells based on the enclosed area in CV curves are tabulated in Table 5.6. The capacitance values are consistent over the 1000 CV cycles and the small drop in the capacitance value ( $\sim 5\%$ ) can be attributed to the water decomposition effects (investigated in Chapter 7) [46].

As mentioned in Chapter 3 section 3.4.3, a Nyquist plot, which is generated from EIS measurements, demonstrates the real (x-axis) and imaginary components (y-axis) of impedance response of an electrochemical system at different charge-discharge frequencies and it is generally divided into 3 regions: low, mid-range and high frequency regions. Figure 5.21b demonstrates the Nyquist plot of the EDLC cell before and after the CV cycles. With the exception of the intercept resistance,  $R_i$ , the shape of the Nyquist plot of the pristine ionic liquid cell remains unaltered after the cycling process. The almost vertical line in the low frequency region is associated with capacitive behaviour [47] and facile penetration of ions into the AC electrode pores [48]. In the high frequency region, the rate of charge-discharge cycling is too high ( $100 \text{ kHz} = 10^{-5} \text{ s}^{-1}$  duration of one charge-discharge cycle) for any mass transport to take place. Therefore, the high frequency intercept resistance is a representation of both the bulk electrolyte resistance [49,50] and electrical contact resistance [48]. Since the electrochemical measurements were conducted at room temperature, ionic conductivity and thus, electrolyte resistance is expected to remain constant [45]. Consequently, the change in  $R_i$  in Figure 5.21b is attributed to a change in electrical contact resistance. As described in Chapter 3 section 3.4, breadboard, CR2032 cell holders and jumper wire connections utilised in this project (based on availability) are not ideal tools for consistent contact resistance measurements and they can be sensitive to slight changes in cell position and connections and can be responsible for the changes in  $R_i$  in this work despite the efforts made to keep the connections and the cells stationary and consistent.

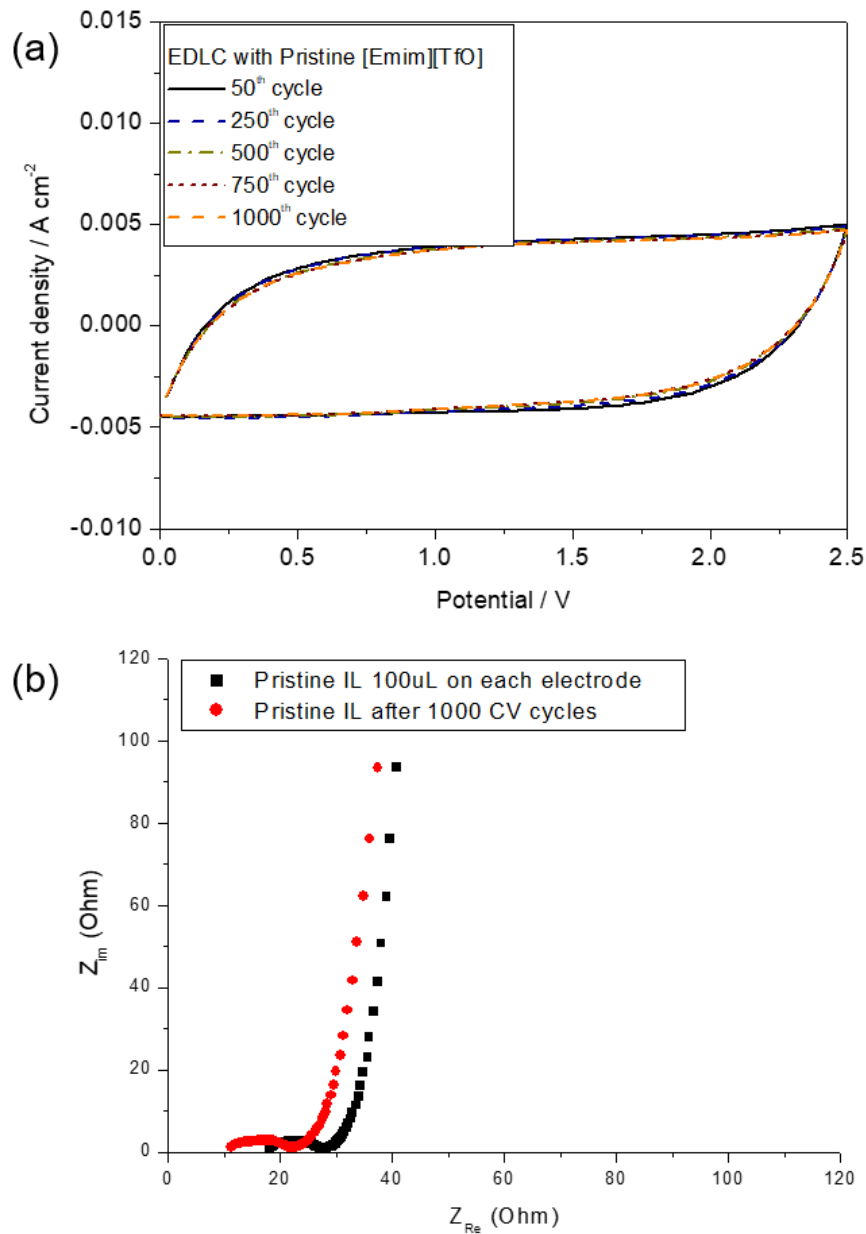


Figure 5.21 (a) CV curves of EDLC cell with pristine [Emim][TfO] ionic liquid electrolyte are displayed after 50, 250, 500, 750 and 1000 cycles and (b) Nyquist plot of the same cell before and after the CV cycles.

Table 5.6 Areal and gravimetric capacitances of EDLC with pristine [Emim][TfO] ionic liquid electrolyte calculated from 50<sup>th</sup>, 250<sup>th</sup>, 500<sup>th</sup>, 750<sup>th</sup> and 1000<sup>th</sup> CV cycles.

Sample	50 <sup>th</sup> cycle	250 <sup>th</sup> cycle	500 <sup>th</sup> cycle	750 <sup>th</sup> cycle	1000 <sup>th</sup> cycle	
Ionic liquid	$C_T / F g^{-1}$	19.09	18.90	18.30	18.04	18.04
	$C_T / mF cm^{-2}$	69.13	68.46	66.28	65.34	65.32

Figure 5.22 demonstrates the 1000<sup>th</sup> CV cycles of EDLCs with ionogel electrolytes. The quasi-rectangular curves of TMOS- and TEOS-based cells are indicative of excellent capacitive behaviour [44,45]. However, the CV curves for cells with MTES and MTMS ionogel electrolytes have more of an elliptical shape rather than quasi-rectangular. The distorted CV curves reflect resistive behaviour of the EDLCs and indicate that the cells behave more like a resistor rather than a supercapacitor [51]. In some circumstances, the distortion of CV curve can be attributed to 'electrolyte starvation', as described by Pell et al. [52] as the withdrawal of electrolyte charge carriers from the electrolyte bulk during the formation of double-layer. Although the underlying theory of this phenomena supports the connection between distortion of CV curves and an increase in the internal resistance of an electrochemical system, this phenomenon is only limited to the cases in which the concentration of electrolyte is low. Since the same volume of ionic liquid was utilised in all of the four EDLCs (36  $\mu\text{L}$  on each electrode), effect of electrolyte starvation can be ignored.

The areal and gravimetric capacitances of the EDLCs after 50, 250, 500, 750 and 1000 CV cycles are recorded in Table 5.7. Based on the encapsulated area in the CV curves, areal capacitance of TMOS, TEOS, MTMS and MTES-based full EDLCs were calculated to be 54.49, 60.43, 39.39 and 19.59  $\text{mF cm}^{-2}$ , respectively after 1000 cycles. An average of 30% drop in the capacitance value of ionogels can be detected, which is 6 times greater than that in the cell with pristine [Emim][TfO] ionic liquid electrolyte (as shown in Table 5.6). Although decomposition of impurities (water, alcohol and ester) is known to cause capacitance degradation [53], it is interesting that the degree of capacitance degradation is more pronounced for ionogels compared to EDLC with pristine ionic liquid (Table 5.6). The TGA results suggest that the impurity content of the ionic liquid (~2%) and the ionogels (2.3-3.3%) are in the same range. During the CV cycling process, two events are expected. First, the ionic liquid electrolyte permeates further into the electrode, wetting more area of the AC electrode and resulting in an increase in the cell capacitance. The second event is the process of impurity decomposition under the electric field applied across the cell which results in formation of by-products on the AC and reduction of the effective area of the electrode [53] (discussed further in Chapter 7, section 7.3.2). These

events are expected to take place in parallel during CV cycling. In the case of pristine ionic liquid, the cell is given no time prior to the electrochemical measurements for the wetting of the electrode whereas the ionogel samples were given between 12 hours and 4 days prior to being tested. Thus, it is believed that for the EDLC with pristine ionic liquid electrolyte, a great degree of wetting takes place during the measurement which masks the effects of impurity decomposition (further discussed in Chapter 7, section 7.3.2).

Figure 5.23 displays the cyclic voltammetry results of the second set of EDLCs containing ionogel electrolytes. The distorted CV curves for the MTMS- and MTES-based EDLCs and the quasi-rectangular CVs of the TMOS- and TEOS-based cells agree well with the results shown in Figure 5.22. The specific capacitance values of the 1000<sup>th</sup> CV cycles recorded in Table 5.8 are close to those in Table 5.7, confirming good agreement between the two sets of results. The shape of the CV curves and the capacitance values recorded for EDLCs with MTMS- and MTES-ionogels electrolytes are indicative of the highly resistive nature of these samples compared to the cells with TMOS- and TEOS-ionogels. To be able to understand the origin of this resistive behaviour, the EIS characteristics of these samples must be studied first.

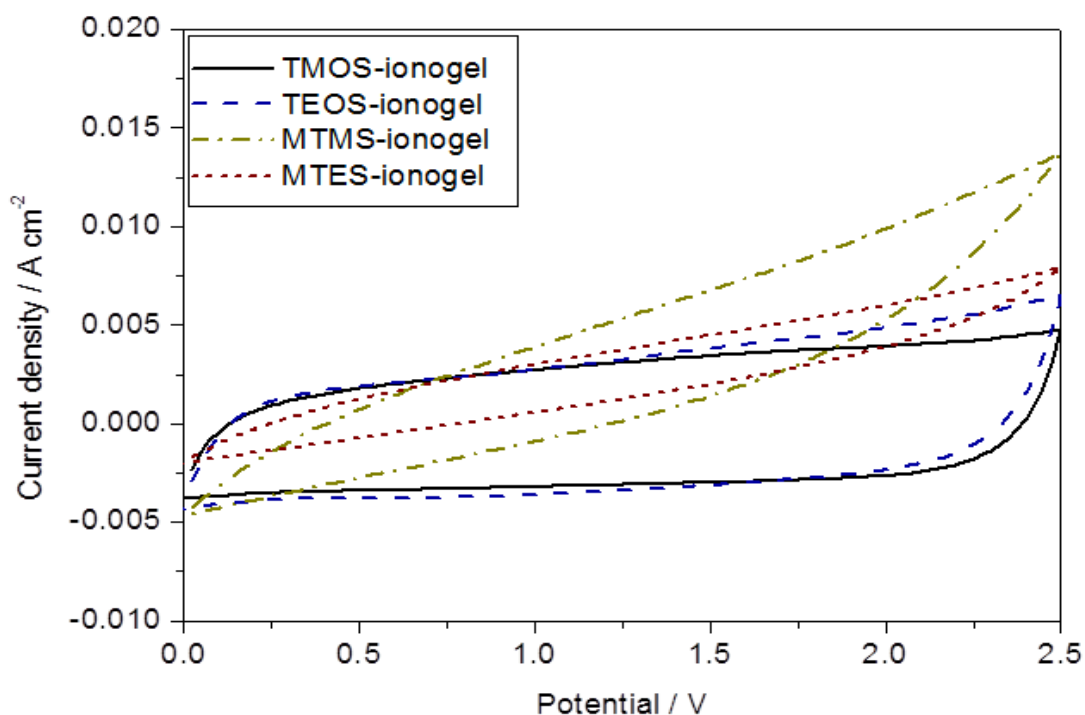


Figure 5.22 The 1000<sup>th</sup> CV curves of EDLCs with TMOS-, TEOS-, MTMS- and MTES-based ionogel electrolytes (set 1).

Table 5.7 Areal and gravimetric capacitance of EDLCs with TMOS-, TEOS-, MTMS- and MTES-based ionogel electrolytes calculated from CV curves 50, 250, 500, 750 and 1000 cycles (set 1).

Set 1		50 <sup>th</sup> cycle	250 <sup>th</sup> cycle	500 <sup>th</sup> cycle	750 <sup>th</sup> cycle	1000 <sup>th</sup> cycle
TMOS-ionogel	$C_T / F g^{-1}$	20.91	18.29	17.00	15.90	15.05
	$C_T / mF cm^{-2}$	75.72	66.25	61.56	57.57	54.49
TEOS-ionogel	$C_T / F g^{-1}$	22.83	19.38	17.73	17.02	16.69
	$C_T / mF cm^{-2}$	82.67	70.18	64.20	61.65	60.43
MTMS-ionogel	$C_T / F g^{-1}$	17.22	13.60	12.25	11.32	10.88
	$C_T / mF cm^{-2}$	62.37	49.26	44.37	40.99	39.39
MTES-ionogel	$C_T / F g^{-1}$	7.67	6.32	5.85	5.61	5.41
	$C_T / mF cm^{-2}$	27.76	22.89	21.19	20.30	19.59

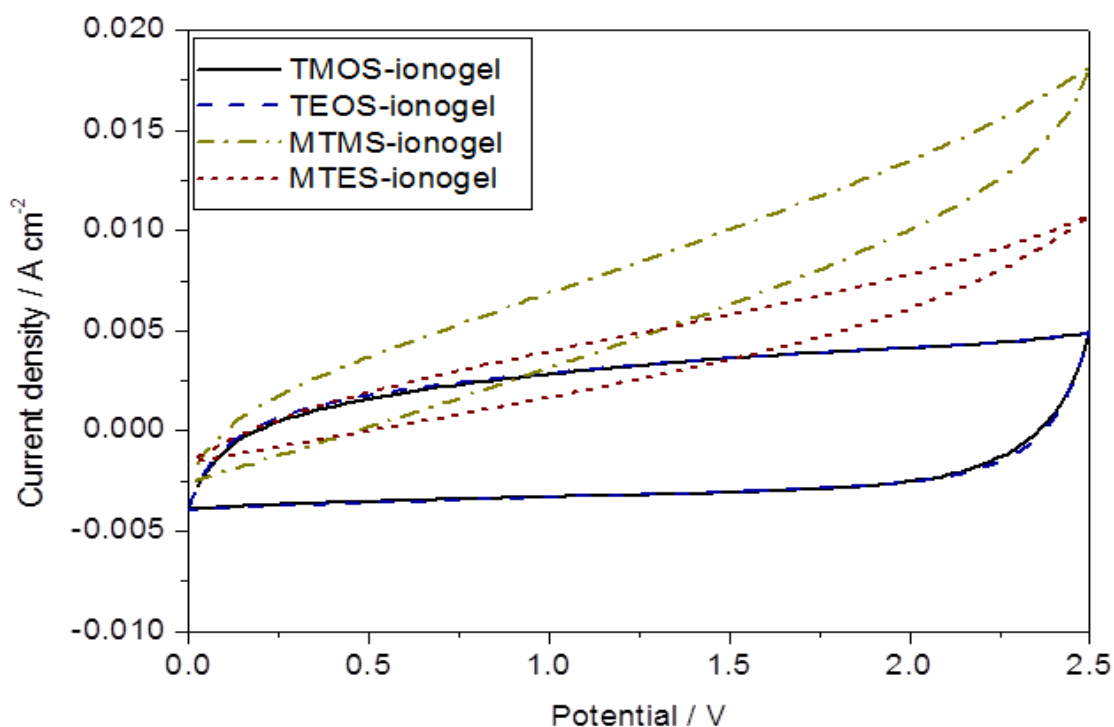


Figure 5.23 The 1000<sup>th</sup> CV curves of EDLCs with TMOS-, TEOS-, MTMS- and MTES-based ionogel electrolytes (set 2).

Table 5.8 Areal and gravimetric capacitance of EDLCs with TMOS-, TEOS-, MTMS- and MTES-based ionogel electrolytes calculated from CV curves 50, 250, 500, 750 and 1000 cycles (set 2).

Set 2		50 <sup>th</sup> cycle	250 <sup>th</sup> cycle	500 <sup>th</sup> cycle	750 <sup>th</sup> cycle	1000 <sup>th</sup> cycle
TMOS- ionogel	$C_T / F g^{-1}$	19.82	18.30	17.16	16.29	15.41
	$C_T / mF cm^{-2}$	71.77	66.28	62.15	58.98	55.81
TEOS- ionogel	$C_T / F g^{-1}$	19.31	17.64	16.45	15.85	15.64
	$C_T / mF cm^{-2}$	69.94	63.87	59.56	57.39	56.63
MTMS- ionogel	$C_T / F g^{-1}$	11.05	10.44	9.81	9.39	9.12
	$C_T / mF cm^{-2}$	40.00	37.81	35.51	33.99	33.03
MTES- ionogel	$C_T / F g^{-1}$	4.92	4.77	4.80	4.84	4.87
	$C_T / mF cm^{-2}$	17.82	17.23	17.39	17.53	17.64

The Nyquist plots of the EDLCs are demonstrated in Figures 5.24 (set 1) and 5.25 (set 2). The insets display the expanded high to mid-range frequency region of each Nyquist plot. As described previously and as can be observed, the variations of  $R_i$  show no specific trend, implying that these variations are associated with the non-ideal connections with the potentiostat. Thus, changes of  $R_i$  are ignored in this study.

As described in Chapter 3, the mid-range frequency semicircle (representing the charge transfer resistance) is associated with a number of electrical and ionic resistance components and, depending on the investigated system, one or more can have a dominating effect. A number of observations can be made in relation to the mid-range frequency region in the displayed Nyquist plots and these observations are discussed one by one in this section. As can be seen in Figure 5.24a and 5.25a, the mid-range semicircle for EDLCs with TMOS-ionogel, increase in size after 1000 CV cycles (by ~55% to 8.91  $\Omega$  in set 1 and by 52% to 12.92  $\Omega$  in set 2). This observation is attributed to the loss of contact between TMOS ionogel and the AC electrode during the electrochemical testing (>24 hours) due to shrinkage of the gel. Figure 5.26 displays the AC electrodes coated with (a) TMOS-ionogel and (b) TEOS ionogel after being aged under ambient conditions for 48 hours. The extreme shrinkage and delamination of TMOS ionogel can clearly be seen while the TEOS ionogel remains unchanged. Although the sol-gel transition point is reached within the first 12 hours of the synthesis for both of these ionogels, the process of condensation continues to proceed and can introduce mechanical stress, shrinkage and delamination. It was shown in section 5.3.2 that the initial sol-gel process kinetics of TEOS is slower than TMOS which could explain the difference in the physical appearance of the two ionogels after 48 hours as shown in Figure 5.26 and the increase in  $R_{ct}$  in TMOS-based cells and not in TEOS-based cells in the Nyquist plots (Figures 5.24 and 5.25). However, based on Figure 5.11, TEOS ionogel will suffer from fracturing and shrinking when aged under ambient conditions for a longer duration, due to continuation of the condensation process.

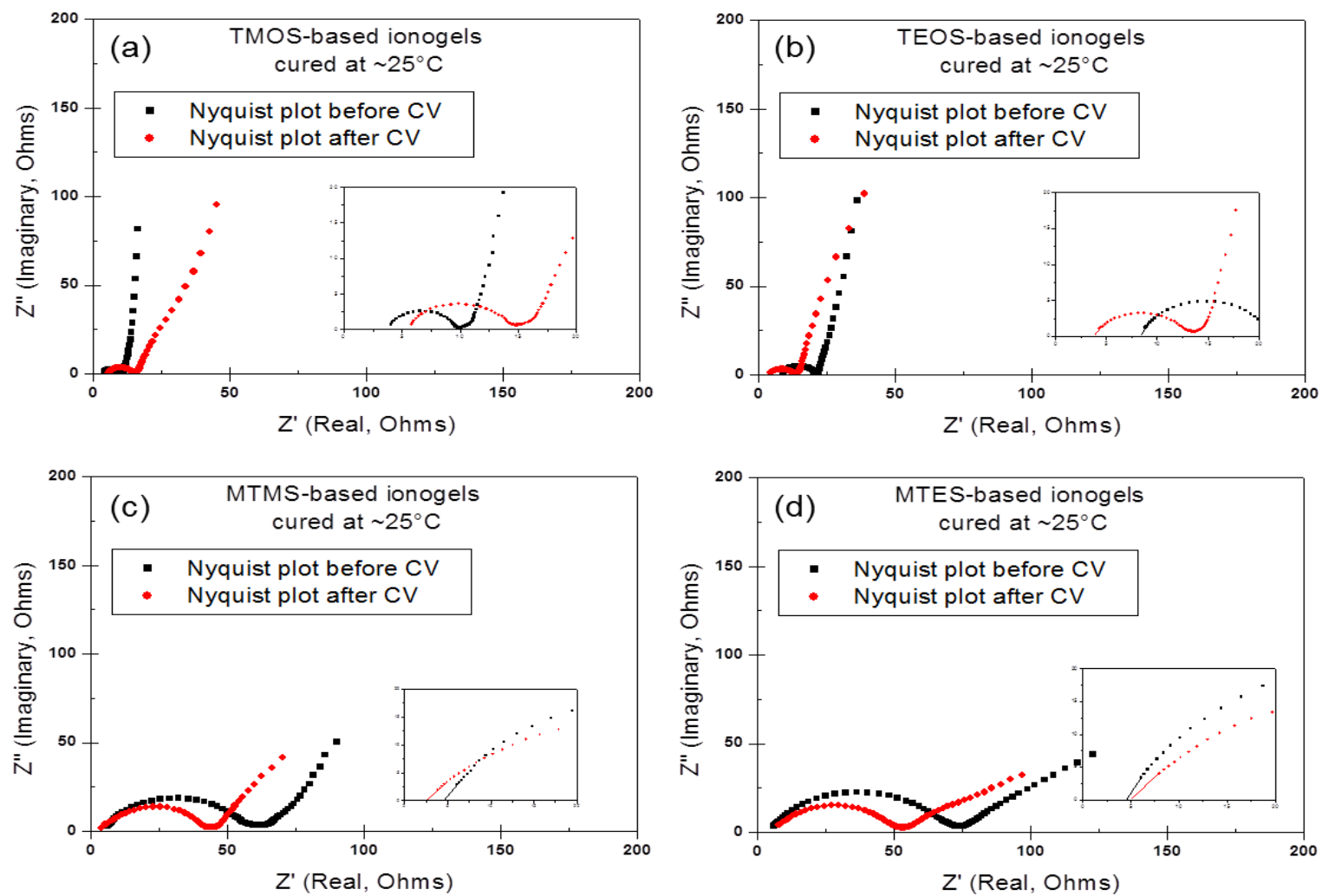


Figure 5.24 First set of Nyquist plots of (a) TMOS-, (b) TEOS-, (c) MTMS- and (d) MTES-based EDLCs before (black) and after (red) 1000 CV cycles.

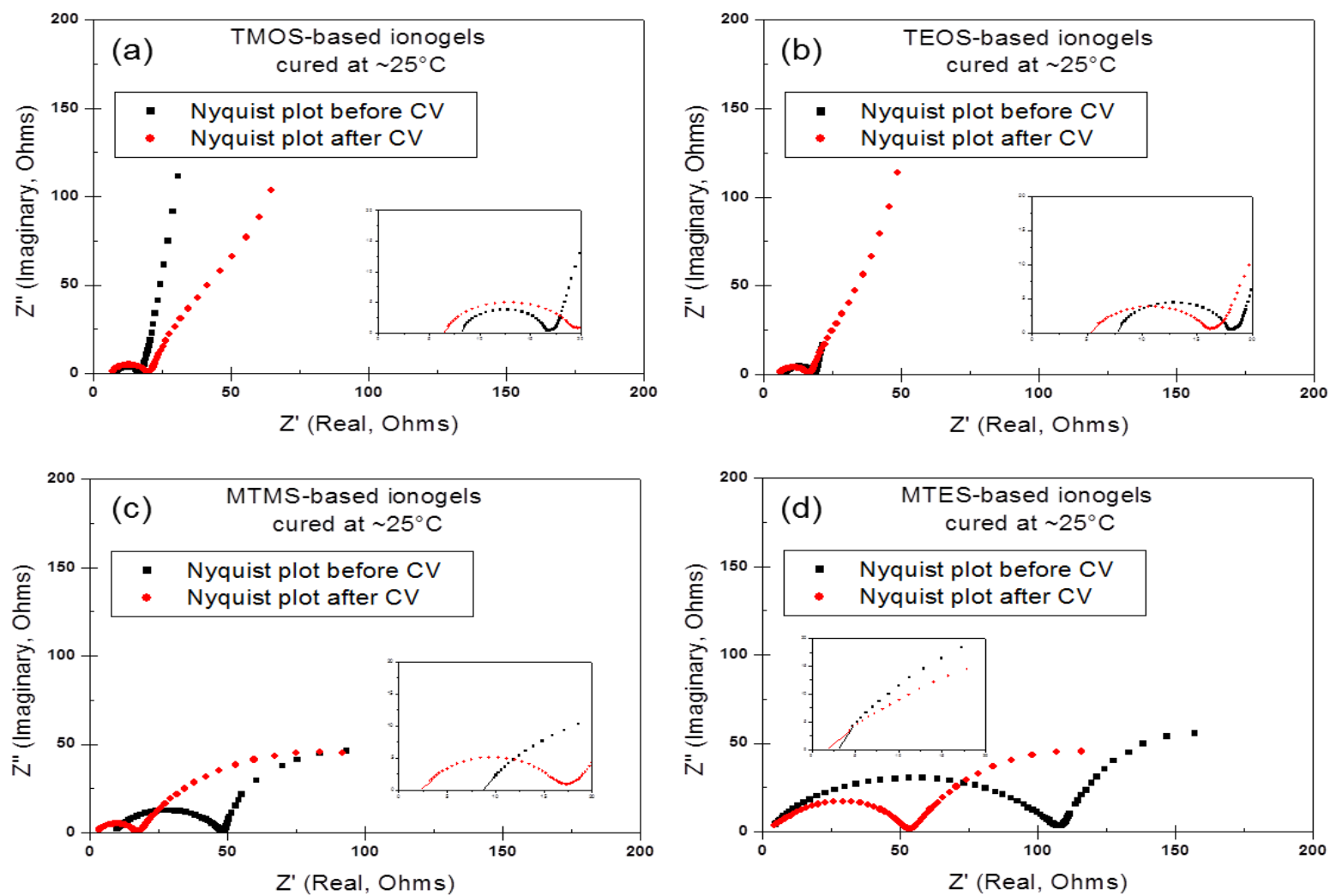


Figure 5.25 Second set of Nyquist plots of (a) TMOS-, (b) TEOS-, (c) MTMS- and (d) MTES-based EDLCs before (black) and after (red) 1000 CV cycles.

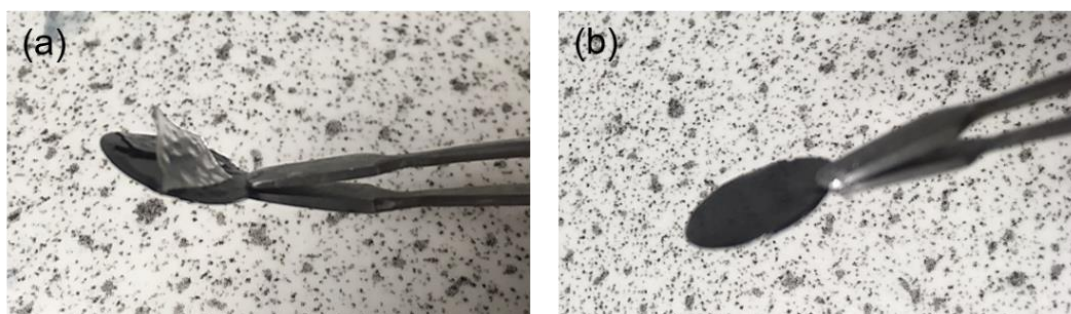


Figure 5.26 Images of (a) TMOS and (b) TEOS-based ionogel-coated AC electrodes after being aged under ambient conditions for 48 hours.

With the exception of the EDLCs with TMOS ionogels and that of TEOS ionogel in the second set (Figure 5.25b, where no change in  $R_{ct}$  is detected before and after the CV scans), the diameter of the semicircle drops after the CV cycling (by ~30-60%). The decrease in  $R_{ct}$  after cycling, which is observed in the MTMS- and MTES-based Nyquist plots, can be attributed to further wetting of the AC electrode by the electrolyte during charge-discharge cycles. During the charging step of the CV cycles, ions are forced towards the opposite electrodes by the applied electric field; This process effectively increases the surface area between AC and ionic liquid, reducing the resistance ( $R$ ) as per the following relationship [54,55]:

$$R = \frac{L}{A \times \sigma} \quad (\text{Eq. 5.1})$$

where  $L$  is the distance between the electrodes,  $A$  is the electrode area (permeated by the ionic liquid) and  $\sigma$  is the ionic conductivity. The  $L$  and  $\sigma$  parameters remain constant during the electrochemical measurements; therefore, changes in the resistance is associated with variation of the area. Further wetting of the electrodes by the ionic liquid is expected to increase the capacitance of the system which contradicts the variation of specific capacitance over time (Tables 5.7 and 5.8). Therefore, it is possible that decomposition of electrolyte impurities has a stronger effect on the overall capacitance of the cell.

Based on Figures 5.24 and 5.25, the overall mid-range frequency semicircle is larger for EDLCs with MTMS and MTES ionogels compared to that of cells with TMOS and TEOS ionogels. This confirms that the lower capacitance values calculated for the two former systems (recorded in Table 5.7 and 5.8) is due to

their larger internal resistance. There are two possible explanations for this observation:

1. Due to a not well-connected porous network or presence of ionic liquid inside closed pores in the MTMS and MTES ionogels, a fraction of the ionic liquid content does not participate in the formation of EDLC.
2. Considering the long gelation time for MTMS and MTES ionogels, ionogel solution might have diffused into the porous AC network and solidified within the pores of the electrode, blocking pores and reducing the effective surface area of the electrode. If ionogel has diffused deep enough, it can also reduce the contact area between the activated carbon and the current collector.

The first hypothesis has not been tested for the current investigation since a meaningful evaluation of the porosity and pore volume of the gel networks synthesised from TMOS, TEOS, MTMS and MTES precursors, requires BET characterisation (after careful removal of the ionic liquid without causing the porous network to collapse) with multiple replicates for each sample which is a costly and time-consuming process due to the lack of availability of this instrumentation at Sheffield Hallam University. Another way to test this hypothesis is to measure and compare the ionic conductivity of the ionogels which relies on the high frequency x-axis intercept or  $R_i$  in the Nyquist plots. However, As described in Chapter 3, section 3.4, the electrical connections utilised (based on availability) between the coin cells and the potentiostat are not ideal for consistent and reliable  $R_i$  measurements.

To test the 2<sup>nd</sup> hypothesis, the cross section of TEOS and MTES ionogel coated electrodes were observed under SEM and the distribution of silicon (representing the gel) was evaluated using EDX. The results of this evaluation are displayed in Figure 5.27. Due to similarities observed between the gelation rate of the TMOS and TEOS ionogels and between MTMS and MTES ionogels, it is believed that the electrodes coated with TEOS and MTES ionogels are representative of that of TMOS and MTMS ionogels, respectively. Figure 5.27a and c display the EDX results after a 12-minutes scan for TEOS and MTES-based samples, respectively. Figure 5.27b and d represent the same measurements at

a different location in both samples after a 45-minutes scan. In both cases it is clear that more silicon and thus, more MTES gel has diffused into the activated carbon compared to that of TEOS. Other than slow gel formation, further ingress of the MTES gel into the activated carbon can be ascribed to the hydrophobicity of the MTES gel which makes its solution more permeable in the hydrophobic AC compared to the hydrophilic TEOS gel network. In either case, the presence of higher silicon and thus, higher silica in the AC could cause pore blockage and an increase in the intrinsic resistance of the AC, as well as higher ionic resistance within AC electrodes.

As it was described in Chapter 3 (section 3.4.3), the low frequency region (straight line) in a Nyquist plot is associated with the intra-particle diffusion of electrolyte ions and double-layer formation ( $Z_{dl}$ ) [48,50]. The large inclining angle ( $>45^\circ$ ) of the low frequency semi-straight lines (with respect to x-axis) of the TMOS and TEOS-based cells are an indication of good capacitive performance [48], which agrees well with their CV results shown in Figures 5.22 and 5.23. For MTMS and MTES-based cells, the inclining angle of the straight line in the low frequency region is  $\leq 45^\circ$  (Figure 5.24c and d). A second semicircle is observed in the low frequency region of the second set of EIS results shown in Figure 5.25c and d. These observations can be attributed to diffusional limitation experienced by the cations and anions at low frequencies [56] and an increase in the distributed resistance in the AC electrodes [57] in cells containing MTMS and MTES ionogels. Based on the CV curves of the MTMS- and MTES-based cells (Figures 5.22 and 5.23) and the EDX results displayed in Figure 5.27, one can speculate that the diffusion of silica into the AC electrode not only blocks inter-particle pores but also influences the intra-particle pores which results in less pronounced capacitive behaviour and more resistive characteristic that is observed in both CV (and its elliptical shape) and EIS (large semicircle and low inclining angle of the low frequency line) results.

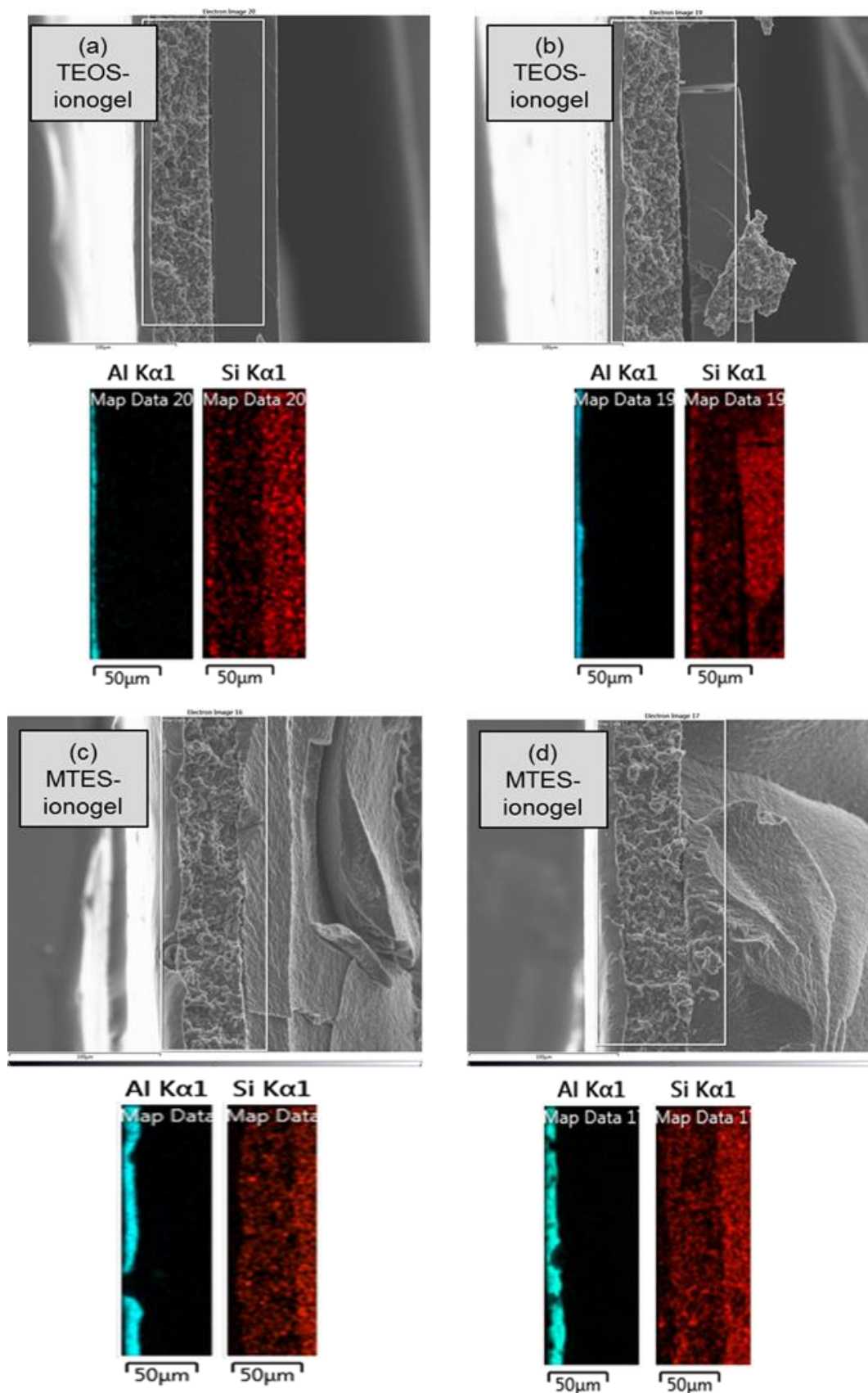


Figure 5.27 Distribution of Al current collector and silicon at the cross section of TEOS ionogel- (a & b) and MTES ionogel-(c & d) coated AC electrodes detected by EDX technique after scanning for 12 (a & c) and 45 minutes (b & d).

## 5.6 Conclusions

This chapter was designed to elucidate the influence of the alkoxide precursor type (TMOS, TEOS, MTMS and MTES) and the presence of [Emim][TfO] ionic liquid on the sol-gel process kinetics, microstructure, thermal stability and electrochemical performance of the resultant ionogel electrolyte.

The *in situ* Raman analysis showed that the rate of alkoxide consumption (evolution of Si–O stretching vibration band associated with Si–OC<sub>x</sub>H<sub>2x+1</sub>) is delayed for ionogel formulations containing TMOS, MTMS and TEOS precursors in relation to their xerogels. The MTES ionogel was the only formulation that showed no change in the precursor consumption rate compared to its counterpart xerogel. This can be associated with non-uniform dispersion of the [Emim][TfO] ionic liquid within the MTES ionogel mixture resulting in no apparent change in the rate of MTES consumption. The rate of  $\nu(\text{Si-O})$  band disappearance from the Raman spectra of the ionogel mixtures followed a similar trend to that of xerogels: MTMS>TMOS~MTES>TEOS. Furthermore, it was observed that the TMOS and TEOS ionogels reach the sol-gel transition point after 12 hours while the gelation process takes 4 days for MTMS and MTES formulations to be achieved. As discussed in Chapter 2, long gelation and drying processes are not practical from an industrial point of view where manufacturing time is paramount. Although TMOS and TEOS ionogels can seem advantageous from the gelation-time point of view, their weak mechanical structure, evidenced by their brittle nature, is a downside for these ionogels. It is possible that by aging these ionogels inside a dry environment, the degree of shrinkage post-gelation can be reduced. This requires further investigation.

In terms of thermal stability, TGA data confirmed that confinement within silica network increases the onset temperature for [Emim][TfO] ionic liquid decomposition.

Weak or low density of interactions was detected between ionic liquid and the silica networks. Further investigation is necessary to confirm this observation and to conclusively determine the nature and degree of these interactions. Moreover, based on the SEM characterisations in Chapter 4 and the current chapter, it is concluded that the topography of the silica network is influenced by

the presence of [Emim][TfO] ionic liquid as well as the type of the precursor. While the presence of this ionic liquid promoted formation of macropores, the non-hydrolysable methyl groups in MTMS and MTES resulted in formation of larger secondary silica particles within the silica network by disturbing the colloidal stability in the sol. The ionogels synthesised from the methoxy-based precursors (TMOS and MTMS) displayed more uniform microstructures compared to the ethoxy-based formulations (TEOS and MTES) which can be due to a better dispersion of [Emim][TfO] ionic liquid within the former ionogels.

The combination of CV and EIS analyses confirmed that cells containing MTMS and MTES ionogels behave more resistive compared to TMOS- and TEOS-based cells which can be associated with ingress of silica gel deep into the AC electrodes during the 4 days gelation time causing the internal resistance of the system to considerably increase. On the other hand, the extensive shrinkage of TMOS ionogel is believed to have caused loss of electrode-ionogel contact, increase in the internal resistance and degradation of capacitance.

Thus, it is fair to conclude that the choice of the alkoxide precursor for ionogel synthesis is important and must be taken into consideration in order to meet the required properties for the application. Although each of the formulations resulted in encapsulation of ionic liquid, the properties of the resultant gels were significantly different. For gelation under ambient conditions, TMOS and TEOS ionogels showed the most suitable electrochemical properties with reduced aging period of 12 hours – this would require further reduction to become industrially viable. However, due to extensive shrinkage and fracturing post-gelation under ambient conditions, their application as electrolyte for EDLCs is jeopardised.

## 5.7 References

- [1] Q. Zhu, Y. Song, X. Zhu, X. Wang, Ionic liquid-based electrolytes for capacitor applications, *J. Electroanal. Chem.* 601 (2007) 229–236. doi:10.1016/j.jelechem.2006.11.016.
- [2] C. Arbizzani, M. Bisio, D. Cericola, M. Lazzari, F. Soavi, M. Mastragostino, Safe, high-energy supercapacitors based on solvent-free ionic liquid electrolytes, *J. Power Sources.* 185 (2008) 1575–1579. doi:10.1016/J.JPOWSOUR.2008.09.016.
- [3] G. Wang, L. Zhang, J. Zhang, A review of electrode materials for electrochemical supercapacitors, *Chem. Soc. Rev.* 41 (2012) 797–828. doi:10.1039/C1CS15060J.
- [4] A. Eftekhari, Supercapacitors utilising ionic liquids, *Energy Storage Mater.* 9 (2017) 47–69. doi:10.1016/j.ensm.2017.06.009.
- [5] Ionic liquids for electrochemical applications, *Aldrich ChemFiles.* 5 (2005) 10. <https://www.sigmaaldrich.com/technical-documents/articles/chemfiles/ionic-liquids-electrochemical.html> (accessed June 20, 2018).
- [6] S. Zhang, X. Lu, Q. Zhou, X. Li, X. Zhang, S. Li, Imidazolium, in: *Ion. Liq. Physicochemical Prop.*, Elsevier, 2009: pp. 23–197. doi:10.1016/B978-0-444-53427-9.00002-6.
- [7] X. Ge, J. Li, C. Zhang, Z. Wang, J. Luo, Superlubricity of 1-ethyl-3-methylimidazolium trifluoromethanesulfonate ionic liquid induced by tribochemical reactions, *Langmuir.* 34 (2018) 5245–5252. doi:10.1021/acs.langmuir.8b00867.
- [8] S. Liu, W. Liu, Y. Liu, J. Lin, X. Zhou, M.J. Janik, R.H. Colby, Q. Zhang, Influence of imidazolium- based ionic liquids on the performance of ionic polymer conductor network composite actuators, *Polym. Int.* 59 (2010) 321–328. doi:10.1002/pi.2771.

- [9] Z. Liu, S.Z. El Abedin, F. Endres, Raman and FTIR spectroscopic studies of 1-ethyl-3-methylimidazolium trifluoromethylsulfonate, its mixtures with water and the solvation of Zinc ions, *ChemPhysChem*. 16 (2015) 970–977. doi:10.1002/cphc.201402831.
- [10] D.K. Singh, B. Rathke, J. Kiefer, A. Materny, Molecular structure and interactions in the ionic liquid 1-ethyl-3-methylimidazolium trifluoromethanesulfonate, *J. Phys. Chem. A*. 120 (2016) 6274–6286. doi:10.1021/acs.jpca.6b03849.
- [11] K.G. Sharp, A two-component, non-aqueous route to silica gel, *Sol-Gel Sci. Technol.* 2 (1994) 35–41.
- [12] R. Winter, J. Chan, R. Frattini, J. Jonas, The effect of fluoride on the sol-gel process, *J. Non. Cryst. Solids*. 105 (1988) 214–222.
- [13] A. Martinelli, L. Nordstierna, An investigation of the sol-gel process in ionic liquid-silica gels by time resolved Raman and <sup>1</sup>H NMR spectroscopy, *Phys. Chem. Chem. Phys.* 14 (2012) 13216–13223. doi:10.1039/C2CP41914A.
- [14] C.A.M. Mulder, A.A.J.M. Damen, Raman analysis of the initial stages of the hydrolysis and polymerization of tetraethylorthosilicate, *J. Non. Cryst. Solids*. 93 (1987) 169–178. doi:10.1016/S0022-3093(87)80036-4.
- [15] J.L. Lippert, S.B. Melpolder, L.M. Kelts, Raman spectroscopic determination of the pH dependence of intermediates in sol-gel silicate formation, *J. Non. Cryst. Solids*. 104 (1988) 139–147. doi:10.1016/0022-3093(88)90193-7.
- [16] A. Martinelli, Effects of a protic ionic liquid on the reaction pathway during non-aqueous sol–gel synthesis of silica: A Raman spectroscopic investigation, *Int. J. Mol. Sci.* 15 (2014) 6488–6503. doi:10.3390/ijms15046488.

- [17] M. Nayeri, K. Nygård, M. Karlsson, M. Maréchal, M. Burghammer, M. Reynolds, A. Martinelli, The role of the ionic liquid  $C_6C_1ImTFSI$  in the sol-gel synthesis of silica studied using in situ SAXS and Raman spectroscopy, *Phys. Chem. Chem. Phys.* 17 (2015) 9841–9848. doi:10.1039/C5CP00709G.
- [18] I.-G. Marino, P.P. Lottici, D. Bersani, R. Raschellà, A. Lorenzi, A. Montenero, Micro-Raman monitoring of solvent-free TEOS hydrolysis, *J. Non. Cryst. Solids.* 351 (2005) 495–498. doi:10.1016/J.JNONCRY SOL.2004.11.023.
- [19] J.-C. Panitz, A. Wokaun, Characterization of the sol-gel process using Raman spectroscopy organically modified silica gels prepared via the formic acid-alkoxide route, *J. Sol-Gel Sci. Technol.* 9 (1997) 251–263. doi:10.1007/BF02437188.
- [20] M.A. Klingshirn, S.K. Spear, J.D. Holbrey, R.D. Rogers, Ionic liquids as solvent and solvent additives for the synthesis of sol-gel materials, *J. Mater. Chem.* 15 (2005) 5174. doi:10.1039/b508927a.
- [21] A. Vioux, L. Viau, S. Volland, J. Le Bideau, Use of ionic liquids in sol-gel; ionogels and applications, *Comptes Rendus Chim.* 13 (2010) 242–255. doi:https://doi.org/10.1016/j.crci.2009.07.002.
- [22] A.A. Pisal, A.V. Rao, Comparative studies on the physical properties of TEOS, TMOS and  $Na_2SiO_3$  based silica aerogels by ambient pressure drying method, *J. Porous Mater.* 23 (2016) 1547–1556. doi:10.1007/s10934-016-0215-y.
- [23] Y. Yu, W. Fan, Y. Wang, X. Zhou, J. Sun, S. Liu, C-H...O interaction in methanol-water solution revealed from Raman spectroscopy and theoretical calculations, *J. Phys. Chem. B.* 121 (2017) 8179–8187. doi:10.1021/acs.jpcc.7b06036.
- [24] H. Olivier-Bourbigou, L. Magna, D. Morvan, Ionic liquids and catalysis: Recent progress from knowledge to applications, *Appl. Catal. A Gen.* 373 (2010) 1–56. doi:10.1016/J.APCATA.2009.10.008.

- [25] A.K. Gupta, Y.L. Verma, R.K. Singh, S. Chandra, Studies on an ionic liquid confined in silica nanopores: Change in  $T_g$  and evidence of organic-inorganic linkage at the pore wall surface, *J. Phys. Chem. C.* 118 (2014) 1530–1539. doi:10.1021/jp408142a.
- [26] M. Nayeri, M.T. Aronson, D. Bernin, B.F. Chmelka, A. Martinelli, Surface effects on the structure and mobility of the ionic liquid  $C_6C_1ImTFSI$  in silica gels, *Soft Matter.* 10 (2014) 5618–5627. doi:10.1039/C4SM00642A.
- [27] C.J. Brinker, G.W. Scherer, *Sol-gel science: The physics and chemistry of sol-gel processing*, 1990. doi:10.1186/1471-2105-8-444.
- [28] A. Taubert, R. Löbbicke, B. Kirchner, F. Leroux, First examples of organosilica-based ionogels: synthesis and electrochemical behavior, *Beilstein J. Nanotechnol.* 8 (2017) 736–751. doi:10.3762/bjnano.8.77.
- [29] K. Liu, C. Lian, D. Henderson, J. Wu, Impurity effects on ionic-liquid-based supercapacitors, *Mol. Phys.* 115 (2017) 454–464. doi:10.1080/00268976.2016.1271154.
- [30] R. Gobel, P. Hesemann, J. Weber, E. Moller, A. Friedrich, S. Beuermann, A. Taubert, Surprisingly high, bulk liquid-like mobility of silica-confined ionic liquids, *Phys. Chem. Chem. Phys.* 11 (2009) 3653–3662. doi:10.1039/B821833A.
- [31] A. Darmawan, R. Utari, R.E. Saputra, Suhartana, Y. Astuti, Synthesis and characterization of hydrophobic silica thin layer derived from methyltrimethoxysilane (MTMS), *IOP Conf. Ser. Mater. Sci. Eng.* 299 (2017) 012041.
- [32] M.A.B.H. Susan, T. Kaneko, A. Noda, M. Watanabe, Ion gels prepared by in situ radical polymerization of vinyl monomers in an ionic liquid and their characterization as polymer electrolytes, *J. Am. Chem. Soc.* 127 (2005) 4976–4983. doi:10.1021/ja045155b.
- [33] J.-Y. Gui, B. Zhou, Y.-H. Zhong, A. Du, J. Shen, Fabrication of gradient density  $SiO_2$  aerogel, *J. Sol-Gel Sci. Technol.* 58 (2011) 470–475. doi:10.1007/s10971-011-2415-x.

- [34] S.J. Kim, S.C. Jana, Effects of skin layers on air permeability in macroporous polymer aerogels, *Polym. (United Kingdom)*. 126 (2017) 432–436. doi:10.1016/j.polymer.2017.03.039.
- [35] A. Nešić, M. Gordić, S. Davidović, Ž. Radovanović, J. Nedeljković, I. Smirnova, P. Gurikov, Pectin-based nanocomposite aerogels for potential insulated food packaging application, *Carbohydr. Polym.* 195 (2018) 128–135. doi:10.1016/J.CARBPOL.2018.04.076.
- [36] G.H. Bogush, C.F. Zukoski IV, Studies of the kinetics of the precipitation of uniform silica particles through the hydrolysis and condensation of silicon alkoxides, *J. Colloid Interface Sci.* 142 (1991) 1–18. doi:10.1016/0021-9797(91)90029-8.
- [37] Y. Zhang, C. Zhao, P. Wang, L. Ye, J. Luo, B. Jiang, A convenient sol–gel approach to the preparation of nano-porous silica coatings with very low refractive indices, *Chem. Commun.* 50 (2014) 13813–13816. doi:10.1039/C4CC05397D.
- [38] F. Endres, S. Zein El Abedin, Air and water stable ionic liquids in physical chemistry, *Phys. Chem. Chem. Phys.* 8 (2006) 2101. doi:10.1039/b600519p.
- [39] R. Newell, J. Faure-Vincent, B. Iliev, T. Schubert, D. Aradilla, A new high performance ionic liquid mixture electrolyte for large temperature range supercapacitor applications (–70°C to 80°C) operating at 3.5 V cell voltage, *Electrochim. Acta.* 267 (2018) 15–19. doi:10.1016/j.electacta.2018.02.067.
- [40] H. Zheng, H. Zhang, Y. Fu, T. Abe, Z. Ogumi, Temperature effects on the electrochemical behavior of spinel  $\text{LiMn}_2\text{O}_4$  in quaternary ammonium-based ionic liquid electrolyte, *J. Phys. Chem. B.* 109 (2005) 13676–13684. doi:10.1021/jp051238i.
- [41] M. He, K. Fic, E. Fęcowskiak, P. Novák, E.J. Berg, Ageing phenomena in high-voltage aqueous supercapacitors investigated by in situ gas analysis, *Energy Environ. Sci.* 9 (2016) 623–633. doi:10.1039/C5EE02875B.

- [42] A.I. Horowitz, M.J. Panzer, High-performance, mechanically compliant silica-based ionogels for electrical energy storage applications, *J. Mater. Chem.* 22 (2012) 16534–16539. doi:10.1039/C2JM33496H.
- [43] Y. Yuan, T.R. Lee, Contact angle and wetting properties, in: G. Bracco, B. Holst (Eds.), *Surf. Sci. Tech.*, Springer Berlin Heidelberg, Berlin, Heidelberg, 2013: pp. 3–34. doi:10.1007/978-3-642-34243-1\_1.
- [44] M.F. El-Kady, R.B. Kaner, Scalable fabrication of high-power graphene micro-supercapacitors for flexible and on-chip energy storage, *Nat. Commun.* 4 (2013) 1475–1479. doi:10.1038/ncomms2446.
- [45] L. Negre, B. Daffos, V. Turq, P.L. Taberna, P. Simon, Ionogel-based solid-state supercapacitor operating over a wide range of temperature, *Electrochim. Acta.* 206 (2016) 490–495. doi:https://doi.org/10.1016/j.electacta.2016.02.013.
- [46] D. Cericola, P.W. Ruch, A. Foelske-Schmitz, D. Weingarth, R. Kötz, Effect of water on the aging of activated carbon based electrochemical double layer capacitors during constant voltage load tests, *Int. J. Electrochem. Sci.* 6 (2011) 988–996.
- [47] R. Signorelli, D.C. Ku, J.G. Kassakian, J.E. Schindall, Electrochemical double-layer capacitors using carbon nanotube electrode structures, *Proc. IEEE.* 97 (2009) 1837–1847. doi:10.1109/JPROC.2009.2030240.
- [48] N.H. Basri, M. Deraman, M. Suleman, N.S.M. Nor, B.N.M. Dolah, M.I. Sahri, S.A. Shamsudin, Energy and power of supercapacitor using carbon electrode deposited with nanoparticles nickel oxide, *Int. J. Electrochem. Sci.* 11 (2016) 95–110.
- [49] C. Lei, F. Markoulidis, Z. Ashitaka, C. Lekakou, Reduction of porous carbon/Al contact resistance for an electric double-layer capacitor (EDLC), *Electrochim. Acta.* 92 (2013) 183–187. doi:10.1016/J.ELECTACTA.2012.12.092.
- [50] H.D. Yoo, J.H. Jang, J.H. Ryu, Y. Park, S.M. Oh, Impedance analysis of porous carbon electrodes to predict rate capability of electric double-layer

capacitors, *J. Power Sources*. 267 (2014) 411–420.  
doi:10.1016/J.JPOWSOUR.2014.05.058.

- [51] O. Fontaine, A. Toudjine, M. Maréchal, C. Bonhomme, F. Ribot, B. Geffroy, B. Jousselme, C. Sanchez, C. Laberty-Robert, A one-pot route to prepare class II hybrid ionogel electrolytes, *New J. Chem.* 38 (2014) 2008–2015. doi:10.1039/C3NJ01272G.
- [52] W.G. Pell, B.E. Conway, N. Marincic, Analysis of non-uniform charge/discharge and rate effects in porous carbon capacitors containing sub-optimal electrolyte concentrations, *J. Electroanal. Chem.* 491 (2000) 9–21. doi:10.1016/S0022-0728(00)00207-2.
- [53] Y. Liu, B. Soucaze-Guillous, P.L. Taberna, P. Simon, Understanding of carbon-based supercapacitors ageing mechanisms by electrochemical and analytical methods, *J. Power Sources*. 366 (2017) 123–130. doi:10.1016/j.jpowsour.2017.08.104.
- [54] M.S. Wu, T.L. Liao, Y.Y. Wang, C.C. Wan, Assessment of the wettability of porous electrodes for lithium-ion batteries, *J. Appl. Electrochem.* 34 (2004) 797–805. doi:10.1023/B:JACH.0000035599.56679.15.
- [55] R.S. Kühnel, S. Obeidi, M. Lübke, A. Lex-Balducci, A. Balducci, Evaluation of the wetting time of porous electrodes in electrolytic solutions containing ionic liquid, *J. Appl. Electrochem.* 43 (2013) 697–704. doi:10.1007/s10800-013-0558-x.
- [56] H. Wang, Z. Xu, A. Kohandehghan, Z. Li, K. Cui, X. Tan, T.J. Stephenson, C.K. King'ondeu, C.M.B. Holt, B.C. Olsen, J.K. Tak, D. Harfield, A.O. Anyia, D. Mitlin, Interconnected carbon nanosheets derived from hemp for ultrafast supercapacitors with high energy, *ACS Nano*. 7 (2013) 5131–5141. doi:10.1021/nn400731g.
- [57] P.W. Ruch, D. Cericola, A. Foelske-Schmitz, R. Kötz, A. Wokaun, Aging of electrochemical double layer capacitors with acetonitrile-based electrolyte at elevated voltages, *Electrochim. Acta*. 55 (2010) 4412–4420. doi:10.1016/j.electacta.2010.02.064.

## **6. Influence of curing temperature on the performance of silica-based ionogels as electrolyte for supercapacitors**

### **6.1 Introduction**

The non-flammable nature of ionogels makes them an attractive replacement for commonly utilised electrolytes in batteries and supercapacitors. However, there is still a long list of criteria for ionogels to improve upon before being industrially applicable and viable for consumer products. Improvement of electrochemical performance and reduction of ionic liquid electrolyte cost are two of the current challenges that researchers in this field are commonly dealing with [1–4]. In addition, depending on the formulation and the fabrication environment, the process of gelation and drying of silica-based ionogels can typically take up to a few days to complete [5–7]. As it was shown in Chapter 5, the type of silica precursor can greatly influence the gelation duration (12 hours for TMOS and TEOS and 4 days for MTMS and MTES ionogels). From an industrial perspective, manufacturing speed is paramount, having a direct impact on the production costs and this is a major drawback. Increasing the reaction temperature is an effective way to speed up condensation and drying stages, as elevated temperature promotes removal of volatiles and formation of covalent Si–O–Si bridges [8,9]. However, fast gelation and drying can introduce high capillary stress to the silica network and cause severe shrinkage and cracking. This can be resolved by incorporating (non-hydrolysable) organic functional groups into the structure to reduce the capillary stress and thus minimise shrinkage during gelation [9]. To the best of our knowledge, the application of high curing temperatures (>100°C) as a catalysing mechanism for ionogel synthesis and its influence on the resultant properties are currently unexplored. Due to their high viscosity, the physiochemical properties of ionic liquids are highly temperature dependant [10,11]. Hence, it is crucial to investigate the influence of curing temperature on the properties of ionogels as this can potentially minimise the gelation and drying time.

Conversely, operating-temperature dependency of the performance of energy storage devices containing ionic liquids has been widely studied. Zheng et al.

investigated the electrochemical behavior of a spinel  $\text{LiMn}_2\text{O}_4$  electrode in trimethylhexylammonium (TMHA) bis(trifluoromethane)sulfonylimide (TFSI) ionic liquid electrolyte containing 1M LiTFSI salt as a function of temperature [10]. They demonstrated that due to the high viscosity of the ionic liquid electrolyte, the electrode-electrolyte interface resistance inside the electrochemical cell is strongly temperature dependant. In fact, they observed a ~90% drop in the electrode-electrolyte interface resistance when the temperature was increased from 20°C to 50°C whilst conducting impedance measurements. Similarly, Rodrigues et al. reported a 50-fold decrease in the electrode-electrolyte interface resistance of a lithium ion half cell containing (methoxymethyl)triethylphosphonium bis(tri-fluoromethylsulfonyl)imid ionic liquid electrolyte and a lithium titanate electrode when the temperature of the test environment was increased from 25°C to 60°C [11]. Negre et al. showed that the ionic conductivity of an ionogel containing a mixture of two bis(fluorosulfonyl)imide-based ionic liquids almost doubled to  $11 \text{ mS cm}^{-1}$  when the temperature was raised from 20 to 80°C [12]. However, the application of supercapacitors and batteries are not limited to high operating temperatures. The major challenge is to improve the performance of such systems at room temperature.

In this chapter, we attempt to address both the slow gelation and poor performance at room temperature by introducing heat during the process of ionogel condensation. The present chapter aims to investigate the influence of curing temperature on:

- a) Gelation time of silica-based ionogels,
- b) Penetration coefficient of the ionic liquid,
- c) Physical structure of ionogels,
- d) Room-temperature electrochemical performance of EDLCs fabricated by sandwiching the heat-cured ionogels between activated carbon (AC) electrodes.

Based on the knowledge gathered from Chapters 4 and 5, TMOS and MTMS are the most compatible precursors in terms of initial sol-gel process kinetics (rate of precursor consumption) in the absence and presence of [Emim][TfO]

ionic liquid among the four silica precursors studied. In this chapter, the most suitable formulation was chosen that enabled heat-cured processing with minimal shrinkage. This is discussed in detail in sections 6.2.1 and 6.3.1.

## **6.2 Experimental procedure**

### **6.2.1 Electrolyte preparation and EDLC fabrication**

The ionogel electrolytes were synthesised using the non-hydrolytic sol-gel route described in Chapter 5. Various formulations were tested for optimisation purposes which are discussed in detail in section 6.3.1. TMOS (Sigma Aldrich,  $\geq 98\%$ ) and MTMS (Sigma Aldrich,  $\geq 98\%$ ) were mixed in a glass vial together with 1-ethyl-3-methylimidazolium trifluoromethanesulfonate ([Emim][TfO] ionic liquid, Sigma Aldrich,  $\geq 98\%$ ) under continuous stirring (600 rpm) for 10 minutes using a magnetic stir bar. The sol-gel process was then initiated by adding formic acid (FA, Aldrich  $\geq 96\%$ ). This was followed by another 10 minutes mixing time. All of the reagents were used as received. The silica precursor: FA molar ratio was kept constant at 4:14 for all samples. After the 20 minutes synthesis process, a fixed volume (containing 36  $\mu\text{L}$  of [Emim][TfO] ionic liquid) of each mixture was deposited onto each activated carbon disk using a micropipette. The electrodes utilised for this investigation were cut into 15 mm diameter disks and had a mass loading of  $\sim 5.4 \text{ mg cm}^{-2}$ . The ionogel-coated electrodes were heated to  $150^\circ\text{C}$  using a furnace (ELF 10/6, Carbolite, UK) at a ramp rate of  $5^\circ\text{C min}^{-1}$  for 60 minutes. Out of 10 different formulations, the one with the most uniform ionogel coating was selected for the remaining of the heat-cure investigation.

Four sets of the selected ionogel formulations were then prepared in the same manner as described previously and were heated at four different temperatures: 125, 150, 175 and  $200^\circ\text{C}$ . As described above, a ramping rate of  $5^\circ\text{C min}^{-1}$  was used and the temperature was held isothermally at its final value for 60 minutes. The total duration of heat-treatment ranged between 75 and 90 minutes. Once the heating process was completed, the ionogel coated AC electrodes were left to cool at ambient temperature for two minutes. The double-layer supercapacitor cells were then sandwiched in CR2032 coin cells inside glove box under a nitrogen atmosphere to avoid any moisture contamination.

### **6.2.2 Electrochemical characterisation**

Electrochemical impedance spectroscopy (EIS) measurements of the EDLC cells were obtained using a PARSTAT 4000A potentiostat (Princeton Applied Research, USA). A 10 mV rms potential was applied oscillating around 0 V bias voltage over a frequency range of 100 k to 10 mHz. The cyclic voltammetry (CV) analysis was performed in a potential window of 2.5 V and at a scanning rate of 50 mV s<sup>-1</sup>. The areal capacitance values were calculated based on the integration of enclosed area in the CV curves after 5 cycles. All electrochemical tests were taken periodically at room temperature across a period of 48 hours. An EIS scan followed by 5 CV cycles were recorded every hour between 0-5 hours and after 24 and 48 hours from EDLC fabrication.

### **6.2.3 Viscosity measurements**

The viscosity of the ionic liquid was measured using a MCR301 Rheometer (Anton Paar, UK) equipped with a bob and cup setup. A shear rate of 10 s<sup>-1</sup> was utilized while the temperature was nominally raised from 25-200°C at 2°C min<sup>-1</sup> ramping rate. These measurements were repeated 3 times and the mean value is reported here. Due to limitations of the instrumentation, the actual maximum temperature achieved during measurement was 188°C. Viscosity at 200°C was therefore estimated by extrapolating the viscosity vs. temperature curve.

### **6.2.4 Surface tension measurements**

The surface tension of [Emim][TfO] ionic liquid was measured using a DCAT25 tensiometer equipped with TEC250 temperature control chamber (DataPhysics Instruments GmbH, Germany).

### **6.2.5 Scanning electron microscopy (SEM) characterisation**

The morphology of the ionogel-coated electrodes' cross section was investigated using a Nova 200 NanoSEM (FEI, USA) at 10 kV. A 20 nm layer of gold was sputtered on the cross sections to prevent charging effect. The topography of the heat-cured ionogels was also investigated using SEM in the fashion described in Chapter 5, section 5.4.1.

### **6.2.6 Raman spectroscopy measurements**

The spatial distribution of [Emim][TfO] ionic liquid at the cross section of the 125 and 200°C cured ionogel coated-AC electrodes was characterised using Raman spectroscopy (200-3200 cm<sup>-1</sup>). A line-map was acquired (1% laser power and

an exposure time of 60 s) across the cross section with a step size of 5  $\mu\text{m}$ , a total of 65 steps and x5 objective which resulted in a degree of oversampling (spot size  $\sim 8 \mu\text{m}$ ).

Figure 6.1 demonstrates the steps involved in deconvolution of Raman-map raw data. The overall spatial distribution of each compound was extracted simultaneously from the Raman line-map using ISys® (version 5.0.0.14) and MCR (multivariate curve resolution) software (version 1.6) using NIPALS (non-linear iterative partial least squares) and ALS (alternating least squares) algorithms to separate the data into i) spectra of different compounds present (referred to as number of factors, represented by matrix  $S^T$ ) and ii) the relative intensity of each compound/factor at each location along the map (represented by matrix C). The maximum number of iterations for the ALS algorithm was set to 500. As can be seen in Figure 6.1, data from both of the samples (125 and 200°C) are combined into one matrix (A1-A65 & A66-A130) in order to use the same model for both of the samples and increase the reliability of the results.

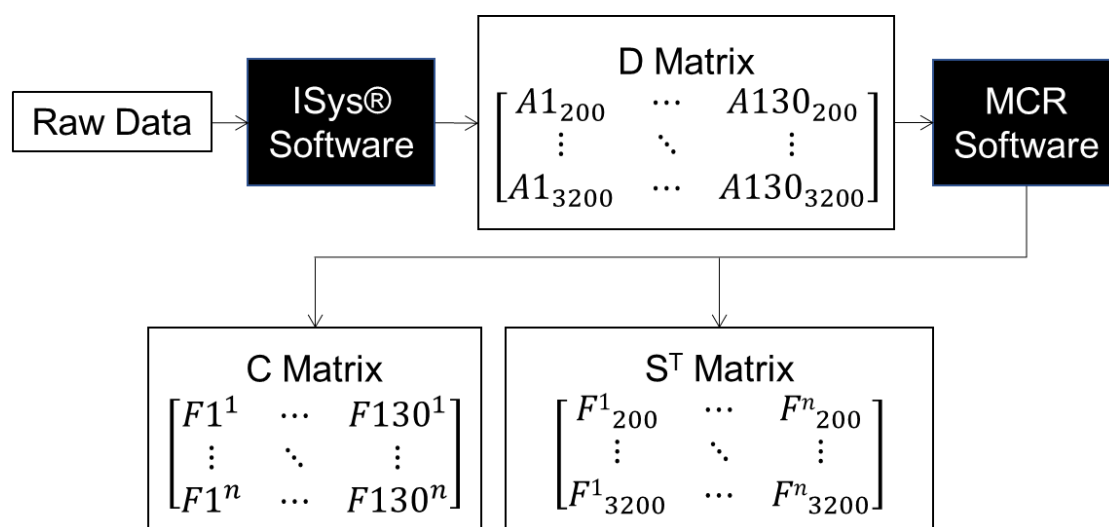


Figure 6.1 Steps involved in transforming Raman-map raw data into D, C and  $S^T$  matrices using ISys® and MCR software. A1-A65 and A66-A130 components in D matrix represent the 125°C and 200°C data set at each point of the line map (130 points in total), respectively.  $F^1$  to  $F^n$  represent the number of components/factors available in the line-map. The subscripts in D and  $S^T$  matrices represent individual wave-numbers at which Raman spectra were collected.

## 6.3 Results and discussion

### 6.3.1 Formulation optimisation

Figure 6.2 shows the optical images that can be used to characterise the physical appearance of ionogel-coated electrodes with different formulations after being heated at 150°C for 60 minutes. The first row of images is associated with

samples of 4:4 silica precursor: ionic liquid molar ratio while the second line has samples with increased ionic liquid molar ratio (4:8). As no flowing behaviour was observed upon tilting the electrode, all samples were considered to have been fully gelled after the heating process except for the sample with TMOS: MTMS: ionic liquid molar ratio of 0:4:8.

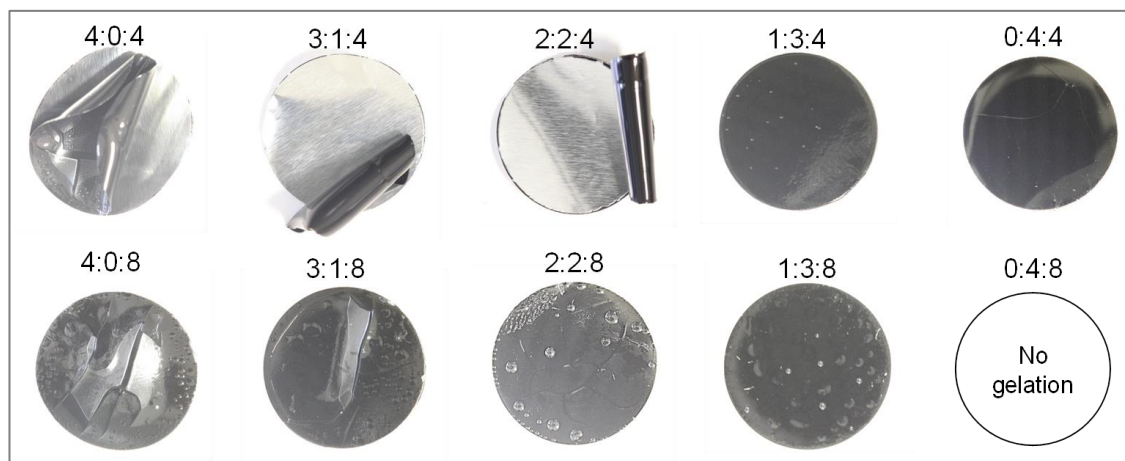


Figure 6.2 Optical images of ionogel coated electrodes with various formulations heated at 150°C for an hour. All formulations are fully gelled during the heating process except for the 0:4:8 formulation (TMOS: MTMS: IL) which showed no signs of gelation after the heat treatment. The ratio of silica precursor to FA was kept at 4:14 in all formulations.

Based on the optical images, as the MTMS and ionic liquid content is increased a more uniform and fracture-free ionogel film is generated. This can be attributed to the formulation utilised in this work. The hydrophobic methyl groups (derived from MTMS precursor) can limit the formation of crosslinking Si–O–Si bridges in certain directions (i.e. where CH<sub>3</sub> groups are located) and hinder the condensation process, counterbalancing the fast gelation tendency at high temperatures (to some extent). By incorporating organic functional groups into the gel network, the capillary tension, shrinkage and fracturing of ionogels (caused by fast gelation) can be reduced. One can rationalise that the presence of stable ≡Si–CH<sub>3</sub> groups in the silica monolith partially offsets the mechanical stress and thus, the overall brittleness of the ionogels [13]. In addition, increase in the ionic liquid content (reduction of silica content) reduces the degree of shrinkage and the subsequent matrix collapse since ionic liquid is capable of forming a non-volatile film on the silica pore walls protecting the pores from drying stresses during evaporation of by-products [14,15]. Based on the optical images, the most stable formulations (generating the most uniform fracture-free coatings)

were 1:3:4 and 1:3:8 (TMOS: MTMS: ionic liquid). Generally, minimised silica content is preferred for electrolyte applications as not only lower scaffold content can result in reduced ionic diffusion resistance [16], it can reduce the density of ionic liquid-silica scaffold interaction due to lower degree of confinement [17]. For these reasons, the 1:3:8 ratio was chosen as the most suitable formulation for the remaining of the heat-cure investigation.

Figure 6.3a represents a hypothesised structure of a typical siloxane network where organic functional groups (represented by R) are located within the structure in a disordered manner. Figure 6.3b displays the optical images of ionogel coated electrodes (with 1:3:8 formulation, TMOS: MTMS: ionic liquid) after being cured at 125, 150, 175 and 200°C. As can be observed, no signs of fracturing or shrinkage have been noted in the samples cured at the two lower temperatures. However, despite the presence of CH<sub>3</sub> groups in the gel matrix, fractures can be observed in samples cured at 175 and 200°C as shown in Figure 6.3b. This can be attributed to a modest degree of shrinkage as a result of fast removal of volatiles from the ionogel network at temperatures  $\geq 175^\circ\text{C}$ . In the case of the 200°C curing temperature, the increased removal rate of volatiles has resulted in high capillary stress (greater than the incorporation of  $\equiv\text{Si}-\text{CH}_3$  could overcome) which caused shrinkage and formation of fractures.

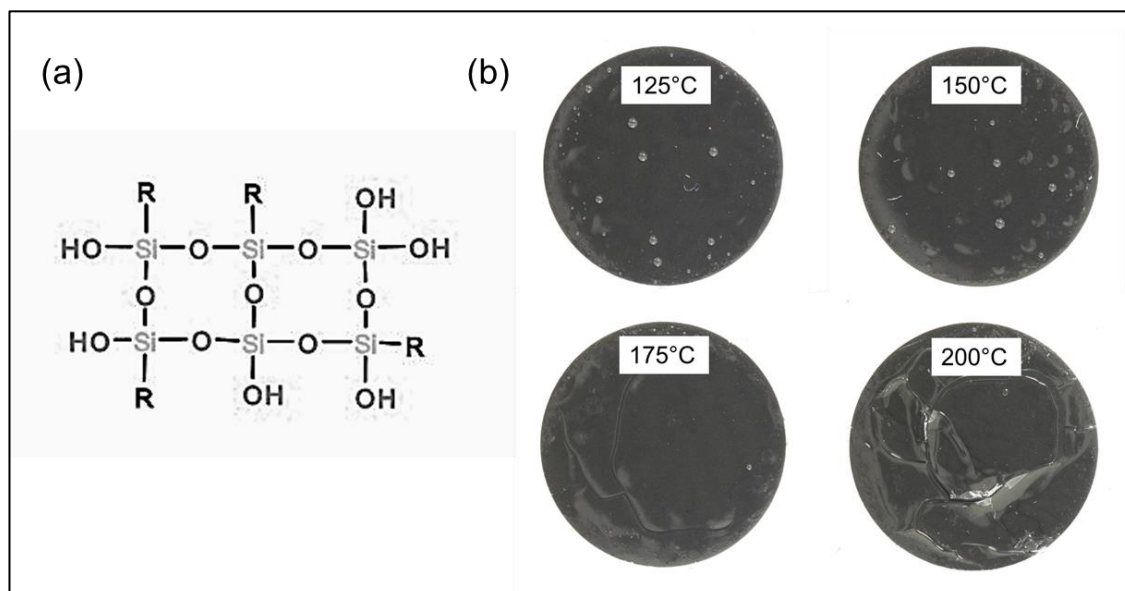


Figure 6.3 (a) The hypothesised chemical structure of a typical silica network containing organic functional groups (R) and (b) the optical images of ionogel coated electrodes when cured at various temperatures ranging from 125 to 200°C. The small drops on the surface of the electrodes are ionic liquid.

Figure 6.4 demonstrates the microstructure of the 150°C heat-cured TMOS-MTMS xerogel (after the removal of the ionic liquid). It is clear that the structure of the silica network has adapted characteristics of both TMOS and MTMS-based networks i.e. small pore sizes and large secondary silica particles, respectively. The overall structure of the network is an intermediate between TMOS and MTMS xerogels shown in Chapter 5 (Figures 5.14-5.17).

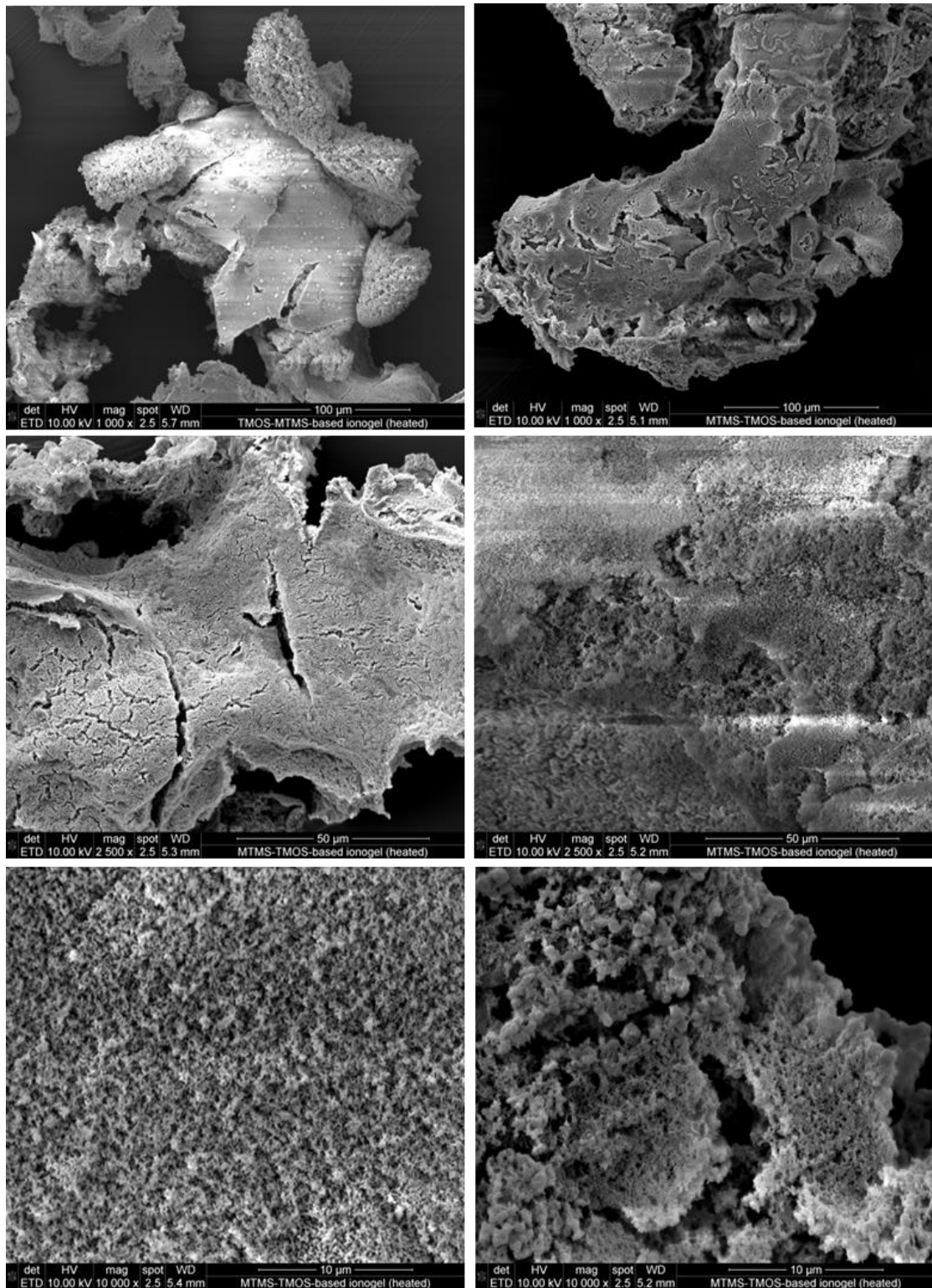


Figure 6.4 SEM images of TMOS-MTMS-based ionogel after the removal of the ionic liquid i.e. xerogel. Heterogeneous structure of the silica network has both TMOS and MTMS-based characteristics. The dense layer visible in the first image is the skin layer formed as a result of faster gelation and drying processes at the air-exposed layer on the very top surface of the gel compared to the bulk of the gel (discussed in Chapter 5, section 5.4.2).

### 6.3.2 Changes in penetration coefficient of [Emim][TfO] ionic liquid with temperature

Ionic liquids are known for their relatively high viscosity at room temperature compared to other commercially used liquid electrolytes [11]. For this reason, when heat is introduced to a system containing ionic liquids, a considerable change in performance of the system is to be expected. In the case of systems where ionic liquid is in contact with a porous structure, these variations are likely to translate into changes in the wetting rate of the porous network. Generally, the wetting rate of a porous electrode is dictated by the degree of spreading and penetration of the electrolyte [18]. The Lucas-Washburn equation (Eq. 6.1) models the electrolyte movement in a porous electrode with the assumption of the porous network being an entity of capillaries (evenly arranged) [2,18]:

$$k = \sqrt{\frac{r_{eff} \sigma \cos \theta}{2\eta}} \quad (\text{Eq. 6.1})$$

where  $k$  is the penetrability or penetration coefficient,  $r_{eff}$  is the effective radius of capillary,  $\sigma$  is the liquid-to-vapor surface tension,  $\theta$  is the three phase contact angle and  $\eta$  is the viscosity. A higher  $k$  value is associated with faster liquid flow within a porous network. One must not forget that most of the porous electrodes are not an ensemble of evenly arranged capillaries but rather a complex network of pores oriented in random directions. Therefore, the focus in this study was not to evaluate the exact value of penetration coefficient but to investigate the relative changes in  $k$  as a function of curing temperature. If one assumes that there are no changes in the effective pore size with temperature, the relative changes of  $k$  can be estimated using equation 6.2:

$$k \propto \sqrt{\frac{\sigma \cos \theta}{2\eta}} \quad (\text{Eq. 6.2})$$

Figure 6.5 demonstrates the variation of [Emim][TfO] ionic liquid viscosity with temperature. As mentioned previously this test was repeated 3 times and the average values together with measured surface tension as well as the cosine of the static contact angle (between the ionic liquid and AC electrode, discussed in Chapter 5, section 5.5.4) are recorded in Table 6.1.

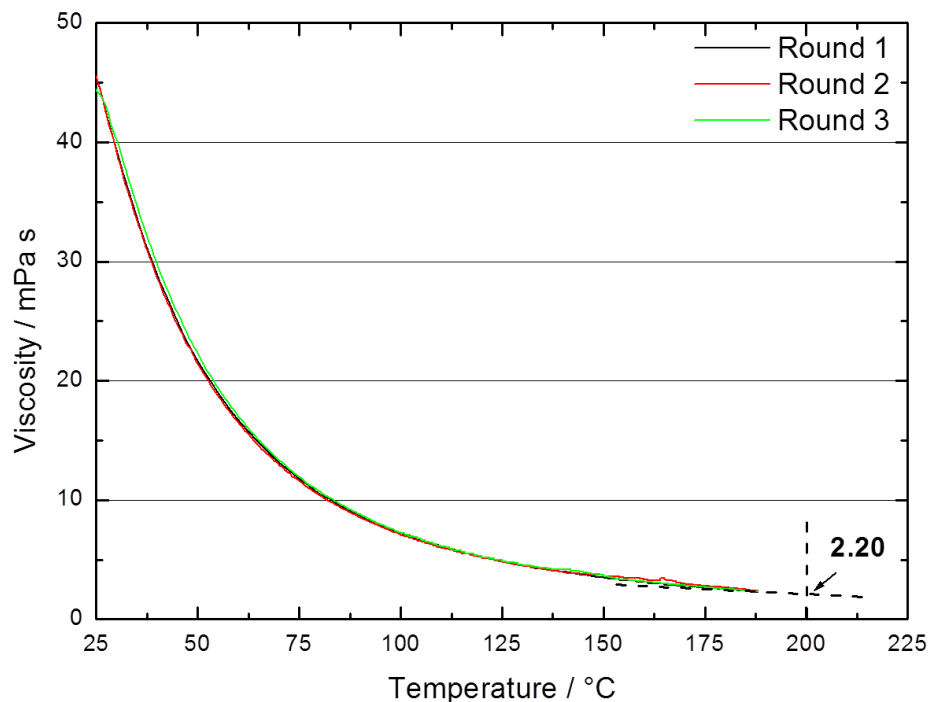


Figure 6.5 Variation of [Emim][TfO] ionic liquid viscosity with temperature (25-188°C). Due to limitations of the instrumentation, the viscosity at 200°C was estimated by extrapolating the viscosity vs. temperature curve.

As presented in Chapter 5 (Figure 5.20c and d), the static contact angle between the activated carbon electrode and ionic liquid approaches 0° within 8 seconds at room temperature (~22°C). Surface tension is reduced with increase in temperature [19], causing the contact angle to decrease [18], thus, one can postulate that  $\theta$  approaches 0° much faster at higher temperatures. For this reason,  $\cos \theta$  is assumed to be 1 in all cases from 22 to 200°C. Thus, changes in  $k$  become dependant on surface tension and viscosity assuming no change takes place in the effective pore radius. It was observed that, the viscosity of ionic liquid drops by ~55% when temperature is increased from 125 to 200°C, while surface tension decreases by ~8%. This agrees with the literature [2,18] considering viscosity to be the main factor influencing wetting rate. Based on these results, ~40% increase in the penetration coefficient is expected when increasing the curing temperature from 125 to 200°C.

Table 6.1 Influence of temperature on physical properties of [Emim][TfO] ionic liquid.

Temperature / °C	$\sigma$ / mN m <sup>-1</sup>	cos $\theta$	$\eta$ / mPa s	$\sqrt{\frac{\sigma \cos \theta}{2\eta}}$ / (m s <sup>-1</sup> ) <sup>1/2</sup>
25°	40.51 $\mp$ 0.02	1	44.00 $\mp$ 0.21	0.68
125°	36.84 $\mp$ 0.04	1	4.90 $\mp$ 0.06	1.94
150°	35.94 $\mp$ 0.03	1	3.60 $\mp$ 0.10	2.23
175°	34.88 $\mp$ 0.06	1	2.70 $\mp$ 0.06	2.54
200°	33.84 $\mp$ 0.07	1	$\cong$ 2.20	2.77

### 6.3.3 Effect of temperature on the physical structure of electrode-electrolyte interface

The SEM images of post-cure electrode cross sections are shown in Figure 6.6. Starting from the left hand side within Figure 6.6a, one can observe a thin layer of Al foil, upon which sits the porous activated carbon electrode and lastly, in direct contact with this, the dense ionogel solid electrolyte can be identified. The high porosity of the activated carbon electrodes explains their extensive application in energy storage systems as they provide large surface area and hence increase the maximum achievable capacity in such devices. Figure 6.6a shows that the interface between the gel electrolyte and the AC electrode is sharp and clearly visible. This interface becomes more diffuse as the temperature is raised above 125°C (Figures 6.6b to 6.6d). At higher curing temperatures (>150°C), ionogel is postulated to penetrate further through the electrode and mask the top surface of electrode as observed in the SEM images (Figures 6.6c and 6.6d). In the latter cases, the electrode and the electrolyte are interpenetrated as a result of the heat-induced interlocking effect [20]. The porous structure of the AC electrodes cannot easily be discerned in samples treated at curing temperatures of 175 and 200°C. In addition, a degree of delamination from the Al foil can be seen in all four samples. The reasons for delamination of the AC

electrode from the Al foil are i) defects caused during the process of cutting the electrodes and ii) the impact of heat on the electrode binder. The PVDF binder in the AC electrodes has a melting point of 177°C [21] and thus, it goes through a melting and re-solidification process when the curing temperature is 175°C and above. The influence of this 'contact loss', melting and re-solidifying of PVDF is discussed in the following section (6.3.4).

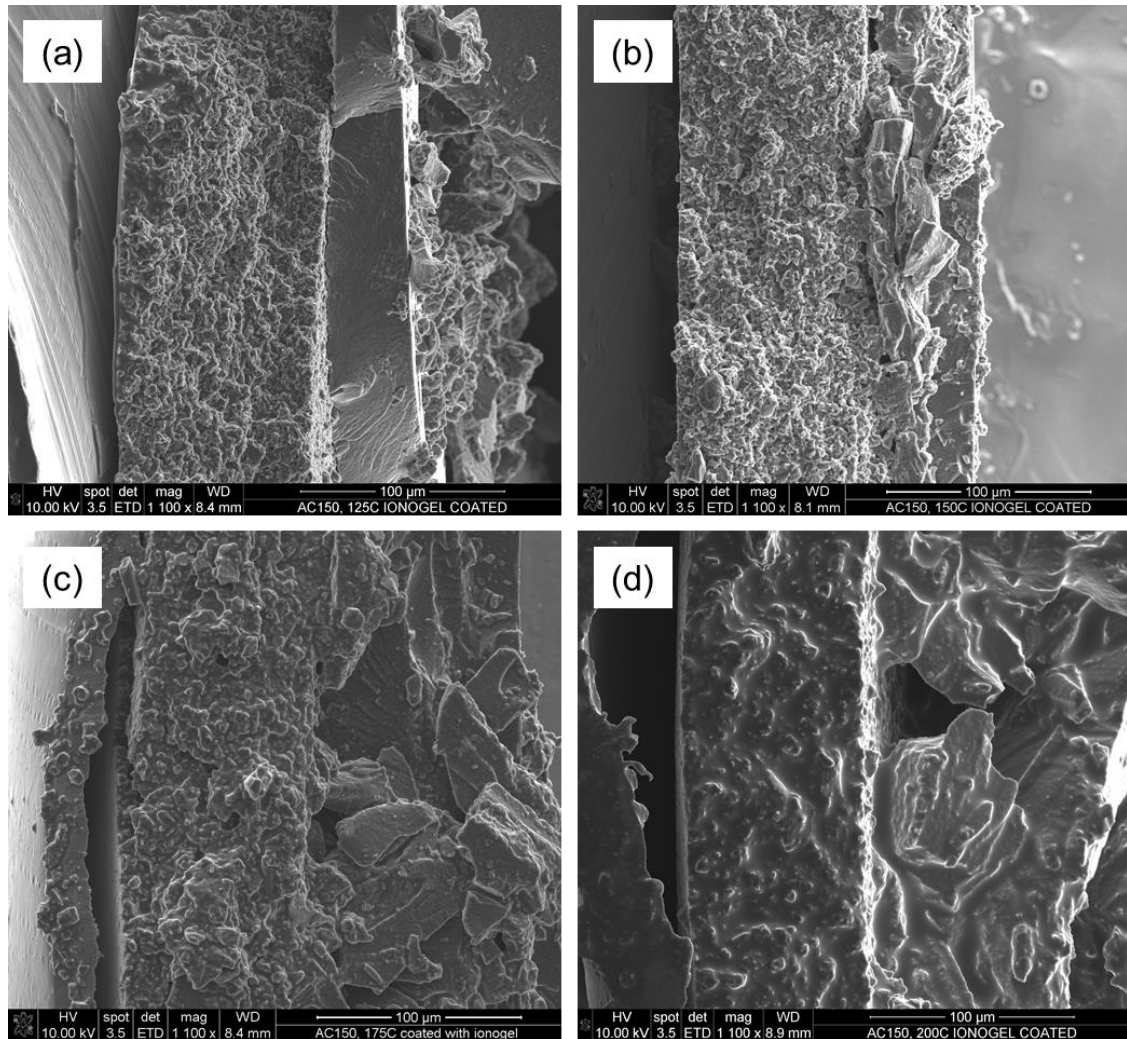


Figure 6.6 (a) Electron microscope cross section images of ionogel-coated AC electrodes cured at: (a) 125°C, (b) 150°C, (c) 175°C and (d) 200°C. From left to right in each image, traces of Al foil, porous activated carbon electrode and ionogel electrolyte can be identified.

### 6.3.4 Evolution of impedance with respect to temperature and time

Figure 6.7 displays the Nyquist plots of cells with ionogel electrolytes cured at four different temperatures after 0, 5, 24 and 48 hours of assembling the cell. Figure 6.7a breaks down the three different regions in a Nyquist plot. As can be observed in Figure 6.7,  $R_i$  ranges between 2 to 5  $\Omega$  among all samples and

does not vary greatly with time. As explained in Chapter 3,  $R_i$  is mainly associated with electrolyte resistance and, since all measurements were taken at room temperature, electrolyte conductivity is assumed to remain unaltered. Thus, the minimal increase in  $R_i$  in the cured samples is assumed to be linked to accumulation of different fractions of otherwise mobile electrolyte ions in closed pores of silica network resulting in a reduced number of free conducting ions. Another possible explanation for the small variations of  $R_i$  is the variation of electrical contact resistance of the external circuit including the wire connections and coin cell holder from one system to another.

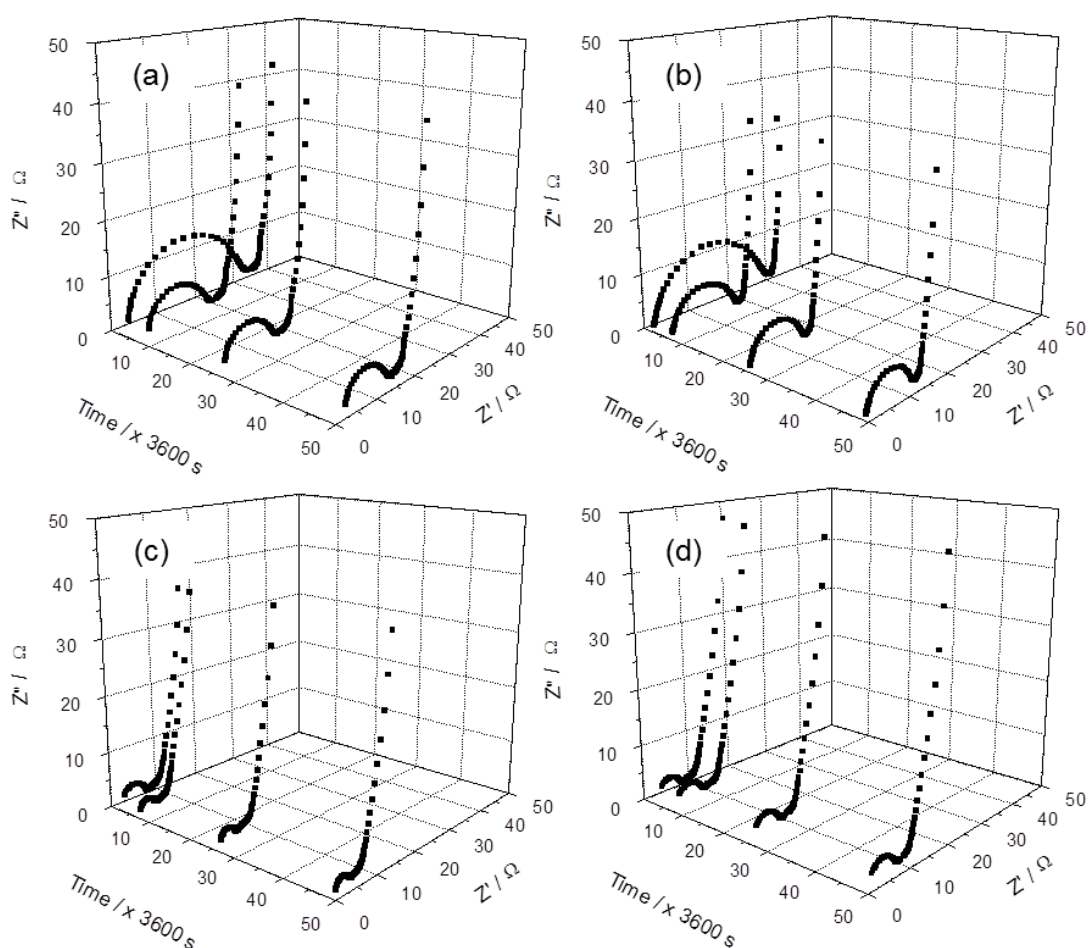


Figure 6.7 Evolution of Nyquist plots with time for nominally identical EDLC full cells cured at (a) 125°C, (b) 150°C, (c) 175°C and (d) 200°C.

The main difference in the electrochemical behavior of the four cells originates from the high to mid-range frequency region (the  $R_{ct}$  influenced semicircle). At the start of the experiment ( $t_0$ ), a charge transfer resistance of  $\sim 30 \Omega$  was ob-

tained for samples cured at 125 and 150°C (Figures 6.7a and 6.7b) while this value dropped to 5  $\Omega$  as the curing temperature was raised to 175 and 200°C (Figures 6.7c and 6.7d). As described previously in Chapter 3,  $R_{ct}$  has been associated with a number of ionic and electrical components inside an EDLC: (a) intrinsic resistance of the electrode [22], (b) electrical contact resistance between current collector and the electrode active material [22,23], (c) interparticle ionic impedance [22,24], (d) ion transport processes [25] and (e) electrolyte starvation (in the case of low electrolyte concentration) [26,27]. Here, the reduced  $R_{ct}$  of cells as a function of curing temperature (at time 0) can partially be attributed to the interlocking/merging effect at the electrode-electrolyte interface (see Figures 6.6c and 6.6d). At higher temperatures, a layer of the gel electrolyte has been observed to immobilise onto the electrode resulting in larger interface area between electrode and electrolyte and reducing the ionic interface resistance. Figure 6.8b and 6.8c demonstrate schematics of the ionogel and porous electrode being fused together after the heating process based on the SEM images shown in section 6.3.3. A similar observation was reported in 2017 by Simotwo et al. who utilised a total of 100 minutes heating process at 90-100°C to infuse a polymer-based ionogel into nanofiber carbon electrodes [20]. They attributed the comparable  $R_{ct}$  between this system and an EDLC containing the same ionic liquid electrolyte without the gel network, to an 'intimate' contact between the gel and the electrode.

Furthermore, the changes in  $R_{ct}$  over the 48 hours test period was most notable for samples with 125 and 150°C curing temperatures. The values of  $R_{ct}$  almost halved within the first 5 hours of the test and continued to drop to ~30% (of  $R_{ct}$  at time 0) in both of these samples after 48 hours; these variations were negligible for samples with the two higher curing temperatures. As mentioned in section 6.3.2, the physiochemical properties of [Emim][TfO] ionic liquid are highly dependent on temperature and a higher  $k$  value is achieved when curing temperature is increased. Thus, one can relate the stability of  $R_{ct}$  in samples with 175 and 200°C curing temperatures to the maximum initial wetting of the AC electrode pores by the ionic liquid in these samples (as opposed to wetting by the unsolidified ionogel mixture discussed in Chapter 5, which results in an increase in  $R_{ct}$ ). A 'maximum wetted state' of activated carbon electrodes by

ionic liquid is assumed to take 48 hours to be achieved in samples with the two lowest curing temperatures, as the capillary forces continuously attract more ionic liquid into the AC electrode until an equilibrium state is reached. Therefore, in the investigated systems described,  $R_{ct}$  is postulated to comprise of the ionic impedance at: (i) the electrode-electrolyte interface [25] and (ii) within the textural pores (i.e. inter-particle pores) of the AC electrodes [22,24].

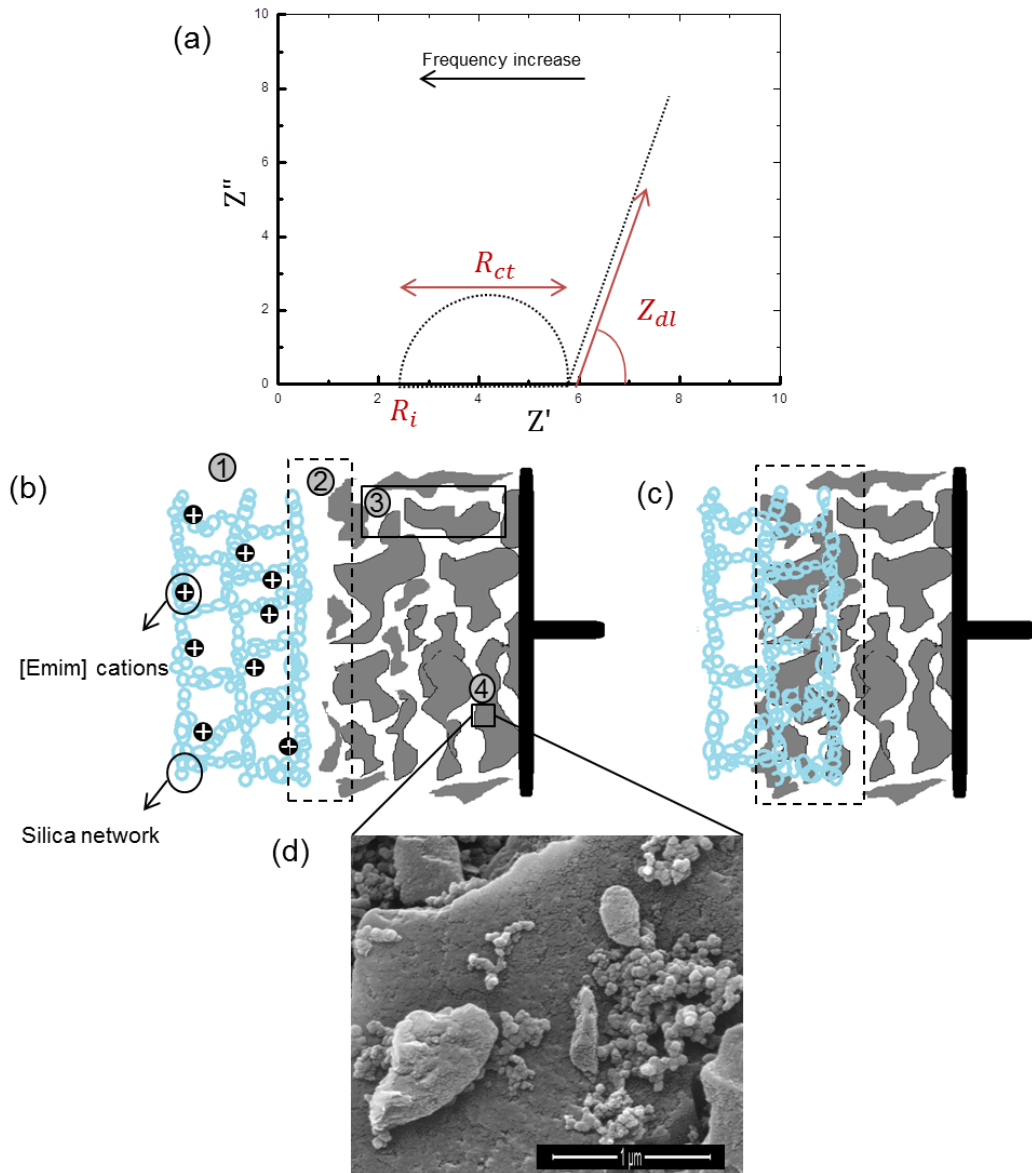


Figure 6.8 (a) The three main impedance components ( $R_i$ ,  $R_{ct}$  and  $Z_{dl}$ ) in a typical Nyquist plot for an EDLC with porous electrodes (as explained in [28]), (b) a schematic illustration of the four processes taking place during an EIS scan: 1) free movement of ions within the bulk electrolyte, 2) ion insertion into the porous electrode, 3) diffusion of ions within the textural pores of the electrode, 4) diffusion into the intra-particle pores, (c) an illustration of interlocking effect caused by curing process and (d) an SEM image demonstrating the intra-particle pores in the activated carbon electrode.

To eliminate any influence from the silica network at the interface (including the possibility of onset gelation or further condensation processes), the behaviour of an EDLC consisting of [Emim][TfO] ionic liquid electrolyte with equivalent volume to that inside ionogels (36  $\mu$ L on each electrode), sandwiched between two activated carbon electrodes (with the same specifications) and separated by a thin separator film (2325 Celgard Inc., USA) was investigated. The EIS measurements were recorded periodically in the same manner as described in section 6.2.2. The resultant Nyquist plots are displayed in Figure 6.9a. As can be seen, the diameter of the semicircle drops (by  $\sim$ 31%) over the 48 hours duration of the experiment which is similar to the behavior of ionogel-based cells. Based on room temperature experimental condition, the ionic conductivity and the physiochemical properties of the electrolyte can be assumed constant throughout the EIS experiment. Thus, these results confirm that the  $R_{ct}$  variations over time are associated with the continuous increase in electrode wetted area by the electrolyte at the interface and the bulk of the activated carbon. The virtually stabilised  $R_{ct}$  between 24 and 48 hours of the experiment indicates a progress towards maximum wetting of the electrode pores.

As illustrated in Figure 6.7 and more clearly in 6.9b, the inclining angle of all Nyquist plots is between  $45^\circ$  and  $90^\circ$  which indicates good ion diffusion into the intra-particle pores of the activated carbon electrode in all samples [29]. The slight reduction in the inclining angle for samples cured at  $175^\circ\text{C}$  and  $200^\circ\text{C}$  is ascribed to the melting and resolidifying of the PVDF binder. It is possible that during the re-solidification of the binder, some AC electrode mesopores have been blocked or narrowed and resulted in higher intra-particle ionic resistance and thus, a slightly reduced inclining angle. Figure 6.8b illustrates the four key ionic impedances that are present in the investigated systems. The SEM image shown in Figure 6.8d illustrates the intra-particle pores available in the activated carbon electrode.

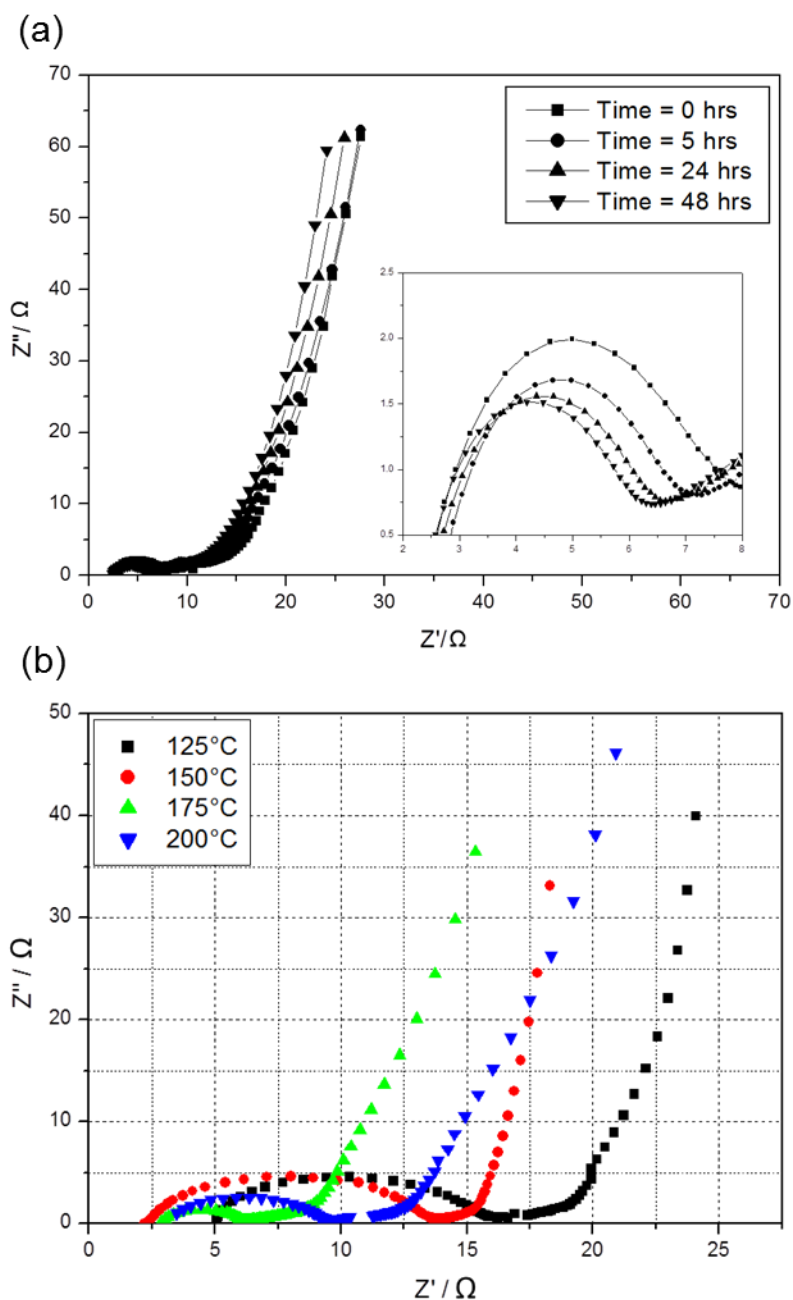


Figure 6.9 (a) Evolution of charge transfer resistance with time for EDLC full cells containing liquid [Emim][TfO] ionic liquid electrolyte (no gel network) and (b) Nyquist plots of nominally identical EDLCs with 125, 150, 175 and 200°C cured ionogel after 48 hours from cell assembly.

To complement the electrochemical measurements, cyclic voltammetry was used to elucidate the charge storage characteristic of the EDLC cells. The CV results at time 0 and after 48 hours are shown in Figures 6.10a and 6.10b, respectively, together with plots of areal capacitance and  $R_{ct}$  variations as a function of time (Figures 6.10c and 6.10d). Based on the CV plots displayed in Figure 6.10a and 6.10b, all the cells showed ideal capacitive behaviour (quasi-

rectangular CV curves) except for the case of 125 and 150°C cured cells at time 0. Nevertheless, both cells showed quasi-rectangular CV curves after 48 hours consistent with the decrease in  $R_{ct}$ . The areal capacitances of these two cells increased by almost 60% after 48 hours, thereby approaching values obtained at higher temperatures. This parameter increased by only 14% for the sample cured at 175°C and the capacitance remained almost unaltered throughout the 48 hours period for the cell with 200°C curing temperature. Conversely, an almost opposite trend can be seen in Figure 6.10d for the variation of  $R_{ct}$  with time (decay in  $R_{ct}$  for samples cured at 125, 150 and 175°C and a slight increase in  $R_{ct}$  for the sample cured at 200°C) which confirms that  $R_{ct}$  is the rate limiting parameter in the electrochemical kinetics of the EDLC cells. For all four stages of ion transport illustrated in Figure 6.8b, charge transfer at the electrode-electrolyte interface was shown to have the most influence on the capacitive response of the EDLCs. The rate limiting effect of  $R_{ct}$  has not been shown before using electrochemical tests at room temperature. Rodrigues et al. [11] concluded that ion bridging at the electrode-electrolyte interface has the highest activation energy compared to ion diffusion within the electrolyte and the electrode. Furthermore, Zheng et al. [10] showed that  $R_{ct}$  is strongly temperature dependent by performing EIS measurements at different operating temperatures. However, these studies failed to show any performance improvement of ionic liquid-based systems at room temperature. In addition, due to safety concerns with electrolyte leakage, the application of ionogels is preferred over ionic liquids.

Based on the results reported here, the  $R_{ct}$  can be reduced by encapsulating ionic liquid inside a gel network and using high temperatures (125-200°C) to cure the ionogel electrolyte. This method not only reduces the electrode wetting time (i.e. higher  $k$  value, Eq. 6.1) but also expands electrode-electrolyte interface area via a heat-induced interlocking effect (as shown in Figure 6.6 and as deduced in [20]). This knowledge can be useful in enhancing the system output at room temperature, which is one of the major challenges with ionic liquid-based energy storage devices.

As demonstrated in Figure 6.10c, the areal capacitance drops in the following order: 175°C>150°C>200°C>125°C-cured sample ranging from ~75 to 95 mF cm<sup>-2</sup> after 48 hours. Based on Eq. 2.8, these values correspond to 300 to 380

mF cm<sup>-2</sup> for a single AC electrode. Table 6.2 shows the equivalent full cell gravimetric capacitances of the four cells over the 48 hours testing time. Even though R<sub>ct</sub> is shown to be responsible for the variations of capacitance over the 48 hours test period, the final capacitance values are influenced by the total internal resistance of each cell which includes R<sub>i</sub> as well as R<sub>ct</sub>. This is clearly seen in the case of the cells cured at 125 and 150°C where their R<sub>ct</sub> values are comparable but their capacitances are noticeably different.

*Table 6.2 Variations of gravimetric capacitances of EDLCs cured at 125, 150, 175 and 200°C over 48 hours.*

Time of scan / hours	C <sub>T</sub> / F g <sup>-1</sup>			
	125°C	150°C	175°C	200°C
0	8.82	10.35	15.60	16.79
1	10.18	10.58	16.97	16.54
2	11.18	13.54	17.55	16.48
3	12.14	14.14	17.44	16.45
4	12.75	14.55	17.99	16.41
5	13.09	14.86	17.96	16.34
24	14.27	15.81	17.02	16.22
48	14.28	16.37	17.71	16.14

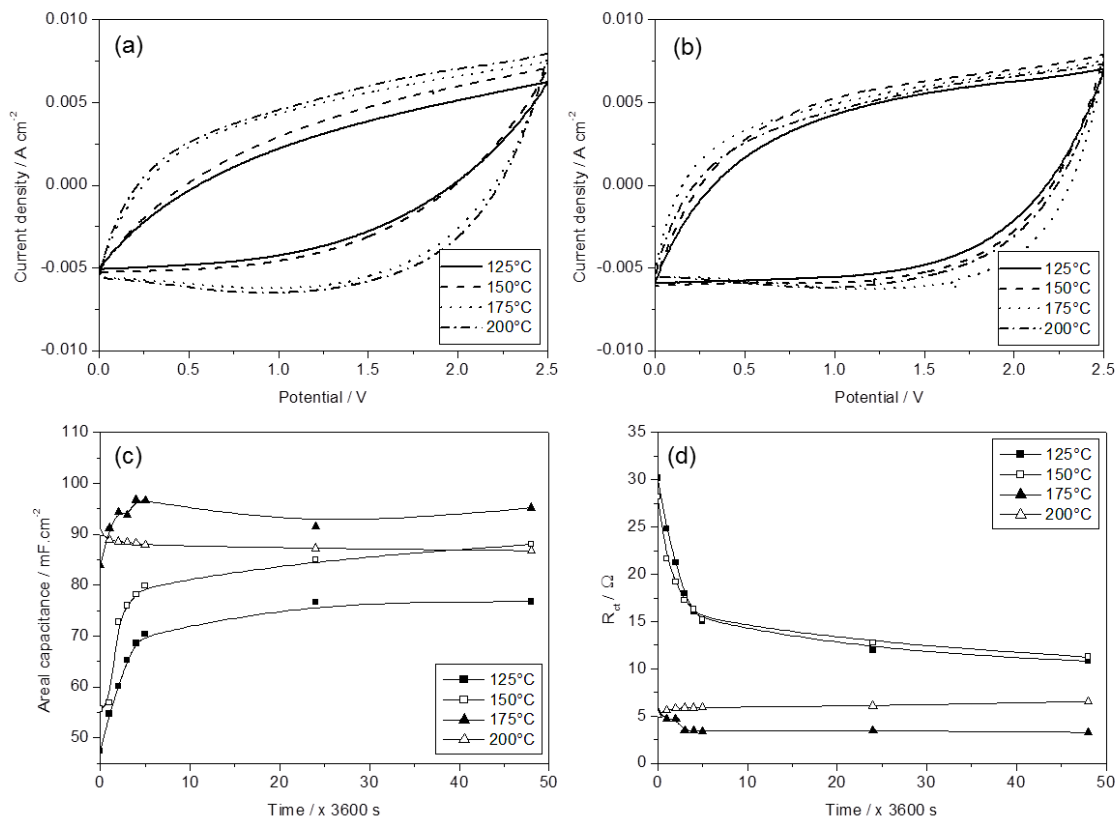


Figure 6.10 Cyclic voltammetry curves of EDLCs with ionogels cured at different temperatures after (a) 0 hours and (b) 48 hours of being assembled, together with the variation plots of (c) areal capacitance and (d)  $R_{ct}$  as a function of time.

In order to evaluate the repeatability of these results and eliminate any possible influence from CV cycling on the electrode wetting rate, an additional series of EIS and CV tests were repeated in which 50 CV cycles were recorded at the end of the 48 hours resting time rather than 5 periodic CV cycles. Figure 6.11a and b demonstrate the  $R_{ct}$  variations with time and the 50<sup>th</sup> CV cycles of each EDLC, respectively. The  $R_{ct}$  variation pattern and their values at  $t=48$  hours agree well with the results shown previously in Figure 6.10c. Furthermore, the CV cycles of all cells demonstrate good capacitive behaviour similar to those shown in Figure 6.10b. The full cell areal capacitances are calculated to be 73.55, 74.07, 91.29 and 80.92 mF cm<sup>-2</sup> for cells cured at 125, 150, 175 and 200°C, respectively. These results are equivalent to 13.68, 13.78, 16.98, 15.05 F g<sup>-1</sup>, respectively.

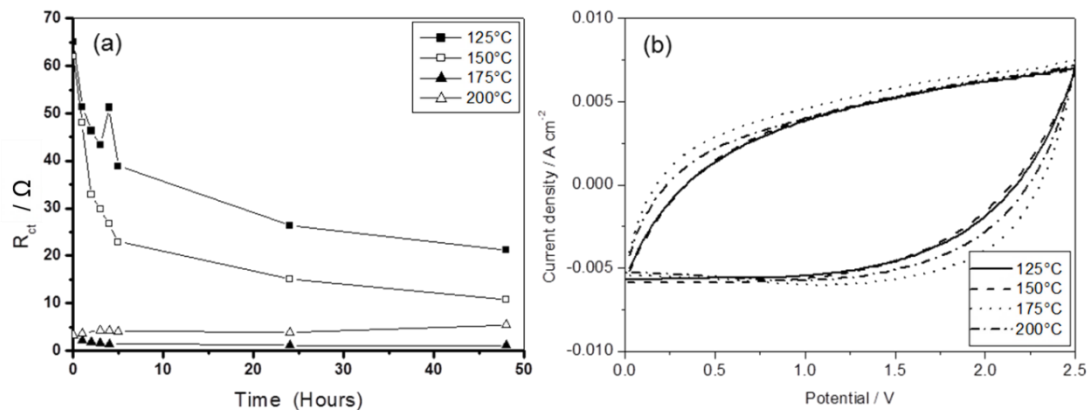


Figure 6.11 (a) Variation of  $R_{ct}$  a function of time in the second round of nominally identical EDLCs cured at 125, 150, 175 and 200°C and (b) cyclic voltammetry curves of EDLCs with heat-cured ionogels after 48 hours of being assembled.

Table 6.3 illustrates recent literature on EDLCs with ionic liquid (no. 5) and ionogel electrolytes (no. 1-4) together with examples of two silica-based ionogel systems comparable to the work conducted in this thesis (no. 6 and 7). A wide range of specific capacitance values have been reported for systems containing [Emim][TfO] ionic liquid (as used in this work) and [Emim][TFSI] ionic liquid which has a similar molecular structure to [Emim][TfO] ionic liquid. Thus, it is evident that establishing a benchmark for systems containing ionic liquid or ionogel electrolytes is not an easy task since multiple factors such as electrode material and its active mass loading, gel network (as shown in Chapter 5), type of ionic liquid(s), and experimental setting (scan rate, temperature, etc.) can influence the final result. However, the results reported here fit within this wide range of reported specific capacitances as it is shown in Table 6.3.

Table 6.3 Some examples of reported work on EDLCs with ionic liquid or ionogel electrolytes. Since the capacitance value is influenced by the scan rate as shown by Pell and Conway [30], the utilised scan rate in each work is provided. Abbreviations: [PMPyrr]= 1-propyl-3-methylpyrrolidinium, PIP13FSI= N-methyl-N-propylpiperidinium bis(fluorosulfonyl)imide, PYR14FSI = N-butyl-N-methylpyrrolidinium bis(fluorosulfonyl)imide, PEDOT: PSS= poly polystyrene sulfonate.

No.	Solid matrix precursor	Ionic liquid	Electrode material	Electrode mass loading	Specific capacitance (full cell)	scan rate	Ref.
1	Poly(dimethylsiloxane)	[Emim][TfO]	PEDOT: PSS	-	11.3 mF cm <sup>-2</sup>	1 mV s <sup>-1</sup>	[31]
2	5wt% methyl cellulose	[Emim][TFSI]	Carbon nano-fiber	a) 3.2 mg cm <sup>-2</sup> b) 5.2 mg cm <sup>-2</sup>	a) 122 mF cm <sup>-2</sup> , 38.25 F g <sup>-1</sup> b) 151 mF cm <sup>-2</sup> , 29.75 F g <sup>-1</sup>	20 mV s <sup>-1</sup>	[20]
3	2 wt% fumed silica and hydroxyethyl cellulose	[Emim][TfO] & Mg[TfO]	Activated carbon	-	25 F g <sup>-1</sup>	5 mV s <sup>-1</sup>	[32]
4	Poly(vinylidene fluoride-co-hexafluoropropylene)	[Emim][TfO]	PEDOT: PSS & Graphene nanoplatelets	-	26.4 F g <sup>-1</sup> (105.6 F g <sup>-1</sup> for each electrode)	Capacitance was evaluated from electrochemical impedance spectroscopy	[33]

No.	Solid matrix precursor	Ionic liquid	Electrode material	Electrode mass loading	Specific capacitance (full cell)	scan rate	Ref.
5	-	[Emim][TFSI] & [PMPyrr][TFSI]	Ni foam	-	0.365 mF cm <sup>-2</sup> (at 80°C)	1000 mV s <sup>-1</sup>	[4]
6	Silica (TMOS & TEOS)	PIP13FSI & PYR14FSI	Activated carbon	5 mg cm <sup>-2</sup>	125 mF cm <sup>-2</sup> (at 20°C)	50 mV s <sup>-1</sup> (window: 0-3 V)	[12]
7	Silica (TMOS)	[Emim][TFSI]	Activated carbon	1 mg cm <sup>-2</sup>	39 mF cm <sup>-2</sup>	2 mV s <sup>-1</sup>	[5]
8	Silica (TMOS & MTMS)	[Emim][TfO]	Activated carbon	5.4 mg cm <sup>-2</sup>	95.63 mF cm <sup>-2</sup> 17.71 F g <sup>-1</sup> (at 20°C) (lonogel curing temperature = 175°C)	50 mV s <sup>-1</sup> (window: 0-2.5 V)	This work

### 6.3.5 Visualisation of wettability using Raman line-mapping

The ionic liquid properties summarized in Table 6.1 and the electrochemical characterisation results suggest that the 'maximum wetted state' of the porous electrodes is achieved more quickly when ionogels are cured at higher temperatures as one might anticipate. By reducing viscosity and improving the penetration coefficient ( $k$ ), ionic liquid is able to travel further through the electrode under the influence of capillary forces and wet larger area of the active material, consequently reducing the wetting time of the porous electrode. In order to visually characterise the ingress of ionic liquid through the depth of ionogel-coated AC electrodes, Raman line-maps of the cross section of electrodes cured at 125 and 200°C were collected. Figure 6.12a illustrates the direction in which the Raman line-map was acquired across the electrode cross section. As it is shown, the coated electrodes were sandwiched between two thin silicon wafers (Czochralski single crystal Si,  $381 \pm 25$   $\mu\text{m}$  in thickness, Virginia Semiconductor) to mark the start and end points of the measurements (labelled as S and E, respectively) and to ensure that the electrode was positioned perpendicularly to the microscope lens.

Raman spectroscopy provides information about the vibrational frequencies of covalent bonds within a sample but does not facilitate separation. Subsequently, if there is more than one component/material within the sampled region,  $\sim 8$   $\mu\text{m}$  in this study, then the spectrum produced will show features for all components, leading to ambiguity of signal and making the determination of the distribution of each material at each sampling point challenging. This can be resolved by MCR analysis, which uses algorithms such as NIPALS and ALS to decompose mixed spectroscopic matrices into pure component (factors) and pure concentration (loadings) matrices [34–36]. In this work, four factors were utilised to account for each individual compound, namely the silicon wafer, the Al foil, activated carbon and the ionic liquid. Figure 6.12b shows a direct comparison of a typical Raman spectrum of each of the pure materials present (ionic liquid, activated carbon, silicon and Al) together with the MCR calculated pure spectral factors. As can be seen, the spectra of the pure compounds and their corresponding factors overlay very well indicating reliable MCR output. The unexpected spikes (e.g. in factor 4) are due to a phenomenon called Rank Deficiency caused by a combi-

nation of instrumental noise and overlap of concentration profiles of different components in the system and can reasonably be ignored [35].

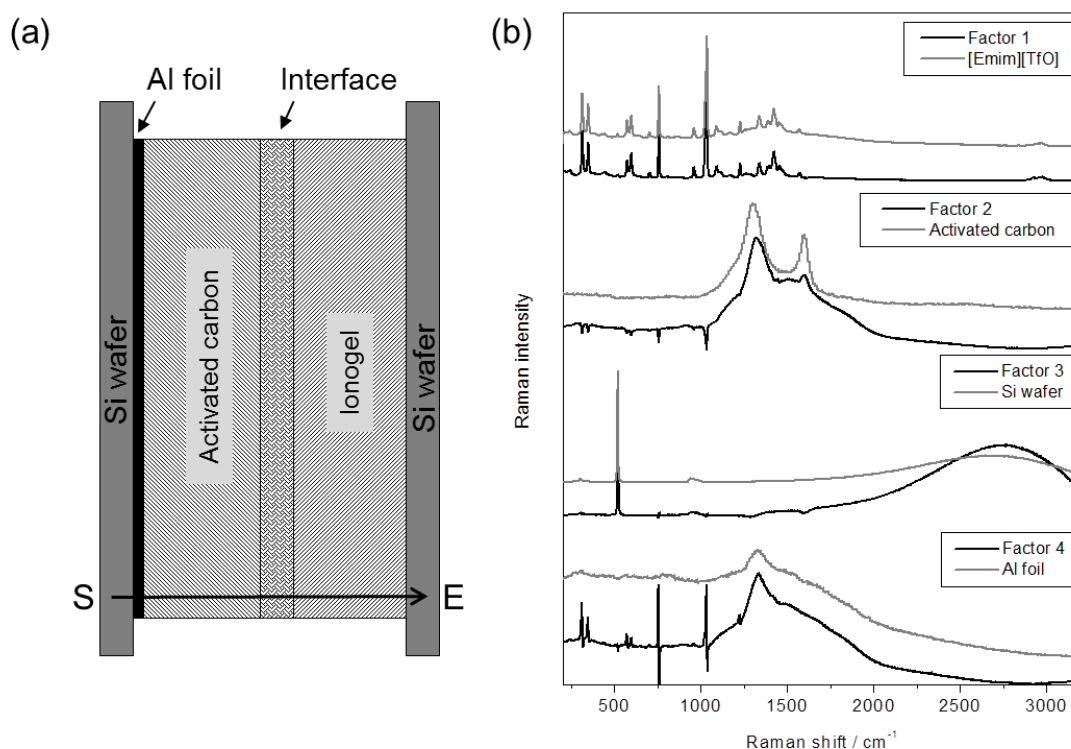


Figure 6.12 (a) An illustration of the line-map direction over the cross section of the ionogel-coated electrodes and (b) Raman spectra of the four components available in the line-map together with the corresponding MCR-recognised factors based on their variation across the cross section.

By plotting the score (or Raman intensity at each point) of each pure component, a quantitative variation of each material across the cross section was realised as a function of location/distance travelled. Figures 6.13a and b show the optical images of the electrodes that have been subjected to curing temperatures of 125 and 200°C respectively, with the region from where the Raman data was collected being marked with dotted white lines. The corresponding Raman intensity variations of the ionic liquid at the cross sections are given in Figures 6.13c and d.

Working from the left hand side of Figure 6.13c relating to the sample which had been treated at 125°C, the intensity of the ionic liquid factor, and therefore its concentration, has a low/zero intensity through the AC electrode until the interface with the ionic liquid region is reached (~70 μm). Through the interface the intensity of the ionic liquid factor increases in a quasi-linear fashion and the gradient of this line, provides information about the sharpness of the interface

and by inference indicates how far [Emim][TfO] ionic liquid has permeated through the AC electrode pores. The analogous data for the sample, which had been treated at 200°C (Figure 6.13d) shows a much broader interface with a shallower gradient. This indicates that for this sample, [Emim][TfO] ionic liquid has permeated a greater distance into the porous AC electrode. This supports the measured  $k$  values reported in Table 6.1, the high-resolution SEM images (Figure 6.6) and the impedance measurement results discussed in section 6.3.4. It is noteworthy to mention that these measurements were taken within 24 hours of synthesis and represent the very early wetting stage of the electrodes by the ionic liquid. Based on the EIS results, a 'maximum wetted state' may be achieved for the sample cured at 125°C if it is aged for an additional 24 hours.

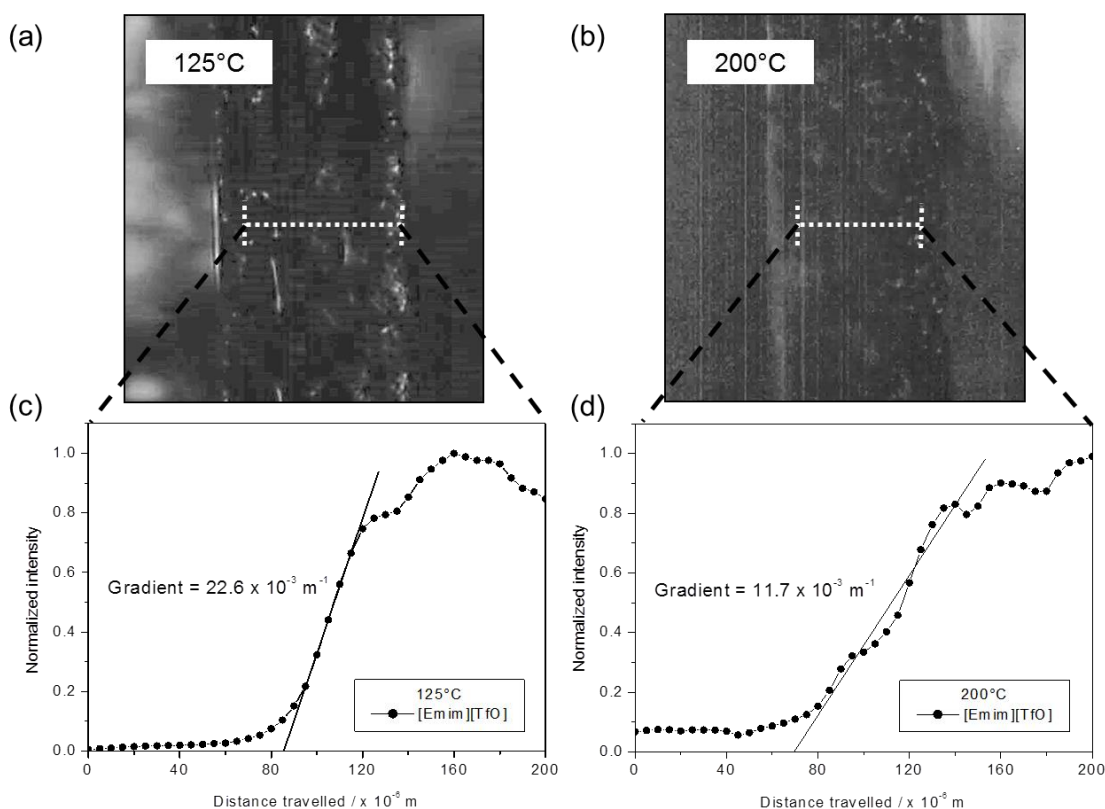


Figure 6.13 (a & b) Optical images of ionogel-coated electrodes cross section cured at 125 and 200°C and (c and d) the corresponding Raman intensity variations of [Emim][TfO] ionic liquid factor across the cross sections. The straight lines represent the best linear fit for ionic liquid distribution at the electrode-electrolyte interfaces within the first 12 hours.

## 6.4 Conclusions

One of the great challenges with using silica-based ionogels as a scalable and industrially applicable solid electrolyte in supercapacitors is their long gelation time. In addition, electrochemical systems containing ionic liquids suffer from high viscosity (compared to the conventional electrolytes), which limits ion mobility and electrode wetting rate, resulting in poor electrochemical performance at room temperature. This chapter reports the influence of heat-assisted gelation of ionogels as a measure to counter both of these limitations. The approach taken towards conducting this study is summarised in the diagram below.

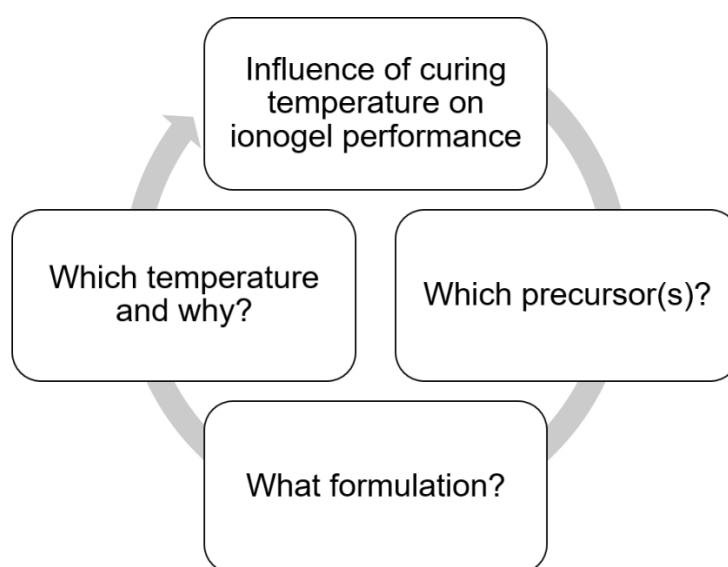


Figure 6.14 Summary of steps undertaken to answer the main question of this investigation.

In this chapter, a mixture of TMOS and MTMS was utilised to elucidate the electrochemical performance of such ionogels cured at 125, 150, 175 and 200°C. The gelation time of TMOS-MTMS-based ionogels was reduced to less than 90 minutes and the charge transfer resistance in the corresponding EDLCs was considerably reduced as the curing temperature was increased from 125 to 200°C. The resultant enhanced ion transport kinetics at room temperature inferred that the electrode-electrolyte interface area was increased as a result of the interlocking effect with increased temperature. Furthermore, the influence of elevated curing temperature on the penetration coefficient of ionic liquid reduced the time needed to achieve the 'maximum wetted state' of the electrode determined by capillary forces. Based on the results, one can conclude that 175°C is the optimal curing temperature for the studied system due to the mini-

mal resultant shrinkage, excellent capacitive behaviour ( $95 \text{ mF cm}^{-2}$ ) and short electrode wetting time (5 hours). Ionogels cured at 125 and 150°C showed no signs of shrinkage with an extended electrode wetting time of 48 hours. This investigation provides an insight towards the design of safer energy storage systems that are not only industrially scalable, due to their short fabrication time, but can also be operated at room temperature as well as higher temperatures.

## 6.5 References

- [1] A. Balducci, R. Dugas, P.L. Taberna, P. Simon, D. Plée, M. Mastragostino, S. Passerini, High temperature carbon–carbon supercapacitor using ionic liquid as electrolyte, *J. Power Sources*. 165 (2007) 922–927. doi:10.1016/J.JPOWSOUR.2006.12.048.
- [2] R.S. Kühnel, S. Obeidi, M. Lübke, A. Lex-Balducci, A. Balducci, Evaluation of the wetting time of porous electrodes in electrolytic solutions containing ionic liquid, *J. Appl. Electrochem.* 43 (2013) 697–704. doi:10.1007/s10800-013-0558-x.
- [3] A. George, A. Brandt, K. Tran, S.M.S.N.S. Zahari, D. Klein-Marcuschamer, N. Sun, N. Sathitsuksanoh, J. Shi, V. Stavila, R. Parthasarathi, S. Singh, B.M. Holmes, T. Welton, B.A. Simmons, J.P. Hallett, Design of low-cost ionic liquids for lignocellulosic biomass pretreatment, *Green Chem.* 17 (2015) 1728–1734. doi:10.1039/c4gc01208a.
- [4] R. Newell, J. Faure-Vincent, B. Iliev, T. Schubert, D. Aradilla, A new high performance ionic liquid mixture electrolyte for large temperature range supercapacitor applications (–70°C to 80°C) operating at 3.5 V cell voltage, *Electrochim. Acta.* 267 (2018) 15–19. doi:10.1016/j.electacta.2018.02.067.
- [5] M. Brachet, T. Brousse, J. Le Bideau, All solid-state symmetrical activated carbon electrochemical double layer capacitors designed with ionogel electrolyte, *ECS Electrochem. Lett.* 3 (2014) A112–A115. doi:10.1149/2.0051411eel.
- [6] A. Taubert, R. Löbbicke, B. Kirchner, F. Leroux, First examples of organosilica-based ionogels: Synthesis and electrochemical behavior, *Beilstein J. Nanotechnol.* 8 (2017) 736–751. doi:10.3762/bjnano.8.77.
- [7] D.S. Ashby, R.H. DeBlock, C.H. Lai, C.S. Choi, B.S. Dunn, Patternable, solution-processed ionogels for thin-film lithium-ion electrolytes, *Joule.* 1 (2017) 344–358. doi:10.1016/j.joule.2017.08.012.

- [8] K.T. Chou, B.I. Lee, Properties of silica gels prepared from high-acid hydrolysis of tetraethoxysilane, *Ceram. Int.* 19 (1993) 315–325. doi:10.1016/0272-8842(93)90044-R.
- [9] C.A. Milea, C. Bogatu, The influence of parameters in silica sol-gel process, *Bull. Transilv. Univ. Brasov Eng. Sci.* 4 (2011) 59–66.
- [10] H. Zheng, H. Zhang, Y. Fu, T. Abe, Z. Ogumi, Temperature effects on the electrochemical behavior of spinel  $\text{LiMn}_2\text{O}_4$  in quaternary ammonium-based ionic liquid electrolyte, *J. Phys. Chem. B.* 109 (2005) 13676–13684. doi:10.1021/jp051238i.
- [11] M.-T.F. Rodrigues, X. Lin, H. Gullapalli, M.W. Grinstaff, P.M. Ajayan, Rate limiting activity of charge transfer during lithiation from ionic liquids, *J. Power Sources.* 330 (2016) 84–91. doi:https://doi.org/10.1016/j.jpowsour.2016.08.119.
- [12] L. Negre, B. Daffos, V. Turq, P.L. Taberna, P. Simon, Ionogel-based solid-state supercapacitor operating over a wide range of temperature, *Electrochim. Acta.* 206 (2016) 490–495. doi:https://doi.org/10.1016/j.electacta.2016.02.013.
- [13] N. Bengourna, F. Despetis, L. Bonnet, R. Courson, P. Solognac, H. Satha, N. Olivi-Tran, Textural, structural and electrical characterizations of EMIMAc silica ionogels and their corresponding aerogels, *Appl. Phys. Res.* 6 (2014) 16–25.
- [14] M.A. Klingshirn, S.K. Spear, J.D. Holbrey, R.D. Rogers, Ionic liquids as solvent and solvent additives for the synthesis of sol-gel materials, *J. Mater. Chem.* 15 (2005) 5174. doi:10.1039/b508927a.
- [15] A. Vioux, L. Viau, S. Volland, J. Le Bideau, Use of ionic liquids in sol-gel; ionogels and applications, *Comptes Rendus Chim.* 13 (2010) 242–255. doi:https://doi.org/10.1016/j.crci.2009.07.002.
- [16] A.I. Horowitz, M.J. Panzer, High-performance, mechanically compliant silica-based ionogels for electrical energy storage applications, *J. Mater. Chem.* 22 (2012) 16534–16539. doi:10.1039/C2JM33496H.

- [17] A. Martinelli, L. Nordstierna, An investigation of the sol-gel process in ionic liquid-silica gels by time resolved Raman and <sup>1</sup>H NMR spectroscopy, *Phys. Chem. Chem. Phys.* 14 (2012) 13216–13223. doi:10.1039/C2CP41914A.
- [18] M.S. Wu, T.L. Liao, Y.Y. Wang, C.C. Wan, Assessment of the wettability of porous electrodes for lithium-ion batteries, *J. Appl. Electrochem.* 34 (2004) 797–805. doi:10.1023/B:JACH.0000035599.56679.15.
- [19] S.J. Palmer, The effect of temperature on surface tension, *Phys. Educ.* 11 (1976) 119–120. <http://stacks.iop.org/0031-9120/11/i=2/a=009>.
- [20] S.K. Simotwo, P.R. Chinnam, S.L. Wunder, V. Kalra, Highly durable, self-standing solid-state supercapacitor based on an ionic liquid-rich ionogel and porous carbon nanofiber electrodes, *ACS Appl. Mater. Interfaces.* 9 (2017) 33749–33757. doi:10.1021/acsami.7b07479.
- [21] Z.H. Liu, P. Maréchal, R. Jérôme, Intermolecular interactions in poly(vinylidene fluoride) and  $\epsilon$ -caprolactam mixtures, *Polymer (Guildf).* 37 (1996) 5317–5320. doi:[https://doi.org/10.1016/0032-3861\(96\)00423-5](https://doi.org/10.1016/0032-3861(96)00423-5).
- [22] I. Yang, S.-G. Kim, S.H. Kwon, M.-S. Kim, J.C. Jung, Relationships between pore size and charge transfer resistance of carbon aerogels for organic electric double-layer capacitor electrodes, *Electrochim. Acta.* 223 (2017) 21–30. doi:10.1016/J.ELECTACTA.2016.11.177.
- [23] K.H. An, W.S. Kim, Y.S. Park, J.M. Moon, D.J. Bae, S.C. Lim, Y.S. Lee, Y.H. Lee, Electrochemical properties of high-power supercapacitors using single-walled carbon nanotube electrodes, *Adv. Funtional Mater.* 11 (2001) 387–392. doi:10.1002/1616-3028(200110)11:5<387::AID-ADFM387>3.0.CO;2-G.
- [24] I. Yang, S.G. Kim, S.H. Kwon, J.H. Lee, M.S. Kim, J.C. Jung, Pore size-controlled carbon aerogels for EDLC electrodes in organic electrolytes, *Curr. Appl. Phys.* 16 (2016) 665–672. doi:10.1016/j.cap.2016.03.019.

- [25] H.D. Yoo, J.H. Jang, J.H. Ryu, Y. Park, S.M. Oh, Impedance analysis of porous carbon electrodes to predict rate capability of electric double-layer capacitors, *J. Power Sources*. 267 (2014) 411–420. doi:10.1016/J.JPOWSOUR.2014.05.058.
- [26] W.G. Pell, B.E. Conway, N. Marincic, Analysis of non-uniform charge/discharge and rate effects in porous carbon capacitors containing sub-optimal electrolyte concentrations, *J. Electroanal. Chem.* 491 (2000) 9–21. doi:10.1016/S0022-0728(00)00207-2.
- [27] B.K. Kim, S. Sy, A. Yu, J. Zhang, Electrochemical supercapacitors for energy storage and conversion, *Handb. Clean Energy Syst.* (2015) 1–25. doi:10.1002/9781118991978.hces112.
- [28] S. Fletcher, V.J. Black, I. Kirkpatrick, A universal equivalent circuit for carbon-based supercapacitors, *J. Solid State Electrochem.* 18 (2014) 1377–1387. doi:10.1007/s10008-013-2328-4.
- [29] E. Frackowiak, Electrode materials with pseudocapacitive properties, in: *Supercapacitors*, Wiley-VCH Verlag GmbH & Co. KGaA, 2013: pp. 207–237. doi:10.1002/9783527646661.ch6.
- [30] W.G. Pell, B.E. Conway, Voltammetry at a de Levie brush electrode as a model for electrochemical supercapacitor behaviour, *J. Electroanal. Chem.* 500 (2001) 121–133. doi:10.1016/S0022-0728(00)00423-X.
- [31] N. Terasawa, High-performance transparent actuator made from poly(dimethylsiloxane)/ionic liquid gel, *Sensors Actuators, B Chem.* 257 (2018) 815–819. doi:10.1016/j.snb.2017.11.003.
- [32] M.Y. Chong, A. Numan, C.W. Liew, H.M. Ng, K. Ramesh, S. Ramesh, Enhancing the performance of green solid-state electric double-layer capacitor incorporated with fumed silica nanoparticles, *J. Phys. Chem. Solids.* 117 (2018) 194–203. doi:10.1016/j.jpcs.2018.02.030.

- [33] S. Ahmed, M. Rafat, M.K. Singh, S.A. Hashmi, A free-standing, flexible PEDOT:PSS film and its nanocomposites with graphene nanoplatelets as electrodes for quasi-solid-state supercapacitors, *Nanotechnology*. 29 (2018) 395401. doi:10.1088/1361-6528/aad0b8.
- [34] J. Jaumot, R. Gargallo, A. de Juan, R. Tauler, A graphical user-friendly interface for MCR-ALS: A new tool for multivariate curve resolution in MATLAB, *Chemom. Intell. Lab. Syst.* 76 (2005) 101–110. doi:<https://doi.org/10.1016/j.chemolab.2004.12.007>.
- [35] M. Garrido, F.X. Rius, M.S. Larrechi, Multivariate curve resolution-alternating least squares (MCR-ALS) applied to spectroscopic data from monitoring chemical reactions processes, *Anal. Bioanal. Chem.* 390 (2008) 2059–2066. doi:10.1007/s00216-008-1955-6.
- [36] K.R. Fega, D.S. Wilcox, D. Ben-Amotz, Application of Raman multivariate curve resolution to solvation-shell spectroscopy, *Appl. Spectrosc.* 66 (2012) 282–288. <http://as.osa.org/abstract.cfm?URI=as-66-3-282>.

## **7. Exploratory investigation of the influence of ionic liquid water content, curing process and cell potential on the long-term stability of EDLCs containing 150°C-cured ionogels**

### **7.1 Introduction**

A 'constant voltage load' or 'float test' is a commonly used technique for evaluation of the long-term stability of supercapacitors [1–3]. During this test, the capacitor is held at a nominal potential and the change in capacitance is recorded as a function of time by occasional charge-discharge cycles. As explained in section 2.5.4, a float test is preferred over cycling for long-term stability characterisation of supercapacitors as it gives a realistic performance evaluation of the electrochemical cell without being as time consuming as the long-term cycling. According to Weingarh et al. commercial supercapacitors are expected to operate for 500,000 to 1,000,000 cycles before reaching 70% of their capacitance [3]; thus, it can be highly time consuming to validate. Generally, the float test is one of the preconditioning methods utilised in industry to ensure consistency of the electrochemical system and to eliminate faulty cells amongst each batch of EDLCs/batteries manufactured.

Different schools of thought exist regarding the end-of-life criteria for supercapacitors. Some research groups [3–5] define failure of an EDLC to be the state at which there is a 100% increase in the equivalent series resistance of the cell and/or 20-30% drop in the capacitance from its original value. In a more recent study, Liu et al. [6] used a 500% increase in the internal resistance or a 50% loss of capacitance as the criteria for the end-of-life of EDLCs. However, the underlying symptoms of performance degradation i.e. a drop of capacitance and an increase in internal resistance of the cell, seems to be agreed upon in all cases. Various mechanisms have been suggested to explain the performance degradation of EDLCs [1,2,4,5,7]. Generally, the application of aqueous based EDLCs is limited due to their moderate potential window (~1.2 V) determined by the thermodynamic stability of water [8]. Thus, it comes as no surprise that presence of water can be detrimental to the performance and stability of EDLCs with organic electrolytes or ionic liquids (ILs) whose operating potential is be-

yond 2.0 V (typically above 3.0 V for ionic liquids). For this reason, EDLC manufacturers utilise organic electrolytes with a water content of 20 ppm or less [2] and some researchers have emphasised on a drying process for ionic liquids under vacuum in order to reduce their water content to less than 20 ppm [9–11].

This chapter explores the long-term stability of cells containing 'dried' and 'as-received' [Emim][TfO] ionic liquid to understand the extent to which ionic liquid water content can degrade the capacitance of EDLCs with 150°C heat-cured ionogel electrolyte and to further examine the influence of the curing process discussed in Chapter 6 on the degradation rate of the EDLCs. The latter is executed by comparing the performance of heat-cured cells with EDLCs that contain liquid electrolyte rather than solid electrolyte. Lastly, this chapter seeks to determine the operational limit of the EDLCs with 150°C-cured ionogel by exposing the cells to potential windows above 2.5 V. The long-term stability tests listed in this chapter have been executed in Warwick University due to lack of suitable instrumentation (such as vacuum oven and Karl fisher titrator) at Sheffield Hallam University.

## **7.2 Experimental**

### **7.2.1 Electrolyte preparation and EDLC fabrication**

The ionogel electrolytes were synthesised as described in Chapter 6. Briefly, 20  $\mu\text{L}$  of TMOS (Sigma Aldrich,  $\geq 98\%$ ) and 55  $\mu\text{L}$  of MTMS (Sigma Aldrich,  $\geq 98\%$ ) were mixed in a glass vial together with 200  $\mu\text{L}$  of [Emim][TfO] (Sigma Aldrich,  $\geq 98\%$ ) under continuous stirring (600 rpm) for 10 minutes using a magnetic stir bar. The sol-gel process was then initiated by adding 65  $\mu\text{L}$  FA (Aldrich  $\geq 96\%$ ). This was followed by another 10 minutes mixing time. All of the chemicals were used as received. The TMOS: MTMS: FA: IL molar ratio was kept constant at 1: 3: 14: 8 for all samples.

A similar procedure was followed for samples containing dried ionic liquid. The [Emim][TfO] ionic liquid was dried at 70°C in a vacuum oven (VDL 115 BINDER GmbH, Germany) for 24 hours. The dried ionic liquid was then securely sealed with parafilm and was transferred into a dry room.

After the 20 minutes synthesis process, 60  $\mu\text{L}$  of the mixture were deposited onto activated carbon disks using a micropipette. The ionogel-coated electrodes were heated in a furnace (CWF 1200, Carbolite GERO, UK) to 150°C using a ramp rate of 5°C  $\text{min}^{-1}$  and held isothermally at 150°C for 60 minutes. Once the heating process was completed, the ionogel coated AC electrodes were immediately transferred into a dry room and were heated at 60°C inside a vacuum oven for another 30 minutes to minimise moisture contamination. The double-layer supercapacitor cells were then assembled and crimped inside the dry room. The EDLCs containing liquid electrolytes (dried and as-received [Emim][TfO]) were assembled by sandwiching two activated carbon electrodes (each wetted by 36  $\mu\text{L}$  of the ionic liquid) with a thin separator film (2325 Celgard Inc., USA), which was cut into disks of 2 cm diameter.

Prior to sandwiching the cells, the activated carbon electrodes, coin cell equipment (CR2032 bottom and top casings, spring, current collector plates) and the separator films were heated at 70°C in a vacuum oven for 2 hours in an attempt to remove/minimise the trapped water on the surface or within the pores of each component.

### **7.2.2 Measurement of ionic liquid water content**

A coulombic Karl Fischer titrator was utilised to determine the water content inside [Emim][TfO] ionic liquid both as received and after the drying process described in the previous section.

### **7.2.3 Thermal stability of TMOS-MTMS ionogel**

The thermogravimetric analysis (TGA) of the 150°C cured ionogels was performed as described in Chapter 3 section 3.3.3. The TGA measurements were repeated 3 times to examine the consistency of the results. The onset temperatures and %mass loss values were calculated in the same manner as that described in Chapter 5, section 5.4.2.

### **7.2.4 Long-term stability characterisation**

Once the EDLCs were fabricated, they were aged for 48 hours for the 'maximum wetted state' to be achieved (as shown in Chapter 6). After this stage, 10 galvanostatic charge-discharge (GCD) cycles were collected with a constant current of 20 mA (equivalent to  $\sim 1.0 \text{ A g}^{-1}$  or  $\sim 5.7 \text{ mA cm}^{-2}$ , based on the active

mass and planar area of both electrodes, respectively) between 0 V and the maximum/critical potential in order to evaluate the initial electrochemical characteristic of each cell. The float test was then executed by continuously applying the critical cell potential to the cell for 24 hours followed by 10 GCD cycles (with the same settings as above). This procedure was repeated for ~500 hours for each cell. Figure 7.1 displays a schematic description of the float test used in this work. The X represents the critical potential used for each test which ranges between 2.5 V to 4.0 V. As can be seen, after each float region, the cell is fully discharged before the GCD cycles begin. All measurements were executed using a MACCOR automated battery tester (series 4000, USA). These measurements were executed in duplicate for each type of system (with dried or as-received ionic liquid and at each critical potential) to examine the reproducibility of the results.

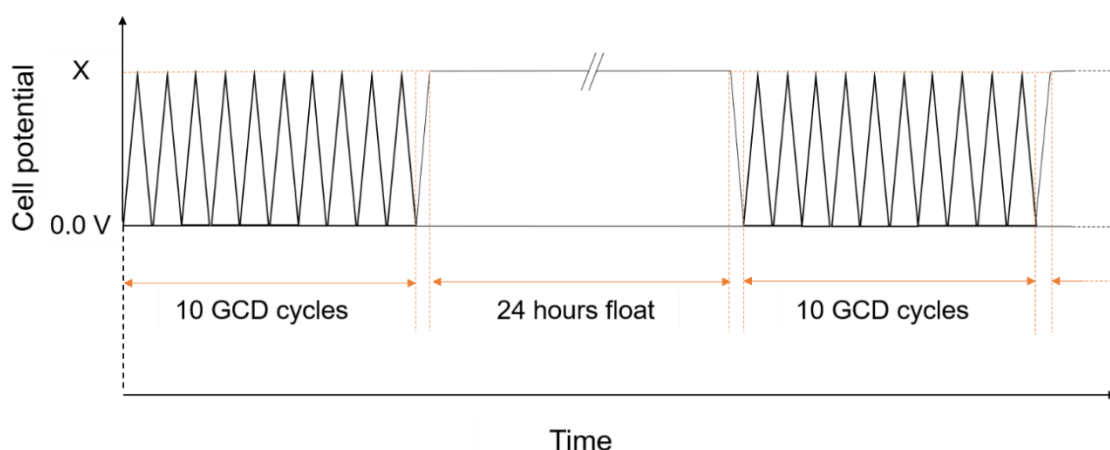


Figure 7.1 Demonstration of the float test settings used in this work. After the initial GCD cycles, the cell is held at the critical potential (X) for 24 hours before being fully discharged followed by another set of 10 GCD cycles (between zero and X). This procedure is continued for ~500 hours for each EDLC.

## 7.3 Results and discussion

### 7.3.1 Ionic liquid water content

Using TGA analysis, the %volatile impurity content (including water) of TMOS-MTMS ionogels after being heat-cured can be estimated with the assumption that the absorption of water from the atmosphere by the heat-cured gel after the curing process and prior to the TGA measurements is negligible. Figure 7.2 displays the TGA plots of 3 sets of 150°C cured TMOS-MTMS ionogels superimposed together with that of 'as-received' [Emim][TfO] ionic liquid (previously shown in Figure 5.13a) and the TMOS- and MTMS-based silica gels (prepared

according to the procedure described in Chapter 4). As can be seen in Figure 7.2 and Table 7.1, the TMOS-MTMS ionogels undergo a gradual mass loss of  $4.6\% \pm 0.2$  as temperature is raised to  $\sim 300^\circ\text{C}$  followed by major mass loss (with an onset of  $430^\circ\text{C} \pm 1$ ) that is (mainly) associated with decomposition of the ionic liquid. This pattern is similar to that of [Emim][TfO] ionic liquid which (as discussed in Chapter 5, section 5.4.2) shows an onset temperature of  $418^\circ\text{C} \pm 4$ . The first stage ( $35\text{-}300^\circ\text{C}$ ) mass loss of the ionogels is associated with the loss of ionic liquid impurities (including water) and sol-gel process volatile by-products (including water, alcohol and ester), which in the case of TMOS-MTMS ionogels partly remained inside the gel even after the curing process. Based on the similarity of the TGA patterns of the TMOS-MTMS ionogels and the 'as-received' ionic liquid, one can postulate that the stage 1 mass loss ( $35\text{-}300^\circ\text{C}$ ) in the ionogels is mainly associated with the water and other impurities content inside the ionic liquid. Deviation in the decomposition rate (observable from the slope of the TGA graph in the  $300\text{-}475^\circ\text{C}$  region) of ionogels compared to that of ionic liquid and the increased stage II onset temperature indicate that the gel network has thermally stabilised the encapsulated ionic liquid.

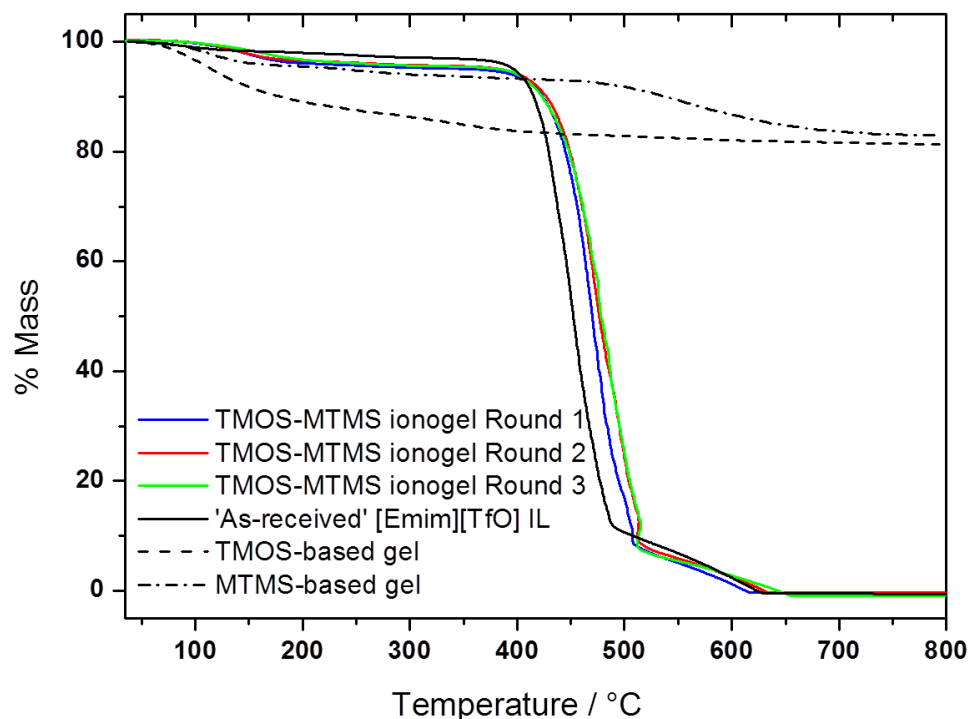


Figure 7.2 Thermogravimetric analysis results of TMOS-MTMS ionogels, [Emim][TfO] ionic liquid (as-received) and TMOS- and MTMS-based gels between 35 to 800°C at 20°C min<sup>-1</sup>.

Table 7.1 Average percentage mass loss in stage I and stage II of the heating process for TMOS-MTMS ionogels.

Sample	Stage I mass loss (35-300°C)	Stage II mass loss (300-475°C)	Onset temperature (300-475°C region)
TMOS-MTMS ionogel	-4.6% ± 0.2	-88.3% ± 0.4	430°C ± 1.4

The TGA results indicated over 100% mass loss for the ionogel samples which is not meaningful. The TGA-determined mass losses ranged between -0.15 and -0.55 mg. In addition, small amount of silica particles remained inside the alumina crucible after the heating process which was expected since the silica network does not decompose within the temperature range experimented here. This is evident by the TMOS and MTMS gel TGA patterns shown in Figure 7.2. Therefore, the final TGA-determined masses are associated with an instrumen-

tation error even though the balance on TGA instrument is expected to have 0.1  $\mu\text{g}$  sensitivity (based on manufacturer specifications). It is speculated that the gradual mass loss of MTMS silica gel beyond 500°C is associated with the condensation of the [Si]OH groups (formed reportedly between 375-550°C [12] as a result of decomposition and oxidation of the methyl groups in MTMS).

Assuming that the majority of the volatile impurities (including water) present inside the TMOS-MTMS ionogel has originated from the ionic liquid, this material was dried using the procedure described in 7.2.1 in order to compare the electrochemical performance of systems with 'as-received' and 'dried' ionic liquids. Based on Karl Fischer titration results, the 'as-received' ionic liquid contains 686.8 ppm water (equivalent to  $\sim 0.05\%$  of total mass of the ionic liquid) while after the drying process this value was reduced to 52.3 ppm. This information proves that the  $2\% \pm 0.6$  mass loss in 35-300°C region for the [Emim][TfO] ionic liquid (shown in Table 5.5, Chapter 5) is mainly ascribed to volatile impurities other than water. According to Liu et al. [13], in addition to water, traces of acids, residual solvent, volatile organics and halide ions can be present in ionic liquids as impurities. Influence of these impurities on the electrochemical performance of supercapacitors is not fully understood to this date and investigating the impact of [Emim][TfO] ionic liquid impurities on the long-term stability of the heat-cured EDLCs are out of the scope of this work. In addition, to consider ionic liquid or ionogel electrolyte to be the only source of water in the EDLCs is potentially flawed. Water present in the activated carbon electrodes, separator and casing components is difficult to quantify and in some cases, difficult to remove (e.g. trapped water in the micropores of the activated carbon [2]). Thus, their contribution to the overall performance should not be ignored.

### **7.3.2 Influence of ionic liquid water content on aging rate of EDLCs**

Figure 7.3 demonstrates the float test results at 2.5 V for EDLCs containing 'as-received' and 'dried' ionic liquid electrolyte sandwiched between activated carbon electrodes. The x-axis represents the duration of the float test with the first data point collected after 48 hours for all samples. This corresponds to the 48 hours wetting time programmed into the MACCOR software. The y-axis is a representation of normalised capacitance derived from the 10<sup>th</sup> discharge curve

of each set of GCD cycles (as explained in section 7.2.4). The initial specific capacitance value in all samples ranged between 94.76 and 101.92 mF cm<sup>-2</sup>, which were used to normalise data to 100% in all cases.

As can be seen, both systems undergo a sharp drop of capacitance (~50%) within the first 3 days of the float test. The term 'burn-in' time or 'infant mortality failure' is often used to address the sudden drop of capacitance which is caused by unwanted electrochemical processes taking place within the cell [14,15]. One common cause of such processes is water splitting where water is decomposed into hydrogen and oxygen. Depending on the cell potential, hydrogen can be adsorbed on the surface of carbon or form H<sub>2</sub> gas. In both cases hydrogen can occupy sites within the activated carbon and block pores reducing the accessible surface area of the electrode [7,16]. 'Burn-in' test is a key screening method in supercapacitor and battery manufacturing that can simulate device operation at accelerated conditions (such as long-term continuous usage, in some cases combined with high temperature [17,18]) in order to eliminate the likelihood of early stage failure of the device. A normal cell is expected to reach a stable state after the 'burn-in' time at which point it is ready to leave the manufacturing plant and into the hands of consumers [19].

As shown in Figure 7.3, the 'burn-in' region is followed by a small increase in capacitance values, which (based on the discussions in Chapter 6) can be explained by further wetting of the activated carbon electrodes with ionic liquid electrolyte during the float test. A similar observation was reported by Dagouset et al. in 2017 [18]. The main driving force for this behaviour is the long-term electric field that is applied to each cell during the float test causing ionic liquid cations and anions to further ingress through the negative and positive electrodes, respectively [7]. It is clear that 48 hours of aging time is not significant for these systems to achieve their 'full wetted state'. After 144 hours of float test (excluding the 48 hours aging time), both systems rapidly degraded once again reaching 5% of the initial capacitance by the end of the float test.

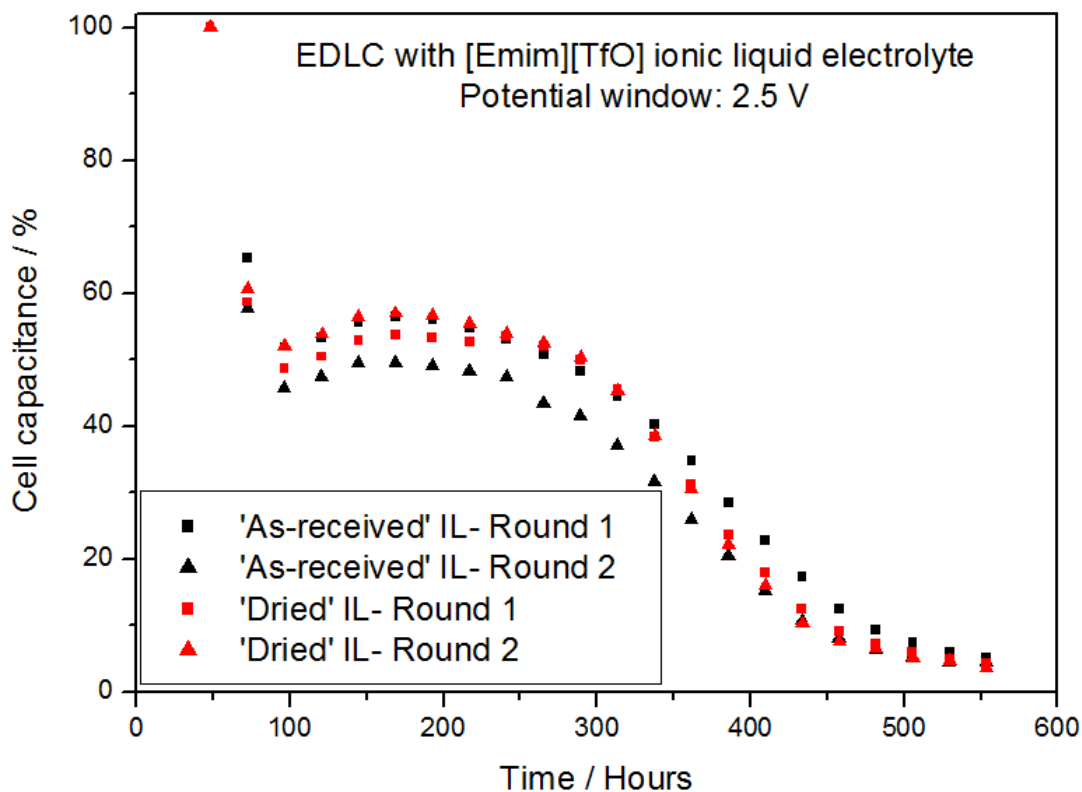


Figure 7.3 Capacitance loss during ~500 hours of float test at 2.5 V in cells with 'as-received' and 'dried' [Emim][TfO] ionic liquid displayed in black and red, respectively. Each test was repeated in duplicate for each sample and the results are displayed as round 1 and 2.

In this work, the capacitance degradation pattern of the 'dried' system demonstrates a similar trend to that of the 'as-received' system, which seems surprising initially. In an interesting study done by Cericola et al. [2] the electrolyte water content was deliberately increased from 30 ppm to 1000 ppm in activated carbon-based EDLCs. At a float potential of 2.75 V and after 100 hours of float test, the cell containing 1000 ppm water showed a 10% drop of capacitance while the cell with 30 ppm water content demonstrated a 4% drop of capacitance. This difference is relatively small considering the big difference in the electrolyte water content. In addition, their investigation demonstrated that the effect of water content is limited to the first few hours of the float test (first 30-50 hours in their case at 2.75 V) and beyond that, the rate of capacitance decay remains unaffected. Similarly, Liu et al. ascribed the initial drop of capacitance to the consumption of impurities (mainly water) [6]. Thus, it can be presumed that in the case of the present work the difference between the 'as-received' and 'dried' ionic liquid water contents is not sufficient to cause a noticeable difference in the %capacitance drop during the 'burn-in' time between the two sys-

tems. However, it is also possible that other degradation mechanisms disguise the effects of water content. Other than water splitting (i.e. hydrogen and oxygen evolution), decomposition of oxygenated functional groups on the activated carbon electrode and carbon corrosion have been suggested as possible capacitance degradation mechanisms [8]. Table 7.2 summarises the possible parasitic reactions taking place inside activated carbon-based EDLC causing capacitance drop.

As can be seen in Table 7.2, decomposition of activated carbon functional groups such as phenol, anhydrides, carbonyl and carboxyl groups takes place at cell potentials above 0.6 V. A comprehensive review on surface functional groups available on activated carbon is presented by Shafeeyan et al. [20]. These functional groups are continuously reduced at the negative electrode forming alcohol-like groups while they are oxidised at the positive electrode forming CO and CO<sub>2</sub> gas, thus, increasing the internal pressure of the cell. Examples of such reactions are provided in Table 7.2 as reactions (1) and (2). In addition, hydrogen and oxygen evolution are expected at cell potentials above 1.2 V. The water present within the cell (inside electrolyte, electrode and the separator film) decomposes into oxygen at the positive electrode based on reaction (6) while at the negative electrode, water is split, and H is adsorbed onto the activated carbon surface as CH<sub>x</sub> via reaction (3). It has been reported that the adsorbed hydrogen atoms further combine into hydrogen gas via reactions (4) and/or (5) at 1.6 V cell potentials and above [16]. At such high cell potentials (1.6 V and above), water oxidation yields H and OH on the positive electrode which react with carbon groups to form phenol and carbonyl groups (carbon corrosion) and are later oxidised and form CO and CO<sub>2</sub> (reactions (7-12)). Carbon corrosion becomes increasingly more likely at high potentials compared to oxygen evolution. It has also been shown that aging can result in point defects in the sp<sup>2</sup> carbon lattice of the activated carbon and lead to the creation of sp<sup>3</sup> sites via attachment of different elements such as O, F, and H [6].

Table 7.2 Summary of the three main degradation mechanisms of activated carbon-based EDLCs and some examples of the corresponding parasitic reactions taking place in the cell. Reactions (4) and (5) are reported to take place mainly at potential windows above 1.6 V [8].

Degradation mechanism	Reported cell Potential / V	Reaction(s)
Carbon surface functional groups decomposition [8,21,22]	>0.6	On negative electrode: e.g. $R_1COR_2 + 2e^- + 2H^+ \rightarrow R_1CHOHR_2$ (1)
		On positive electrode: e.g. $(RCO)_2O - 4e^- \rightarrow 2R + CO + CO_2$ (2)
		On negative electrode: $C + xH_2O + xe^- \rightarrow CH_x + xOH^-$ (3)
Water splitting [8,16,23]	>1.2	$CH_{ads} + H_2O + e^- \rightarrow H_2 + OH^- + C$ (4)*
		$CH_{ads} + CH_{ads} \rightarrow H_2 + 2C$ (5)*
		On positive electrode: $2H_2O - 4e^- \rightarrow O_2 + 4H^+$ (6)
Carbon Corrosion [8,24,25]	>1.6	$H_2O - e^- \rightarrow OH^\cdot + H^+$ (7)
		$H_2O - 2e^- \rightarrow O^\cdot + 2H^+$ (8)
		$C + O^\cdot / OH^\cdot \rightarrow C=O, C-OH$ (9)
		$C - OH_{ads} \rightarrow CO + H^+$ (10)
		$C + 2H_2O - 4e^- \rightarrow CO_2 + 4H^+$ (11)
		$C + H_2O - 2e^- \rightarrow CO + 2H^+$ (12)

Formation of gas bubbles (CO, CO<sub>2</sub>, H<sub>2</sub> and O<sub>2</sub>), alcohol-like products and the adsorbed hydrogen (and other elements such as F) can block activated carbon pores, obstructing ionic transport. In addition, increase in the internal pressure caused by the evolved gases can cause electrode cracks and connectivity issues [26]. Finally, carbon corrosion can result in a reduction of conductivity of the activated carbon electrode [7]. Therefore, capacitance drop is an indication of reduction in accessible electrode surface area and increase in the internal resistance of the supercapacitor. In the case of the present work where the cell potential is set to 2.5 V, a combination of all the above-mentioned degradation

mechanisms is expected to cause the fast performance degradation of the 'as-received' and 'dried' systems. Figure 7.4 displays the GCD curves of the two systems at different times during float test. The IR drop i.e. the instantaneous drop in cell potential is highlighted in Figure 7.4a. As can be seen, the GCD curves shrink as the float test reaches 500 hours while the IR drop increases. Liu et al. reported a similar observation and using comparative EIS analysis they demonstrated that increase in the internal resistance is the cause for this shrinkage [6]. They attributed this resistance increase to the change in the electrical percolation network in the electrode as well as formation of a passive layer on the carbon electrode surface during the float test. As it is shown in Table 7.3, which summarises the initial specific capacitance and equivalent series resistance (ESR) values calculated based on the GCD IR drops, the internal resistance of the 'as-received and' 'dried' systems increases dramatically during the float test. The influence of water content (686.8 ppm versus 52.3 ppm) does not seem to be pronounced in the investigated systems as the float test and the GCD results of the 'as-received' and 'dried' cells are comparable. The reason for this observation is unclear.

*Table 7.3 Initial capacitance (at t=48 hours) and ESR values at t=48, 121, 313 and 553 hours calculated from the GCD discharge curves displayed in Figure 7.4 associated with EDLCs with 'as-received' and 'dried' ionic liquids.*

Sample	Floating potential / V	Initial Capacitance / mF cm <sup>-2</sup>	ESR / $\Omega$			
			t=48 hours	t=121 hours	t=313 hours	t=553 hours
'As-received' IL, Round 1	2.5	102.53	14.00	21.00	56.00	98.50
'As-received' IL, Round 2	2.5	97.55	15.34	20.95	53.21	110.86
'Dried' ionic IL, Round 1	2.5	102.83	15.65	23.00	55.00	123.09
'Dried' ionic IL, Round 2	2.5	103.76	14.05	23.13	48.46	125.00

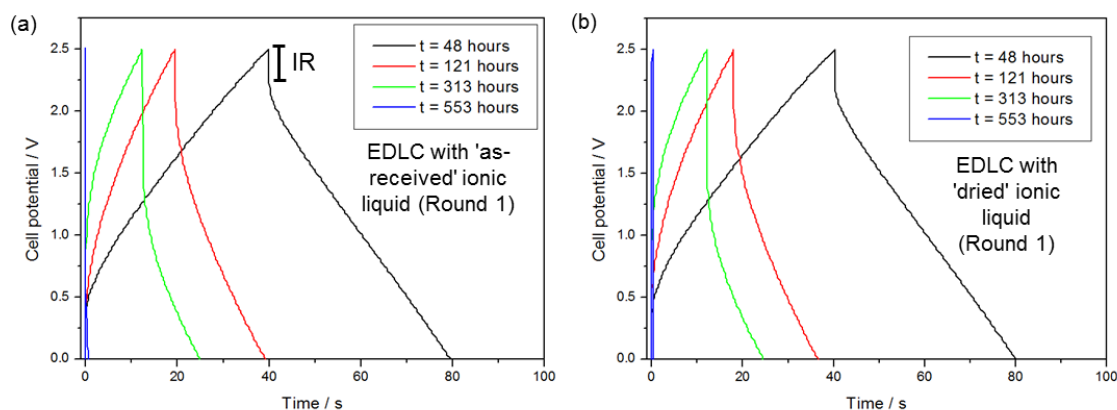


Figure 7.4 GCD curves of EDLCs with (a) 'as-received' and (b) 'dried' ionic liquid at  $t=48, 121, 313$  and  $553$  hours of float test at  $2.5$  V. The displayed GCD curves correspond to the round 1 of the float tests for each sample.

### 7.3.3 Influence of curing process on aging rate of EDLCs

The float test results of the  $150^{\circ}\text{C}$ -cured ionogels at  $2.5$  V are displayed in Figure 7.5. In both the 'dried' and 'as-received' systems, the rate of capacitance degradation slows down after the 'burn-in' time. After losing 25-50% of the initial capacitance value, the four tested EDLCs reach a steady state for the remaining of the float test with minimal change in the capacitance value. Based on the GCD curves shown in Figure 7.6, the initial specific capacitance values for the cells with 'as-received' ionic liquid were  $84.69$  and  $85.40$   $\text{mF cm}^{-2}$ , while the values obtained for the cells with 'dried' ionic liquid were  $86.70$  and  $99.68$   $\text{mF cm}^{-2}$ . It is worth noting that the values of specific capacitance for the 'as-received' systems are close to that of the nominally identical system calculated from CV curves in Chapter 6 ( $85.98$  and  $74.07$   $\text{mF cm}^{-2}$  for Rounds 1 and 2, respectively). Based on Figure 7.6, samples with 'as-received' and 'dried' ionic liquids have similar charge-discharge profiles after  $\sim 3$  days of the float test ( $t=121$  hours) indicating that the initial water content in the ionic liquid has negligible influence on the capacitance after the 'burn-in' time. Table 7.4 provides more detailed information about each heat-cured cell. The initial capacitance values of the heat-cured cells are slightly less than that of the EDLCs with ionic liquid electrolyte tabulated in Table 7.3. This is not surprising as the presence of the porous gel network can limit mobility of the ionic species leading to lower electrolyte conductivity [27–29].

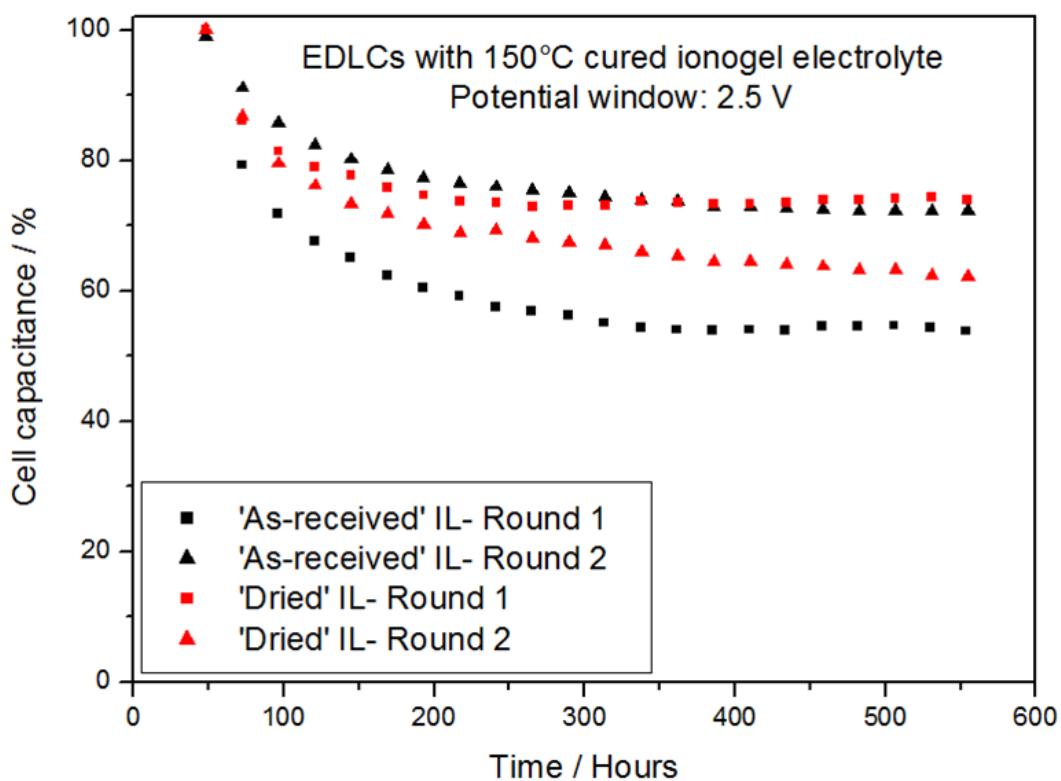


Figure 7.5 Capacitance loss of 150°C-cured ionogel EDLCs with 'as-received' (in black) and 'dried' (in red) ionic liquid during aging at 2.5V for ~500 hours of float test. Each test was repeated in duplicate for each sample and the results are displayed as round 1 and 2.

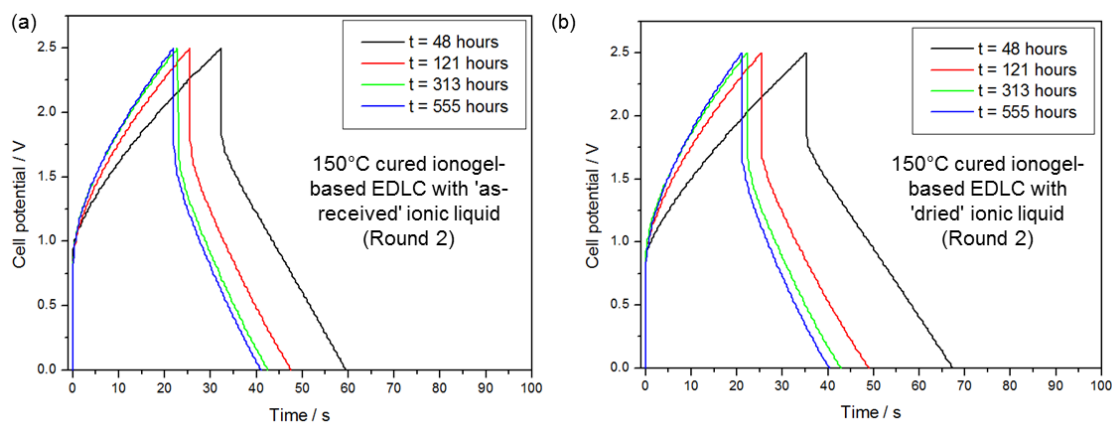


Figure 7.6 GCD curves of 150°C-cured EDLCs with (a) 'as-received' and (b) 'dried' ionic liquid at  $t=48, 121, 313$  and  $555$  hours of float test at 2.5 V. The displayed GCD curves correspond to the round 2 of the float tests done for each sample.

Table 7.4 Initial capacitance (at t=48 hours) and ESR values at t=48, 121, 313 and 555 hours calculated from the GCD discharge curves displayed in Figure 7.6 associated with EDLCs with 150°C cured ionogels with 'as-received' and 'dried' ionic liquids.

Sample	Floating potential / V	Initial Capacitance / mF cm <sup>-2</sup>	ESR /Ω			
			t=48 hours	t=121 hours	t=313 hours	t=555 hours
150°C-cured ionogel- 'as-received' IL, Round 1	2.5	84.69	35.98	52.70	56.42	58.67
150°C-cured ionogel- 'as-received' IL, Round 2	2.5	85.40	33.75	36.00	43.01	38.04
150°C-cured ionogel- 'dried' IL, Round 1	2.5	86.70	35.70	40.51	42.60	42.84
150°C-cured ionogel- 'dried' IL, Round 2	2.5	99.68	33.50	41.00	41.50	42.50

Based on the ESR values calculated and reported in Tables 7.4, the increase in the internal resistance of heat-cured cells were limited to ~10-60%, which was negligible compared to that of cells with ionic liquid electrolyte (~600-700%, as can be deduced from Table 7.3). The initial ESR values of the EDLCs with ionic liquid electrolyte (no gel network) were smaller than the cells with heat-cured ionogels but they exceed the values of the ionogel systems after ~300 hours of the float test (Tables 7.3 and 7.4). It is clear that the EDLCs containing 150°C-cured ionogels have better long-term stability compared to the cells with ionic liquid (without the gel network). This improvement can be ascribed to the main differences between the two systems i.e. (a) the gel network encapsulating the ionic liquid electrolyte and (b) the curing process. In the context of long-term stability and based on the main degradation mechanisms listed in Table 7.2, not enough evidence exists to support that encapsulation of ionic liquid within silica network has a stabilising influence on long-term stability. A suitable route to examine this hypothesis is to compare the long-term stability of EDLCs with

heat-cured and room temperature-cured ionogel electrolytes (beyond the scope of current project due to time limitation). However, because of the curing process at 150°C, the water content (and other impurities such as alcohol and ester) in the electrolyte and the electrode structure are reduced resulting in a smaller number of parasitic reactions (i.e. water decomposition and carbon corrosion) taking place within the cell during float test. In addition, using temperature programmed desorption analysis technique it has been shown that carboxylic functional groups on activated carbon begin to be liberated as CO<sub>2</sub> at 100°C [20]. Thus, it can be assumed that a fraction of the carboxylic groups, present on the activated carbon electrodes, decompose during the ionogel curing process, thereby resulting in fewer decomposable functional groups during the float test.

### **7.3.3 Influence of cell potential on aging rate of EDLCs**

As described in Chapter 2, one of the advantages of ionic liquids is their wide electrochemical potential window that is defined as the potential range within which the electrolyte is not oxidised or reduced at the electrode surface [9]. As it is shown in equation 2.11 (section 2.5.3), the energy density is proportional to the capacitance and square of the potential window. Therefore, widening the potential window is more influential in terms of the amount of energy stored in an EDLC compared to the specific capacitance.

In order to determine the stable potential window for EDLCs containing 150°C-cured ionogels (containing 'dried' ionic liquid), a series of float tests were conducted at 3.0, 3.5 and 4.0 V, the results of which are displayed in Figure 7.7. Based on the float test results, the rate of capacitance decay increases with potential window of the cell with capacitance of the cell operated at 4.0 V degrading to 25% of its initial value after only 24 hours of the float test.

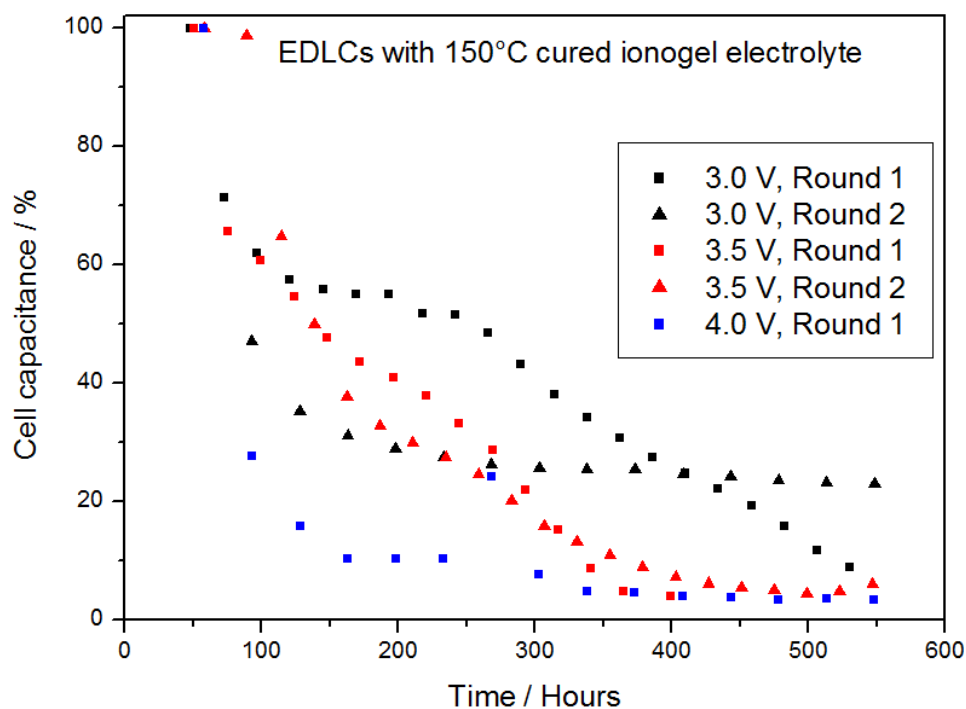


Figure 7.7 Capacitance loss of 150°C-cured ionogel EDLCs with 'dried' ionic liquid during aging at 3.0 V (in black), 3.5 V (in red) and 4.0 V (in blue) for ~500 hours of float test. Each test was repeated in duplicate for each sample and the results are displayed as round 1 and 2 except for the cell operated at 4.0 V. One of the two cells operated at 4.0 V failed immediately which is assumed to be due to short circuit.

Previous studies have considered the accelerated deterioration of performance when using a larger potential window [1,3,8]. When the cell potential is increased the applied electric field between the positive and the negative electrodes becomes stronger. This causes the parasitic reactions to take place at a higher rate. Ruch et al. [1] investigated the aging mechanism of EDLCs with activated carbon electrodes and acetonitrile-based organic electrolyte (1.0 M solution of tetraethylammonium tetrafluoroborate) as a function of cell potential. The aging rate for their reported system became more severe above 3.0 V potential. It was also indicated that above 3.5 V and as a result of decomposition of the electrode binder (polytetrafluoroethylene), the negative electrode went through significant embrittlement once disassembled. Thus, additional degradation mechanisms can be introduced when the potential window exceeds the electrochemical limit of an EDLC. These could include degradation of the electrolyte, reaction between electrolyte and the current collector or the active material and/or corrosion of the current collector. In the case of the present work, [Emim][TfO] ionic liquid is reportedly capable of withstanding up to 4.3 V before degrading

[30], which means that below this potential the possibility of electrolyte decomposition is limited and can be ignored. However, it is likely that PVDF binder in the activated carbon electrode degrades with time resulting in formation of 'isolated zones' [26] within the electrode. This could partly explain the faster decay of cell performance at higher cell potentials shown in Figure 7.7. Based on the results, 2.5 V seems to be confirmed as the maximum suitable potential window for the current heat-cured EDLCs. Thorough understanding of the degradation mechanisms within the heat-cured cells is required in order to make suitable measures toward expanding the cell potential window. It is known that even though a 4.0 V potential window is very attractive from an electrochemical point of view, it requires the ionic liquid electrolyte to be free of water [31]. Furthermore, every other component in the cell must have the electrochemical stability not to undergo degradation at such high cell potential.

## 7.4 Conclusions

This chapter provided a preliminary investigation of the influence of ionic liquid water content, 150°C curing process and cell potential window on the long-term stability of EDLCs. The float test results did not indicate a clear difference between the performance of EDLCs with 'as-received' and 'dried' ionic liquids (with 686.8 and 52.3 ppm water content, respectively). Further investigation is required to determine the stability of the EDLCs containing ionic liquid with water content <20 ppm. However, it was shown that the ionogel curing process at 150°C improves long-term stability of the EDLCs. The exact reason for this observation requires further investigation to elucidate the influence of the heating process on the reduction of electrode and electrolyte water content, impurity content and the removal of activated carbon functional groups such as carboxylic groups. The long-term stability results indicated that a maximum stable potential window of 2.5 V can be achieved for EDLCs with 150°C ionogel electrolytes. Improvements in the EDLC potential window and its long-term stability are dependent on a deeper understanding of the degradation mechanisms at higher potential window. In this regard, examples of suitable studies are listed in the future works (Chapter 8, section 8.4). Whether the main cause of capacitance decay is the water content in the electrolyte and the electrode or the functional groups on the activated carbon, appropriate measures can be undertaken to improve cell performance.

## 7.5 References

- [1] P.W. Ruch, D. Cericola, A. Foelske-Schmitz, R. Kötz, A. Wokaun, Aging of electrochemical double layer capacitors with acetonitrile-based electrolyte at elevated voltages, *Electrochim. Acta.* 55 (2010) 4412–4420. doi:10.1016/j.electacta.2010.02.064.
- [2] D. Cericola, P.W. Ruch, A. Foelske-Schmitz, D. Weingarh, R. Kötz, Effect of water on the aging of activated carbon based electrochemical double layer capacitors during constant voltage load tests, *Int. J. Electrochem. Sci.* 6 (2011) 988–996.
- [3] D. Weingarh, A. Foelske-Schmitz, R. Kötz, Cycle versus voltage hold – Which is the better stability test for electrochemical double layer capacitors?, *J. Power Sources.* 225 (2013) 84–88. doi:10.1016/J.JPOWSOUR.2012.10.019.
- [4] R. Kötz, P.W. Ruch, D. Cericola, Aging and failure mode of electrochemical double layer capacitors during accelerated constant load tests, *J. Power Sources.* 195 (2010) 923–928. doi:10.1016/J.JPOWSOUR.2009.08.045.
- [5] D. Weingarh, H. Noh, A. Foelske-Schmitz, A. Wokaun, R. Kötz, A reliable determination method of stability limits for electrochemical double layer capacitors, *Electrochim. Acta.* 103 (2013) 119–124. doi:10.1016/J.ELECTACTA.2013.04.057.
- [6] Y. Liu, B. Soucaze-Guillous, P.L. Taberna, P. Simon, Understanding of carbon-based supercapacitors ageing mechanisms by electrochemical and analytical methods, *J. Power Sources.* 366 (2017) 123–130. doi:10.1016/j.jpowsour.2017.08.104.
- [7] P. Ratajczak, K. Jurewicz, F. Béguin, Factors contributing to ageing of high voltage carbon/carbon supercapacitors in salt aqueous electrolyte, *J. Appl. Electrochem.* 44 (2014) 475–480. doi:10.1007/s10800-013-0644-0.

- [8] M. He, K. Fic, E. Fr̄ckowiak, P. Novák, E.J. Berg, Ageing phenomena in high-voltage aqueous supercapacitors investigated by in situ gas analysis, *Energy Environ. Sci.* 9 (2016) 623–633. doi:10.1039/C5EE02875B.
- [9] F. Endres, S. Zein El Abedin, Air and water stable ionic liquids in physical chemistry, *Phys. Chem. Chem. Phys.* 8 (2006) 2101. doi:10.1039/b600519p.
- [10] R. Newell, J. Faure-Vincent, B. Iliev, T. Schubert, D. Aradilla, A new high performance ionic liquid mixture electrolyte for large temperature range supercapacitor applications (−70°C to 80°C) operating at 3.5 V cell voltage, *Electrochim. Acta.* 267 (2018) 15–19. doi:10.1016/j.electacta.2018.02.067.
- [11] H. Zheng, H. Zhang, Y. Fu, T. Abe, Z. Ogumi, Temperature effects on the electrochemical behavior of spinel  $\text{LiMn}_2\text{O}_4$  in quaternary ammonium-based ionic liquid electrolyte, *J. Phys. Chem. B.* 109 (2005) 13676–13684. doi:10.1021/jp051238i.
- [12] A. Darmawan, R. Utari, R.E. Saputra, Suhartana, Y. Astuti, Synthesis and characterization of hydrophobic silica thin layer derived from methyltrimethoxysilane (MTMS), *IOP Conf. Ser. Mater. Sci. Eng.* 299 (2017) 012041.
- [13] K. Liu, C. Lian, D. Henderson, J. Wu, Impurity effects on ionic-liquid-based supercapacitors, *Mol. Phys.* 115 (2017) 454–464. doi:10.1080/00268976.2016.1271154.
- [14] L. Rescalvo, Burn-in test, electronic components-EEE parts, ALTER Technol. Gr. (n.d.). <https://wpo-altertechnology.com/burn-in-test-eee-components/> (accessed November 8, 2018).
- [15] D.J. Wilkins, The bathtub curve and product failure behavior part one - The bathtub curve, infant mortality and burn-in, *Reliab. HOTWIRE.* (2002). <https://www.weibull.com/hotwire/issue21/hottopics21.htm>.

- [16] K. Jurewicz, E. Frackowiak, F. Béguin, Towards the mechanism of electrochemical hydrogen storage in nanostructured carbon materials, *Appl. Phys. A Mater. Sci. Process.* 78 (2004) 981–987.  
doi:10.1007/s00339-003-2418-8.
- [17] Y. Huang, Y. Zhao, Q. Gong, M. Weng, J. Bai, X. Liu, Y. Jiang, J. Wang, D. Wang, Y. Shao, M. Zhao, D. Zhuang, J. Liang, Experimental and correlative analyses of the ageing mechanism of activated carbon based supercapacitor, *Electrochim. Acta.* 228 (2017) 214–225.  
doi:10.1016/j.electacta.2017.01.059.
- [18] L. Dagousset, G. Pognon, G.T.M. Nguyen, F. Vidal, S. Jus, P.H. Aubert, Electrochemical characterisations and ageing of ionic liquid/ $\Gamma$ -butyrolactone mixtures as electrolytes for supercapacitor applications over a wide temperature range, *J. Power Sources.* 359 (2017) 242–249.  
doi:10.1016/j.jpowsour.2017.05.068.
- [19] A. J. Roberts and R. Bhagat, In-situ quantification of gas evolution in pouch cell supercapacitors and its effect on device performance and operation, in: *Poster Present. Am. Int. Meet. Electrochem. Solid State Sci., Cancun, 2018.*  
<https://ecs.confex.com/ecs/aimes2018/webprogram/Paper115703.html>.
- [20] M.S. Shafeeyan, W.M.A.W. Daud, A. Houshmand, A. Shamiri, A review on surface modification of activated carbon for carbon dioxide adsorption, *J. Anal. Appl. Pyrolysis.* 89 (2010) 143–151.  
doi:10.1016/j.jaap.2010.07.006.
- [21] B.D. Epstein, E. Dalle-Molle, J.S. Mattson, Electrochemical investigations of surface functional groups on isotropic pyrolytic carbon, *Carbon N. Y.* 9 (1971) 609–615. doi:10.1016/0008-6223(71)90082-0.
- [22] A.H. Van Pelt, O.A. Simakova, S.M. Schimming, J.L. Ewbank, G.S. Foo, E.A. Pidko, E.J.M. Hensen, C. Sievers, Stability of functionalized activated carbon in hot liquid water, *Carbon N. Y.* 77 (2014) 143–154.  
doi:10.1016/J.CARBON.2014.05.015.

- [23] P.K. Dubey, A.S.K. Sinha, S. Talapatra, N. Koratkar, P.M. Ajayan, O.N. Srivastava, Hydrogen generation by water electrolysis using carbon nanotube anode, *Int. J. Hydrogen Energy*. 35 (2010) 3945–3950. doi:10.1016/J.IJHYDENE.2010.01.139.
- [24] H. Tang, Z. Qi, M. Ramani, J.F. Elter, PEM fuel cell cathode carbon corrosion due to the formation of air/fuel boundary at the anode, *J. Power Sources*. 158 (2006) 1306–1312. doi:10.1016/J.JPOWSOUR.2005.10.059.
- [25] B. Avasarala, R. Moore, P. Haldar, Surface oxidation of carbon supports due to potential cycling under PEM fuel cell conditions, *Electrochim. Acta*. 55 (2010) 4765–4771. doi:10.1016/J.ELECTACTA.2010.03.056.
- [26] R. German, P. Venet, A. Sari, O. Briat, J.M. Vinassa, Electrochemical double layer capacitors (supercapacitors) ageing impacts and comparison on different impedance models, *EPE J. (European Power Electron. Drives Journal)*. 24 (2014) 6–13. doi:10.1080/09398368.2014.11742747.
- [27] H. Every, A.G. Bishop, M. Forsyth, D.R. MacFarlane, Ion diffusion in molten salt mixtures, *Electrochim. Acta*. 45 (2000) 1279–1284. doi:10.1016/S0013-4686(99)00332-1.
- [28] A.I. Horowitz, M.J. Panzer, Poly(dimethylsiloxane)-supported ionogels with a high ionic liquid loading, *Angew. Chemie - Int. Ed.* 53 (2014) 9780–9783. doi:10.1002/anie.201405691.
- [29] M. Brachet, T. Brousse, J. Le Bideau, All solid-state symmetrical activated carbon electrochemical double layer capacitors designed with ionogel electrolyte, *ECS Electrochem. Lett.* 3 (2014) A112–A115. doi:10.1149/2.0051411eel.
- [30] Ionic liquids for electrochemical applications, *Aldrich ChemFiles*. 5 (2005) 10. <https://www.sigmaaldrich.com/technical-documents/articles/chemfiles/ionic-liquids-electrochemical.html> (accessed June 20, 2018).

- [31] M. Koel, Ionic liquids in chemical analysis, *Crit. Rev. Anal. Chem.* 35 (2005) 177–192. doi:10.1080/10408340500304016.

## 8. Conclusions and future work

### 8.1 Summary of the research questions

The ultimate aim of this thesis was to expand the current understanding of sol-gel processed ionogels as electrolytes for EDLCs. This work was designed to answer some of the key questions in relation to these ionogels:

- Can TMOS, TEOS, MTMS and MTES precursors influence the properties and performance of ionogels and if so, how (in terms of sol-gel process kinetics, microstructure, thermal stability and electrochemical performance)?
- How does [Emim][TfO] ionic liquid influence the kinetics of the sol-gel process for each investigated formulation?
- What influence a heat-curing process has on the resultant ionogels regarding:
  - a) Gelation time,
  - b) Penetration coefficient of the ionic liquid,
  - c) Physical properties,
  - d) Room-temperature electrochemical performance as electrolyte for activated carbon-based EDLCs.
- What factors can influence the long-term stability of EDLCs containing heat-cured ionogels?

### 8.2 Summary of the findings

Through a series of thorough investigations facilitated by Raman spectroscopy, SEM, EDX, TGA, and a series of electrochemical characterisation techniques, the influence of the nature of the alkoxide precursor, and the presence of [Emim][TfO] ionic liquid on the kinetics of the sol-gel process were identified and the physical properties of the resultant ionogels were characterised.

- Thermal stability of the ionic liquid was shown to improve when encapsulated inside a silica scaffold (the on-set decomposition temperature of [Emim][TfO] ionic liquid was increased by  $\geq 10^\circ\text{C}$ ) while the type of the alkoxide precursor had no apparent influence on the thermal stability of the ionogels.

- The presence of the ionic liquid promoted the formation of macropores within the gel scaffolds. The non-hydrolysable methyl groups in MTMS and MTES resulted in the formation of larger secondary silica particles and larger pore sizes within the silica network compared to systems containing TMOS and TEOS.
- It was shown that the sol-gel transition point is achieved at a slower rate for MTMS and MTES ionogels (4 days) compared to the TMOS and TEOS ionogels (12 hours). This delay is thought to be caused by (a) the presence of the non-hydrolysable methyl groups which retards the formation and crosslinking of the secondary silica particles (due to steric hindrance) as well as (b) the presence of the ionic liquid which acts as a barrier between the secondary silica particles.
- According to the electrochemical analysis results, EDLCs based on MTMS and MTES ionogels demonstrate more resistive behaviour than capacitive behaviour, in contrast to cells containing TMOS and TEOS ionogels, where the inverse is true. The delayed gelation of MTMS and MTES ionogels is believed to have resulted in greater ingress of the electrolyte solution into the AC electrode, as seen via EDX analysis. Gelation within the electrode is believed to result in blockage of the electrode pores and reduction of surface area of the electrode which causes an increase in the internal resistance of the cell as indicated in the EIS analysis results. This phenomenon was not observed when the gelation process was accelerated by heating.
- The *in situ* Raman analyses showed that the rate of silicon alkoxide consumption (evolution of Si–O stretching vibration band associated with Si–OC<sub>x</sub>H<sub>2x+1</sub>) is reduced in the presence of [Emim][TfO] ionic liquid for formulations containing TMOS, MTMS and TEOS precursors and followed the order of MTMS>TMOS~MTES>TEOS. The MTES ionogel was the only formulation that showed no change in the precursor consumption rate compared to its counterpart xerogel. This can be associated with the non-uniform dispersion of the [Emim][TfO] ionic liquid within the MTES ionogel mixture resulting in no apparent change in the rate of MTES consumption.

- Although TMOS and TEOS showed better electrochemical properties, their brittle structure can cause delamination from the AC electrode over time and result in an increase in the internal resistance of the EDLCs.
- TMOS and MTMS were shown to be the most compatible precursors in terms of precursor consumption rate in both the absence and the presence of [Emim][TfO] ionic liquid among the four silica precursors studied.

Long gelation periods of the investigated ionogels are not industrially favourable or scalable, therefore, a series of thermally cured ionogels were synthesised at 125, 150, 175 and 200°C, in order to accelerate the gelation process. To ensure successful gelation with minimum shrinkage, a formulation containing 75 mol% MTMS and 25 mol% TMOS precursors was utilised.

- The ionogels were found to fully gel between 75 and 90 minutes.
- The EDLCs fabricated using thermally-cured ionogels were analysed electrochemically and demonstrated a reduction in resistivity with increased curing temperature. This was associated with (a) enhanced wetting of the AC electrode by the ionic liquid and (b) the interlocking effect at the electrode-electrolyte interface as a result of the heat-curing. The interlocking effect was shown to reduce  $R_{ct}$  value of the AC-based EDLCs at room temperature enhancing the room-temperature ion transport kinetics.
- Ionogels cured at 125 and 150°C showed no signs of shrinkage with an extended electrode wetting time of 48 hours.
- It was shown that 175°C is the optimal curing temperature for the studied systems due to the minimal resultant shrinkage, excellent capacitive behaviour ( $95 \text{ mF cm}^{-2}$ ) and short electrode wetting time (5 hours).
- Ionogels thermally cured at 200°C suffered from fracturing, making them an unsuitable candidate for solid electrolytes.
- Based on the preliminary investigation on long-term stability (characterised by float test at 2.5 V) of the EDLCs, it was shown that the ionogel curing process at 150°C improves long-term stability of the EDLCs relative to cells with [Emim][TfO] ionic liquid without the gel network.

- The long-term stability results indicated that a maximum stable potential window of 2.5 V can be achieved for activated carbon-based EDLCs containing ionogels cured at 150°C.
- The float test results did not indicate a clear difference between the performance of EDLCs with 'as-received' and 'dried' ionic liquids (with 686.8 and 52.3 ppm water content, respectively).

### 8.3 Key conclusions

From the findings summarised in section 8.2, the following key conclusions have been drawn from this body of research. These conclusions are aimed at answering the initial research questions and providing direct solutions to the industry.

- The choice of alkoxide precursor for ionogel solid matrix has significant influence on the resulting microstructure and electrochemical performance of the ionogel as an electrolyte in EDLCs.
- For gelation under ambient conditions, TMOS and TEOS ionogels have been shown to be advantageous compared to MTMS and MTES ionogels in terms of gelation rate and electrochemical performance. However, these precursors can suffer from extensive shrinkage and fracturing when aged under ambient conditions, which jeopardises their application as solid electrolytes.
- A one-step heat-cure process can be utilised to improve not only the gelation rate of the sol-gel derived ionogels but also the electrode wetting rate and room-temperature ion transport kinetics in the resultant EDLCs. For the investigated system in this project, 175°C curing temperature demonstrated the shortest electrode wetting time of 5 hours and the highest specific capacitance of  $\sim 95 \text{ mFcm}^{-2}$  compared to other curing temperatures investigated (125, 150 and 200°C).
- The heat-curing process at 150°C has been shown to improve the long-term stability of the EDLCs compared to cells without the gel network. The reason for this observation requires further investigation to characterise the key capacitance degradation mechanisms of EDLCs containing activated carbon electrodes and [Emim][TfO] ionic liquid electrolyte.

### 8.4 Placement of this work against published works

As it was highlighted in Chapter 2, supercapacitors possess higher power densities compared to batteries. A specific power density versus specific energy density plot, referred to as Ragone plot, is often used to demonstrate the difference in the performance of energy storage devices. In order to evaluate where this work stands against other published works in the field of energy storage, the specific energy and power density of the fabricated EDLC were calculated (as shown below) based on the specifications of the cell with 150°C-cured ionogel with 'dried' IL (as summarised in Table 7.4). Based on the calculated values, the Ragone plot (retrieved from [1]) in Figure 8.1 was modified accordingly.

$$E = \frac{1}{2} C_{sp} V^2 = \frac{1}{2} (12.04)(2.5)^2 \frac{1000}{3600} = 10.45 \text{ Wh kg}^{-1}$$

$$P_{max} = \frac{V^2}{4 \times ESR \times m_T} = \frac{2.5^2}{4 \times 42.82 \times 19.12 \times 10^{-6}} = 1908.47 \text{ W kg}^{-1}$$

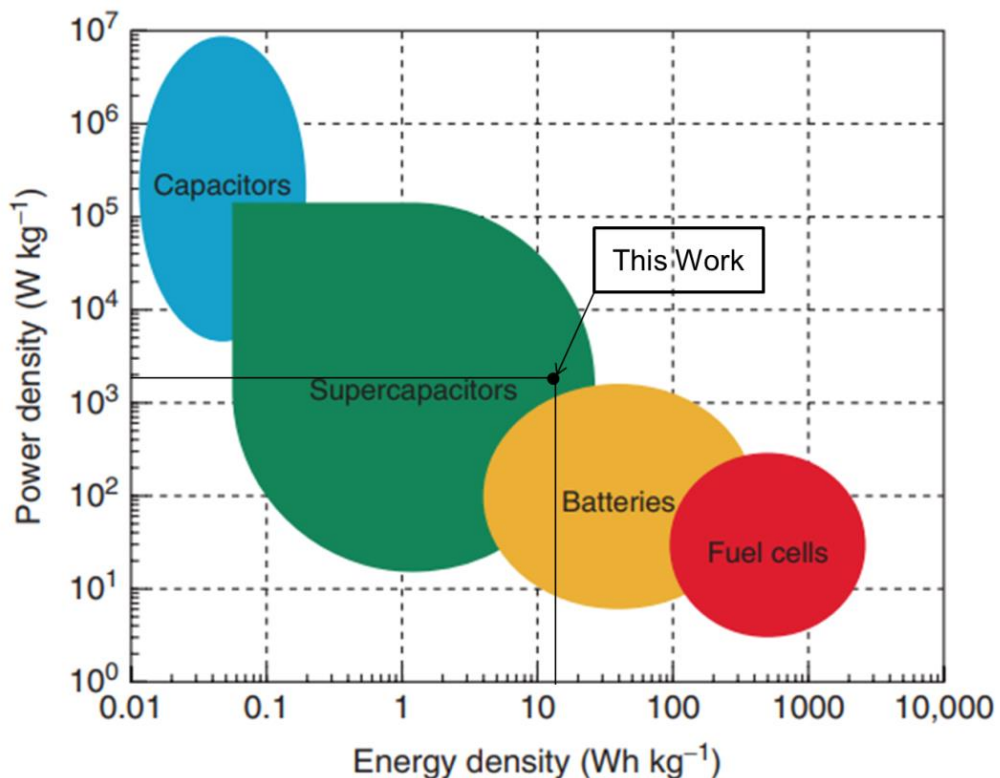


Figure 8.1 Ragone plot retrieved and modified from [1]. Specifications of the cell utilised for energy and power densities calculations: 150°C-cured ionogel with 'dried' IL, Round 1 after 555 hours of float test, (Chapter 7, Table 7.4).

## 8.5 Future work

The work in this thesis has provided new beneficial insights into sol-gel derived ionogels as the electrolyte for EDLCs and investigated a number of influencing factors, including formulation, curing temperature and ionic liquid water content. The studies presented, while yielding new information that may be of interest to the energy storage industry, could benefit from further studies that were either out-of-scope of this project, or were not possible due to facility limitations:

The porous structure of the ionogels could be better understood through additional experimentation, such as through BET analysis, to understand the influence of the precursor material on the pore volume and pore size distribution of the silica skeleton.

The influence of environmental humidity on TMOS and TEOS based ionogels must be elucidated in order to prevent extensive shrinkage post gelation (as observed in Chapter 5 under ambient conditions) and to help develop the best handling practice of these ionogels.

More *in situ* and *ex situ* Raman analysis are needed to complement the conducted study on the IL-silica interactions when different alkoxide precursors are used in order to conclusively determine the nature and degree of these interactions.

Smaller step sizes could be investigated between 150 and 175°C in order to isolate an ideal temperature range for thermal curing, improving on the given ideal temperature of 175°C. The shelf-life of the heat-cured ionogels can be characterised using a combination of Raman spectroscopy and electrochemical analysis techniques after aging the ionogels or the ionogel-coated AC electrodes in a dry environment for 6 to 12 months.

A number of studies could be conducted to characterise the degradation mechanisms of the heat-cured EDLCs. Such studies can be categorised into two groups: *in situ* and post-failure. For the latter, the aged cells have to be disassembled. It would be necessary to wash the electrolyte from different components such as the electrode and the separator (if available) using D.I. water and drying them in a vacuum oven prior to any characterisations to

ensure no electrolyte or water residue has remained. It must be noted that during this preparation process, some of the parasitic products may be washed away. In the case of the present work, extra effort must be made to remove traces of silica scaffold infused within the surface of the activated carbon electrode (the heat-induced interlocking effect that was demonstrated in Chapter 6). Examples of the two categories of studies are provided here:

1) *In-situ* studies:

- a. Differential electrochemical mass spectroscopy (DEMS) can be used to characterise the real-time gas products from parasitic reactions throughout the float test of the EDLC [2].
- b. Raman spectroscopy (as suggested by Kim *et al.* in 2016 [3]) can be utilised instead of DEMS to carry out real-time characterisation of evolved gases as the EDLC is being aged.

2) Post-failure studies:

- a. Raman spectroscopy to evaluate the structural changes of the activated carbon [4] caused by the aging process. This study requires comparative analysis between fresh and aged positive and negative electrodes.
- b. SEM to monitor the variation in the morphology and microstructure of the electrode and current collector [5].
- c. BET analysis to characterise variations in the porosity of the activated carbon electrodes after being aged [6].

## 8.6 References

- [1] B.K. Kim, S. Sy, A. Yu, J. Zhang, Electrochemical supercapacitors for energy storage and conversion, *Handb. Clean Energy Syst.* (2015) 1–25. doi:10.1002/9781118991978.hces112.
- [2] M. Hahn, A. Würsig, R. Gallay, P. Novák, R. Kötz, Gas evolution in activated carbon/propylene carbonate based double-layer capacitors, *Electrochem. Commun.* 7 (2005) 925–930. doi:10.1016/J.ELECOM.2005.06.015.
- [3] J. Kim, E. Kim, U. Lee, I. Lee, S. Han, H. Son, S. Yoon, Nondisruptive in situ Raman analysis for gas evolution in commercial supercapacitor cells, *Electrochim. Acta.* 219 (2016) 447–452. doi:10.1016/J.ELECTACTA.2016.10.030.
- [4] M. Zhu, C.J. Weber, Y. Yang, M. Konuma, U. Starke, K. Kern, A.M. Bittner, Chemical and electrochemical ageing of carbon materials used in supercapacitor electrodes, *Carbon N. Y.* 46 (2008) 1829–1840. doi:10.1016/j.carbon.2008.07.025.
- [5] Y. Huang, Y. Zhao, Q. Gong, M. Weng, J. Bai, X. Liu, Y. Jiang, J. Wang, D. Wang, Y. Shao, M. Zhao, D. Zhuang, J. Liang, Experimental and correlative analyses of the ageing mechanism of activated carbon based supercapacitor, *Electrochim. Acta.* 228 (2017) 214–225. doi:10.1016/j.electacta.2017.01.059.
- [6] P.W. Ruch, D. Cericola, A. Foelske-Schmitz, R. Kötz, A. Wokaun, Aging of electrochemical double layer capacitors with acetonitrile-based electrolyte at elevated voltages, *Electrochim. Acta.* 55 (2010) 4412–4420. doi:10.1016/j.electacta.2010.02.064.